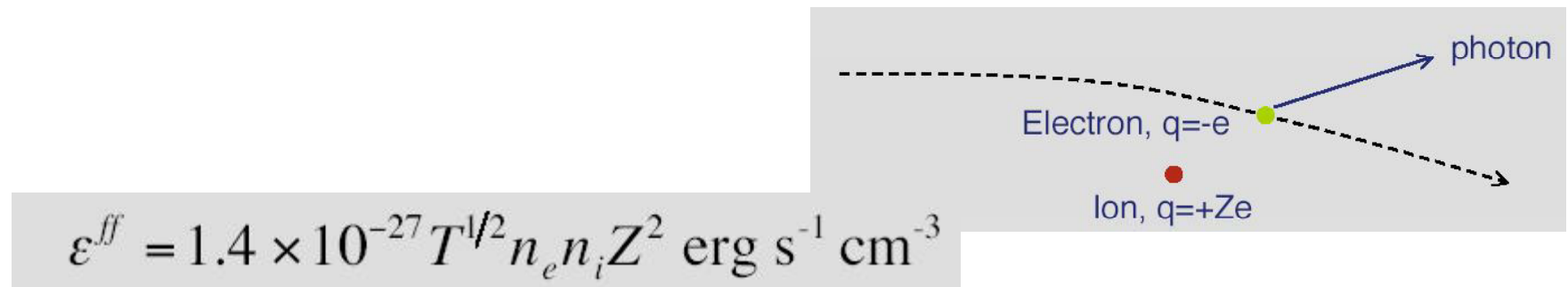
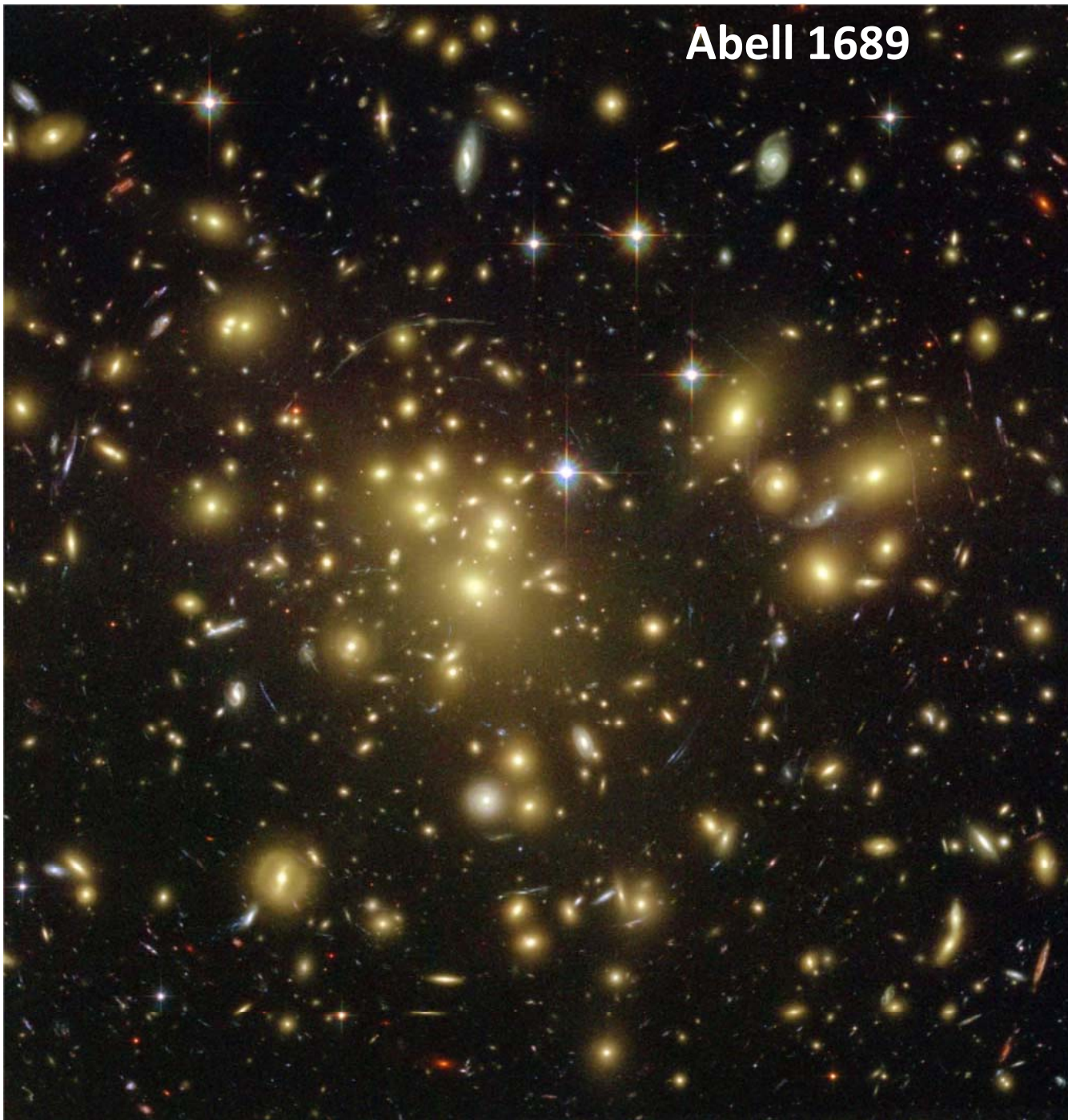


Aglomerados de Galáxias (ou de ME?)

- Os maiores sistemas gravitacionalmente conectados no Universo.
- 10^{2-3} galáxias, $10^{14-15} M_{\odot}$, $R \sim 1-3$ Mpc
- $\sim 16\%$ M_{total} é ICM, $\sim 3\%$ M_{total} está em galáxias
- A maior parte da matéria bariônica (não escura) está sob a forma de gás intergalático (Meio Intra-Aglomerado – ICM) com $T \sim 10^{7-8}$ K, que emite fortemente em raios-X através de radiação Bremstrahlung
- Emissividade



Abell 1689



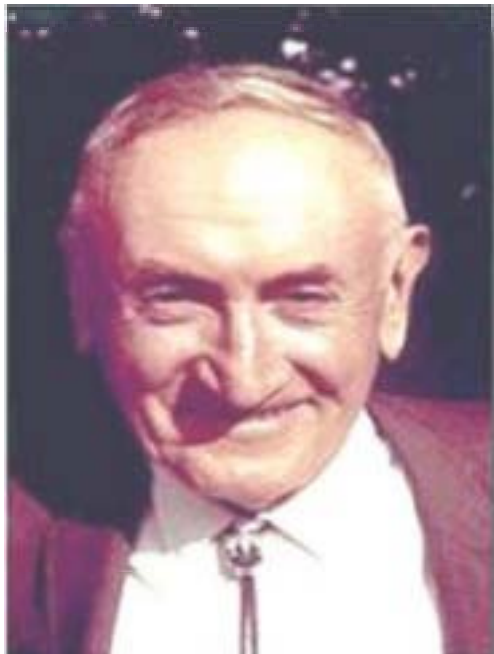
Cluster – Wolf 1906 – Abell 1958

Virial Method => $2T + \Omega = 0$

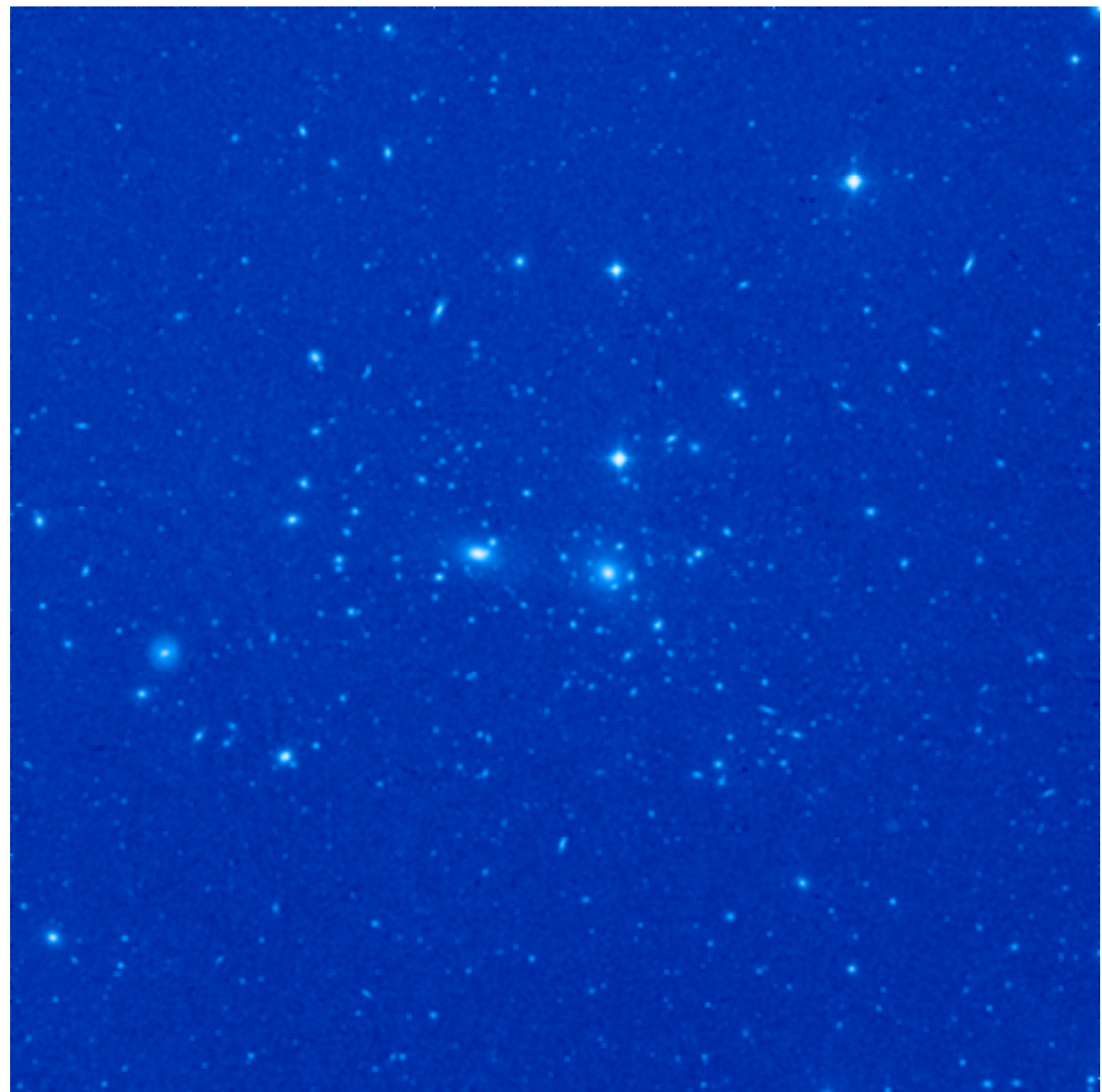
$$T = \frac{1}{2} M v^2 = \frac{3}{2} M \sigma_{\text{los}}^2$$

$$\Omega = - GM^2/R$$

$$M = 3 \sigma_{\text{los}}^2 R / G$$



Fritz Zwicky, 1933



All these masses are bigger than the sum of galaxies by >10 times! **Missing Mass**

Keplerian relation $v_c^2 = GM_{obs}/r$.

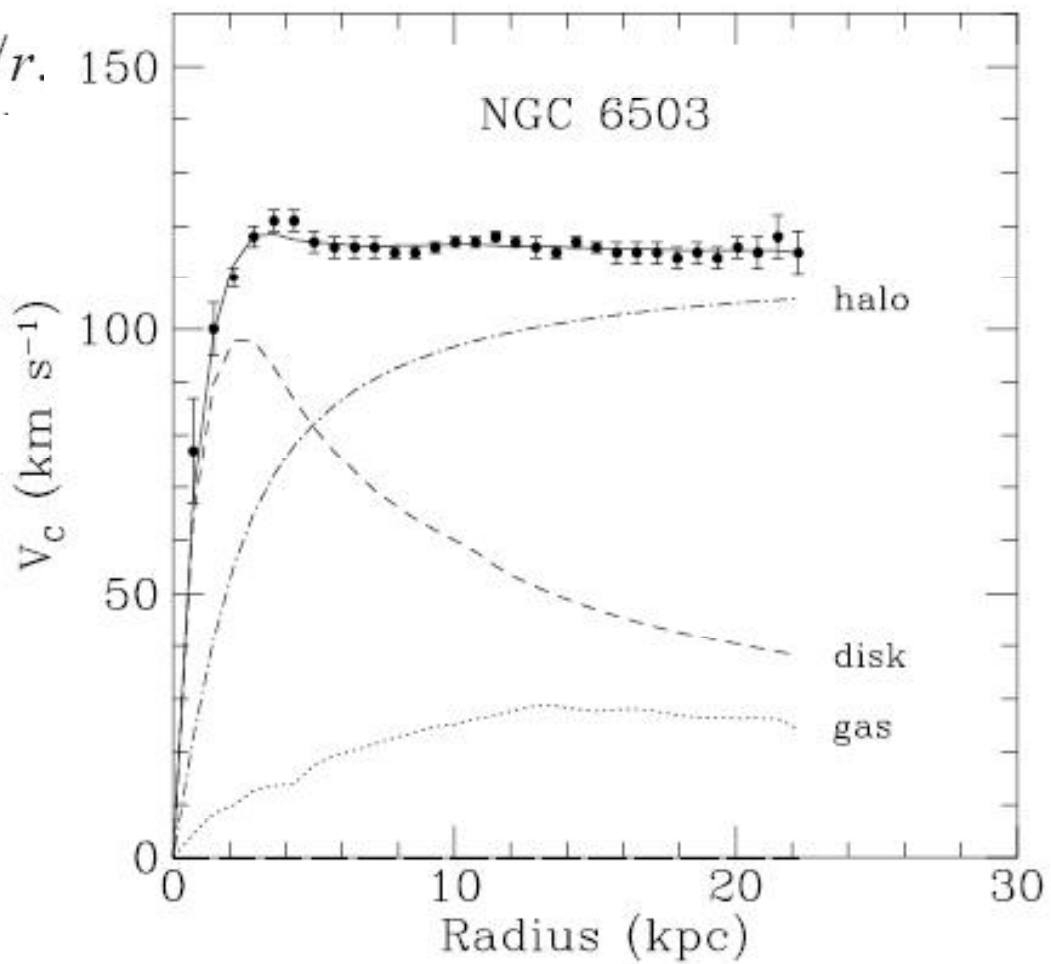
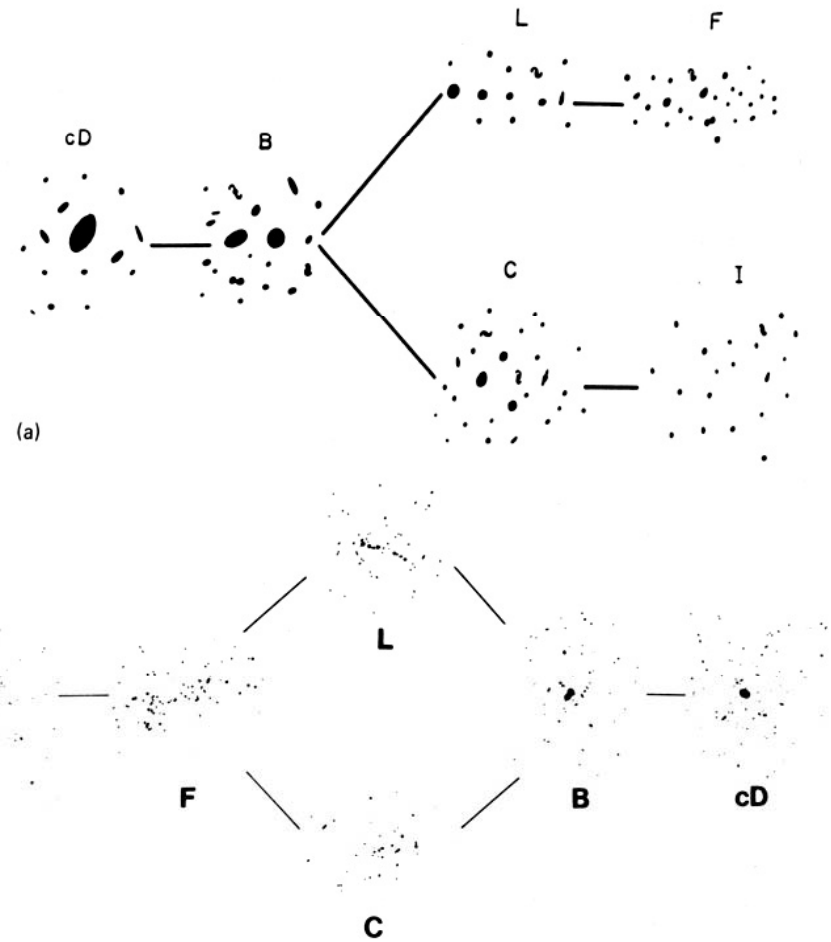


Fig. 1: Measured rotation curve of NGC6503 with best fit and contributions from halo, disk and gas. From Ref. [8]

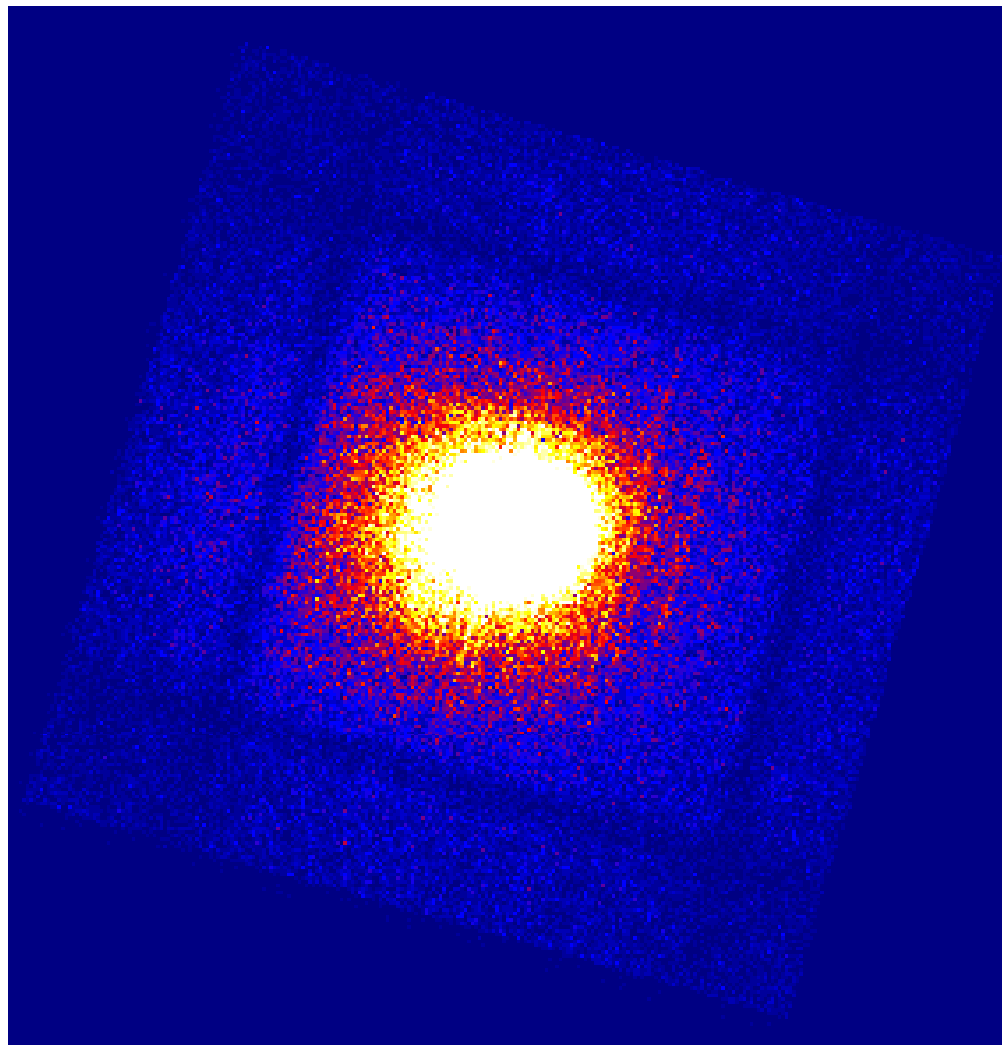
Property	Regular	Intermediate	Irregular
Zwicky Type	Compact	Medium-Compact	Open
Bautz-Morgan Type	I,I-II,II	II,II-III	II-III,III
Rood-Sastry Type 1971	cD,B,L,C	L,C,F	F,I
Galactic Content E:SO:Sp	Elliptical-rich 3:4:2	Spiral-poor 1:4:2	Spiral-rich 1:2:3
Morgan Type	ii	i-ii	i
Oemler Type	cD,Spiral-poor	Spiral-poor	Spiral-rich
Symmetry	Spherical	Intermediate	Irregular
Central Concentration	High	Moderate	Low _(b)
Subclustering	Absent	Moderate	Significant
Richness	Rich $n^* 10^2$	Rich-Moderate $n^* 10^1$	Rich-Poor $n^* 10^0$



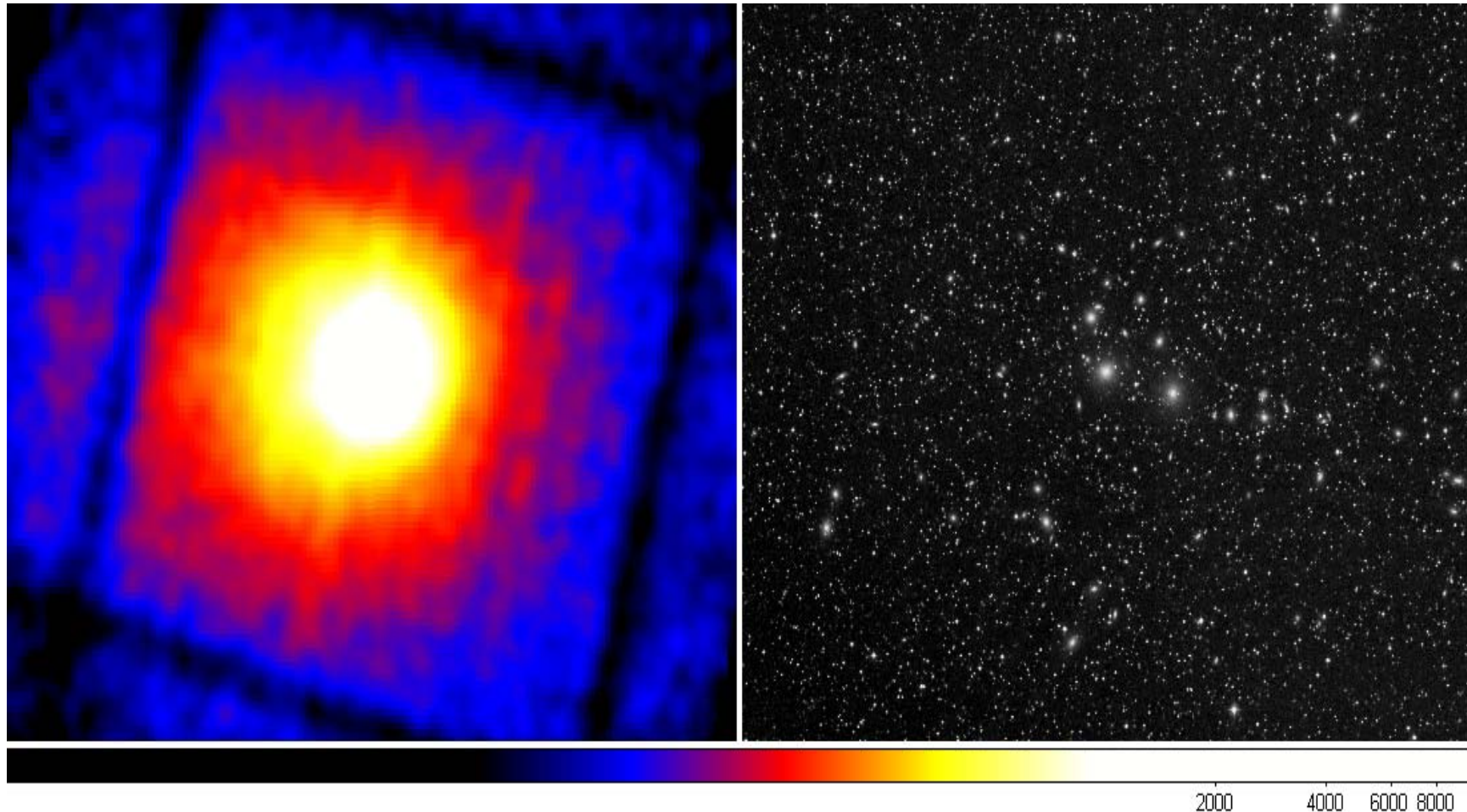
Descoberta de emissao de raios-X

Foguetes com proportional counters – Perseus e Coma clusters

Satelite Uhuru – Giacconi et al. 72, 10^{43} - 10^{45} erg/s

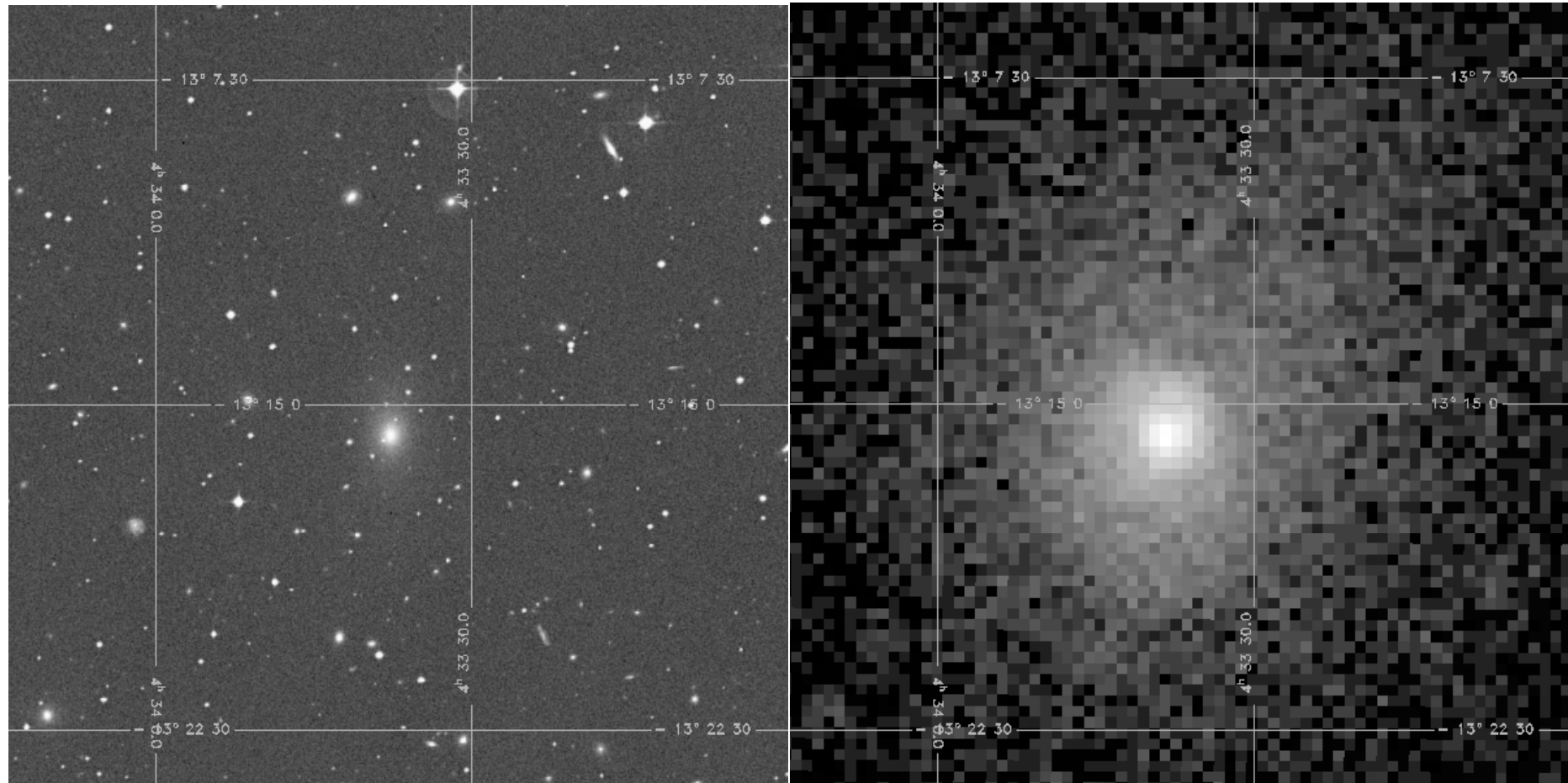


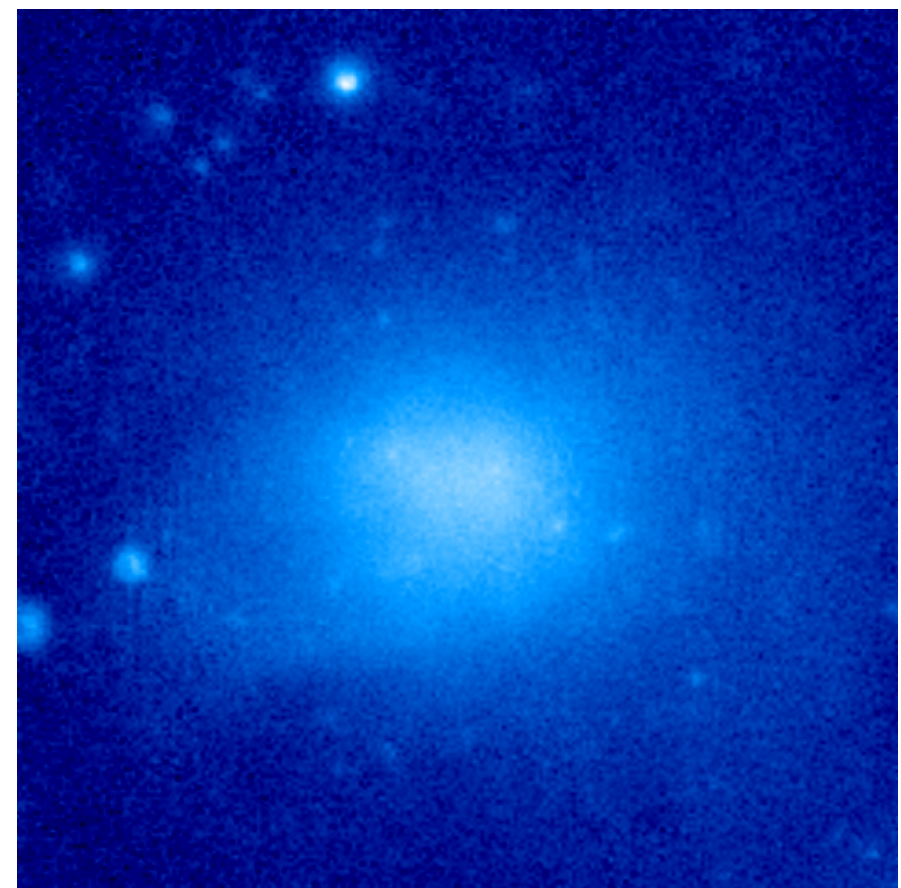
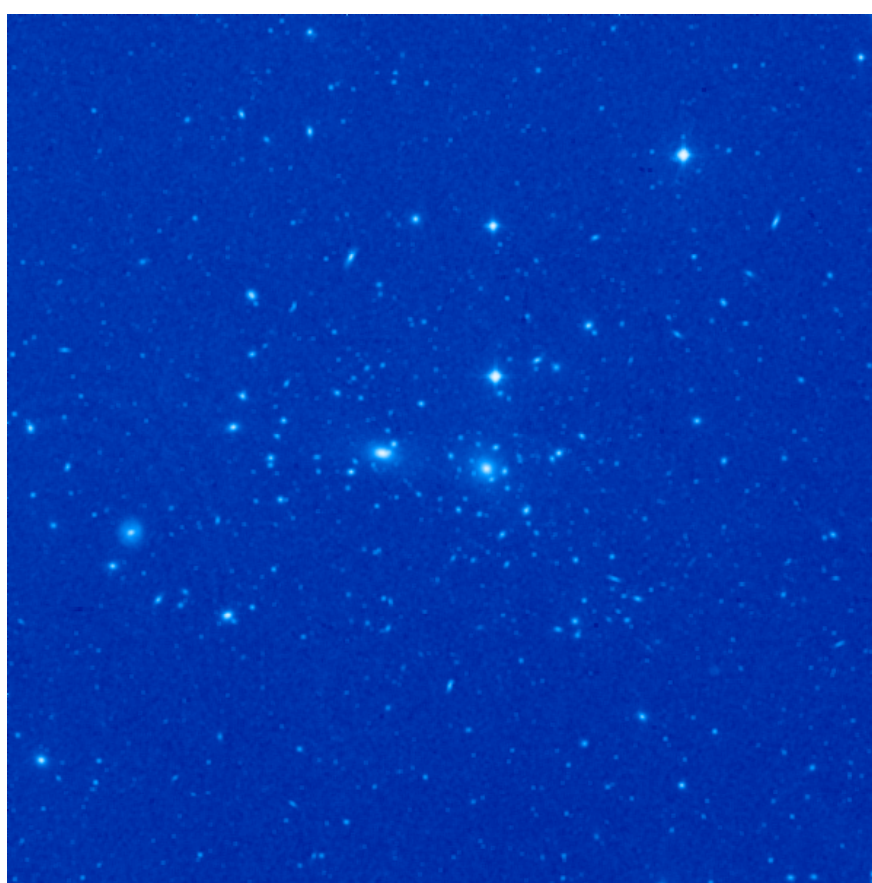
Perseus Cluster z=0.018 → 77 Mpc = 250 milhoes de anos-luz



Abell 496

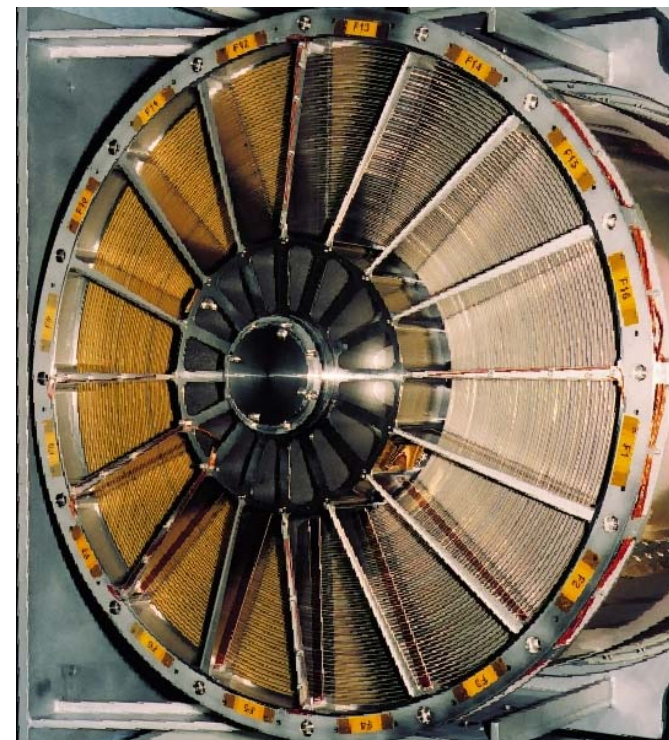
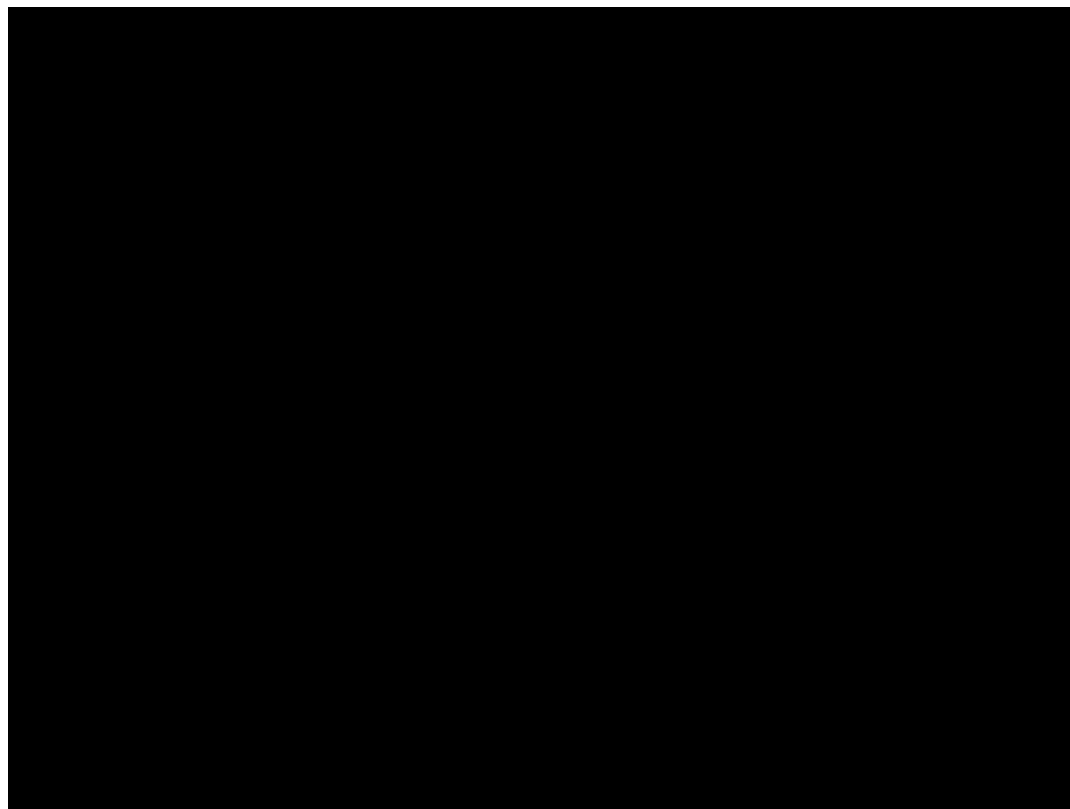
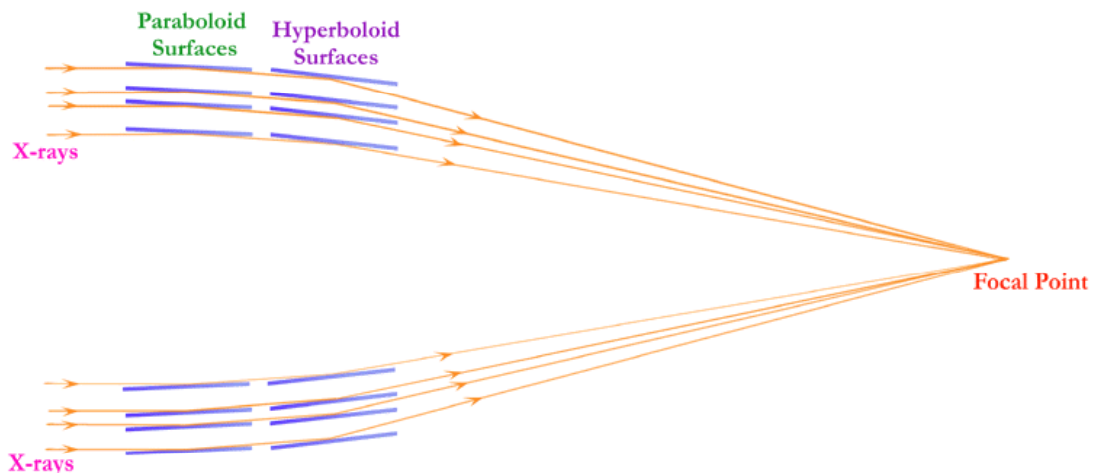
$z=0.032$





COMA, $z \sim 0.023$

Grazing incidence x-ray X-configuration



$1 \text{ keV} \sim 10 \text{ Angstrom} - 10 \text{ keV} \sim 1 \text{ Angstrom}$ $1 \text{ keV} \sim 10^7 \text{ Kelvin} - 10 \text{ keV} \sim 10^8 \text{ Kelvin}$
 $E = h\nu$ $E = 3/2 kT$

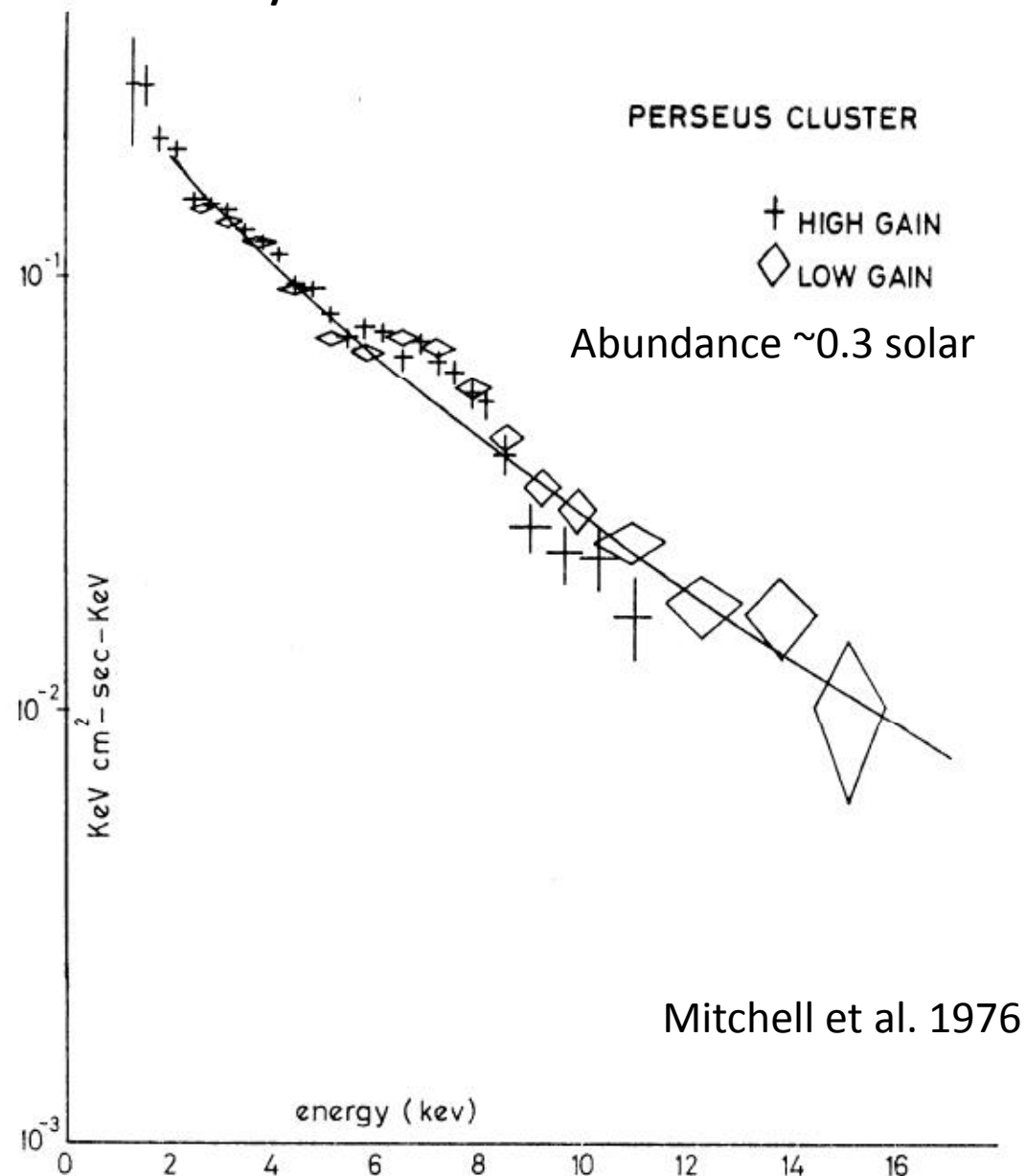
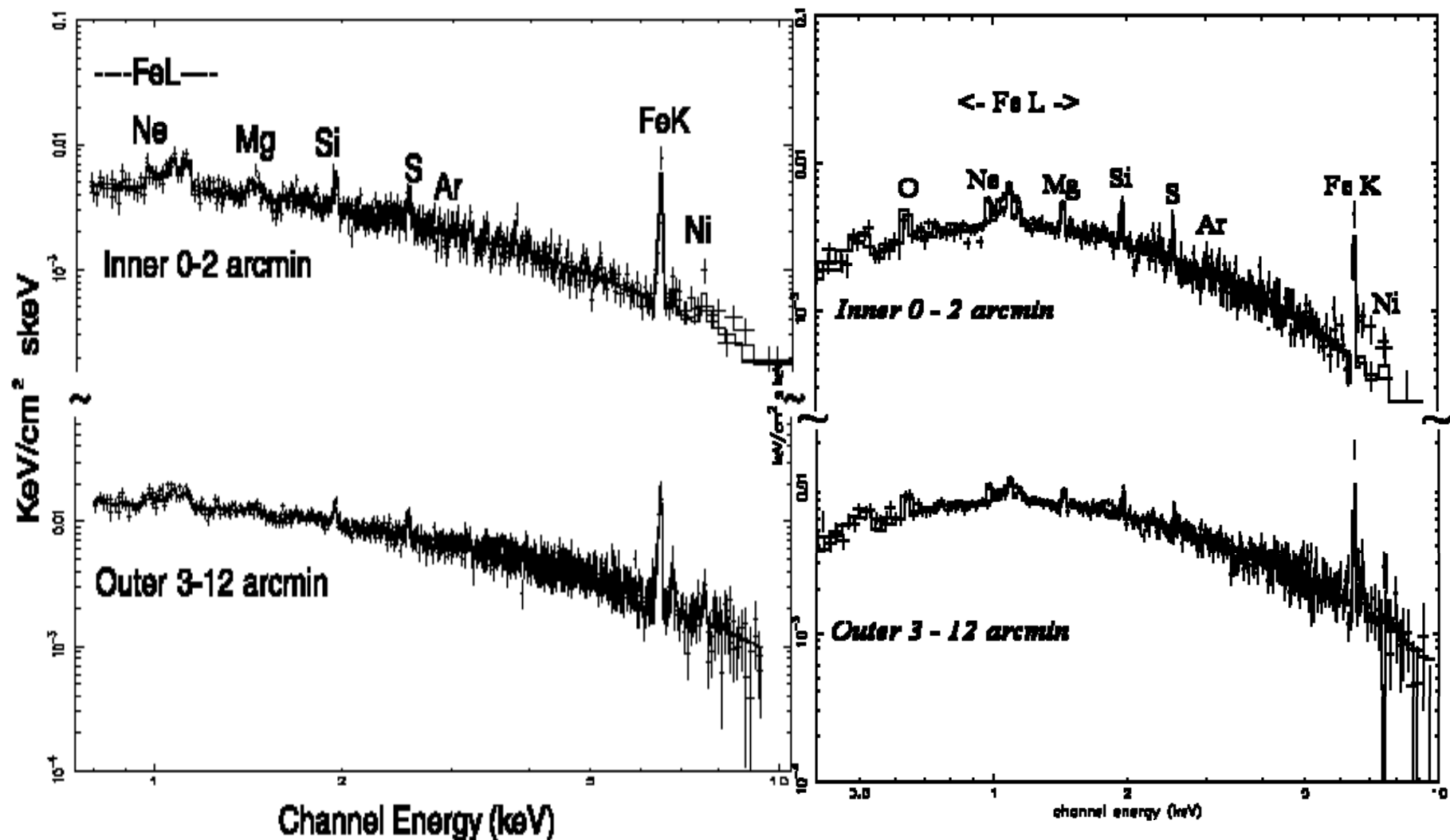


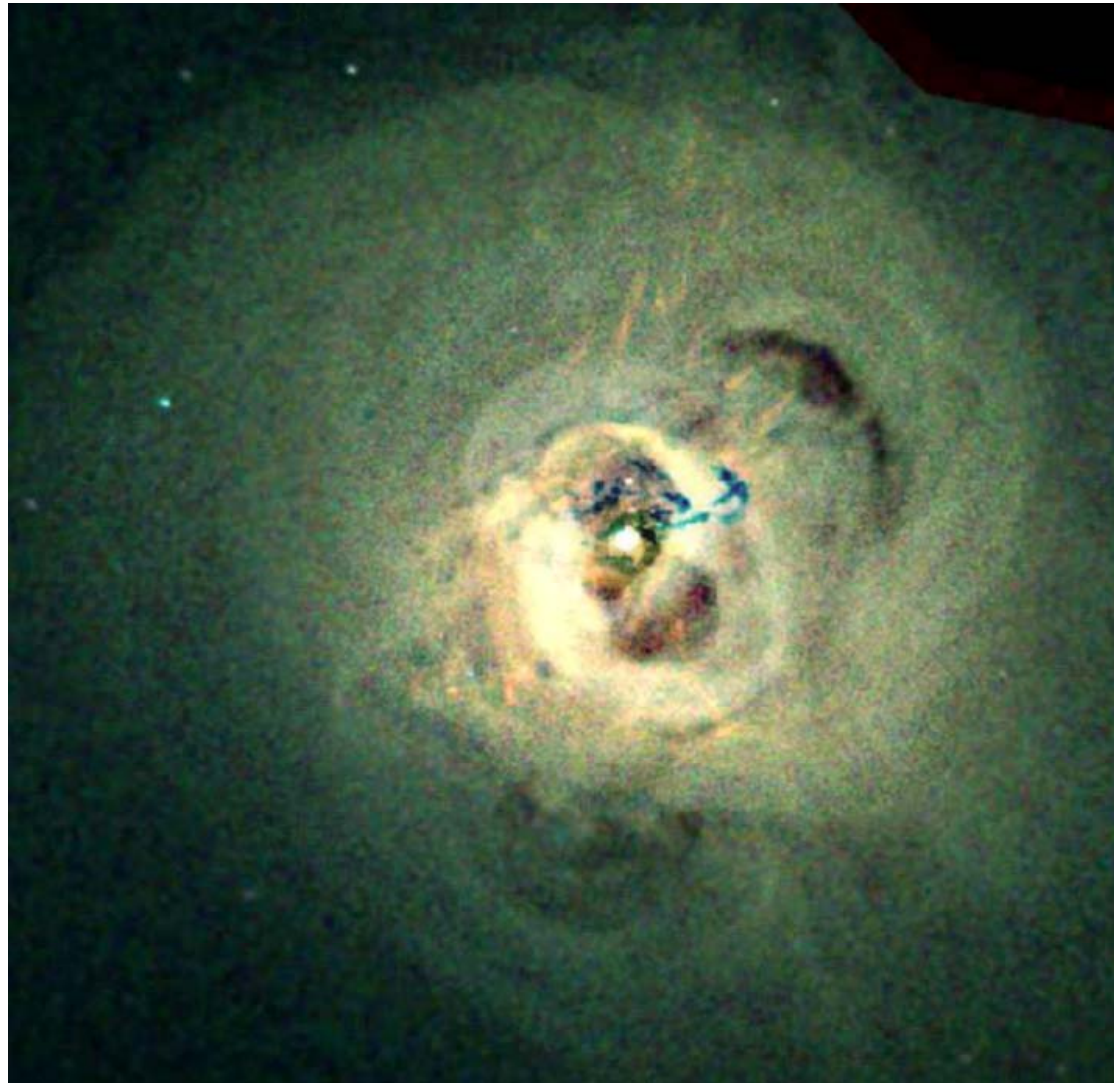
FIG. 1. The Ariel 5 X-ray spectrum of the Perseus Cluster in the energy range 1.3-16 keV.



Chandra

Superpoder – Imageamento

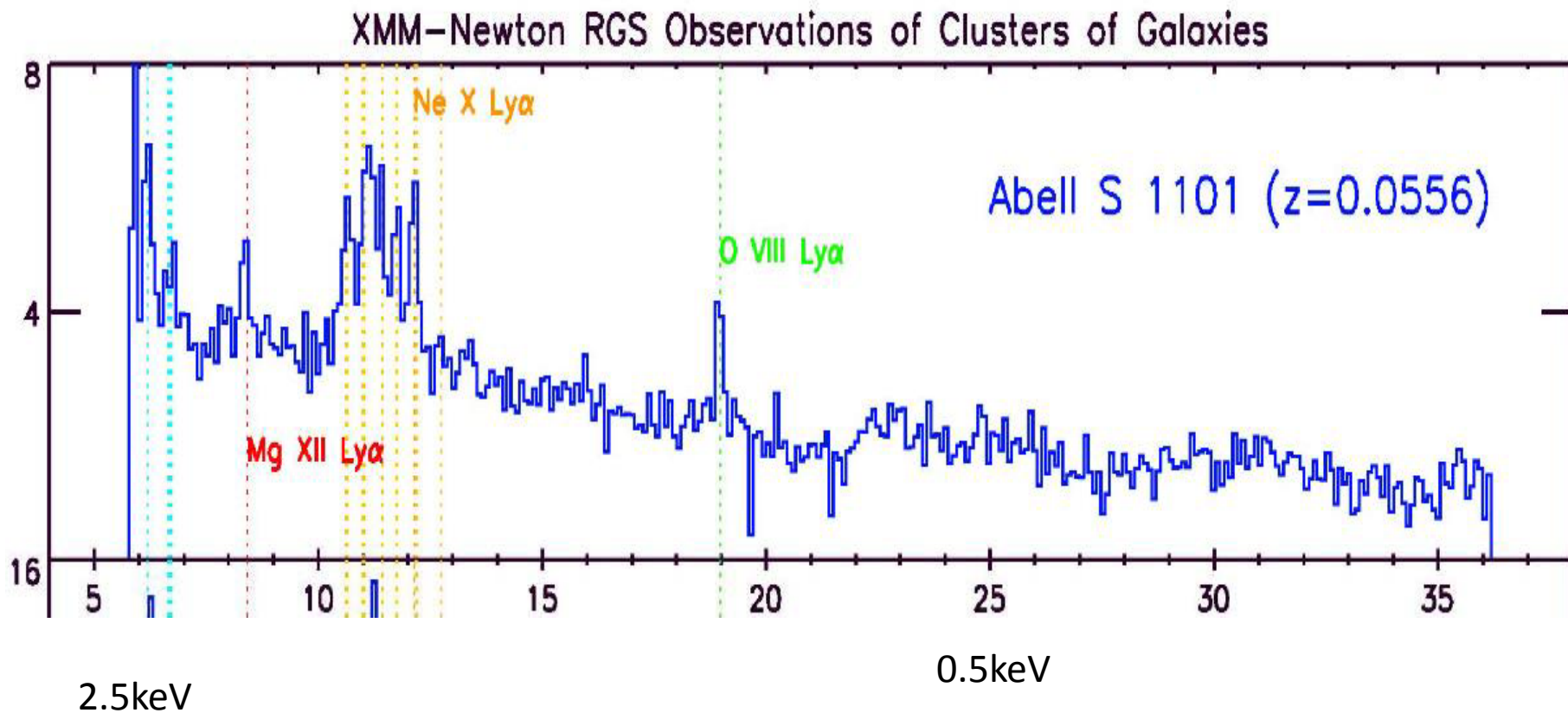
Mas espectroscopia tambem e' boa



XMM-Newton

Superpoder – Resolucao espetroscopica

Mas imagem tambem e' boa



$$\lambda_{mfp} = \frac{3\sqrt{3\pi}}{4\pi} \frac{(kT)^2}{e^4 n \ln \Lambda} \rightarrow 37.8 + \ln \frac{T_8}{\sqrt{n-3}}$$

$$\lambda_{mfp} \approx 23 T_8^2 / n_{-3}$$

$$t_{ep} \approx \frac{\lambda_{mfp}}{\langle v_{rel} \rangle} \simeq 10^7 T_8^{3/2} / n_{-3}$$

$$t_{cross} \approx R/c_s \sim 6.5 \times 10^8 \sqrt{T_8} \text{ pc}$$

$$R_f = R_i/2 \rightarrow \text{if } v \propto r^{-1/2}$$

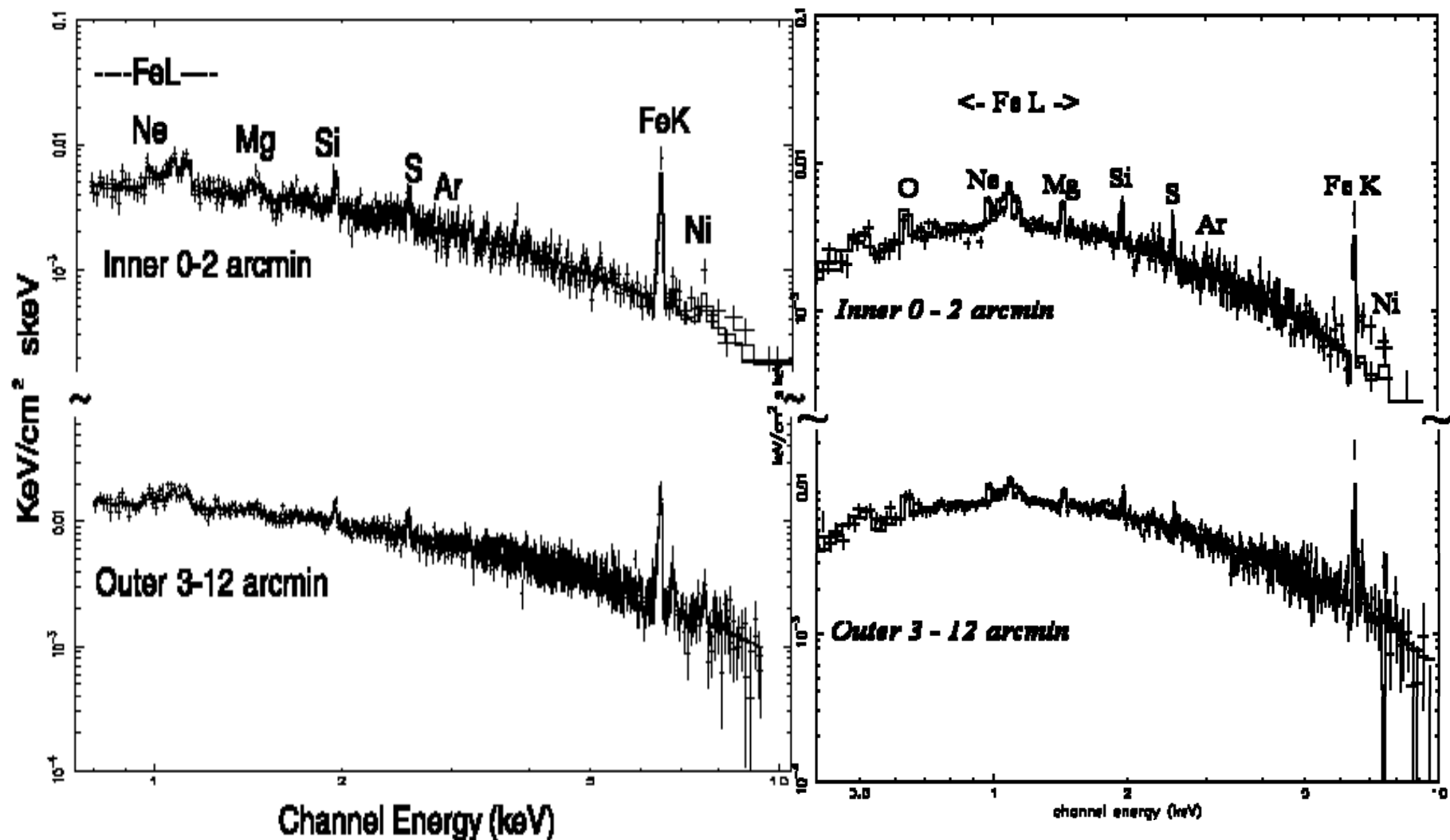
$$M(<\eta) = -\frac{\kappa T \eta}{\mu m_e G} \left(\frac{d \ln \rho}{d \ln \eta} + \frac{d \ln T}{d \ln \eta} \right)$$

$$\rho \approx \rho_0 \left(1 + \frac{\eta^2}{\eta_c^2}\right)^{-3/2}$$

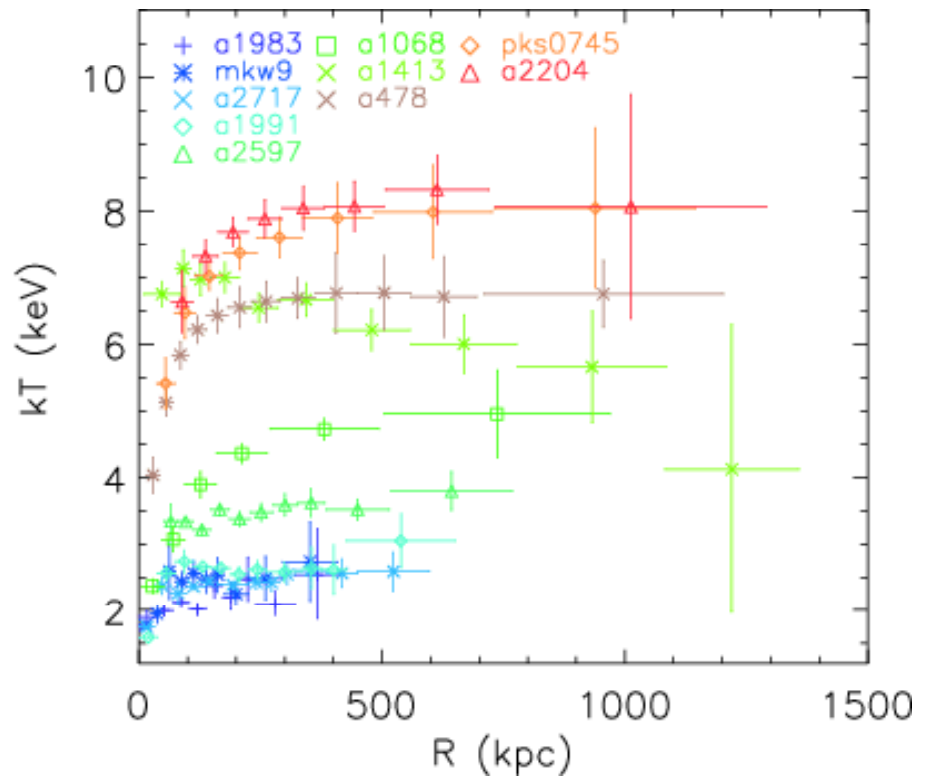
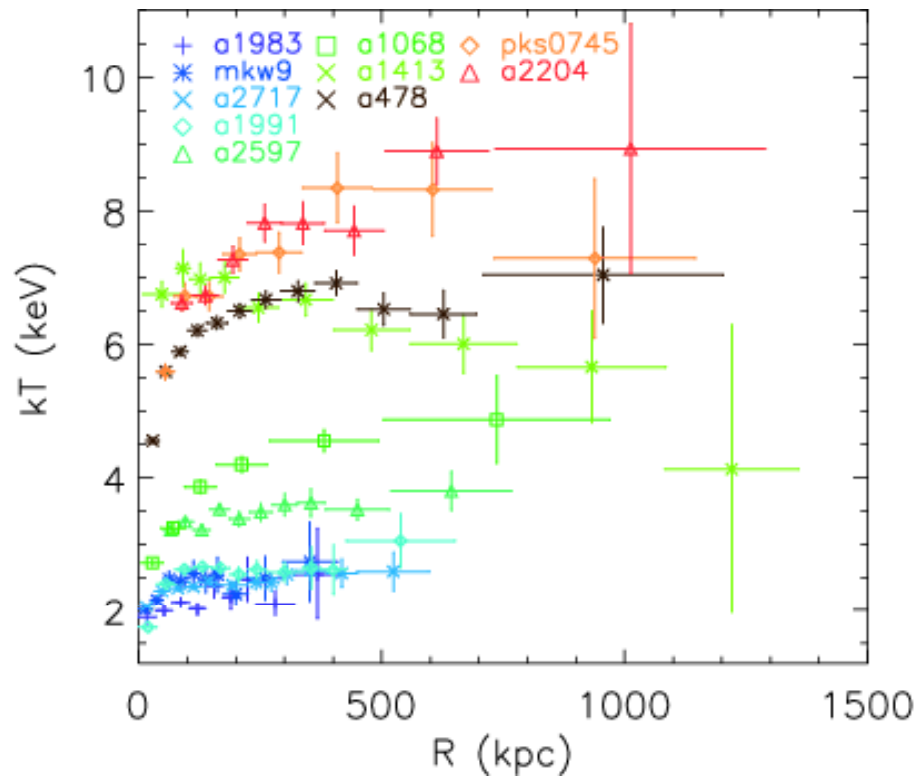
$$F(b) = 2 \int_b^R \frac{f(\eta) \eta d\eta}{\sqrt{\eta^2 - b^2}}$$

b invert

$$f(\eta) = -\frac{1}{\pi \eta} \frac{d}{d\eta} \int_{\eta}^{\infty} \frac{F(b) b db}{\sqrt{b^2 - \eta^2}}$$



Cooling Flows



Pointecouteau, Arnaud & Pratt 2005

$$\varepsilon^{ff} = 1.4 \times 10^{-27} T^{1/2} n_e n_i Z^2 \text{ erg s}^{-1} \text{ cm}^{-3}$$

$$emissivity = \frac{energy}{volume * time} \left[\frac{\text{erg}}{\text{cm}^3 \text{s}} \right]$$

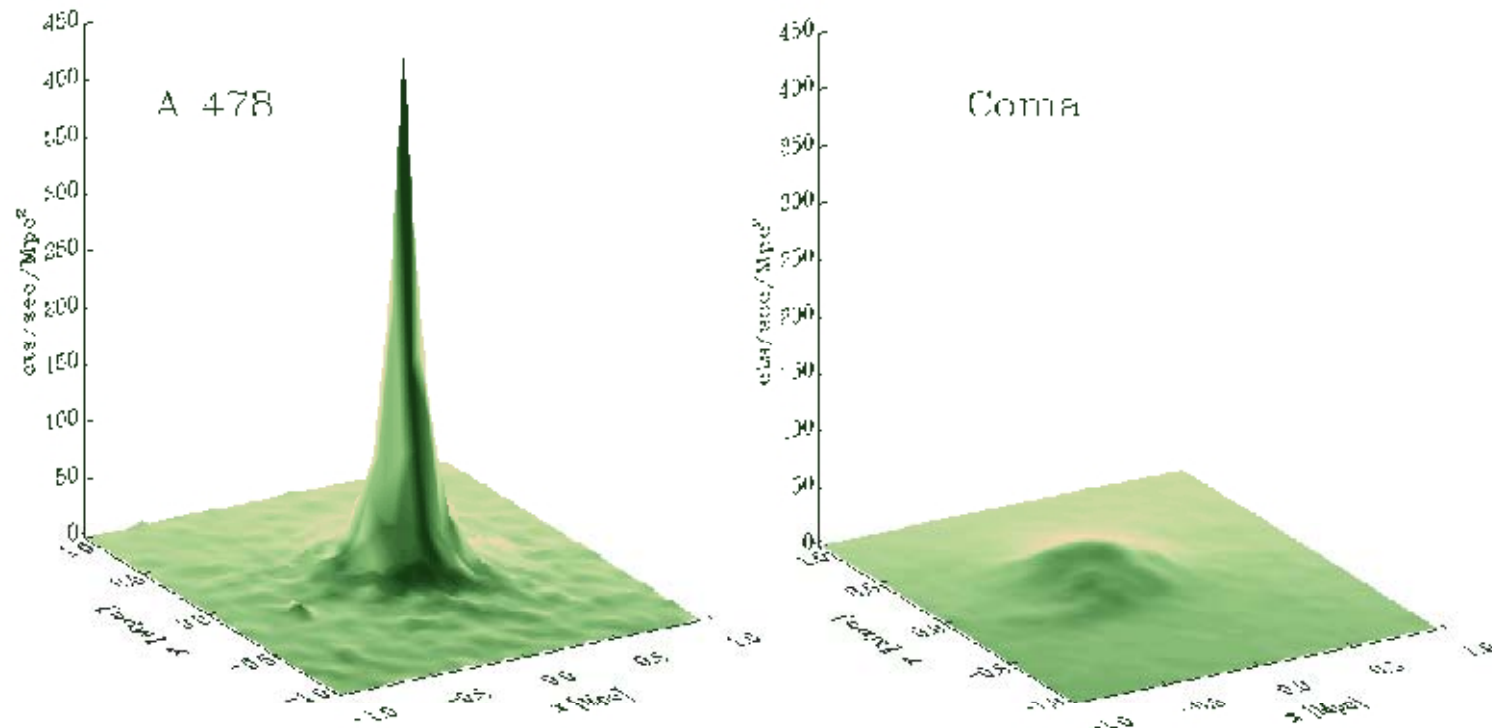
$$E_{particle} = \frac{3}{2} kT \Rightarrow \frac{E_{gas}}{volume} = \frac{3}{2} nkT$$

$$\varepsilon(emissivity) = \frac{1}{volume} \frac{dE_{gas}}{dt} = \frac{3}{2} nk \frac{dT}{dt}$$

$$time_{cool} = \frac{T}{dT/dt} \quad t_{cool} = 8.5 \times 10^{10} \text{ yr} \left(\frac{n_p}{10^{-3} \text{ cm}^{-3}} \right)^{-1} \left(\frac{T_g}{10^8 \text{ K}} \right)^{1/2},$$

Se botar os numeros $time_{cool} < 10^{10}$ years!

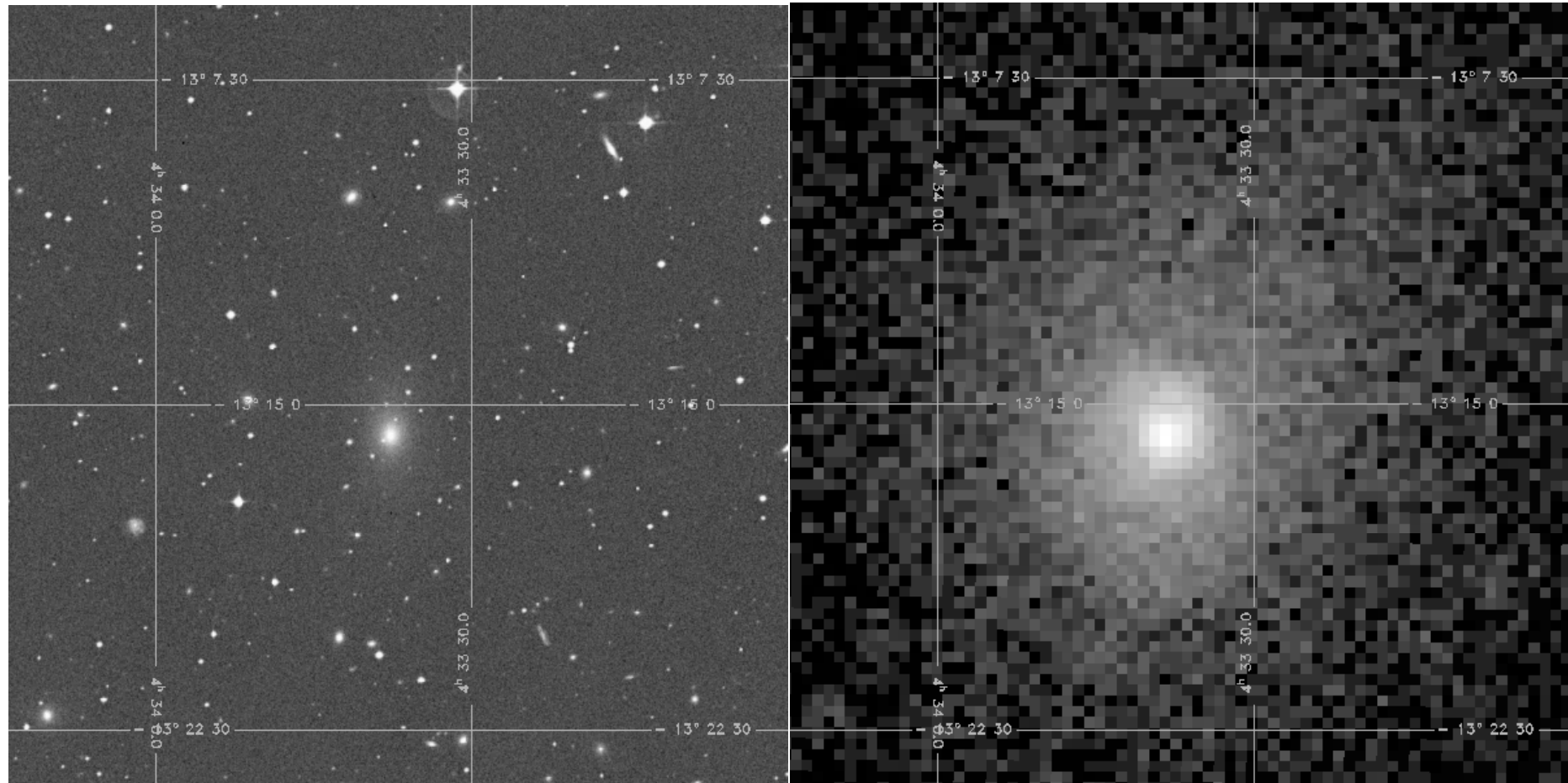
Evidencia para cooling

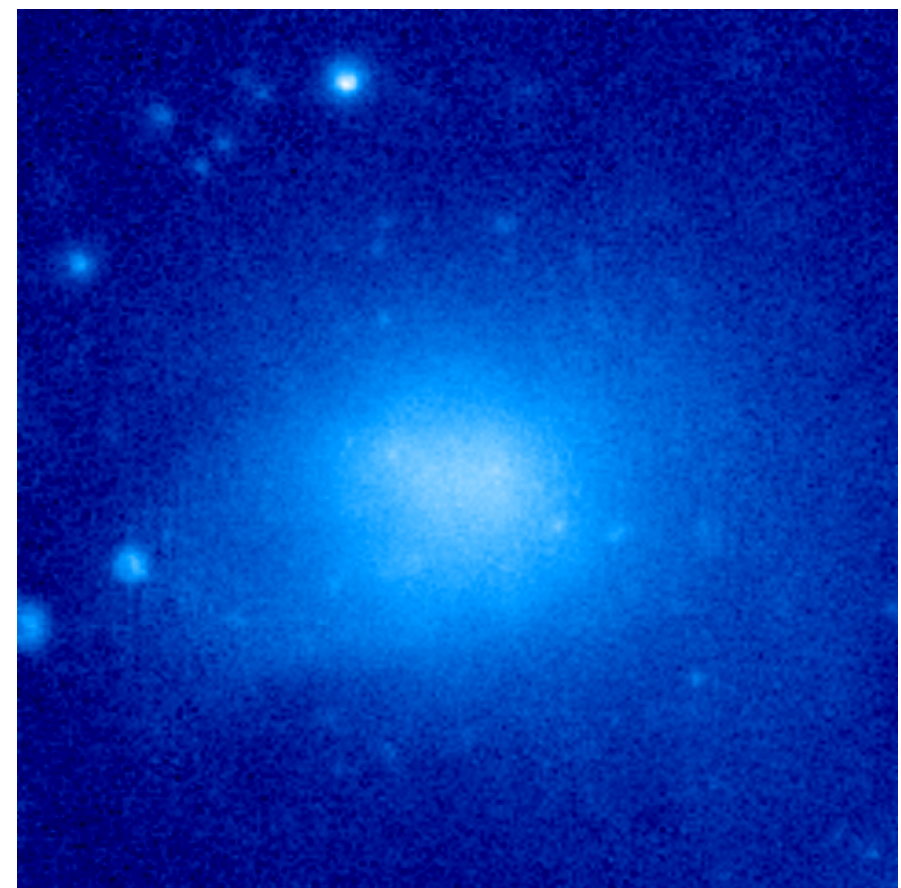
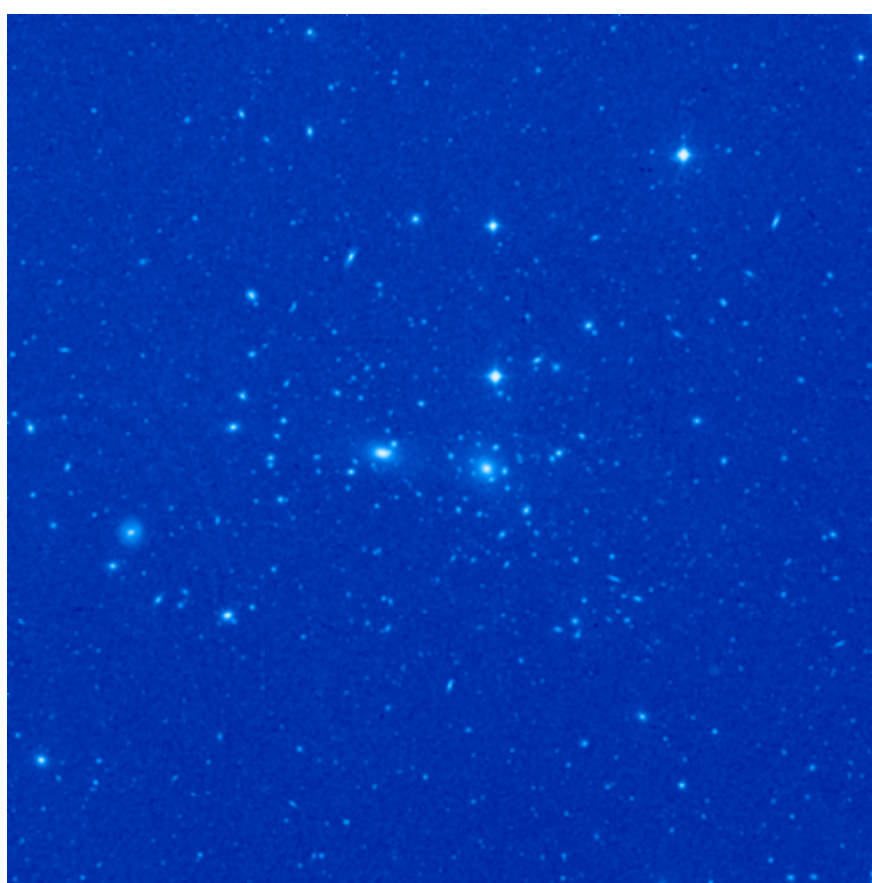


A luminosidade central e' extraordinariamente alta.

Abell 496

$z=0.032$



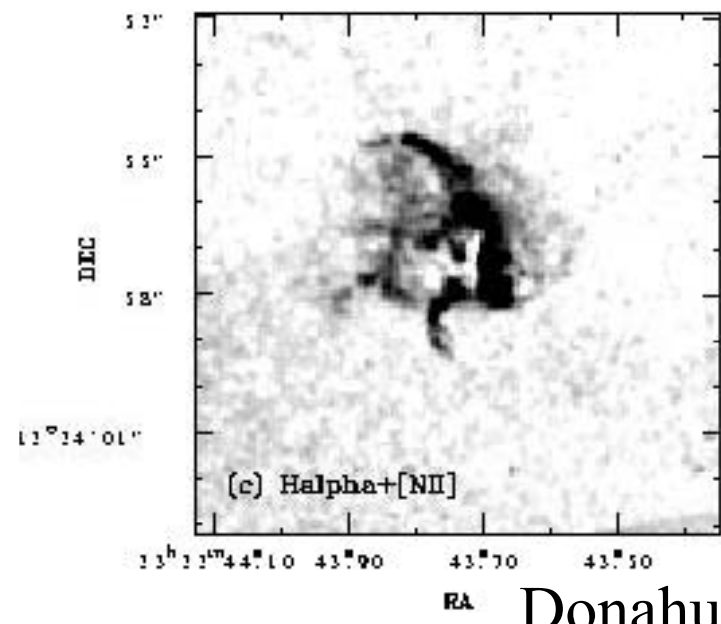
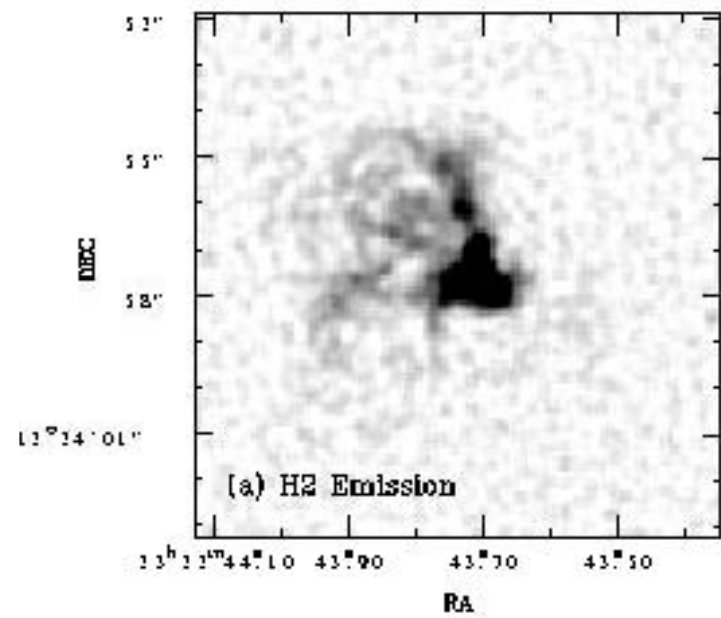


COMA, $z \sim 0.023$

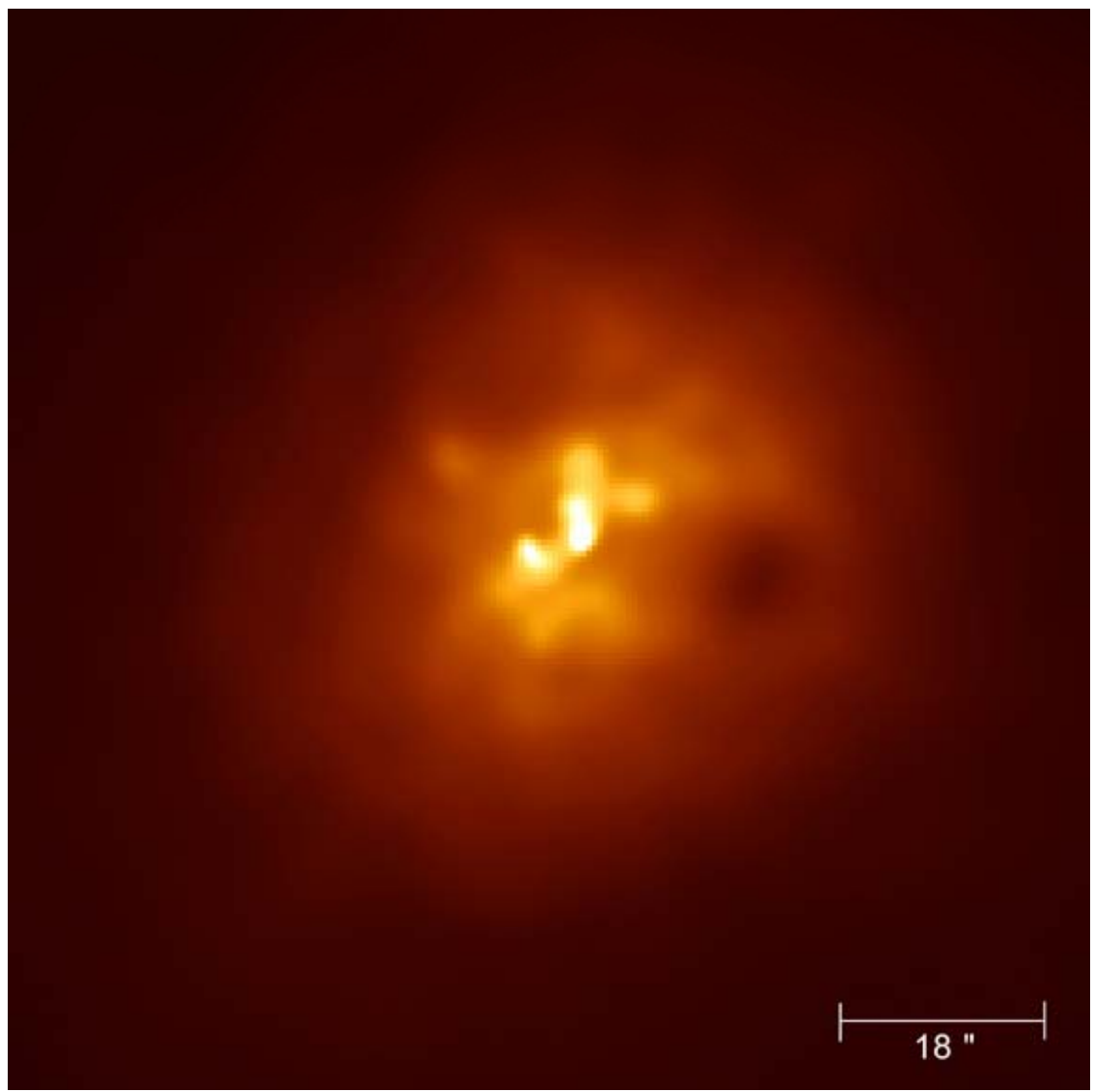
Trouble with “Cooling Flows”?

- Aglomerados tipo “cooling flows” foram definidos como tendo o tempo de resfriamento menor que o tempo de Hubble (idade do Universo).
- Se nenhum aquecimento para o resfriamento teria 100-1000s de massas solares por ano caindo no centro dos aglomerados.
- No inicio dos anos 90 a busca começo .

A busca por materia barionica fria

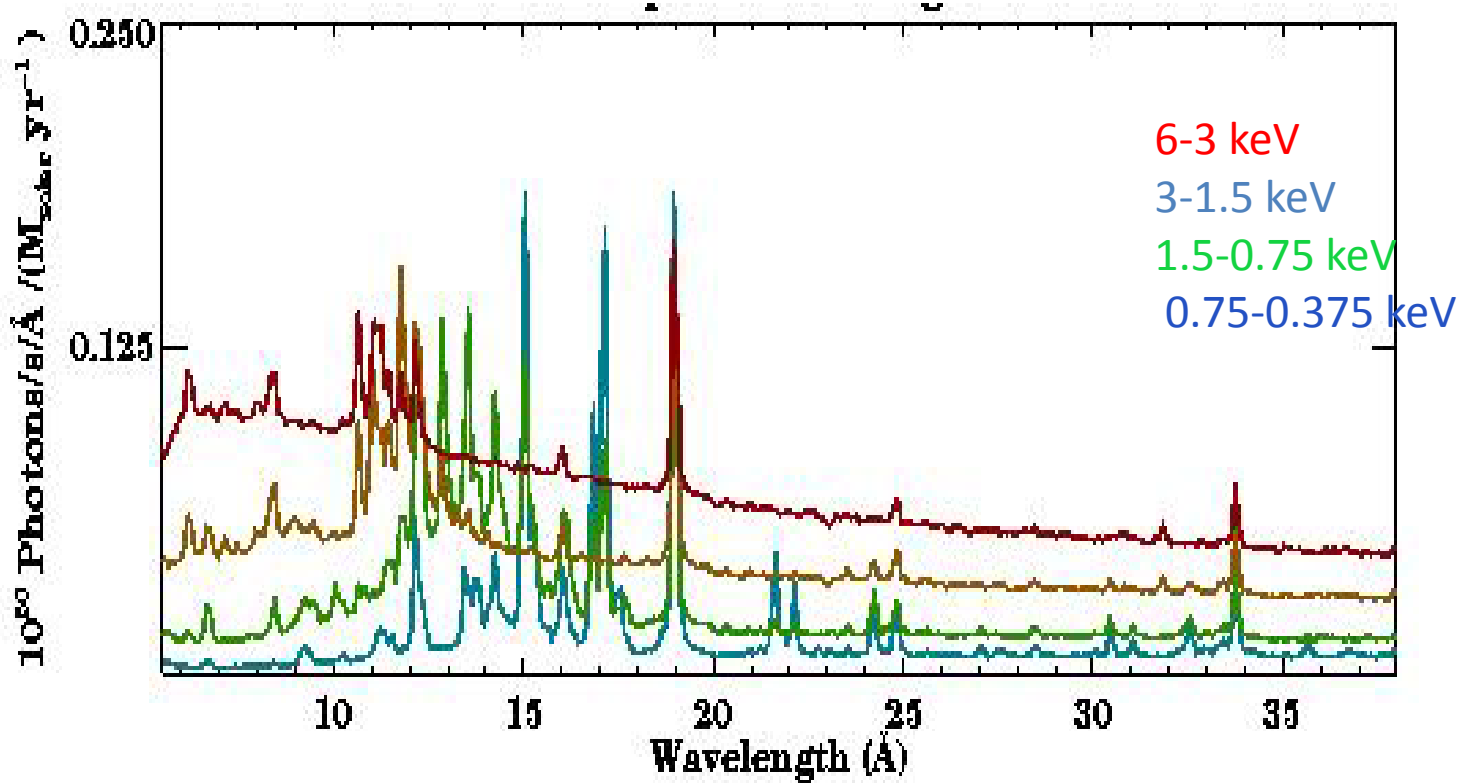


Donahue et al. 2001



Abell 2597
McNamara et al. 2002

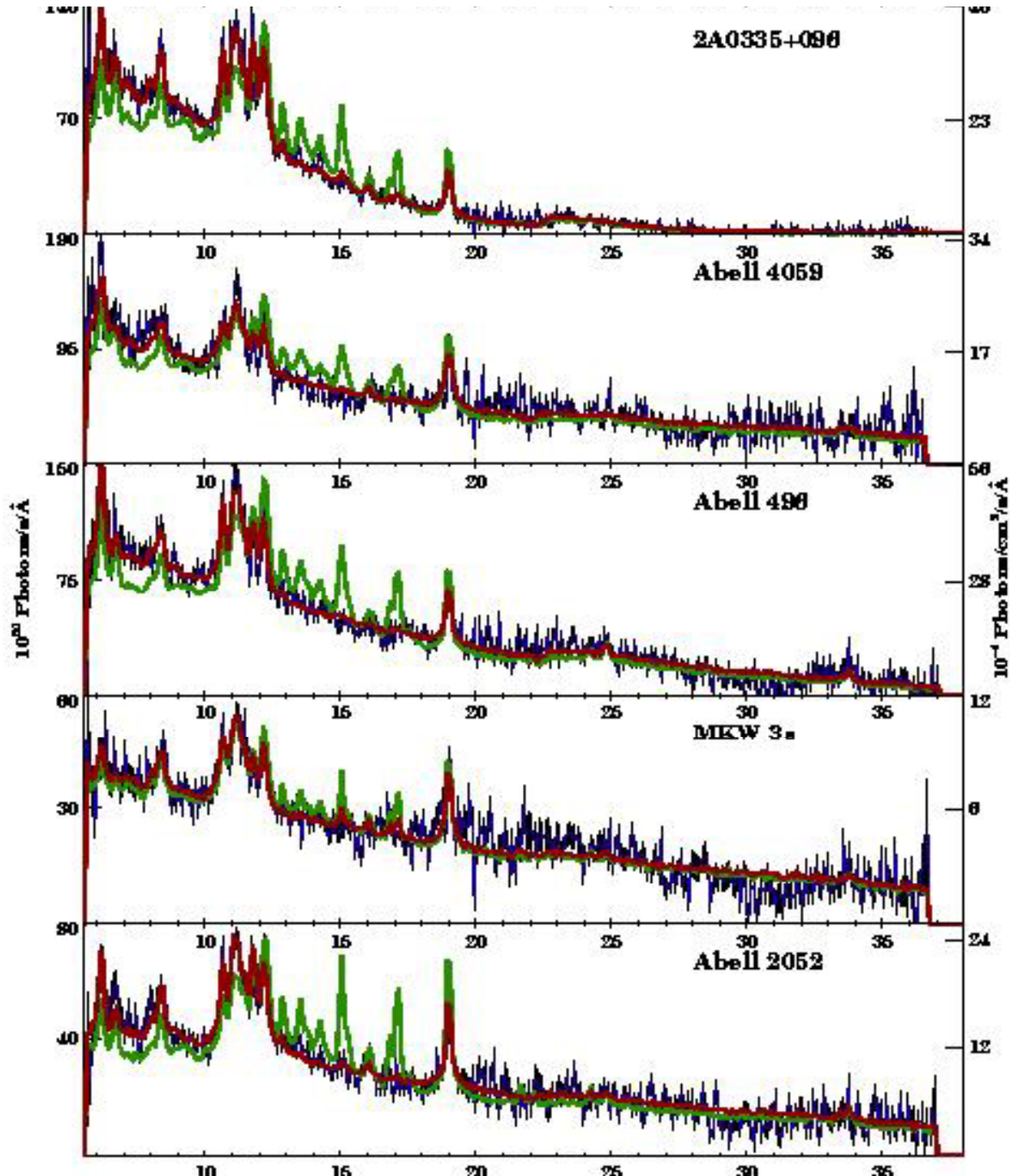
Cooling-Flow Model (T-ranges)



Peterson et al. 2003

XMM spectroscopy

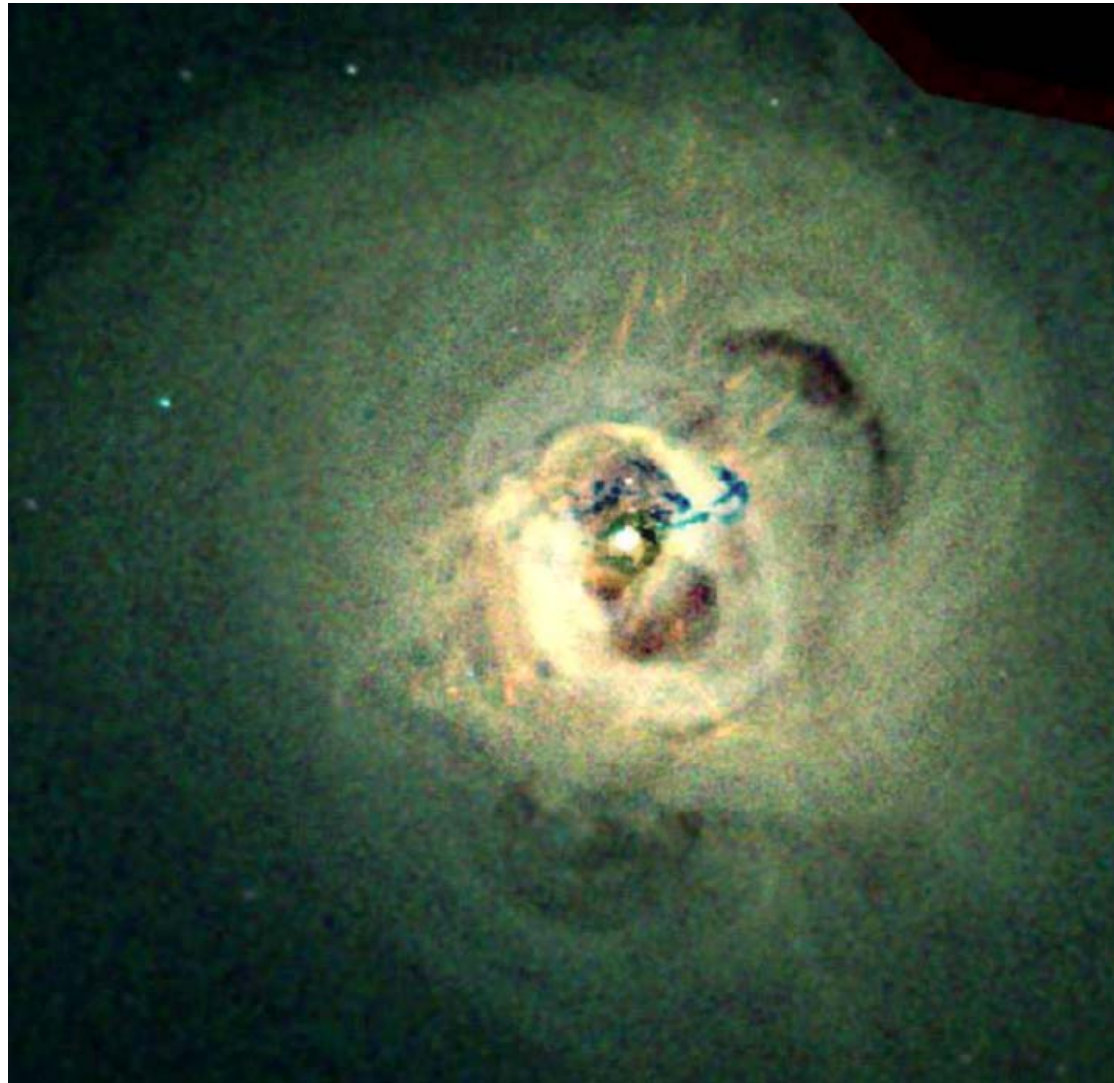
- Peterson, et al.
2003
- FeXVII e outras
linhas de gas a <1
keV ausentes.
- Cooling flow e'
parado a $\sim T/3$ -
 $T/2$)



Chandra

Superpoder – Imageamento

Mas espectroscopia tambem e' boa

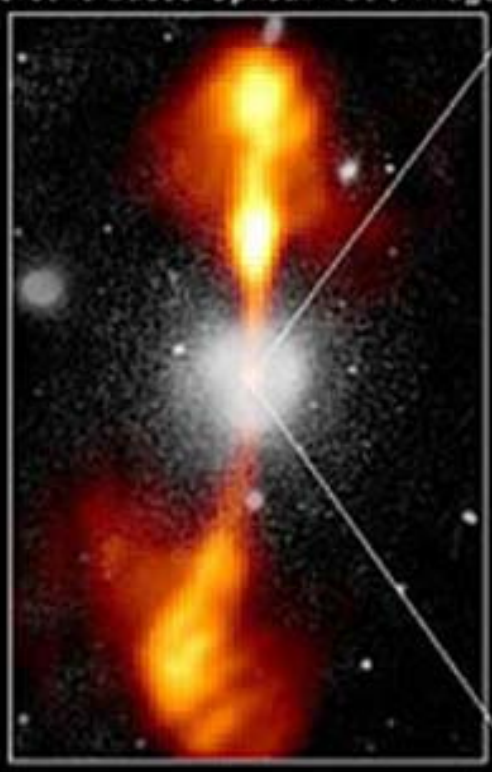


Core of Galaxy NGC 4261

Hubble Space Telescope

Wide Field / Planetary Camera

Ground-Based Optical/Radio Image



380 Arc Seconds
68,000 LIGHTYEARS

HST Image of a Gas and Dust Disk



17 Arc Seconds
400 LIGHTYEARS

Figure 5: Active galaxy NGC 4261 at radio and optical wavelengths.

Inner Structure of an Active Galaxy

0.1

lightyears

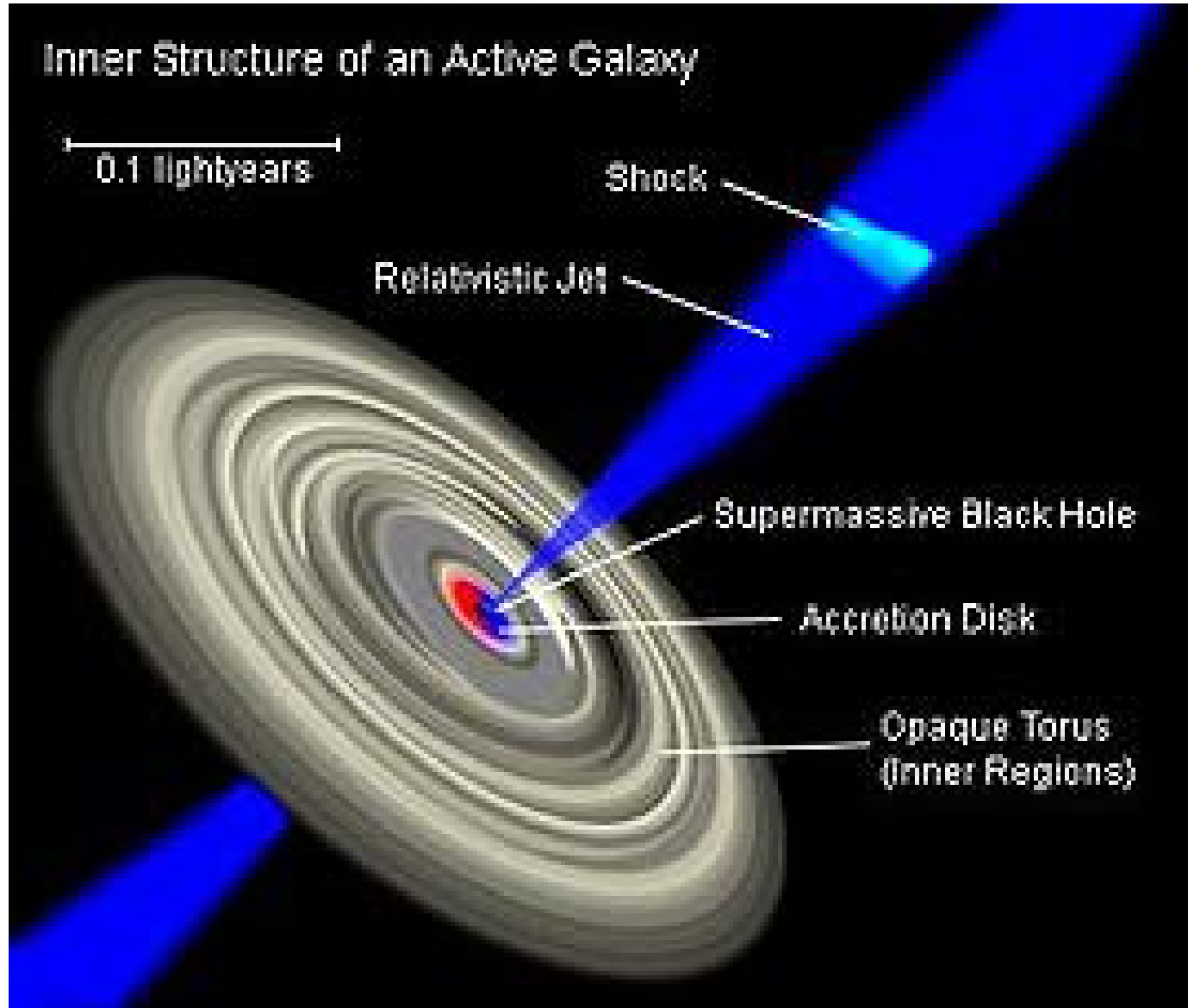
Shock

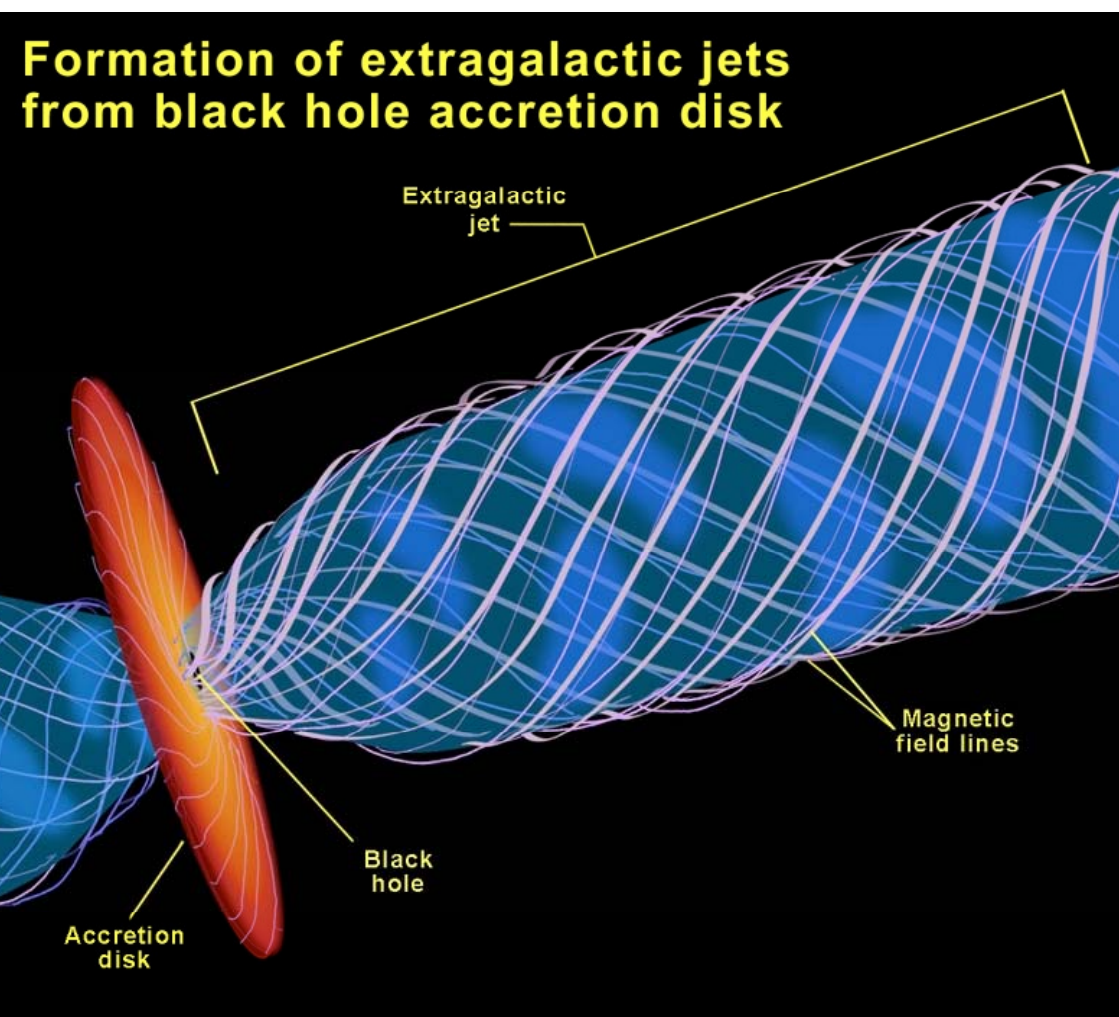
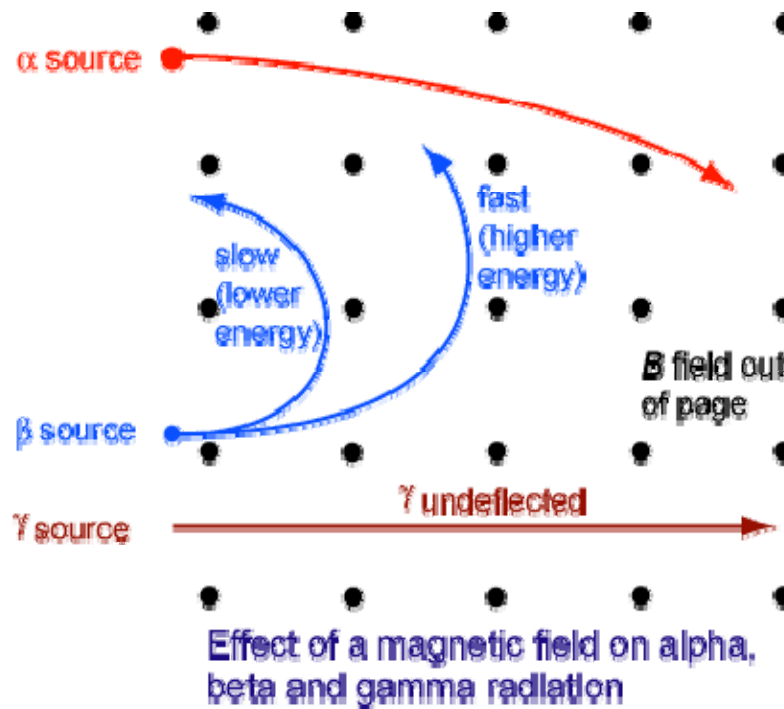
Relativistic Jet

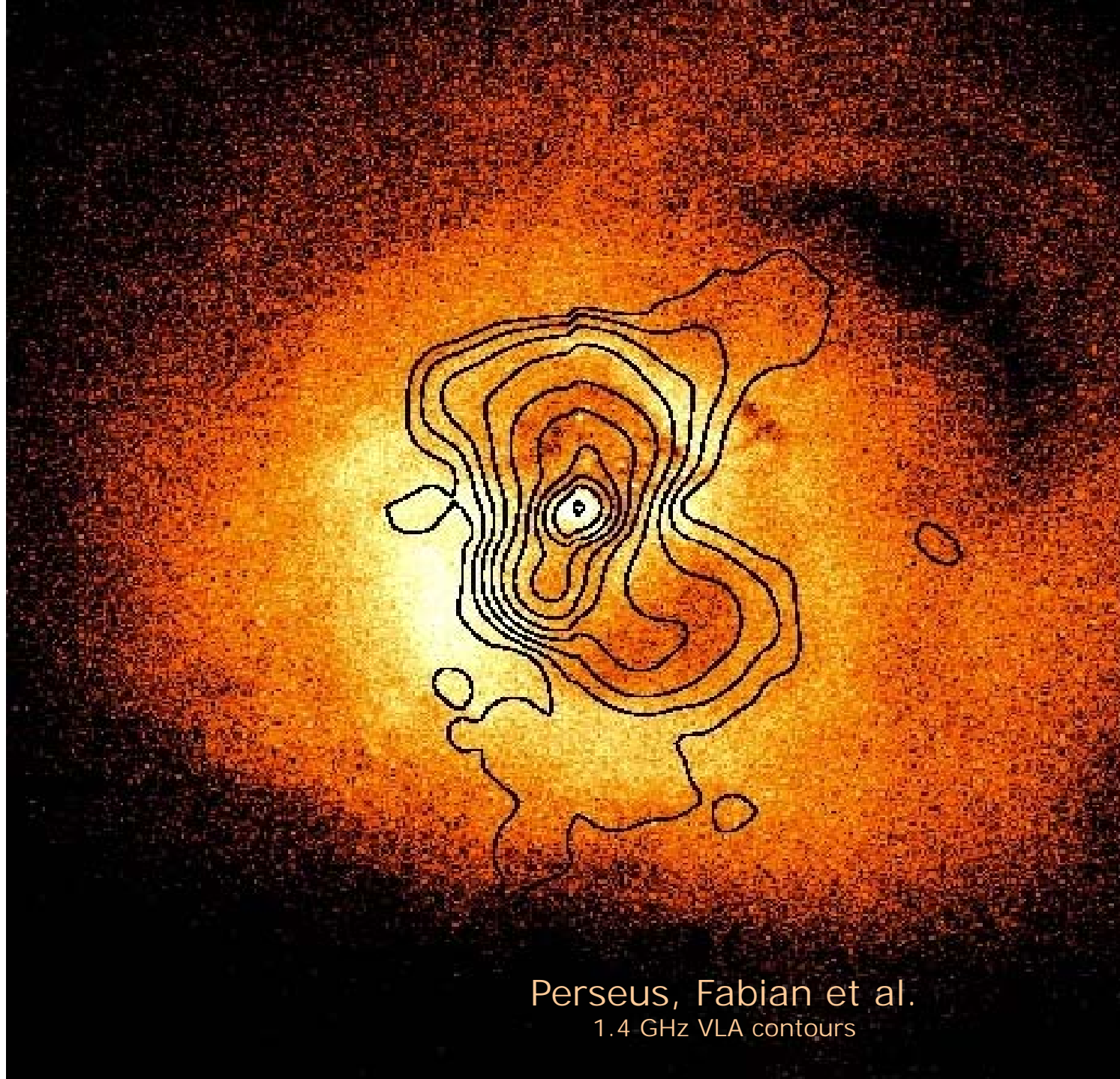
Supermassive Black Hole

Accretion Disk

Opaque Torus
(Inner Regions)

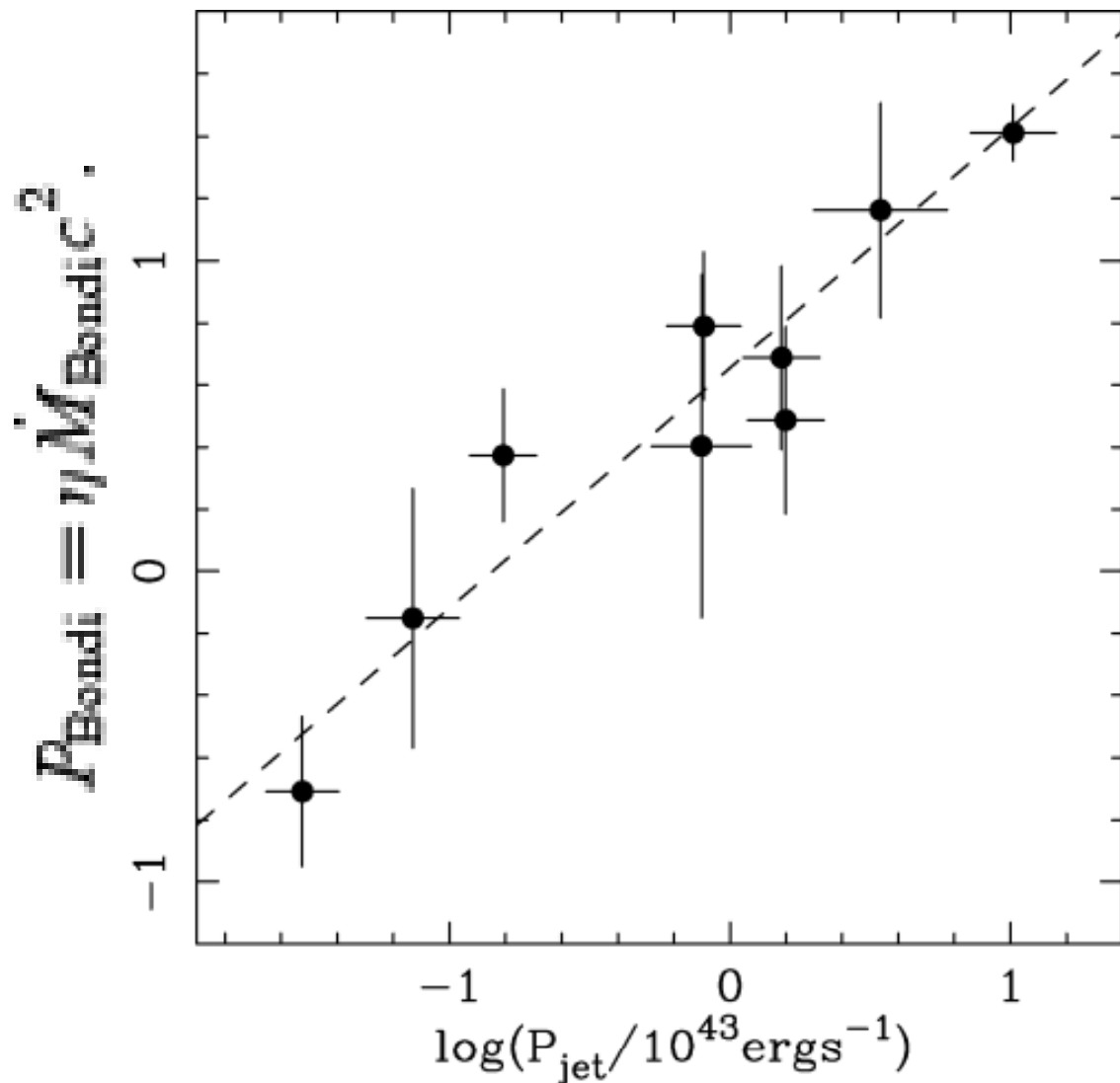






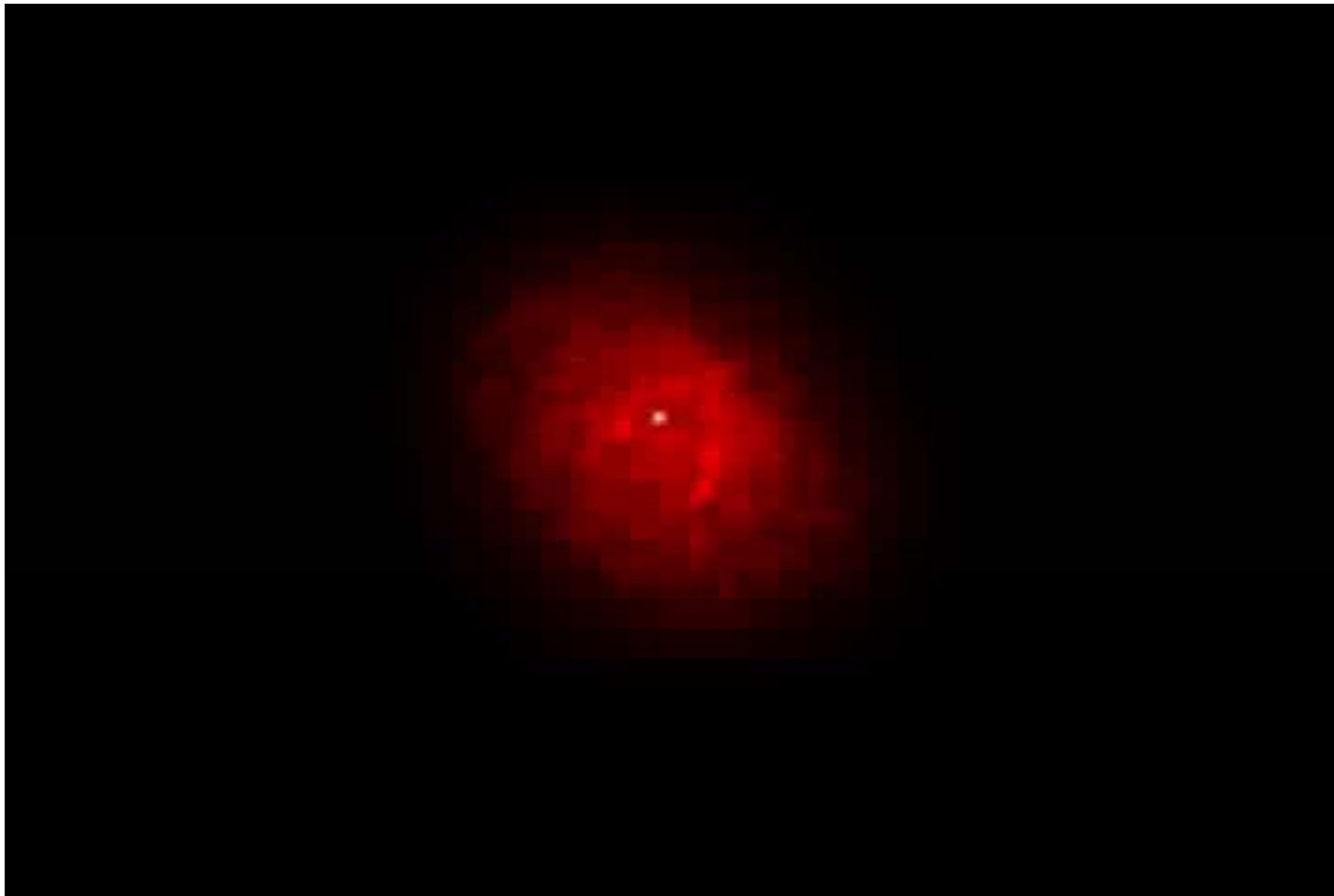
Perseus, Fabian et al.
1.4 GHz VLA contours

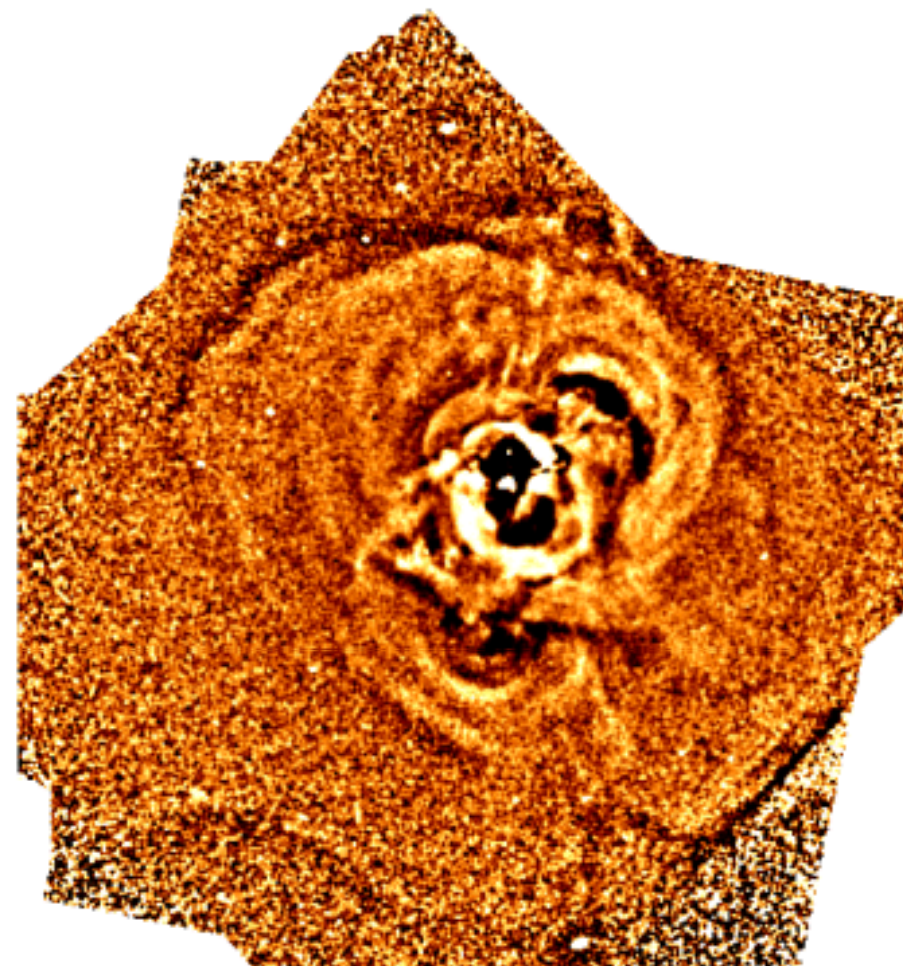
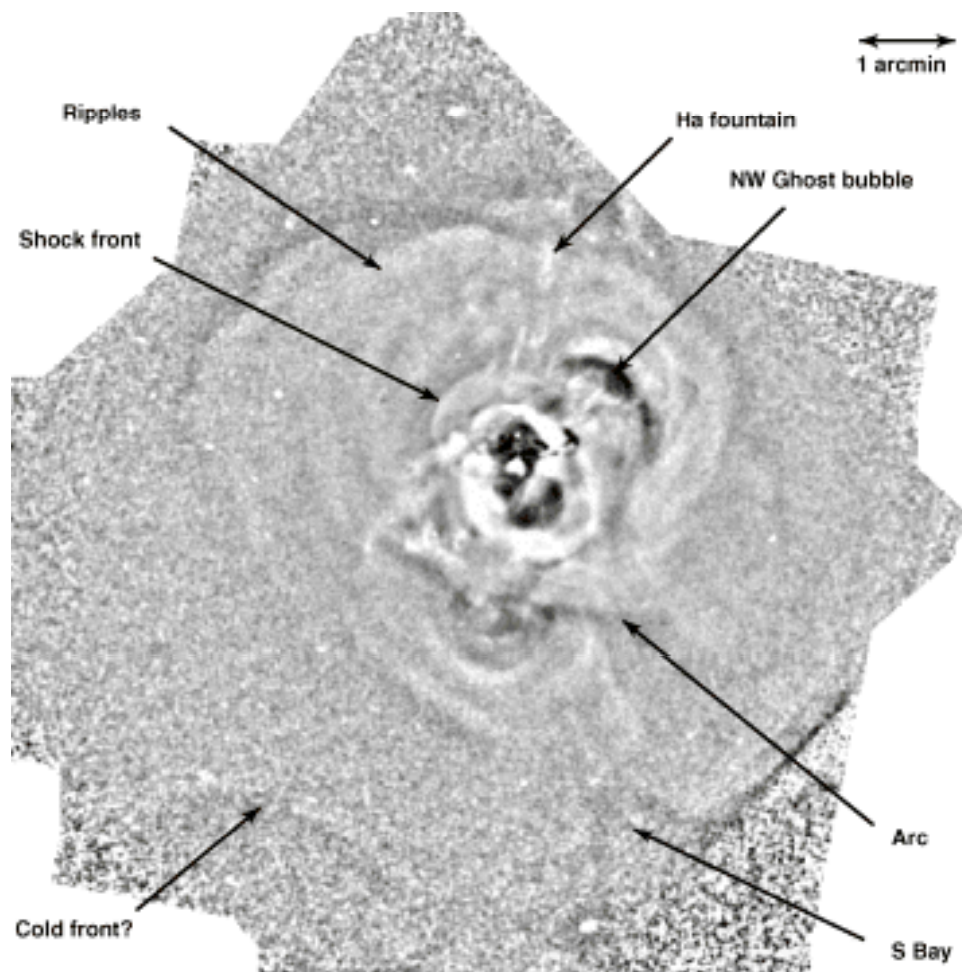
$$\dot{M}_{\text{Bondi}} = 4\pi \lambda (GM_{\text{BH}})^2 c_s^{-3} \rho = \pi \lambda c_s \rho r_A^2,$$



$$E = \frac{1}{\gamma_2 - 1} PV + PV = \frac{\gamma_2}{\gamma_2 - 1} PV,$$

Problema: Mas o aquecimento nao e' distribuido

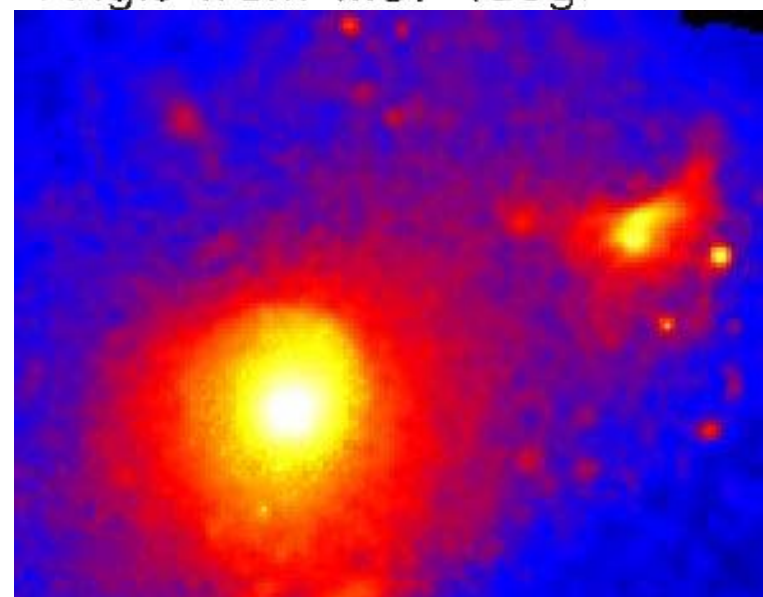
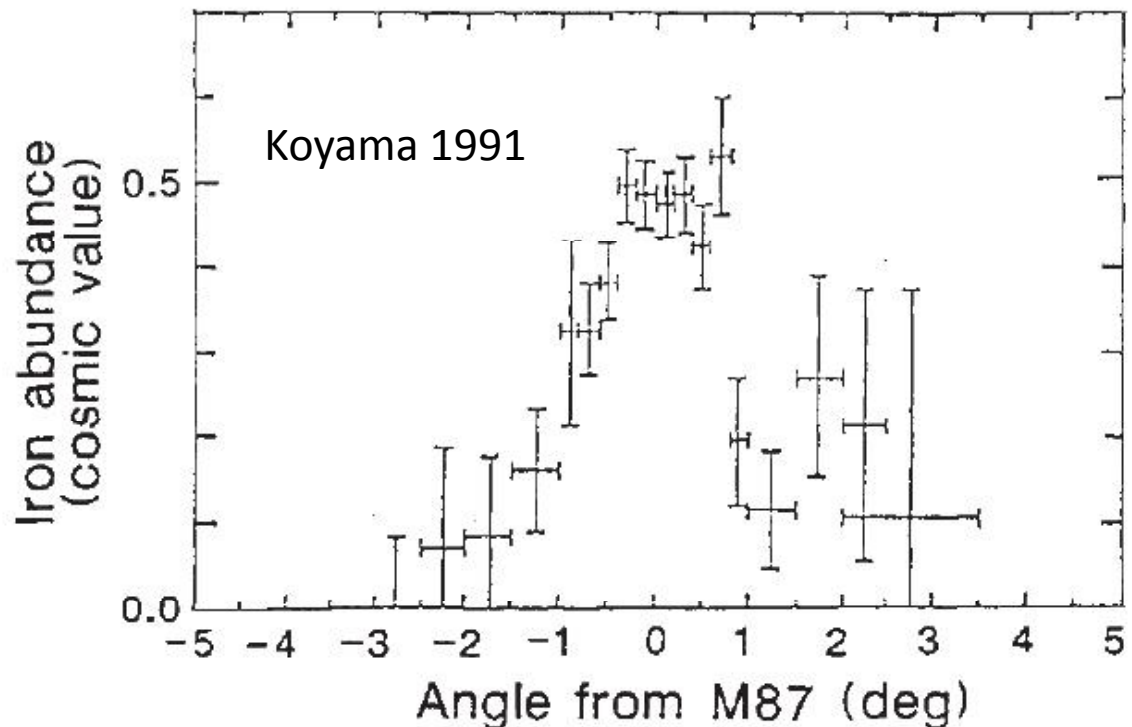




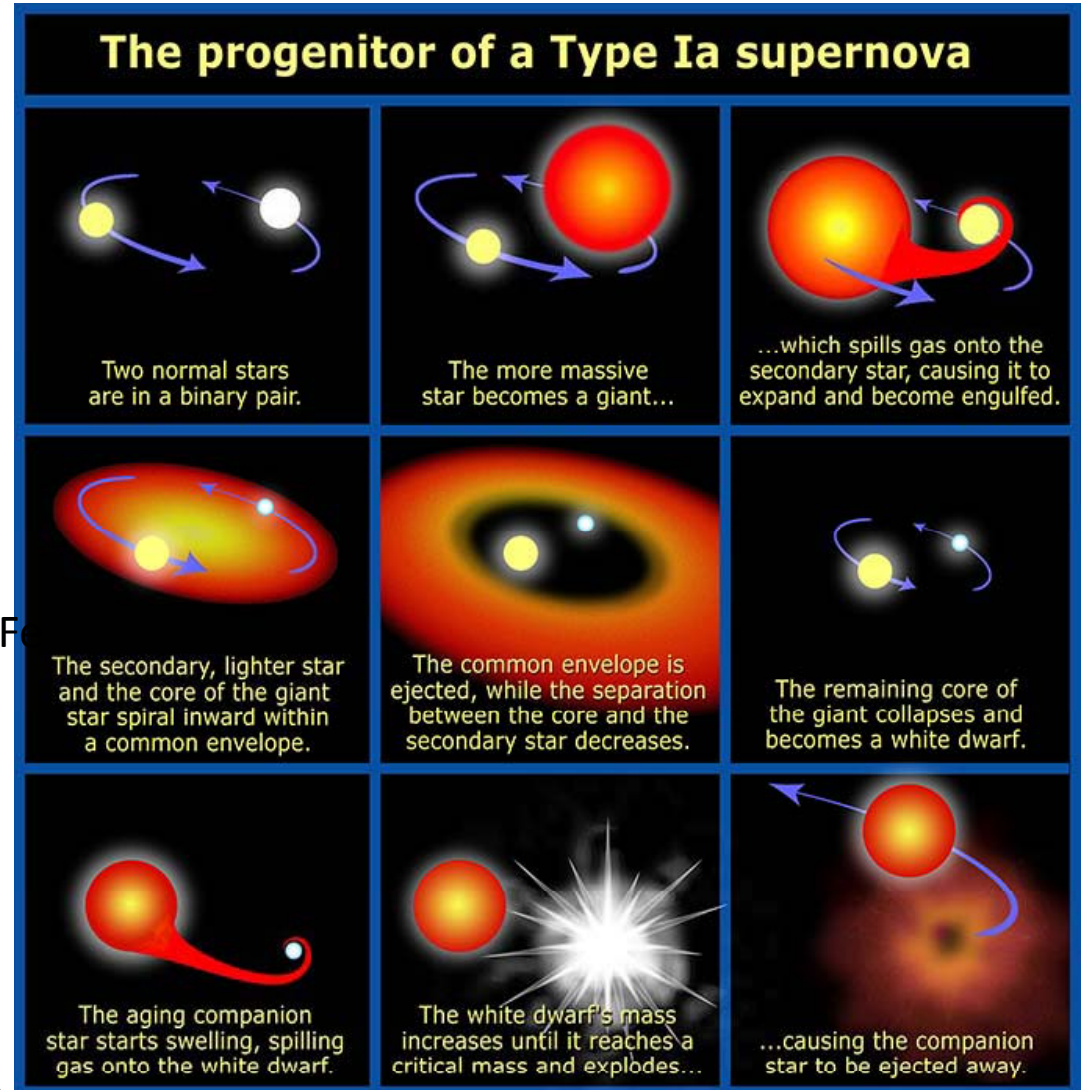
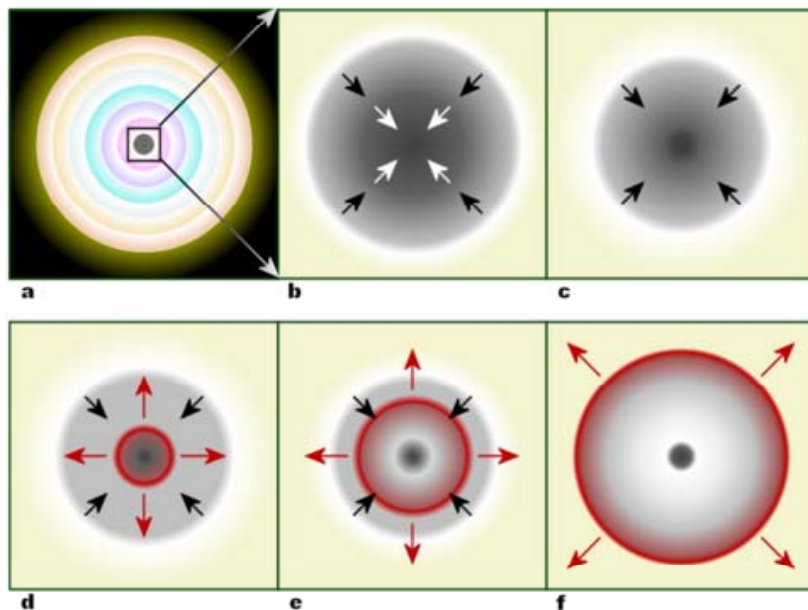
Gradientes de Abundancia



M87 © Anglo-Australian Observatory
Photo by David Malin



Supernovae II e Ia



Ventos Galaticos

Chandra
Spitzer
HST

M82



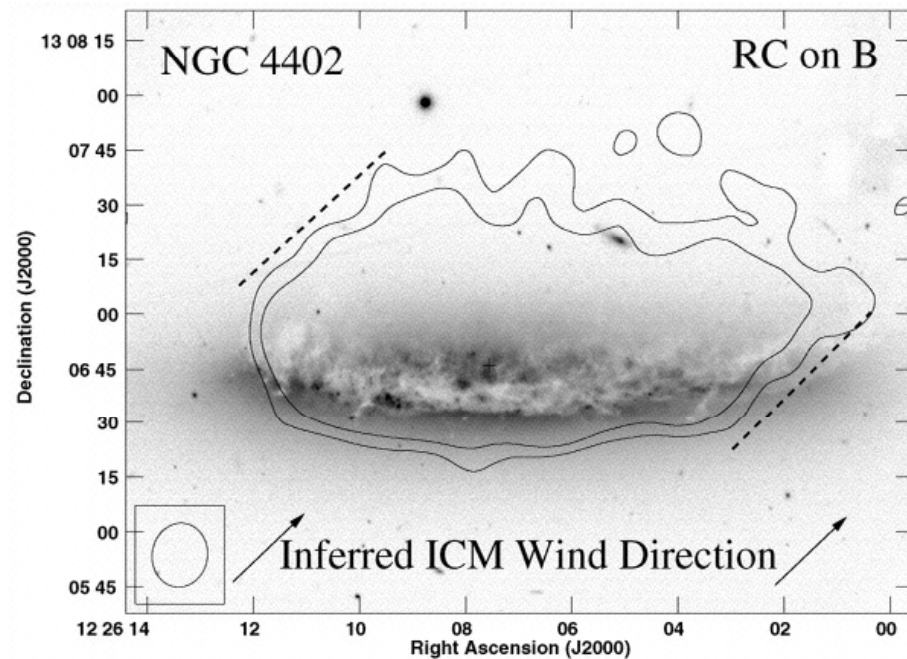
Pressão de Arrasto

$$P_{rps} = \rho V^2 > 2\pi G \sigma_D \sigma_{ISM}$$

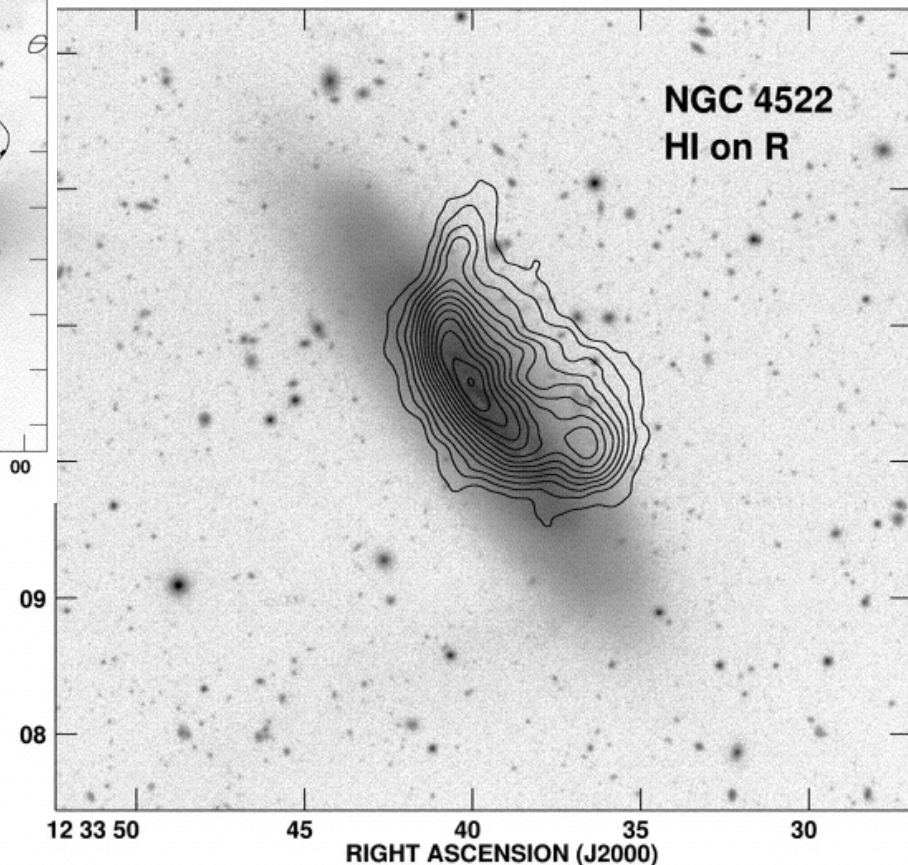
Aumento da Ram-Pressure Stripping das galáxias
Crowl, H., et al. 2005

Simulações

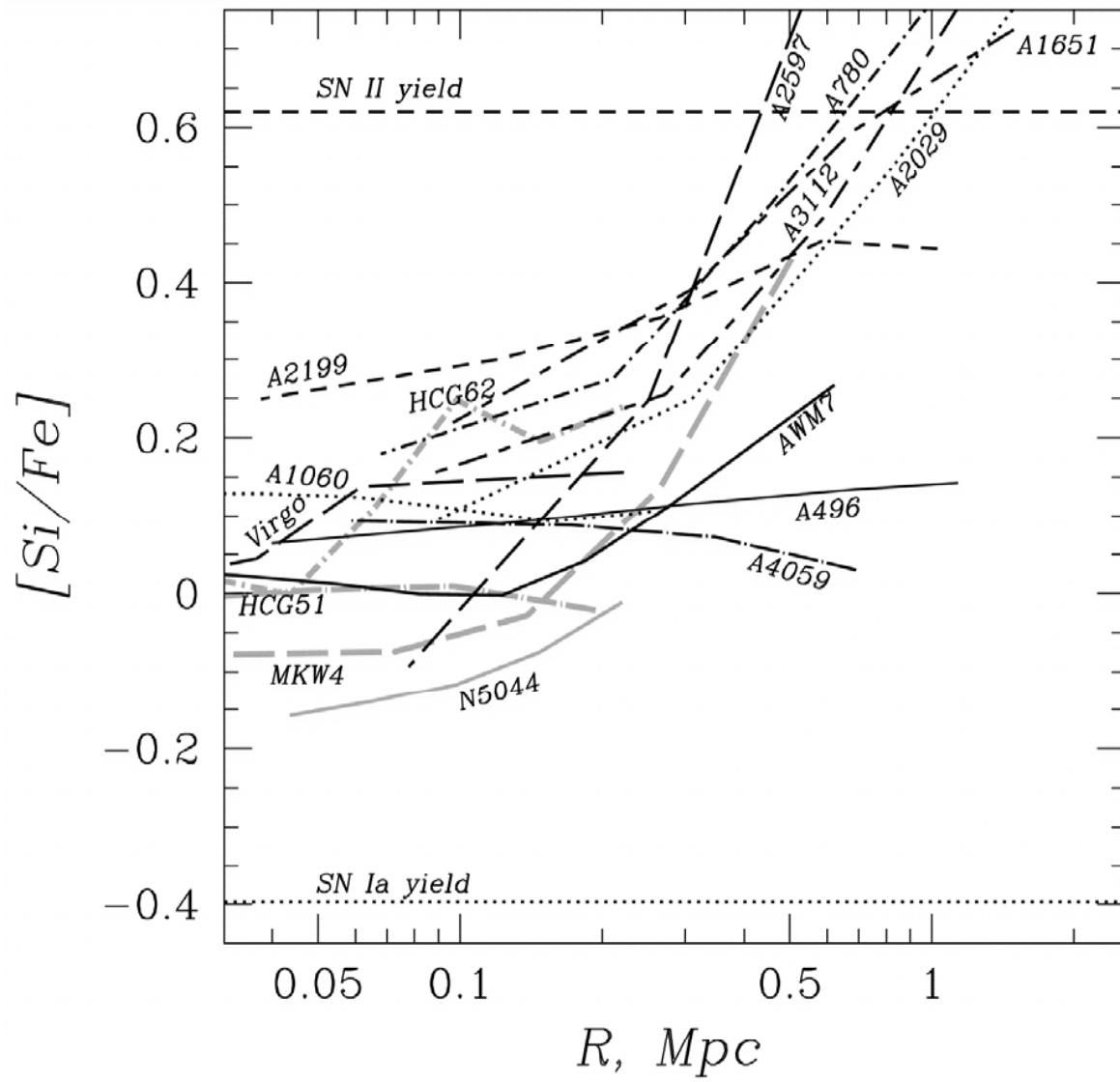
$$P_{rps.} > 2 f_{ISM} \sigma_*^2$$



2 externos 1.4 GHz radio continuum
contornos na *B* image.



Kenney, J., van Gorkom, J. & Vollmer, B. 2004



Finoguenov 1999

Problemas em aberto:

- Até que raio RPS é efficiente?
- Como isso afeta as galáxias?
- Algum tipo morfológico contribui mais DENTRO do AG?
- $\Psi(M) \rightarrow$ diferença entre grupos e AGs, ou massivos de não massivos?
- Accreção de “clumps” altera (contribui ou mistura) os metais?

Cluster mass

Virial Method => $2T + \Omega = 0$

$$T = \frac{1}{2} M v^2 = \frac{3}{2} M \sigma_{\text{los}}^2$$

$$\Omega = - GM^2/R$$

$$M = 3 \sigma_{\text{los}}^2 R/G$$

X-ray Method

Hydrostatic Equilibrium

$$\frac{dP}{dr} = -g\rho = -\frac{GM(< r)}{r^2} \rho \quad M(< r) = \frac{-kTr}{\mu m_p G} \left(\frac{d \ln T}{d \ln r} + \frac{d \ln \rho}{d \ln r} \right)$$

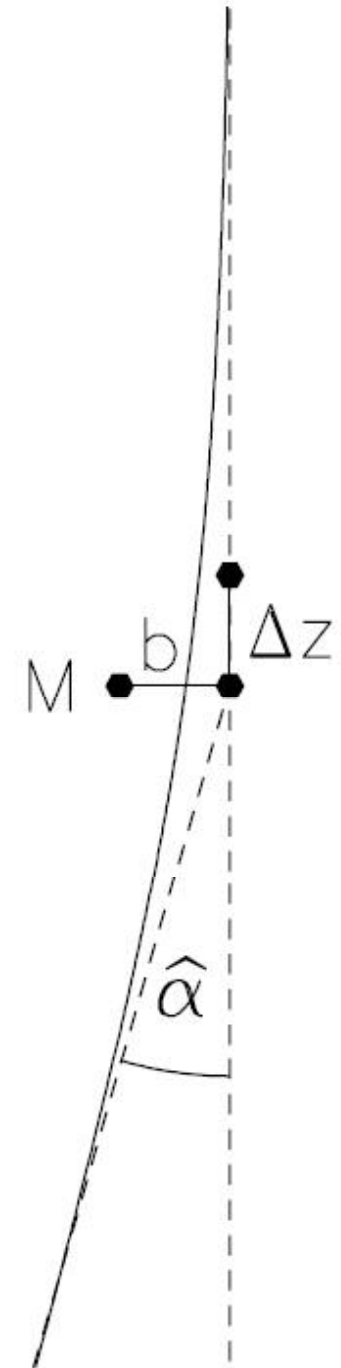
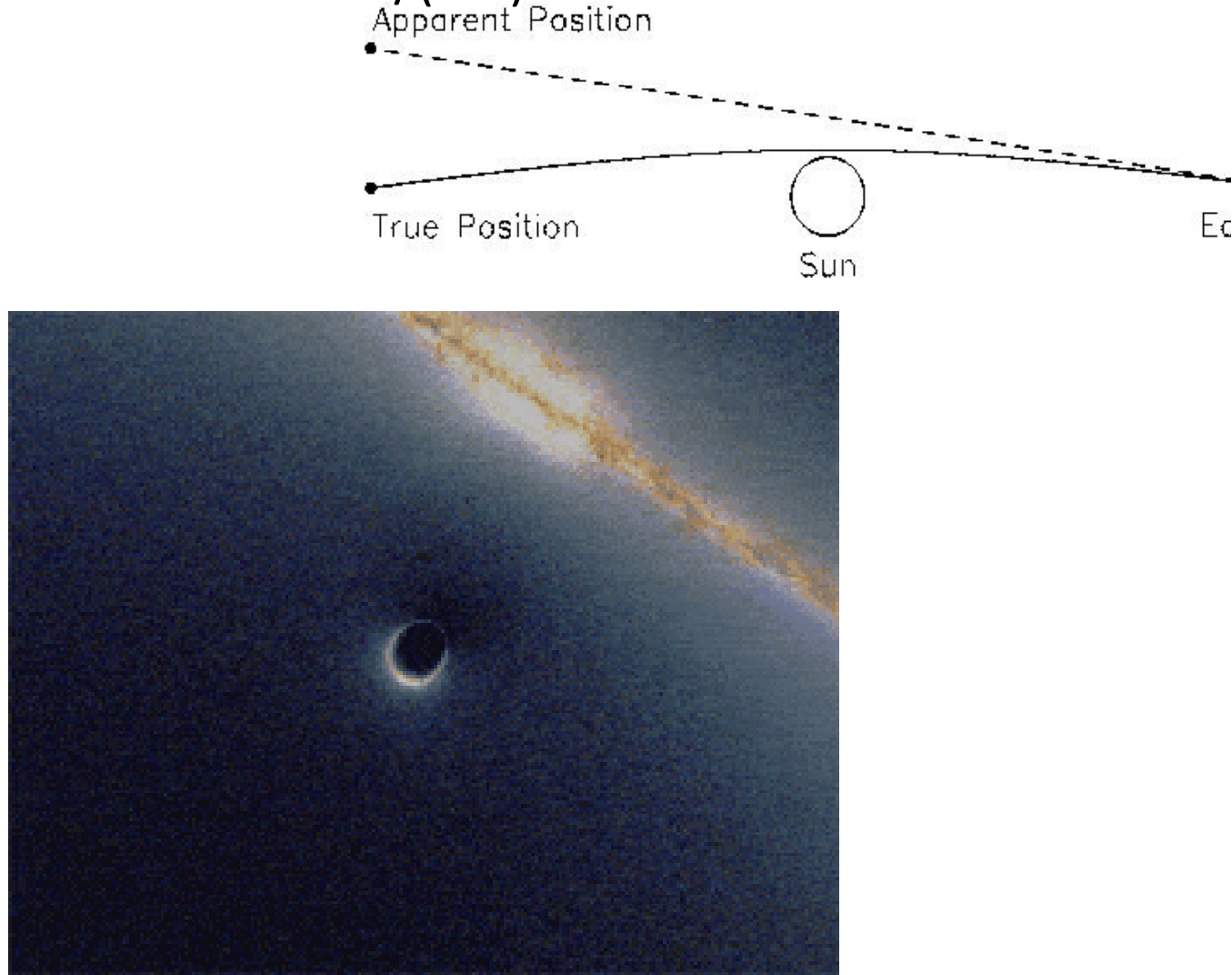
All these masses are bigger than the sum of the gas and galaxies by ~ 6 times!

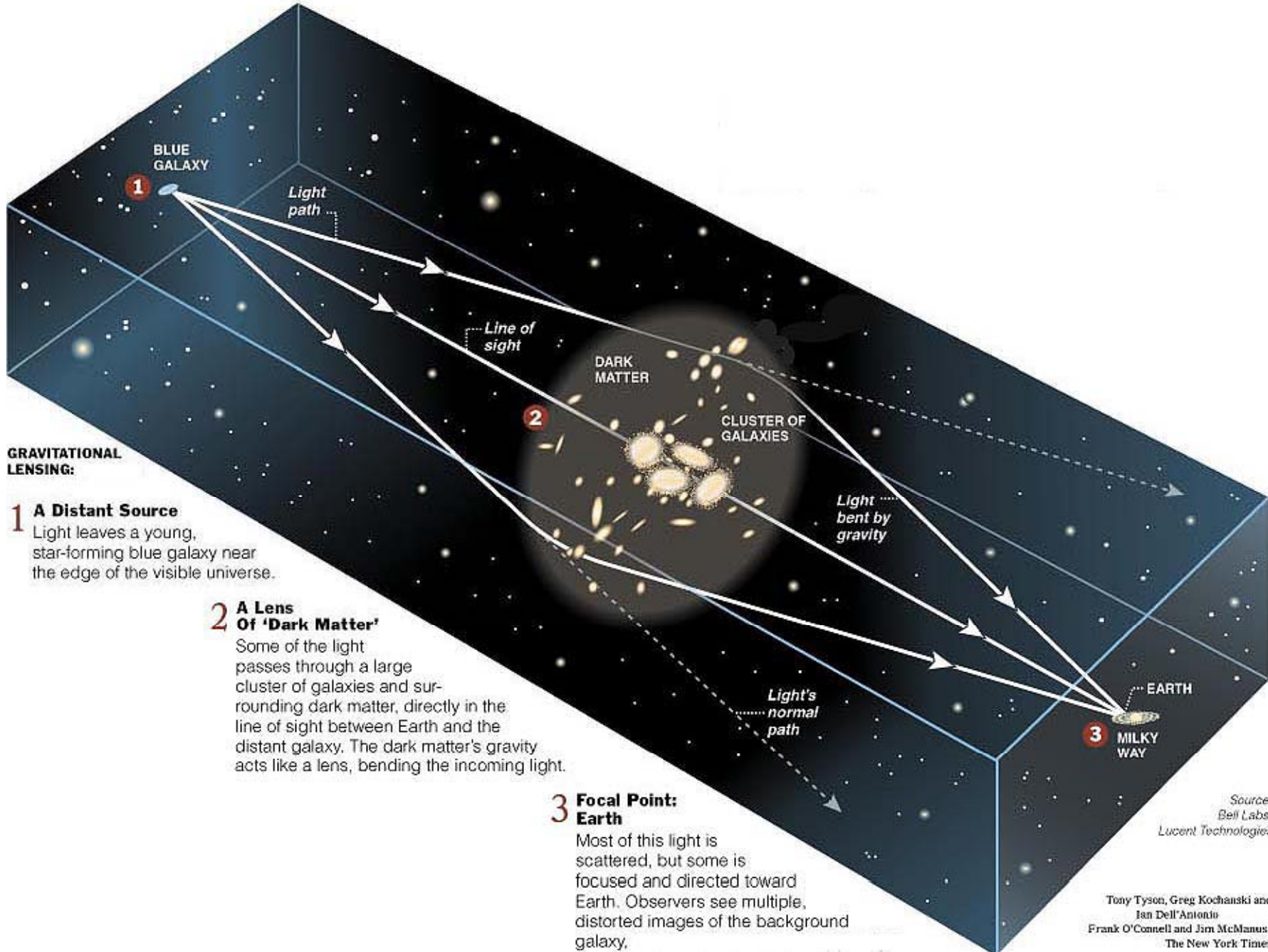
DARK MATTER

Cluster mass

Gravitational Lensing

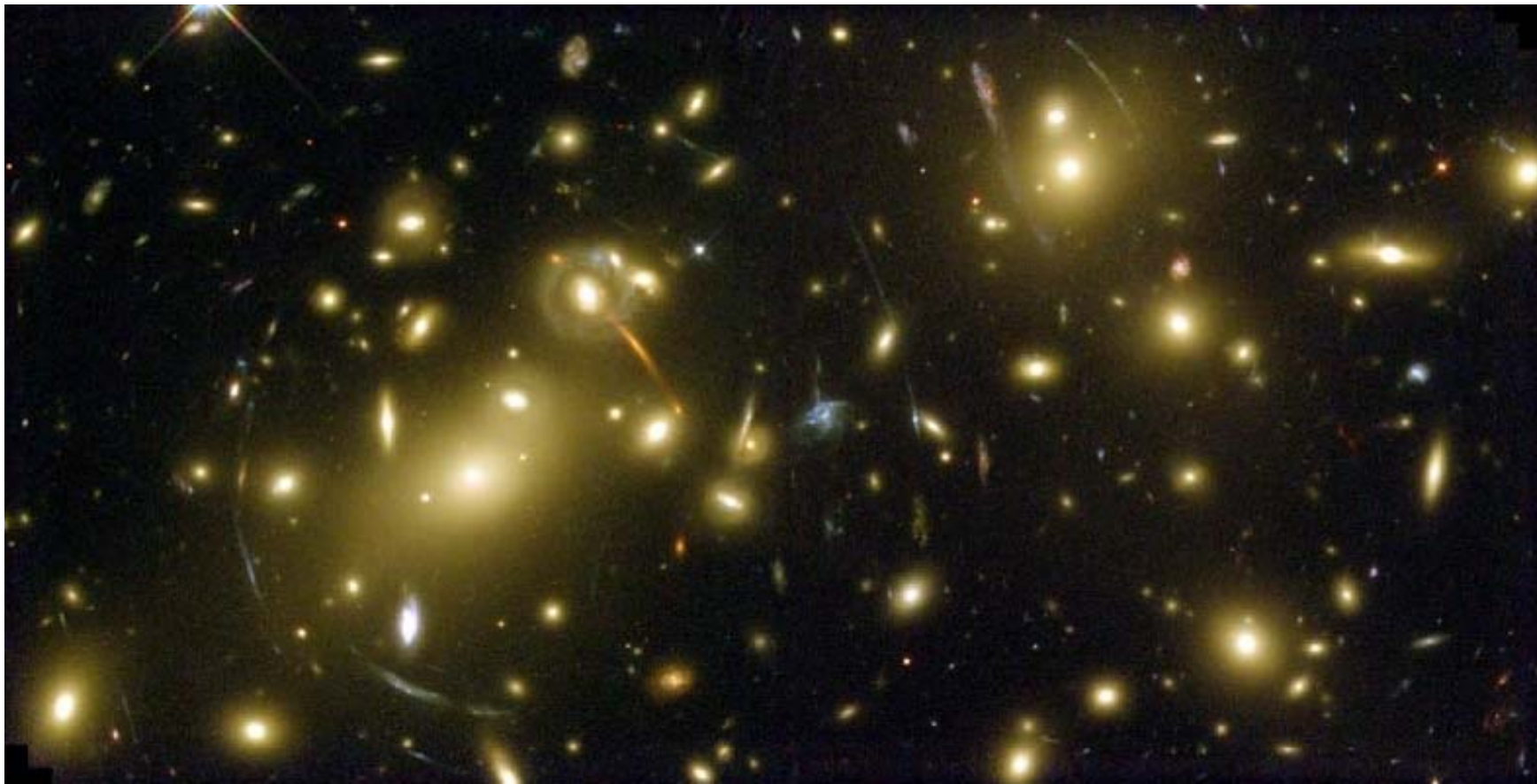
$$\alpha = 4GM/(c^2 b)$$

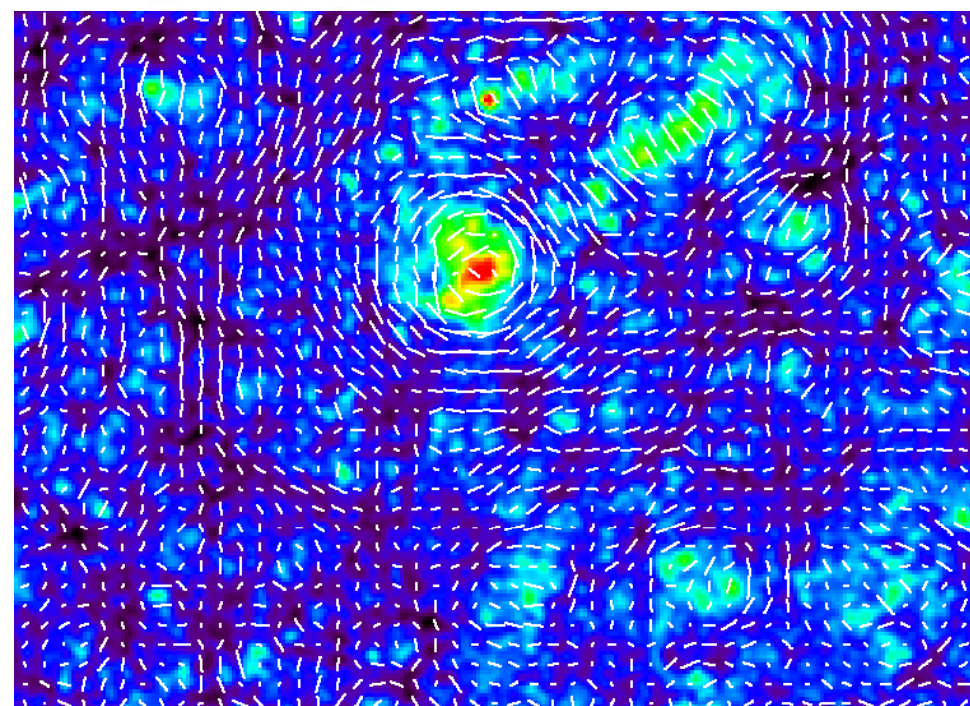
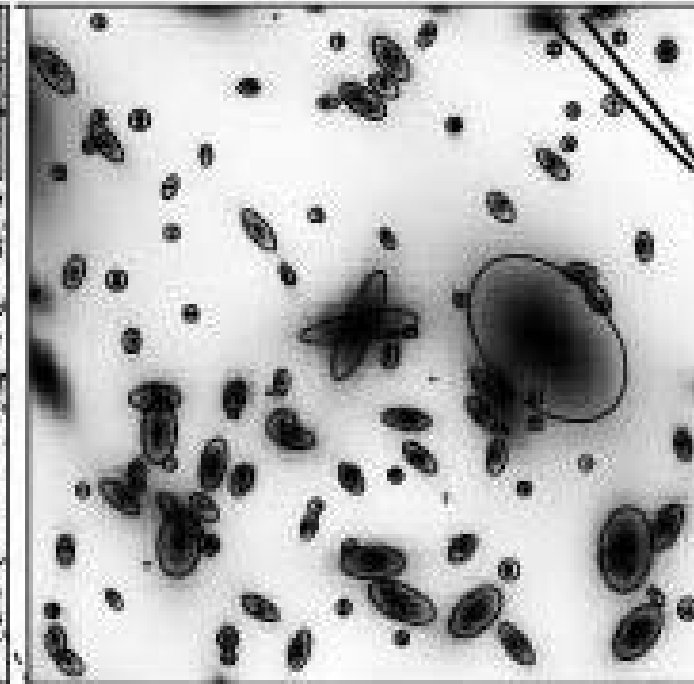
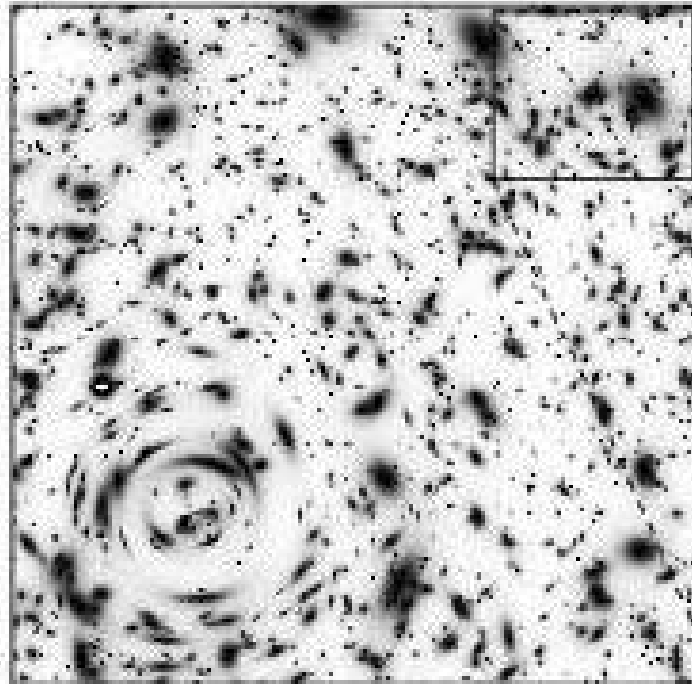




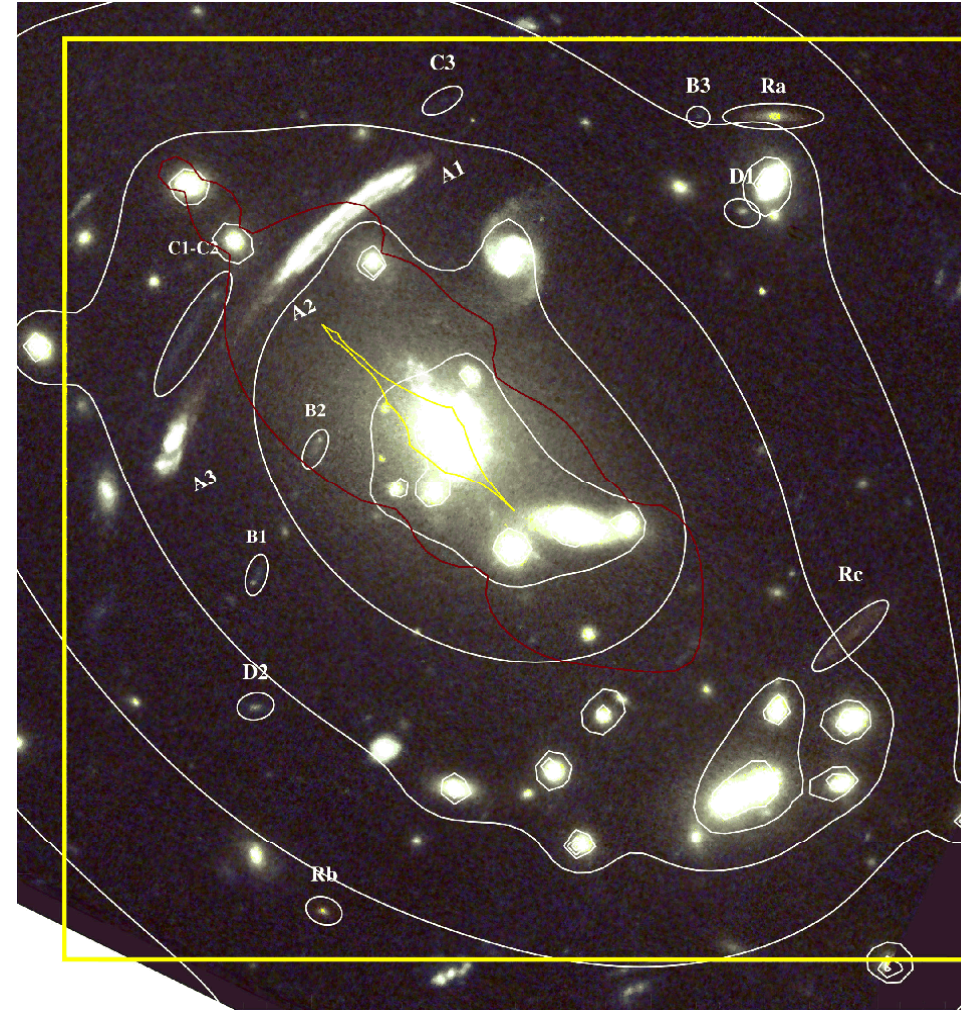
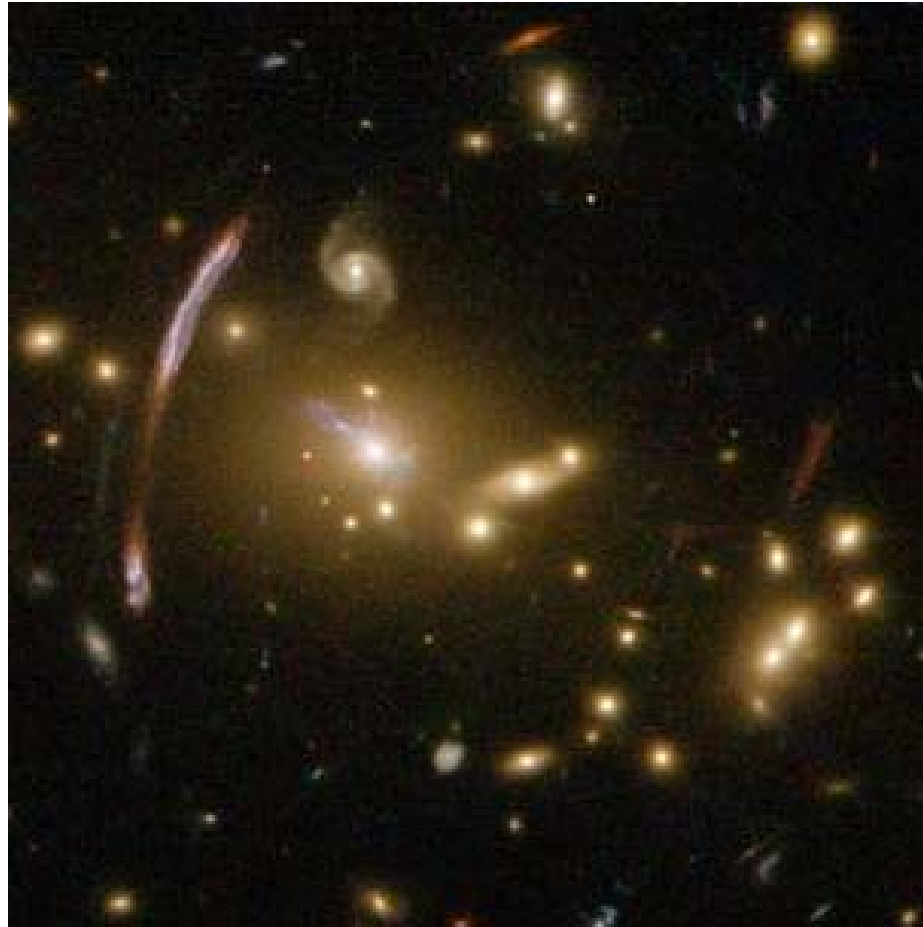
Tony Tyson, Greg Kochanski and Ian Dell'Antonio
Frank O'Connell and Jim McManus/
The New York Times

Abell 2218



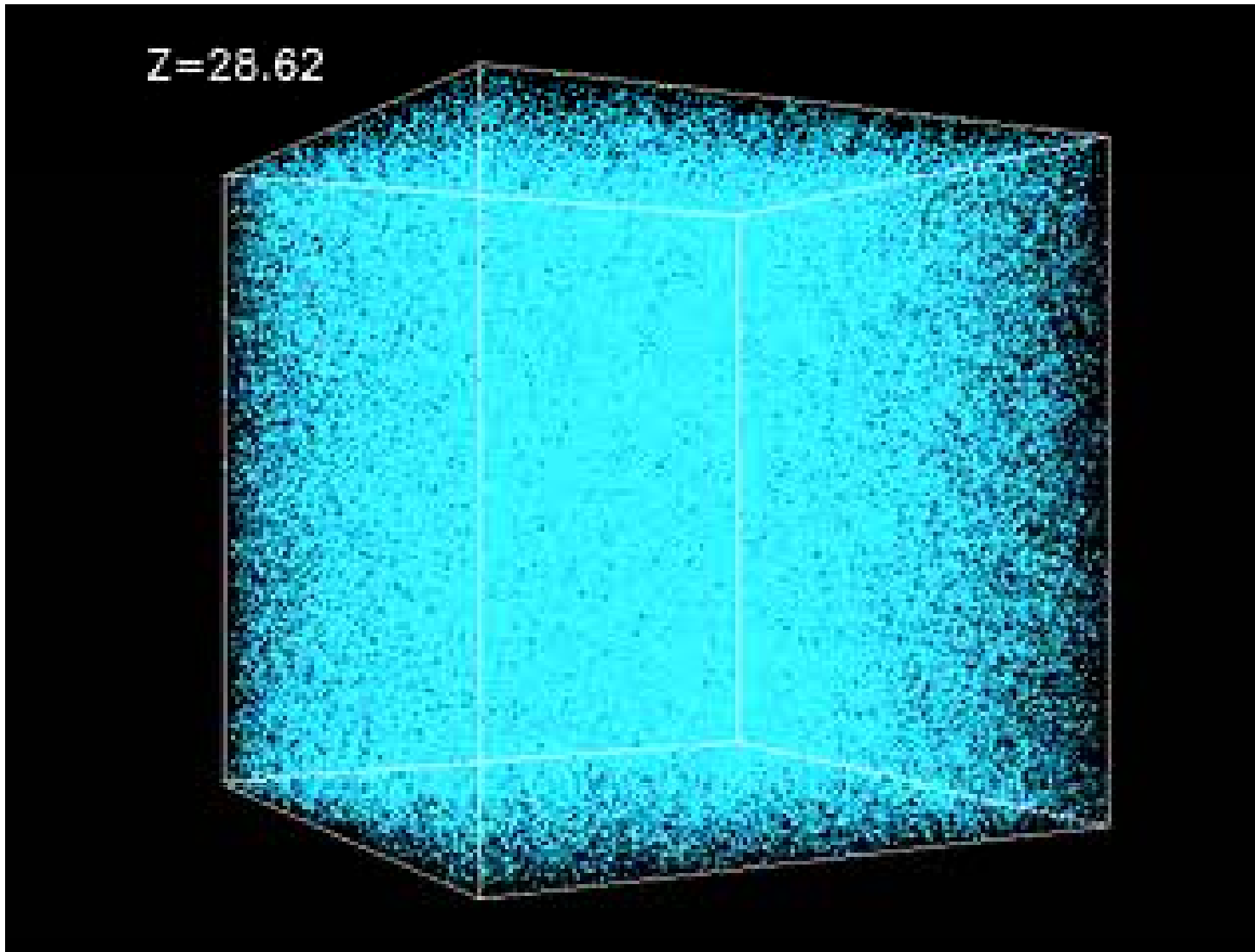


Abell 2667

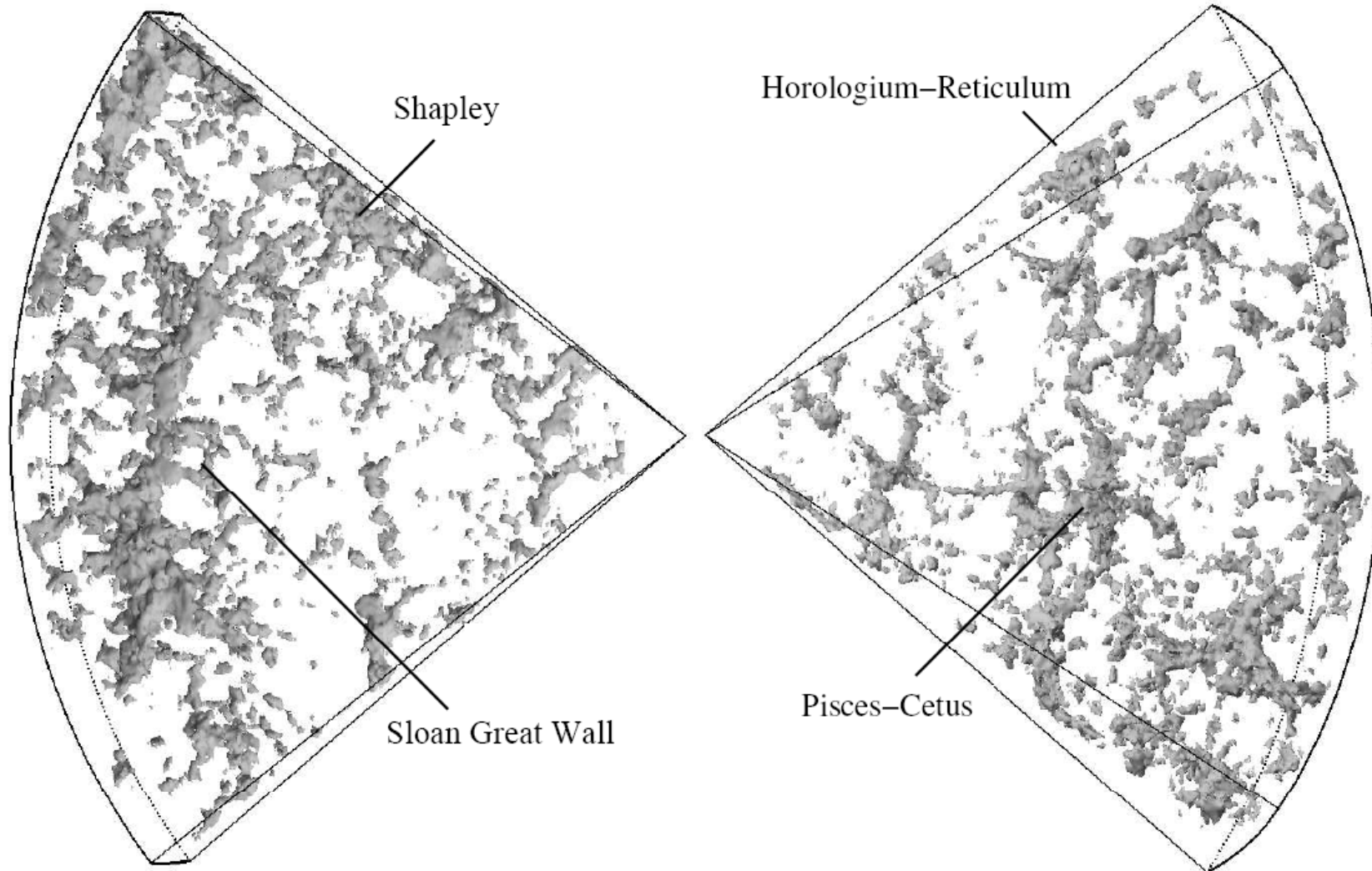


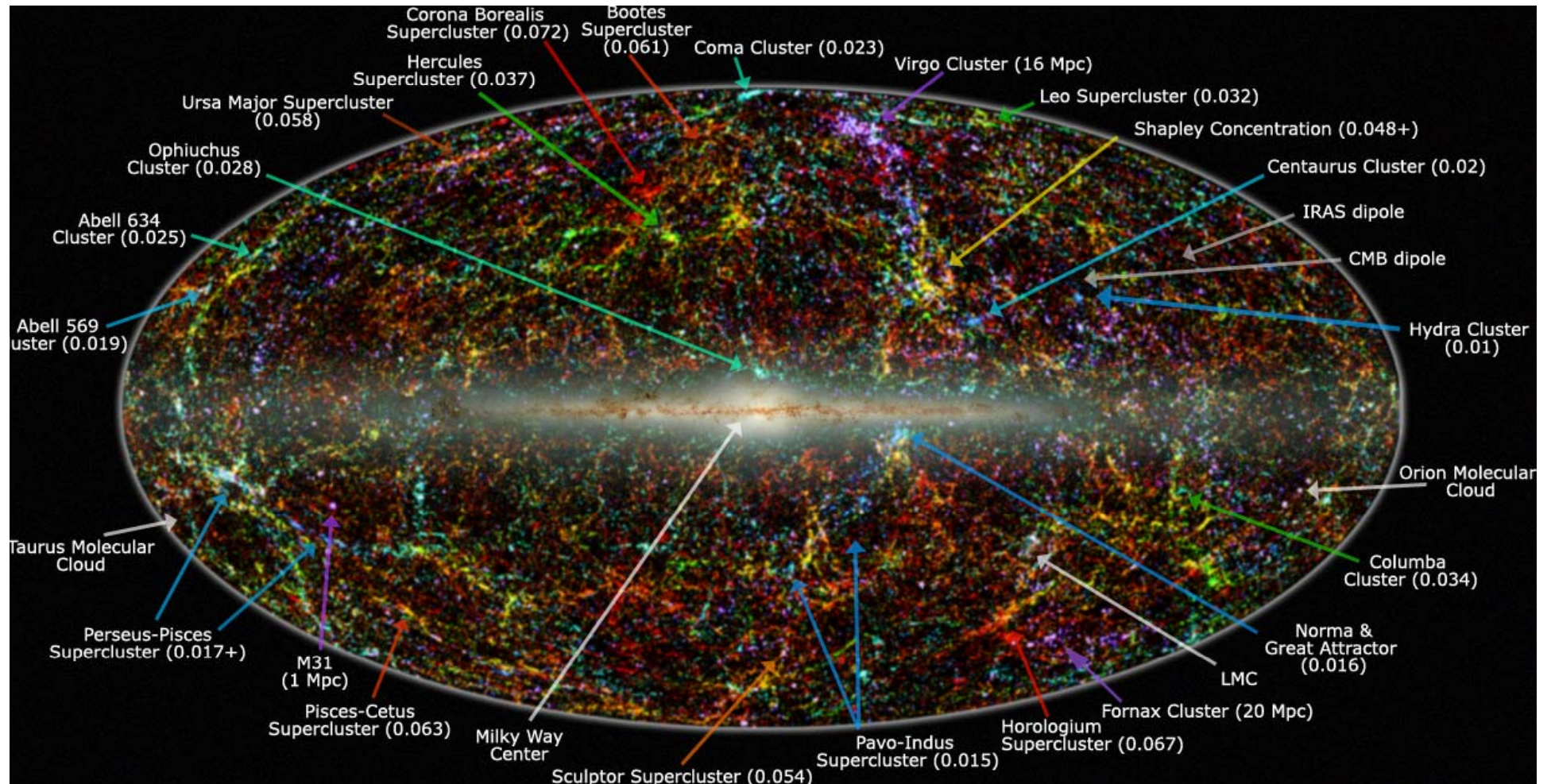
**Massa 2 vezes maior que
achada por raios-X!!!**

Visão moderna de formação de um cluster



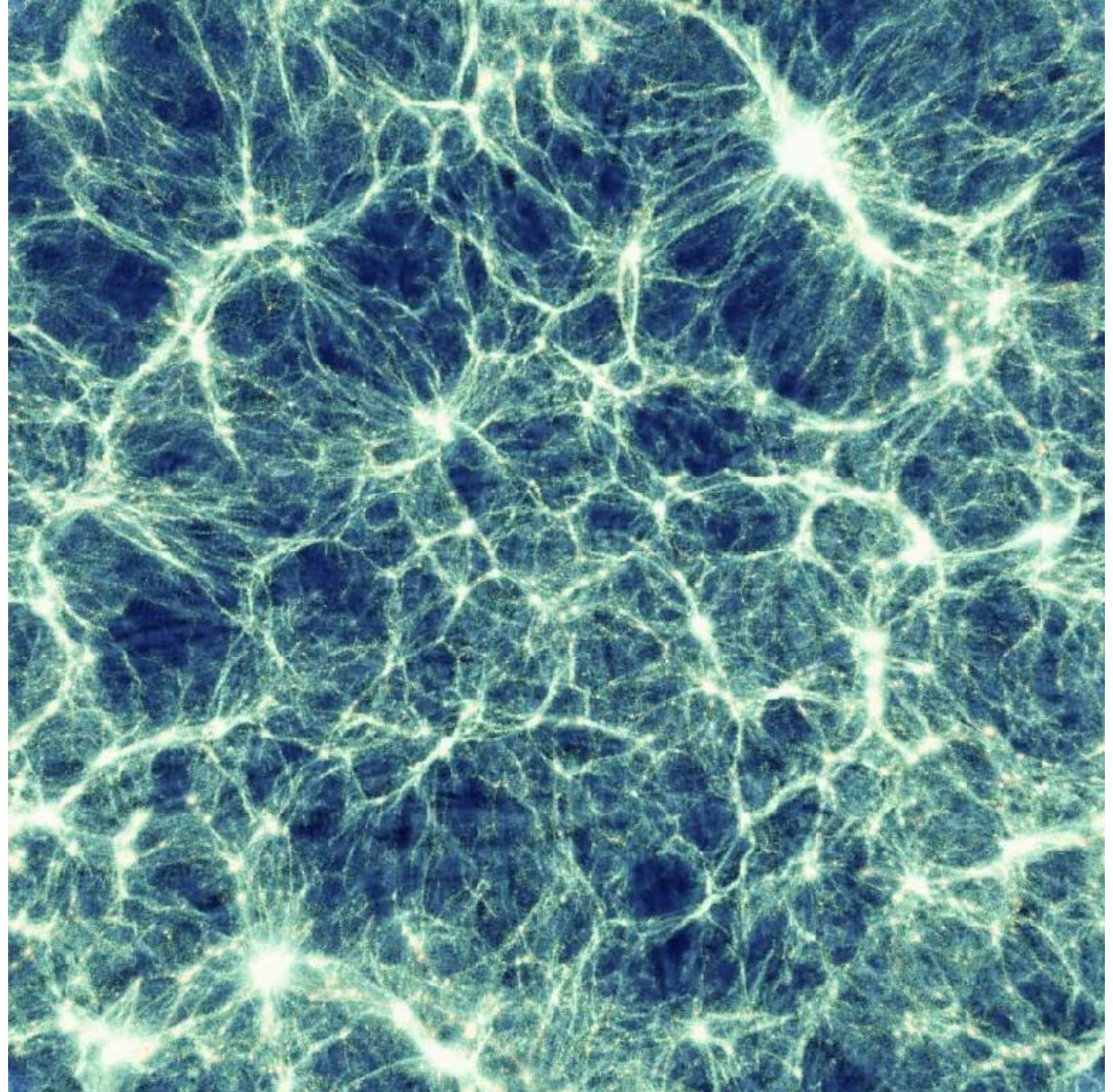
Andrey Kravtsov/U. Chicago
Anatoly Klypin/NMSU
NCSA



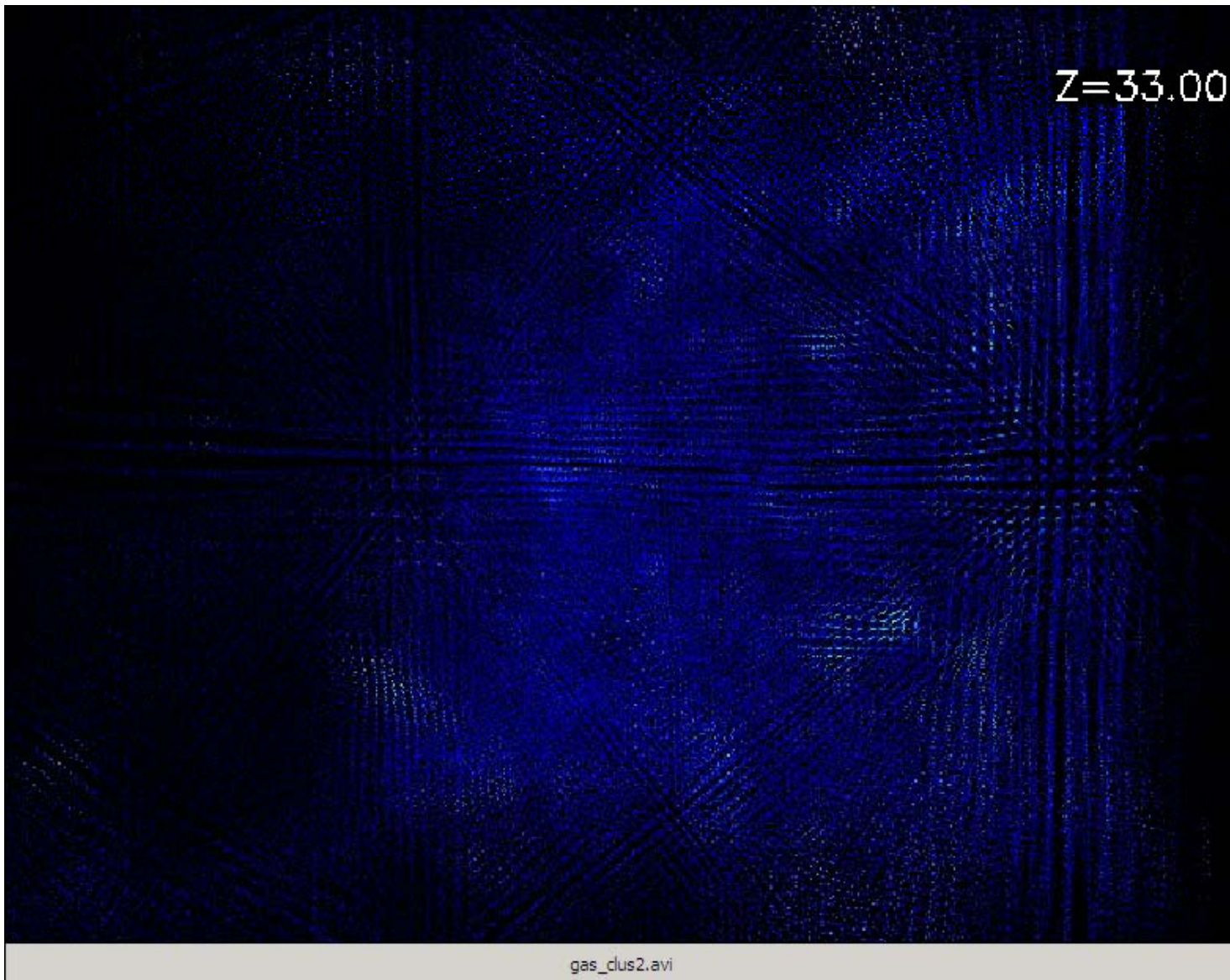


near-infrared sky reveals the distribution of galaxies beyond the Milky Way. The image is derived from the 2MASS Extended Source Catalog (XSC)--more than 1.5 million galaxies, and the Point Source Catalog (PSC)--nearly 0.5 billion Milky Way stars. Blue are the nearest sources ($z < 0.01$); green are at moderate distances ($0.01 < z < 0.04$) and red are the most distant sources that 2MASS resolves ($0.04 < z < 0.1$).

- structure formation
 - filaments connect nodes (clusters)
 - width of filaments \sim cluster virial radius ~ 3 Mpc



8 Mpc de lado -- Ascasibar

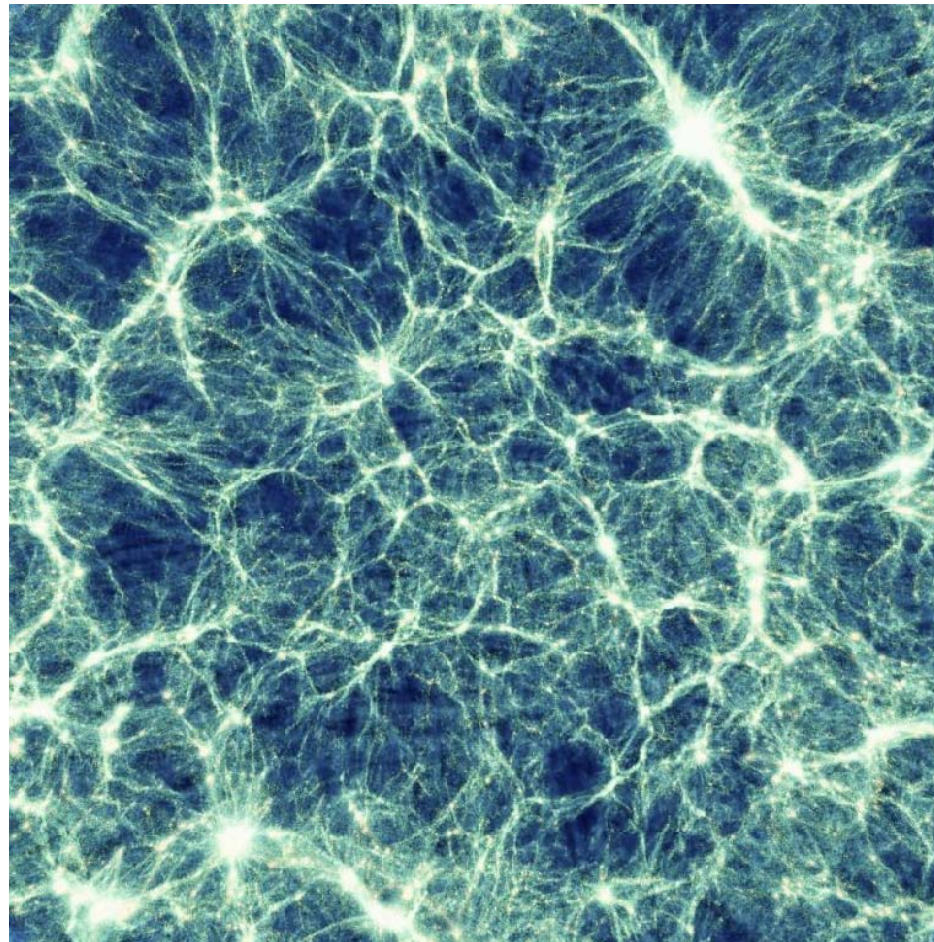


Calculo de massa de aglomerados – suposicoes

Metodo Virial – contaminacao de galaxias de campo

Metodo de raios-X – Equilibrio Hidrostatico

Metodo de lentes – Massa projetada



Gradientes de Velocidade

Equação de Euler

$$\underbrace{\frac{\partial \bar{V}}{\partial t} + (\bar{V} \nabla) \bar{V}}_{0?} = -\frac{\nabla P}{\rho} + \bar{g}$$

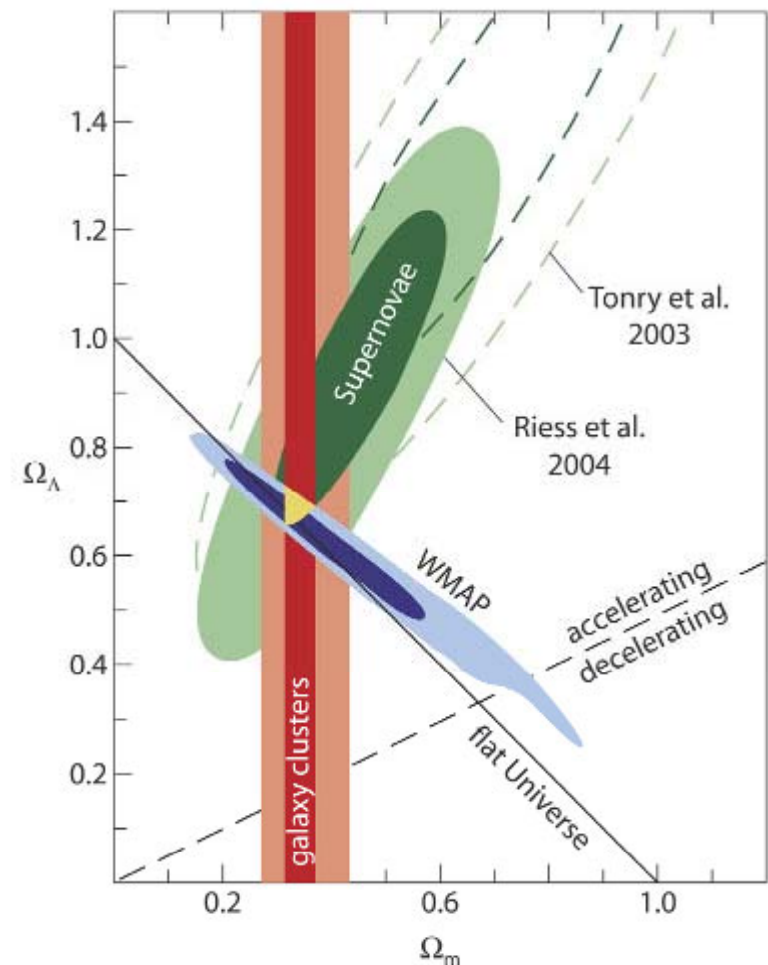
$$M(< r) = \frac{-kTr}{\mu m_p G} \left(\frac{d \ln T}{d \ln r} + \frac{d \ln \rho}{d \ln r} \right) + C(V_r, V_\tau) ?$$

Por que a massa é importante?

Testes Cosmológicos Independentes

- AGs uma amostra representativa do Universo
- Logo $f_b \sim \Omega_b/\Omega_m$ ([White et al 1993](#)).
- Ω_b é estimado através dos modelos de Big Bang nucleosíntese ([Schramm & Turner 1998](#))
- Pode-se por limites em Ω_m

$$\Omega_m = \frac{\Omega_b}{f_{\text{gas}}(1 + 0.19h^{0.5})}$$



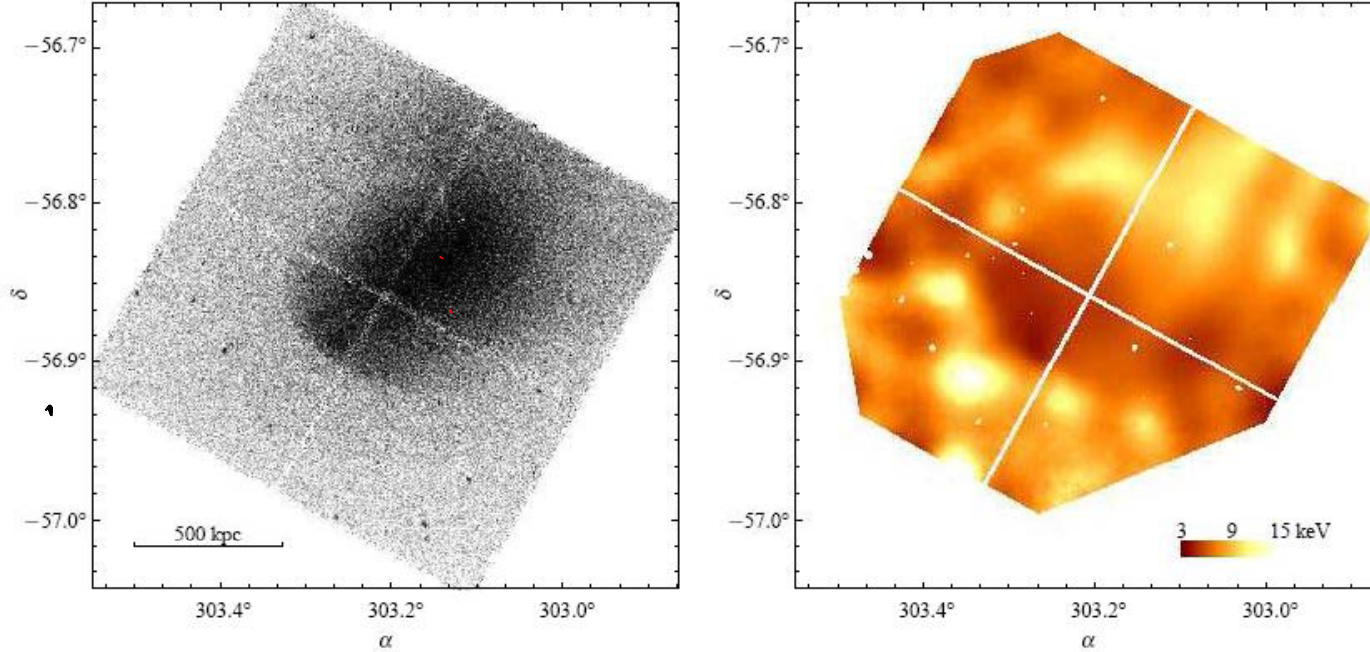
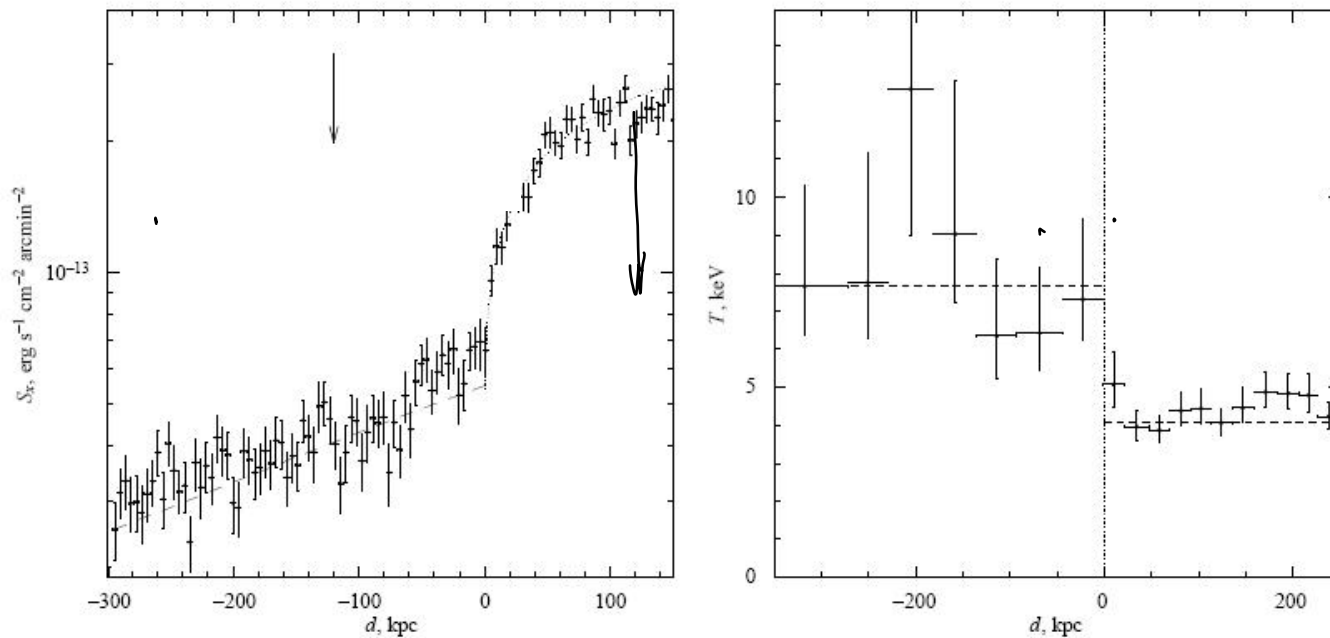
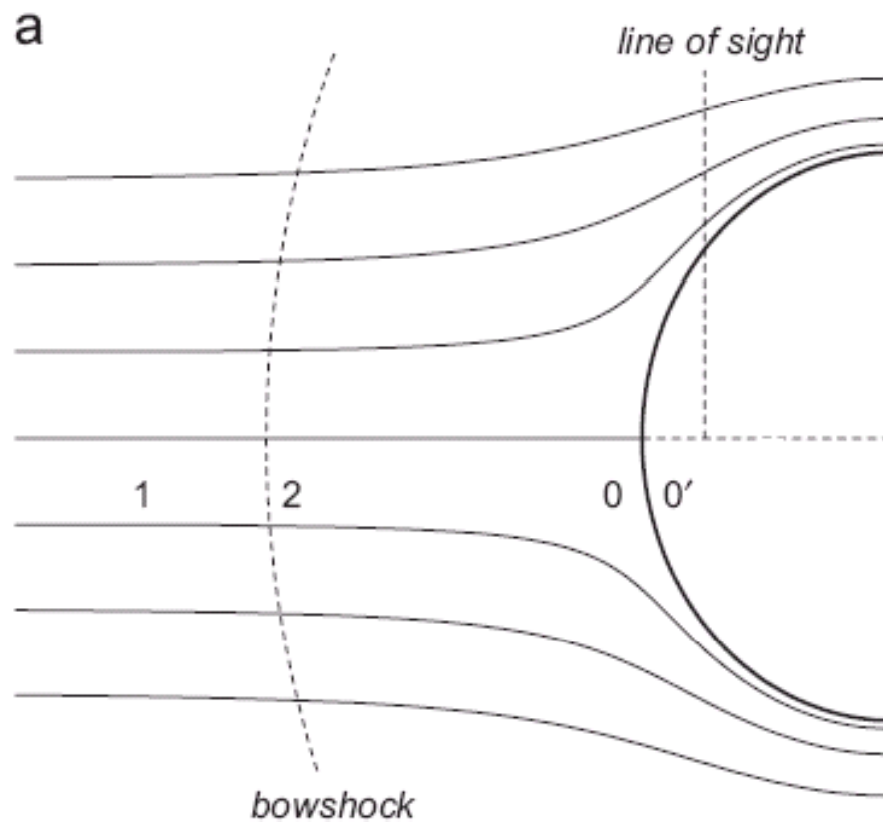


FIG. 3.— (a) Photon image in the 0.5–4 keV band binned to 2'' pixels. (b) Temperature map. The corners are not shown due to poor statistics. The typical statistical error in this image is ± 1 keV. The cold, ~ 4 keV, region near the center of the map coincides with the inside of the surface brightness edge. The very high temperature in several spots just outside the edge is insignificant. All other temperature variations greater than ± 1 keV are significant.



$$P = n kT = \text{cont}$$

FIG. 4.— (a) X-ray surface brightness profile (expressed in the units of energy flux in the 0.5–2 keV band) across the cold front. The profile was measured in the sector shown in Fig. 2. The *Chandra* photon flux in the 0.5–4 keV band was converted to an energy flux in the 0.5–2 keV band. The distance is measured relative



$$\frac{p_0}{p_1} = \left(1 + \frac{\gamma - 1}{2} M_1^2 \right)^{\frac{\gamma}{\gamma-1}}, \quad M_1 \leq 1$$

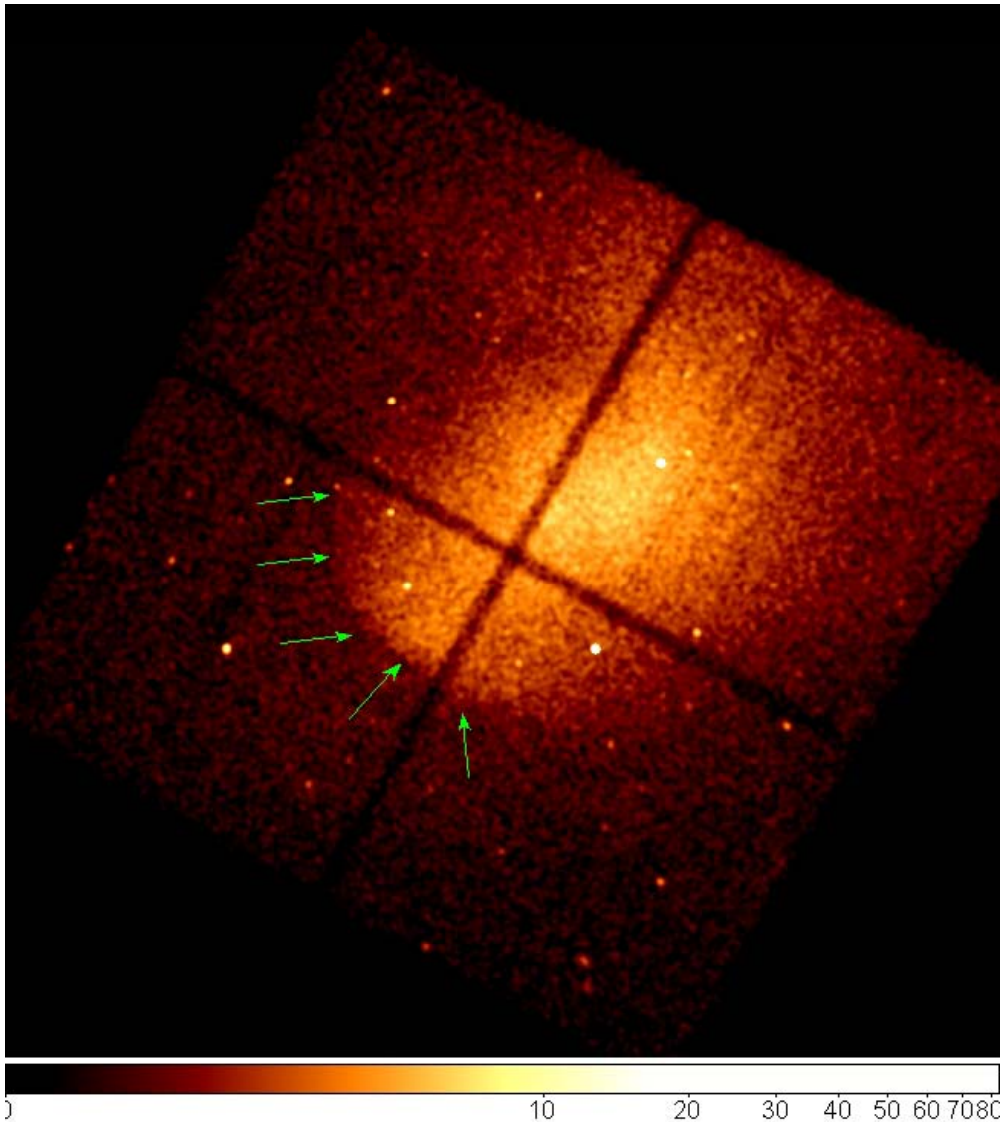
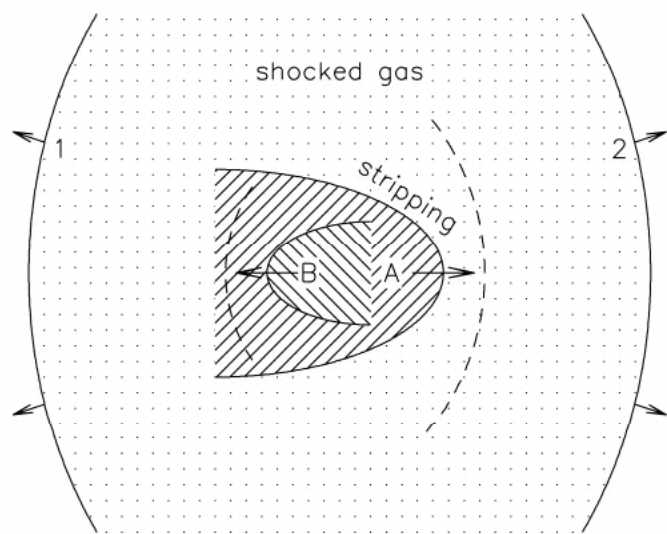
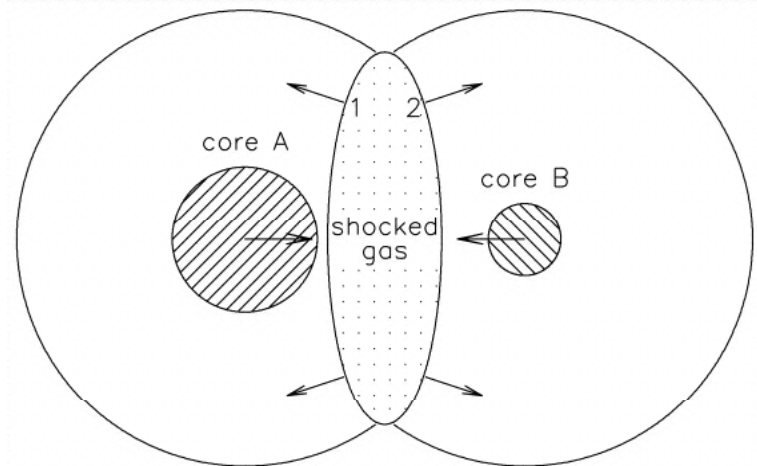
$$\frac{p_0}{p_1} = \left(\frac{\gamma + 1}{2} \right)^{\frac{\gamma+1}{\gamma-1}} M_1^2 \left[\gamma - \frac{\gamma - 1}{2M_1^2} \right]^{-\frac{1}{\gamma-1}}, \quad M_1 > 1,$$

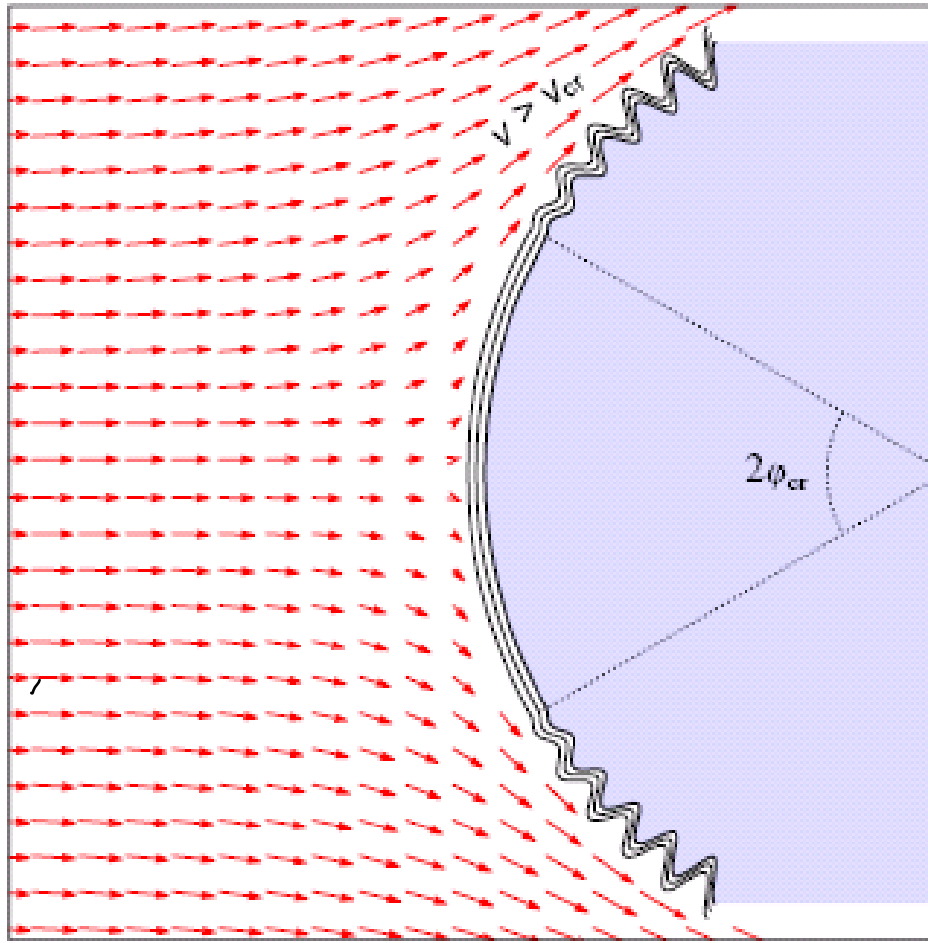
Modelo Original – Markevitch 2000

Para os casos mais comuns subsônicos.

Abell 3667 a $z=0.055$, tem
varios indicadores de que está
em um merger.

$$v \approx 1400 \text{ Km/s}$$
$$m \approx 1 \pm 0.2$$

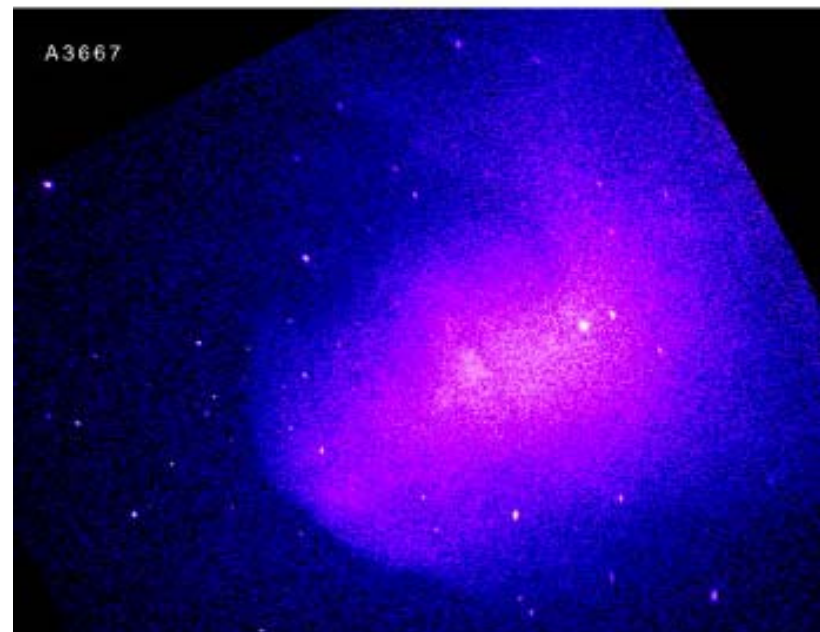
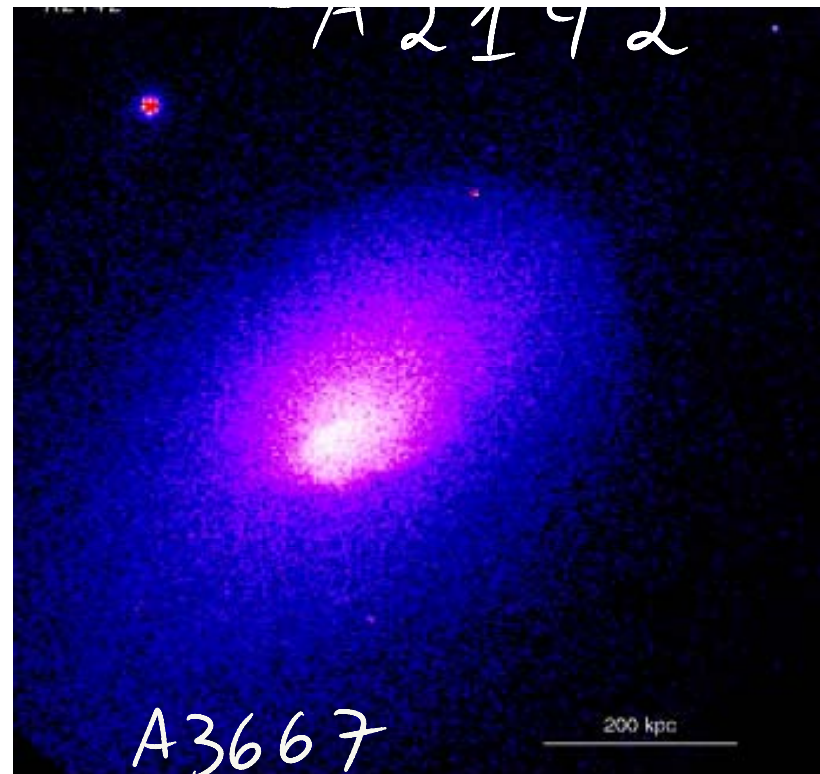
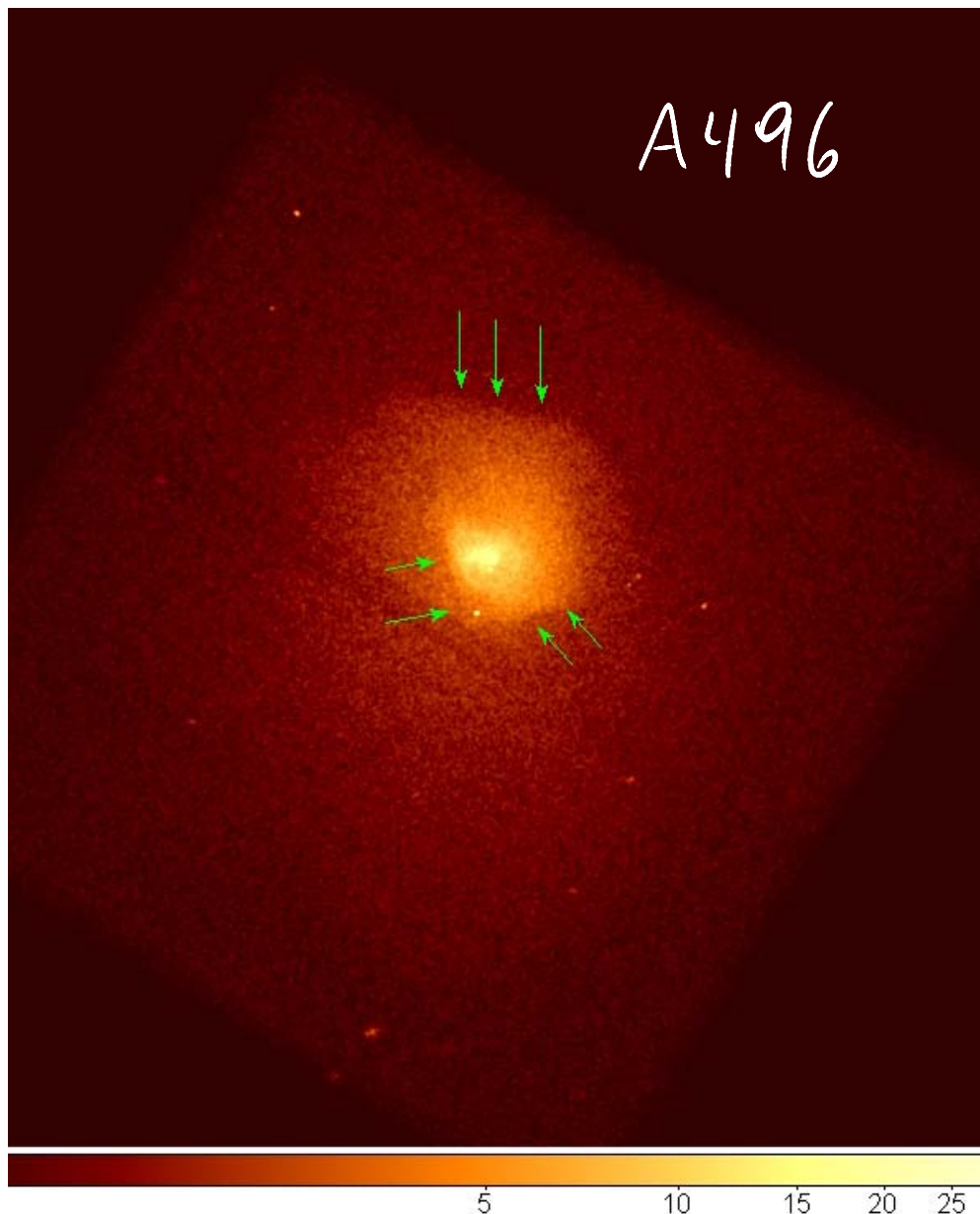




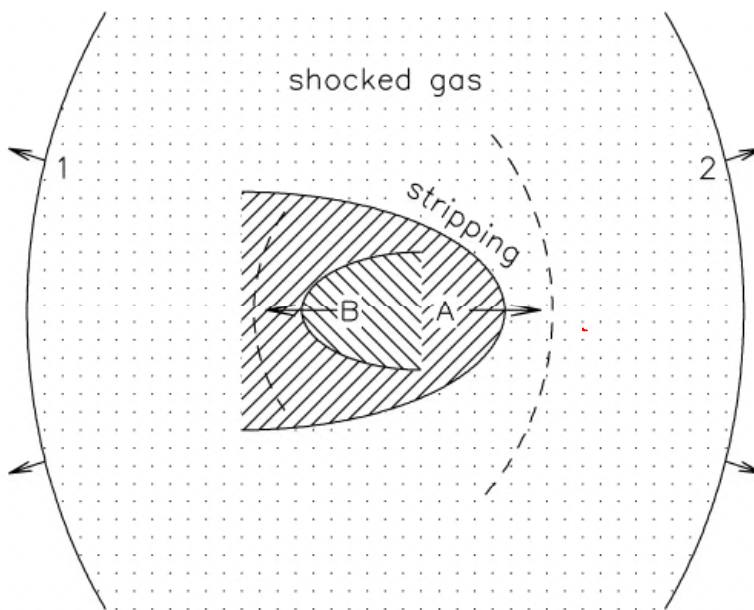
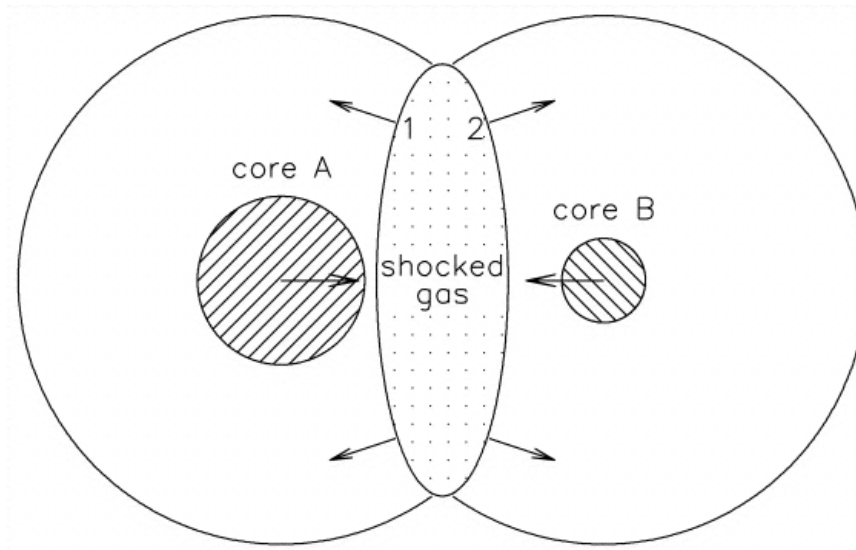
$$B \gtrsim \gamma \mu^6$$

A schematic illustration of the suppression of Kelvin–Helmholtz instability at the surface of the A3667 cold front. The magnetic layer (shown by red dashed lines along the front) can provide surface tension that suppresses the growth of perturbations in the region where the tangential velocity is greater than some critical value V_{cr} . The velocity field (arrows) corresponds to the flow of incompressible fluid around a sphere. (Reproduced from Chlinin et al., 2001a.)

“Classic” Cold Fronts

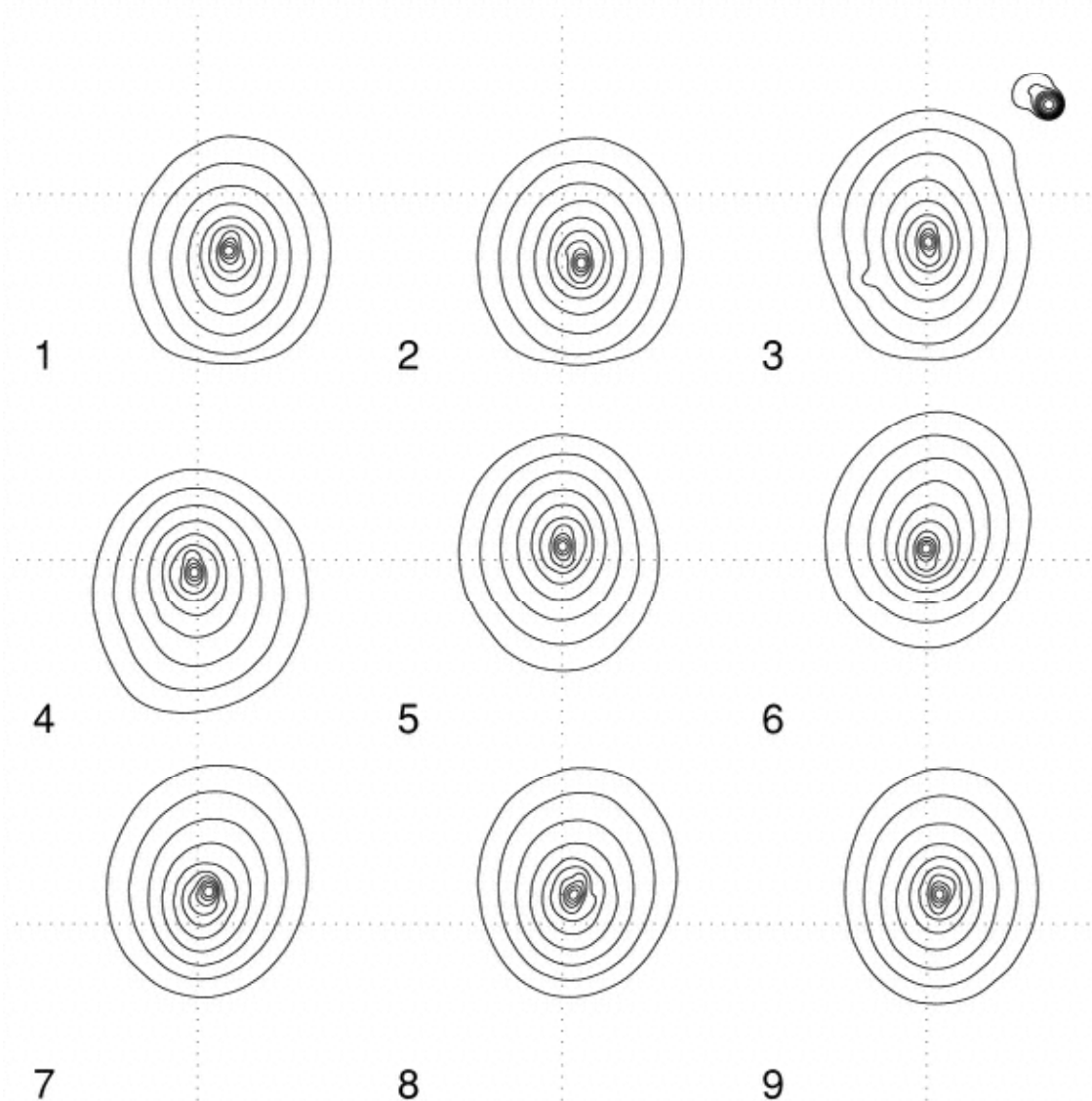


External Mechanisms (Markevitch et al. 2000)

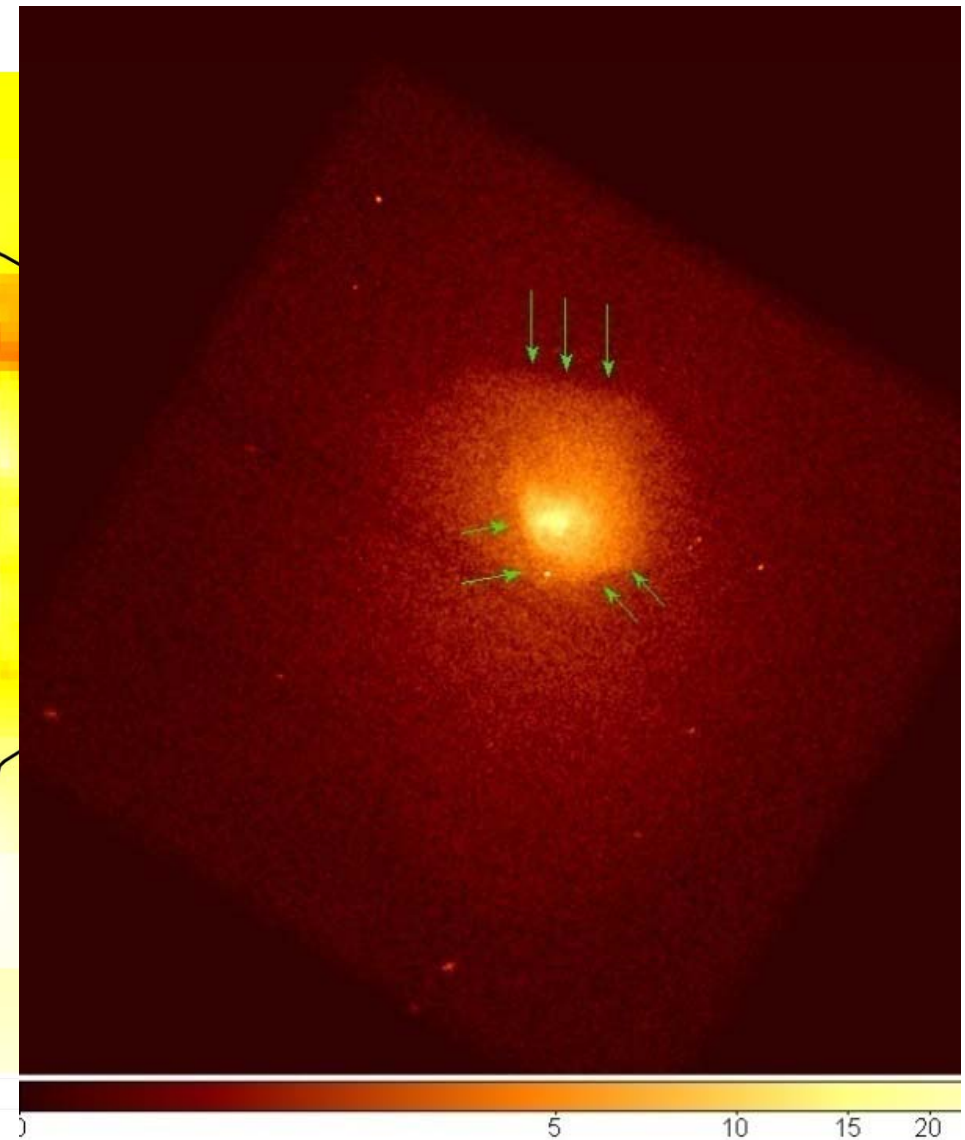
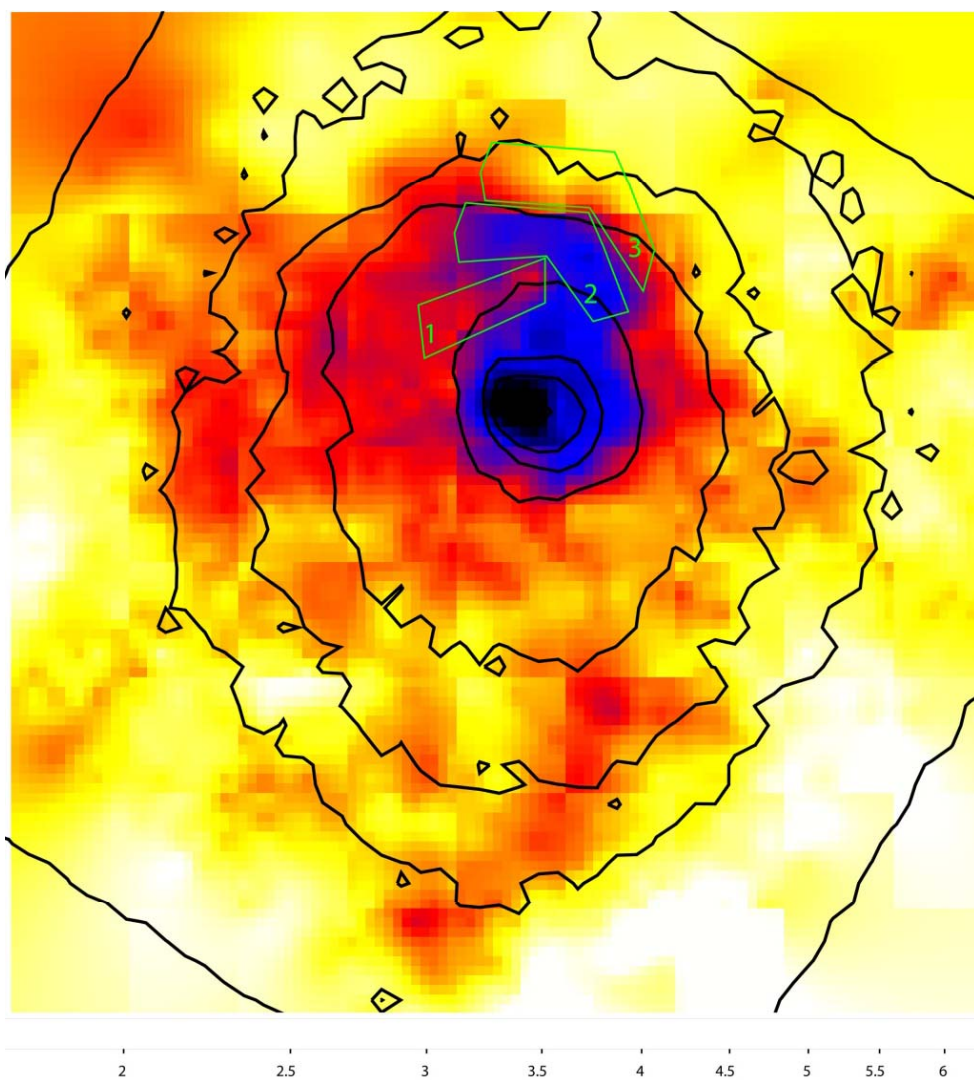


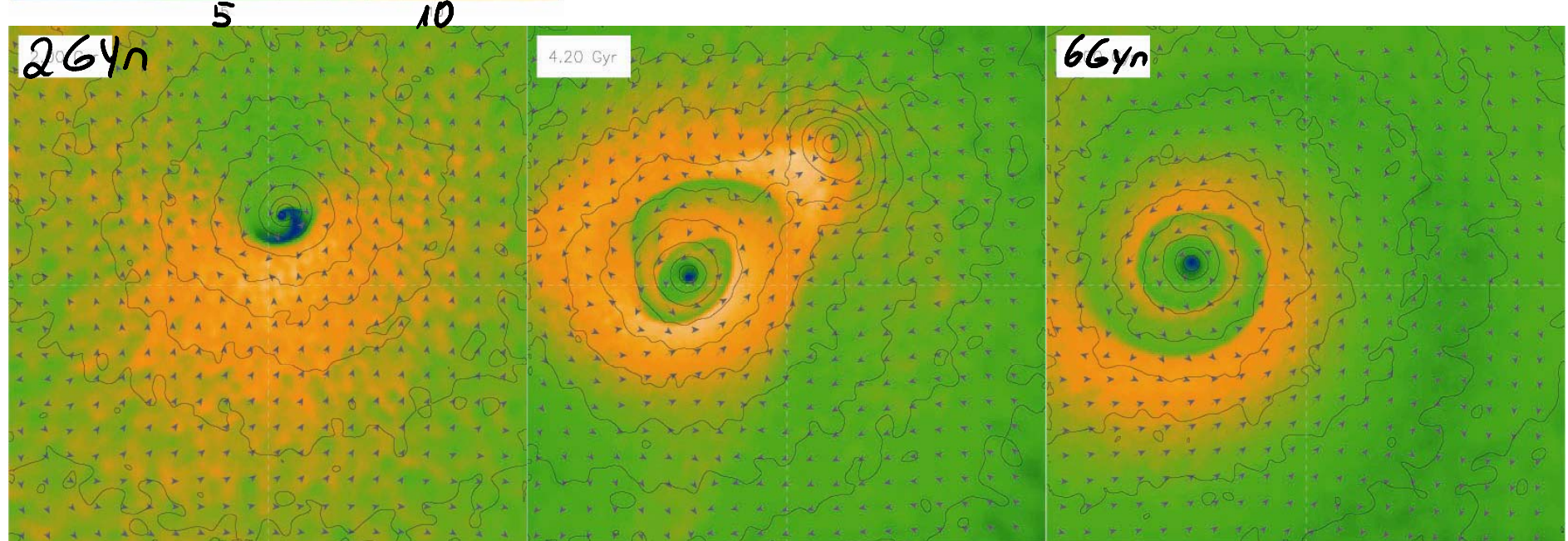
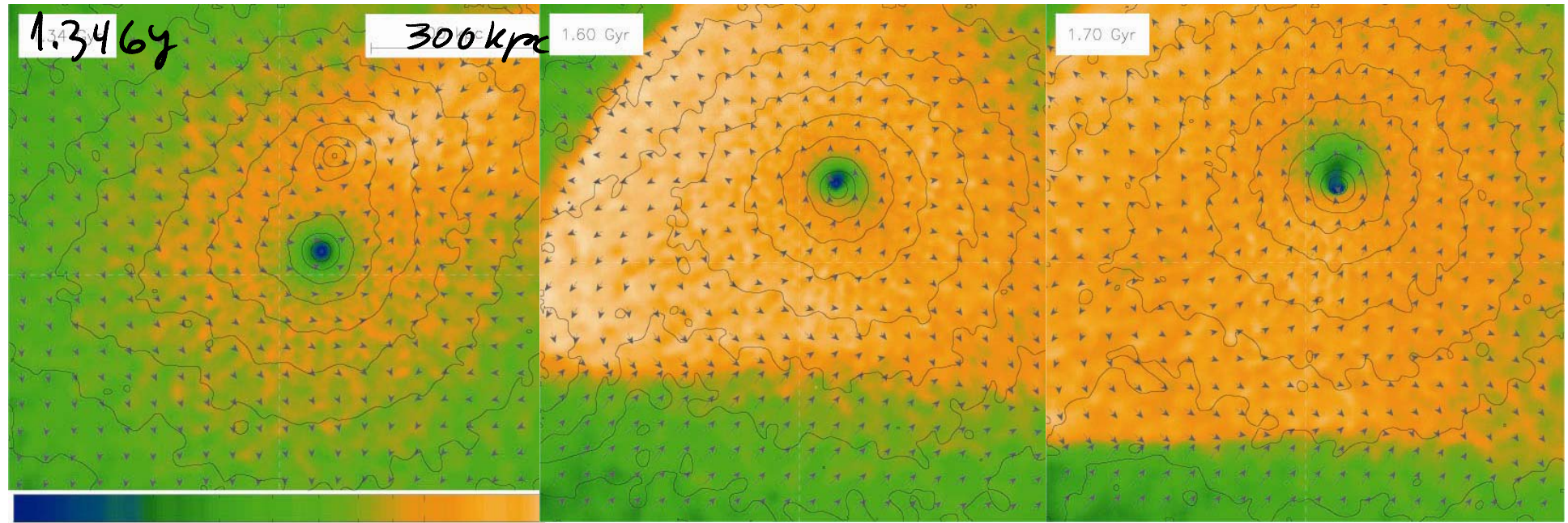
From LCDM w/ cooling
30:1 mass ratio
200kpc boxsize
50Myr time step

Induced Internal
Mechanisms
(Tittley et al.
2005)



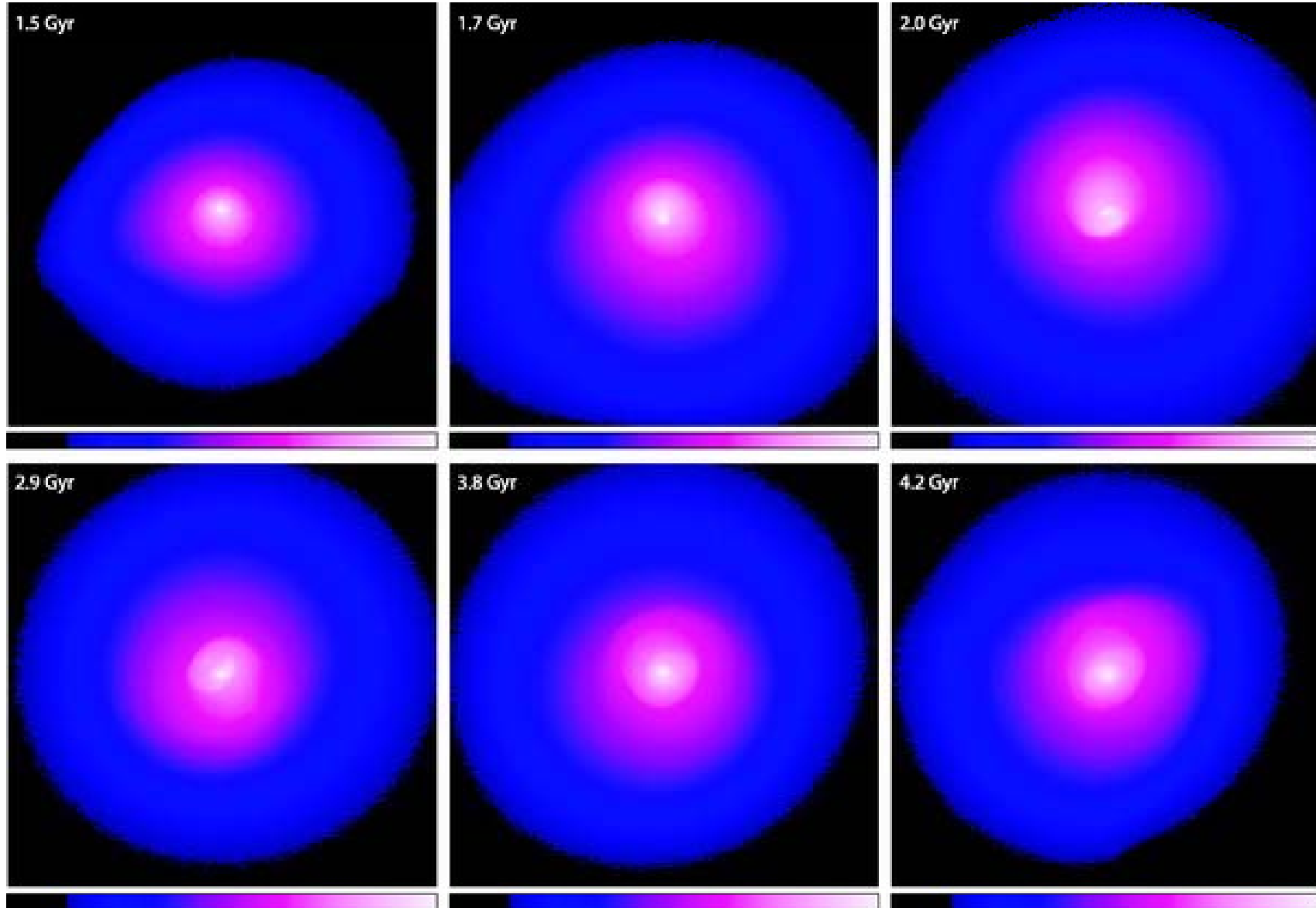
Dupke 2007

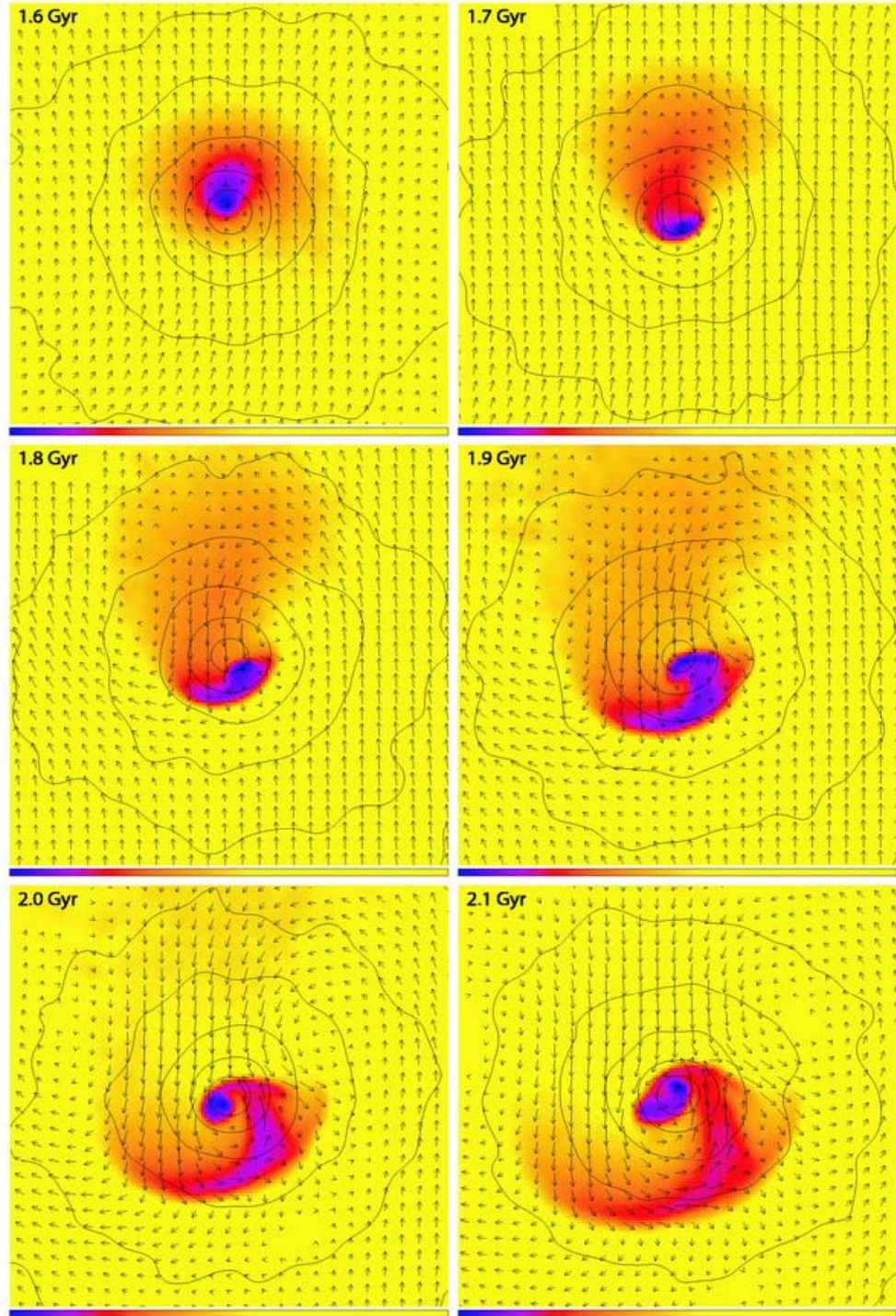


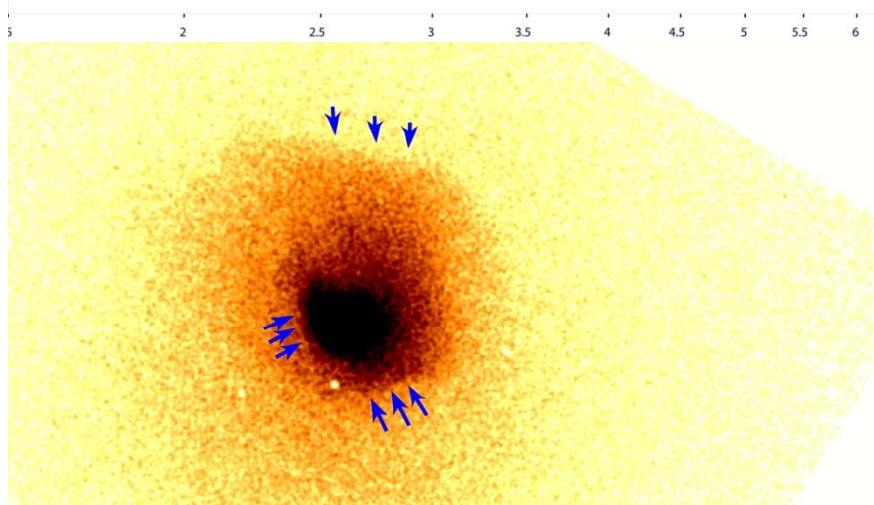
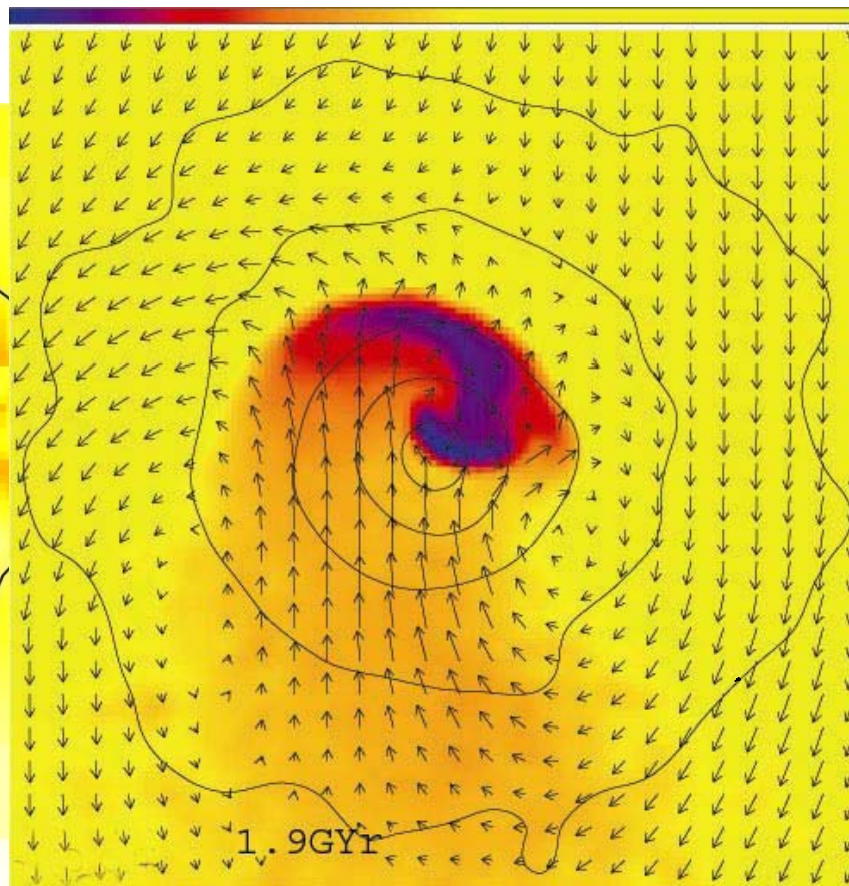
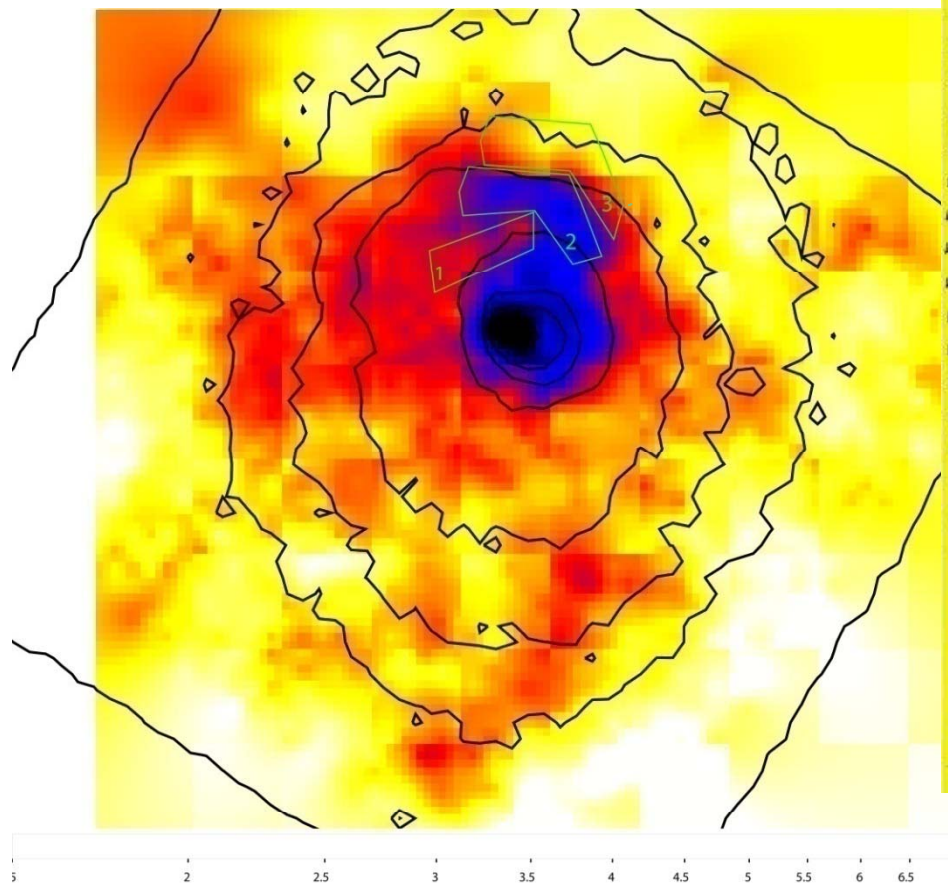


parallel PM tree+SPH code GADGET2

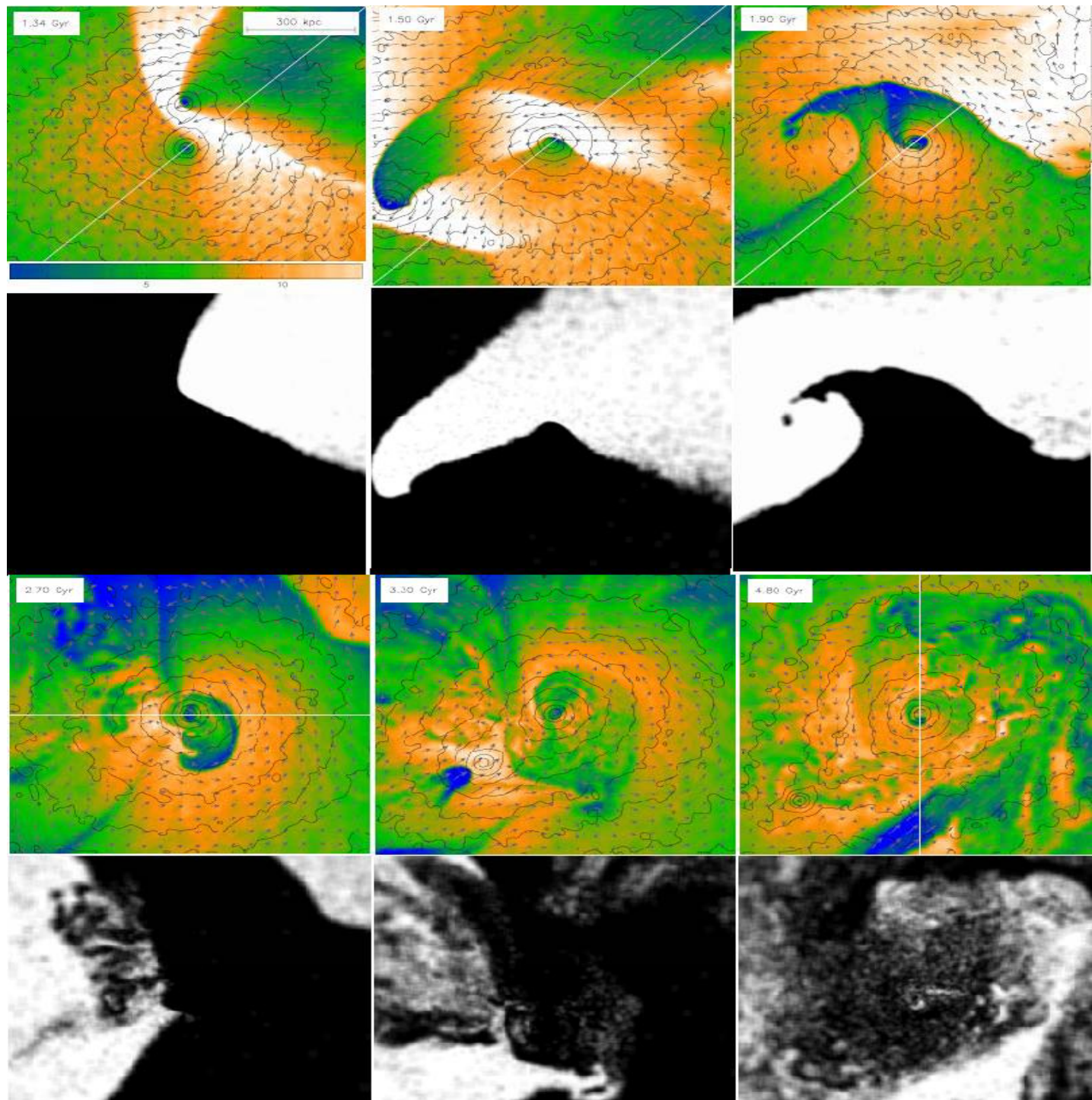
Ascasibar & Markevitch 2006 – DM blob passage – $M_{DM2}/M_{DM1}=5$, $b=500\text{kpc}$,
panel size 1 Mpc, Temp scale shown, arrows show gas velocity wrt DM center

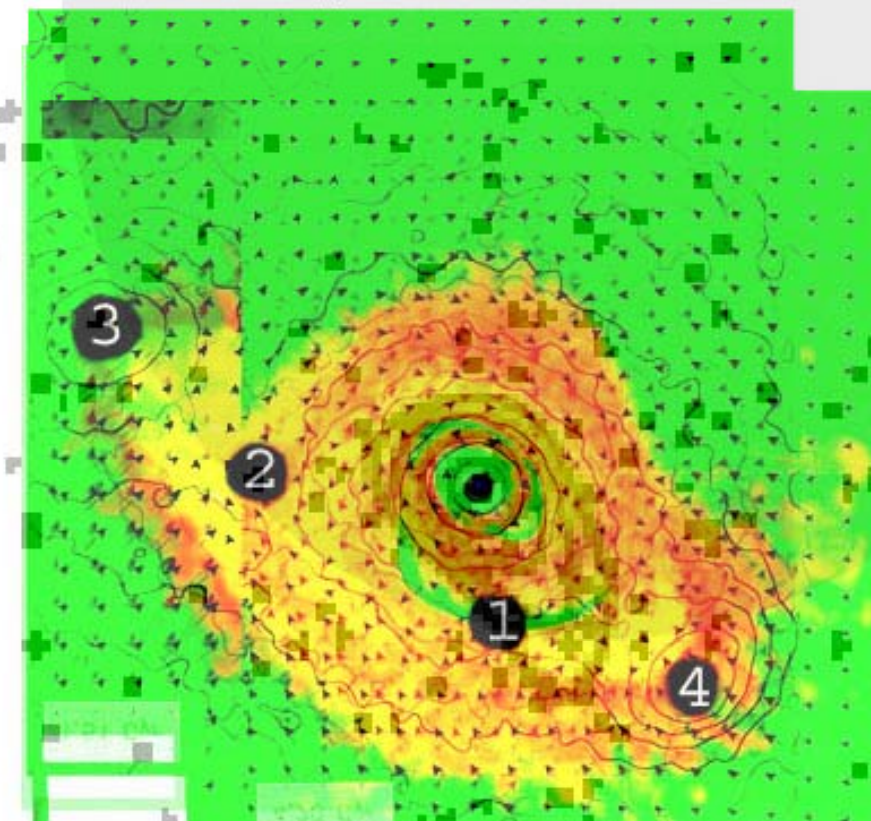






Ascasibar &
Markevitch 2006 –
blob passage –
same as before but
with gas

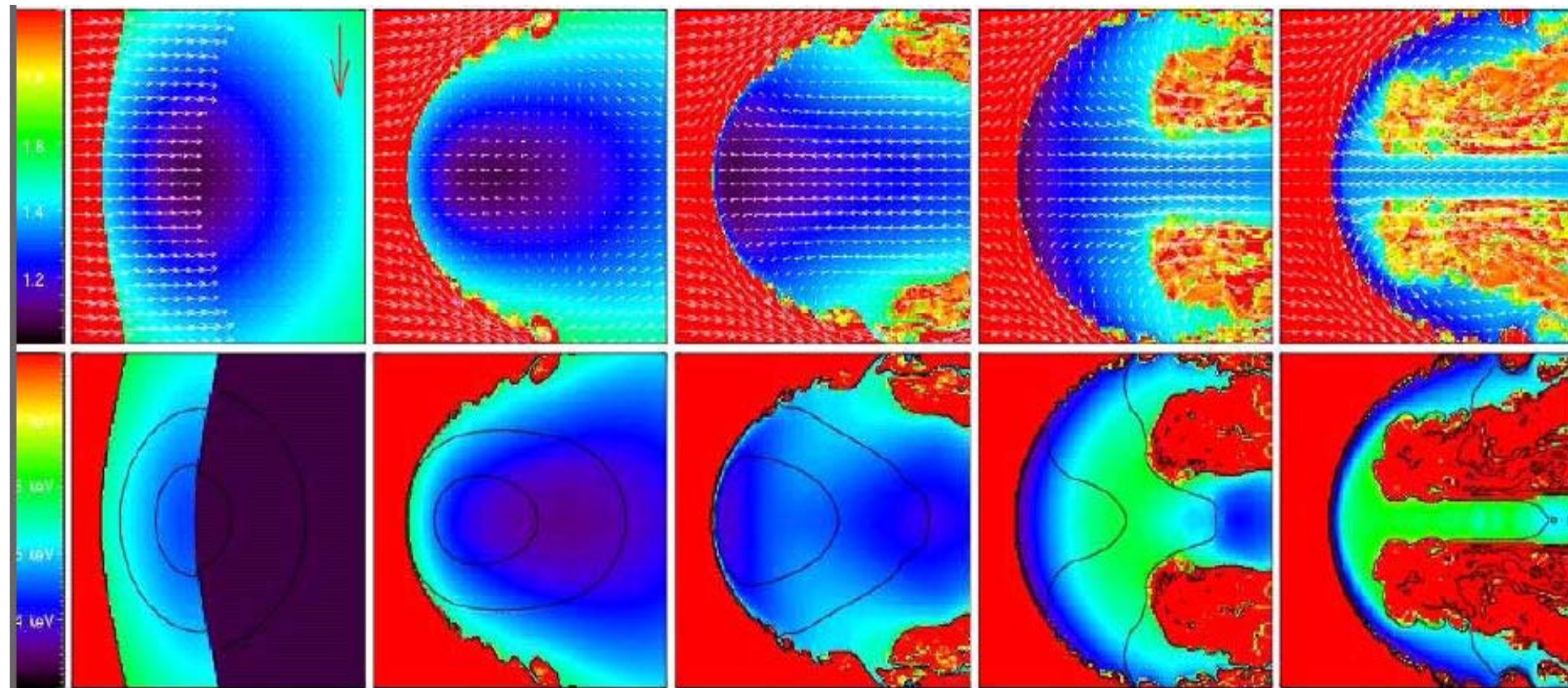




129

Flint Blob, 2006

2 Mpc

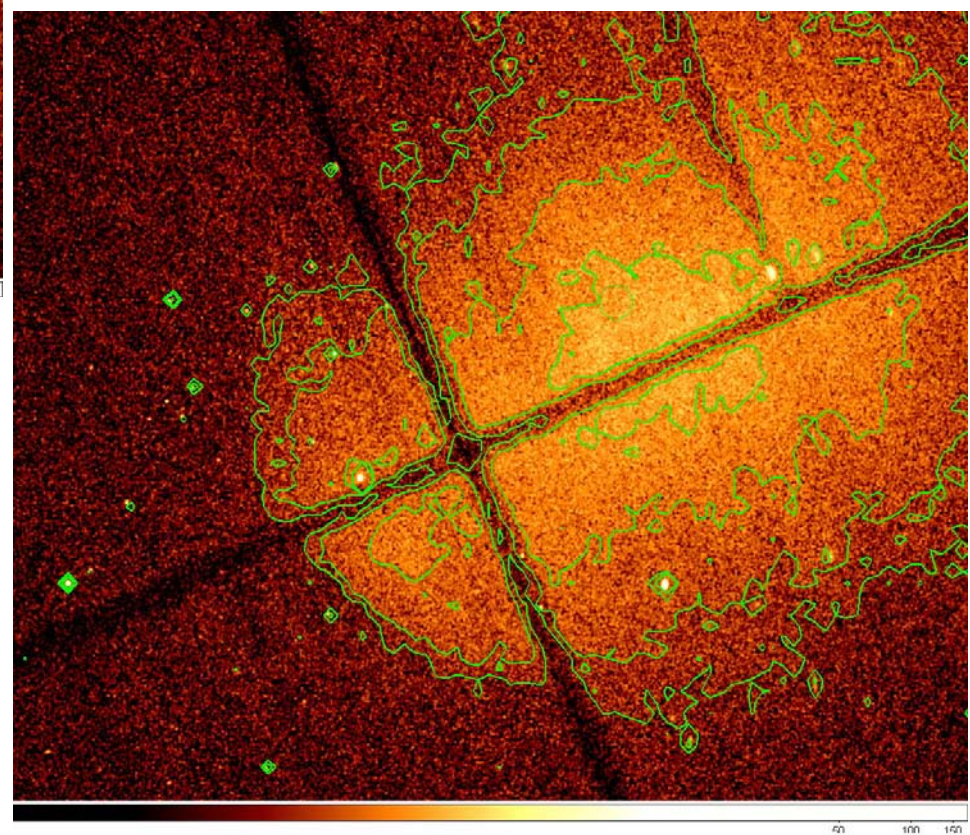
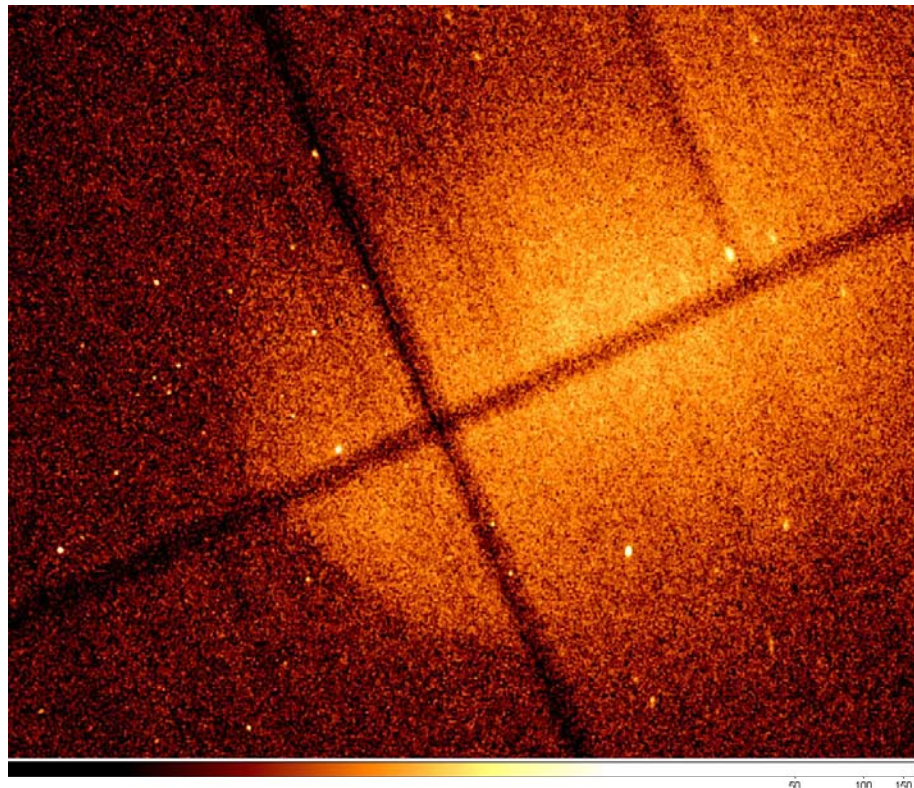


Heinz et al. 2003
Top – entropy
Bottom –Temp
Contours- SB

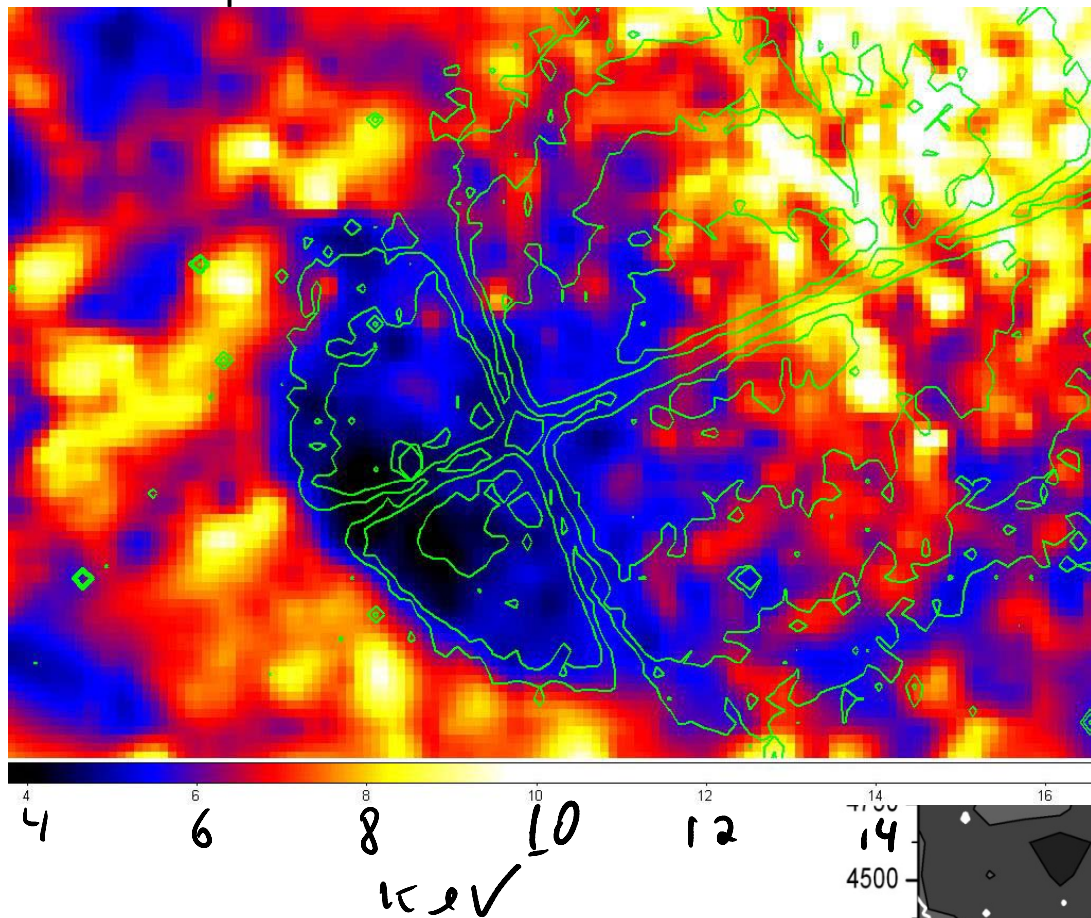
A3667 parameters
R=1 Mpc

A 3667

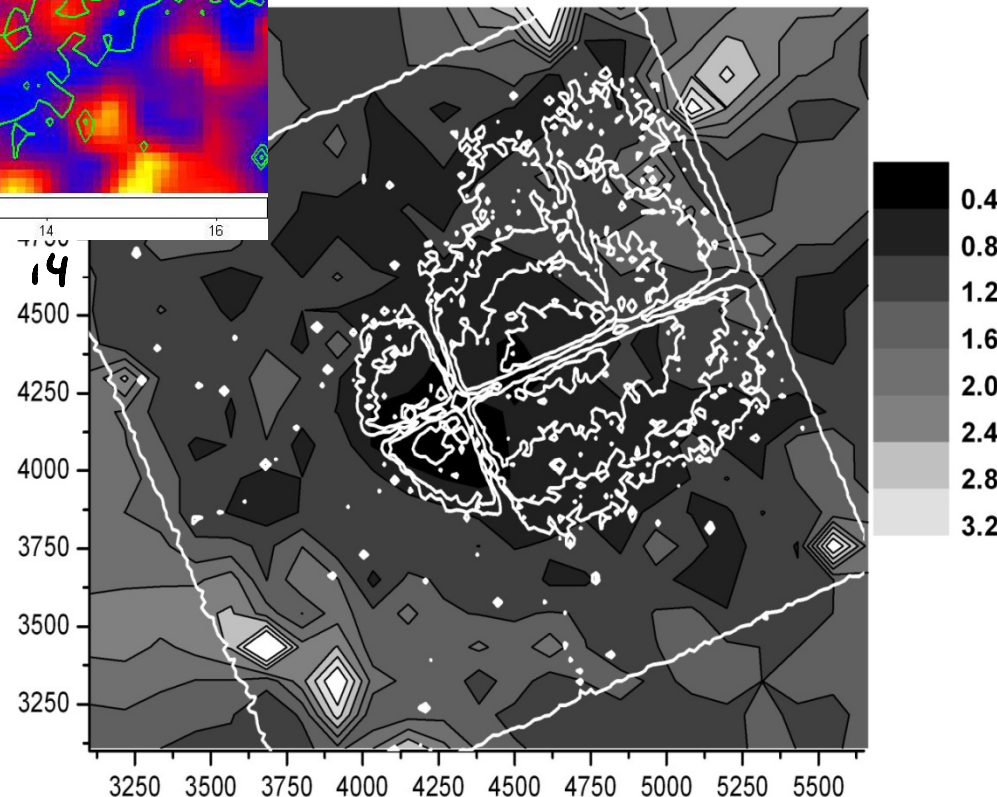
~ 350 ksec



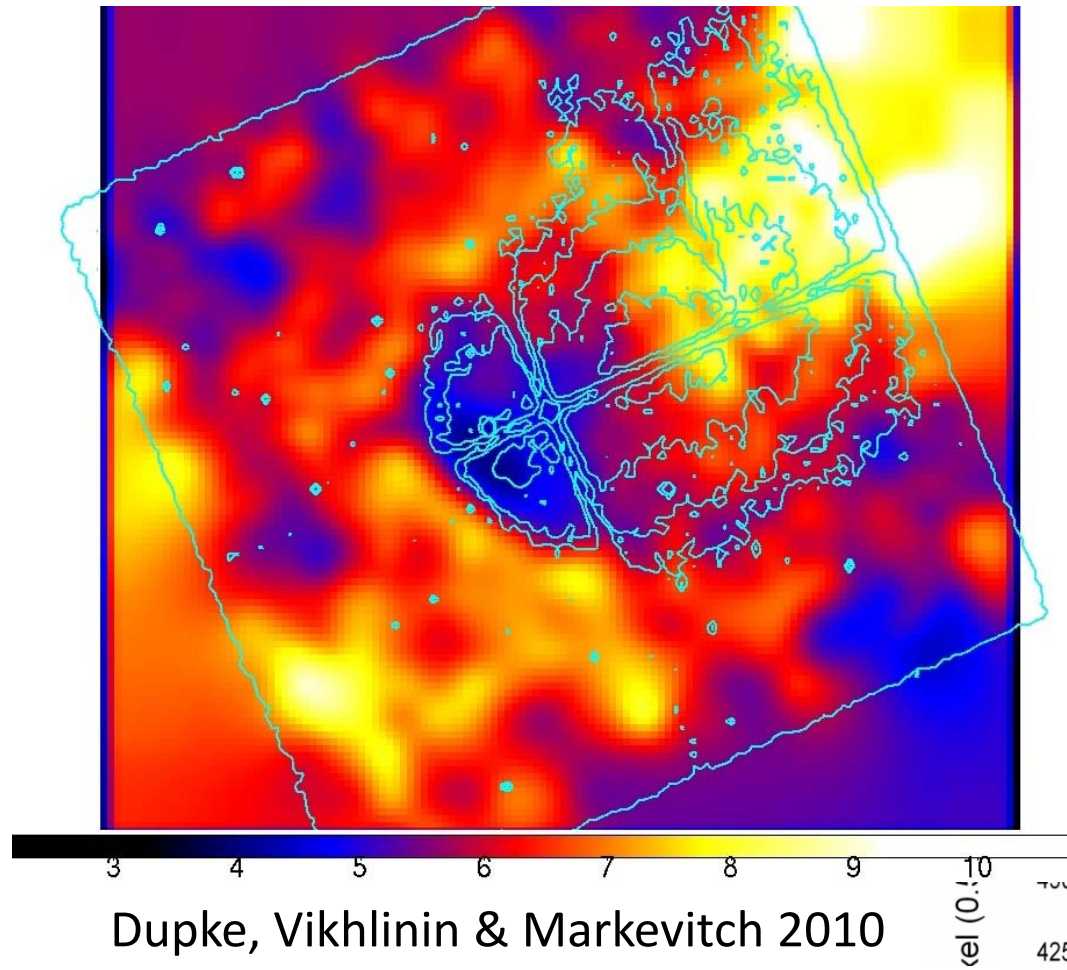
A 3667 Temperature keV



A3667-T error-3k - keV

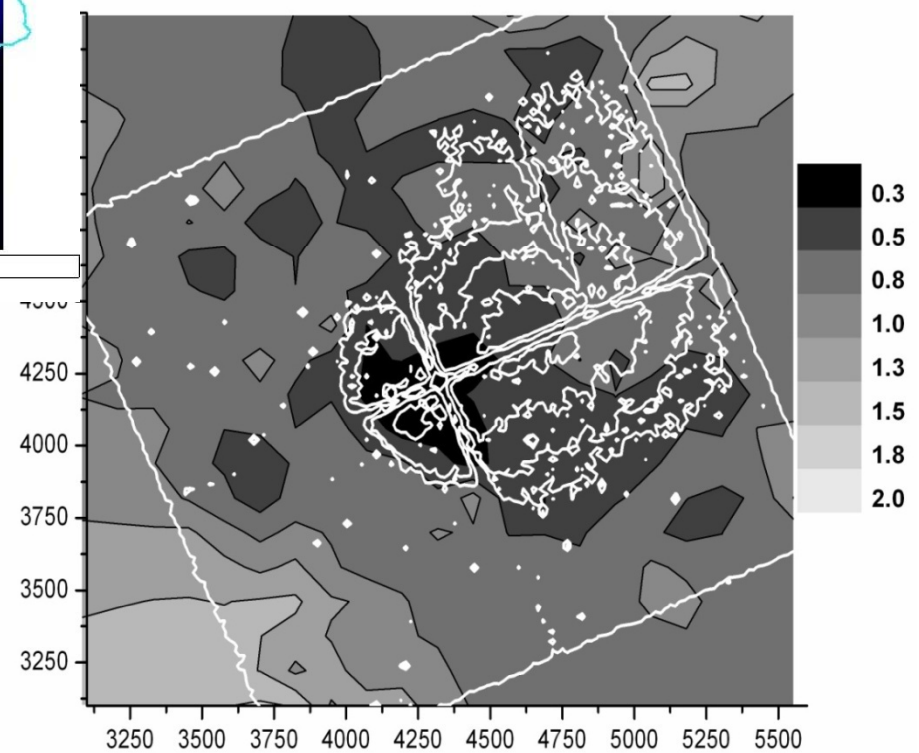


A 3667 Temperature 7k - keV



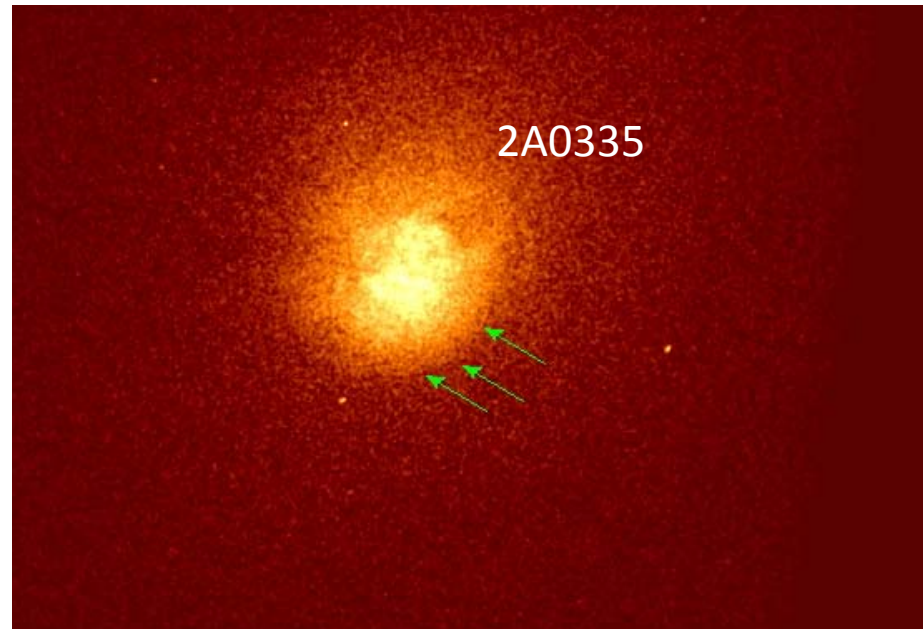
$V \sim 1100 \text{ km/s}$

A3667-Temp 1σ error -7k-smo3-132cell

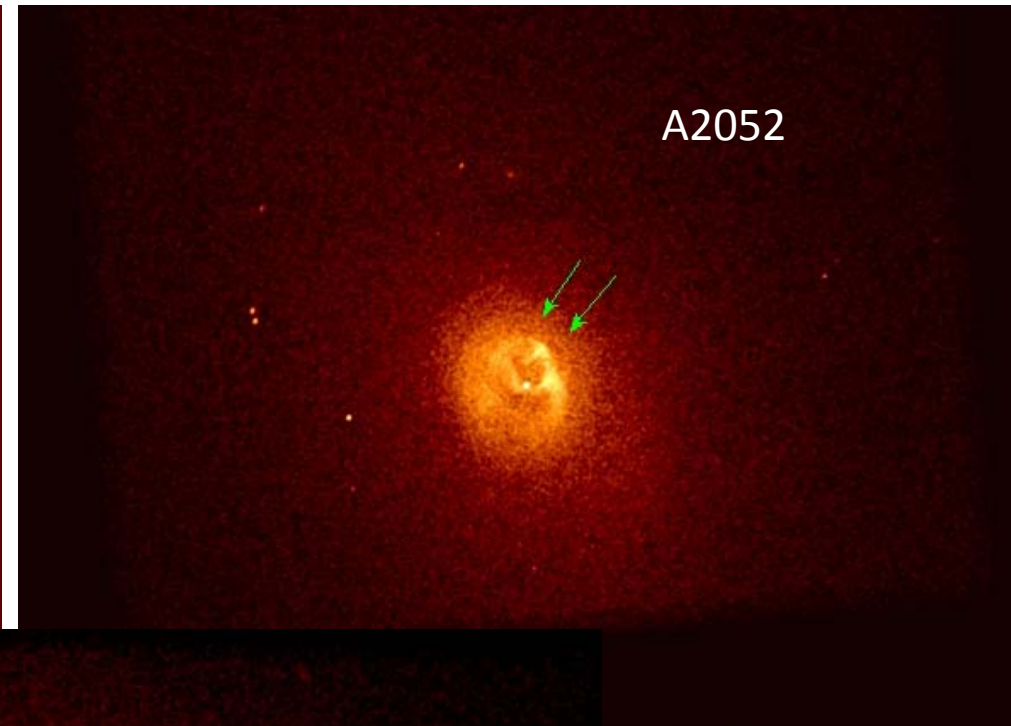


$$\frac{p_0}{p_1} = \left(1 + \frac{\gamma-1}{2} M_1^2\right)^{\frac{\gamma}{\gamma-1}}, \quad M_1 \leq 1$$

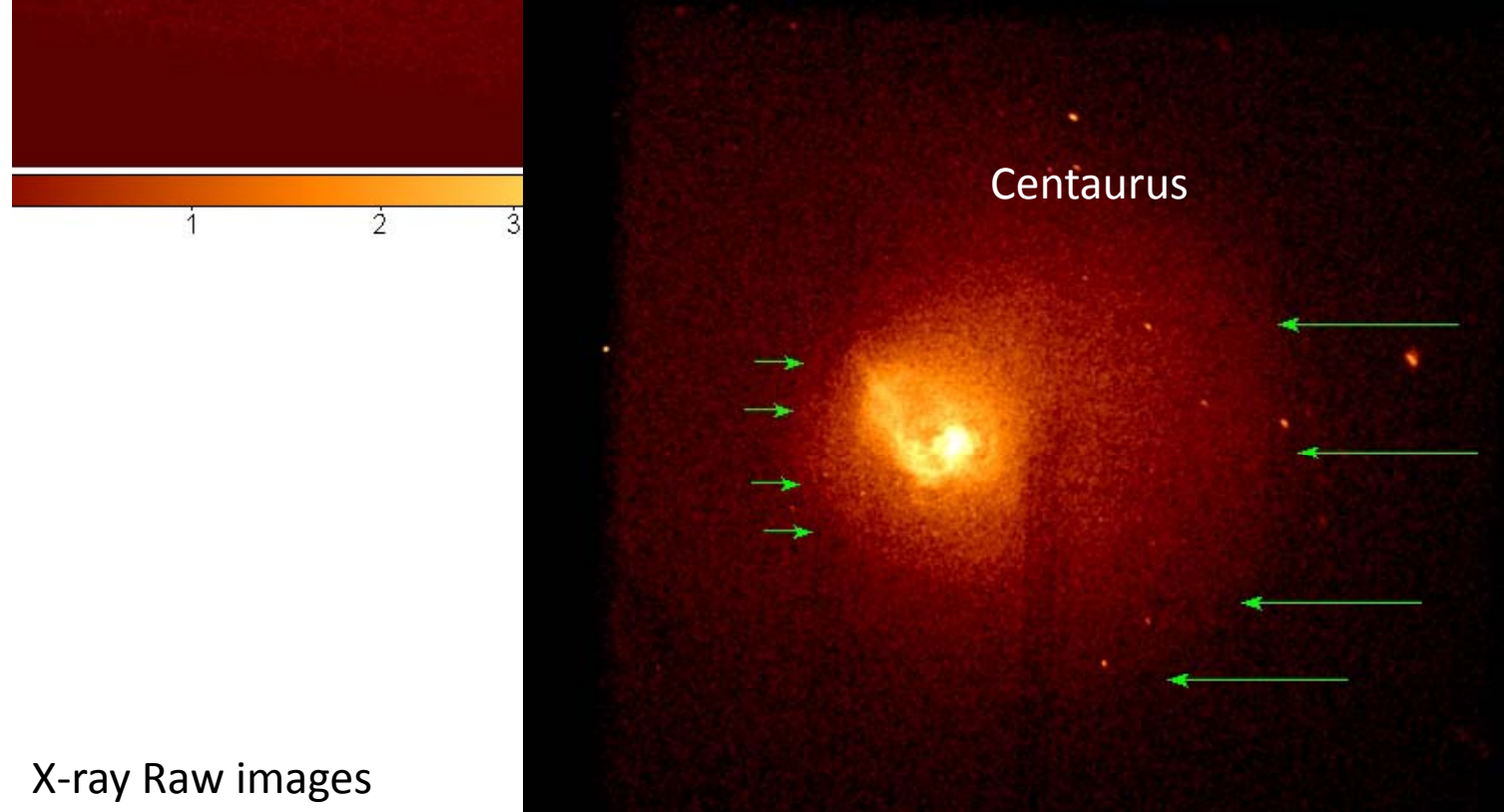
$$\frac{p_0}{p_1} = \left(\frac{\gamma+1}{2}\right)^{\frac{\gamma+1}{\gamma-1}} M_1^2 \left[\gamma - \frac{\gamma-1}{2M_1^2}\right]^{-\frac{1}{\gamma-1}}, \quad M_1 > 1,$$



2A0335



A2052



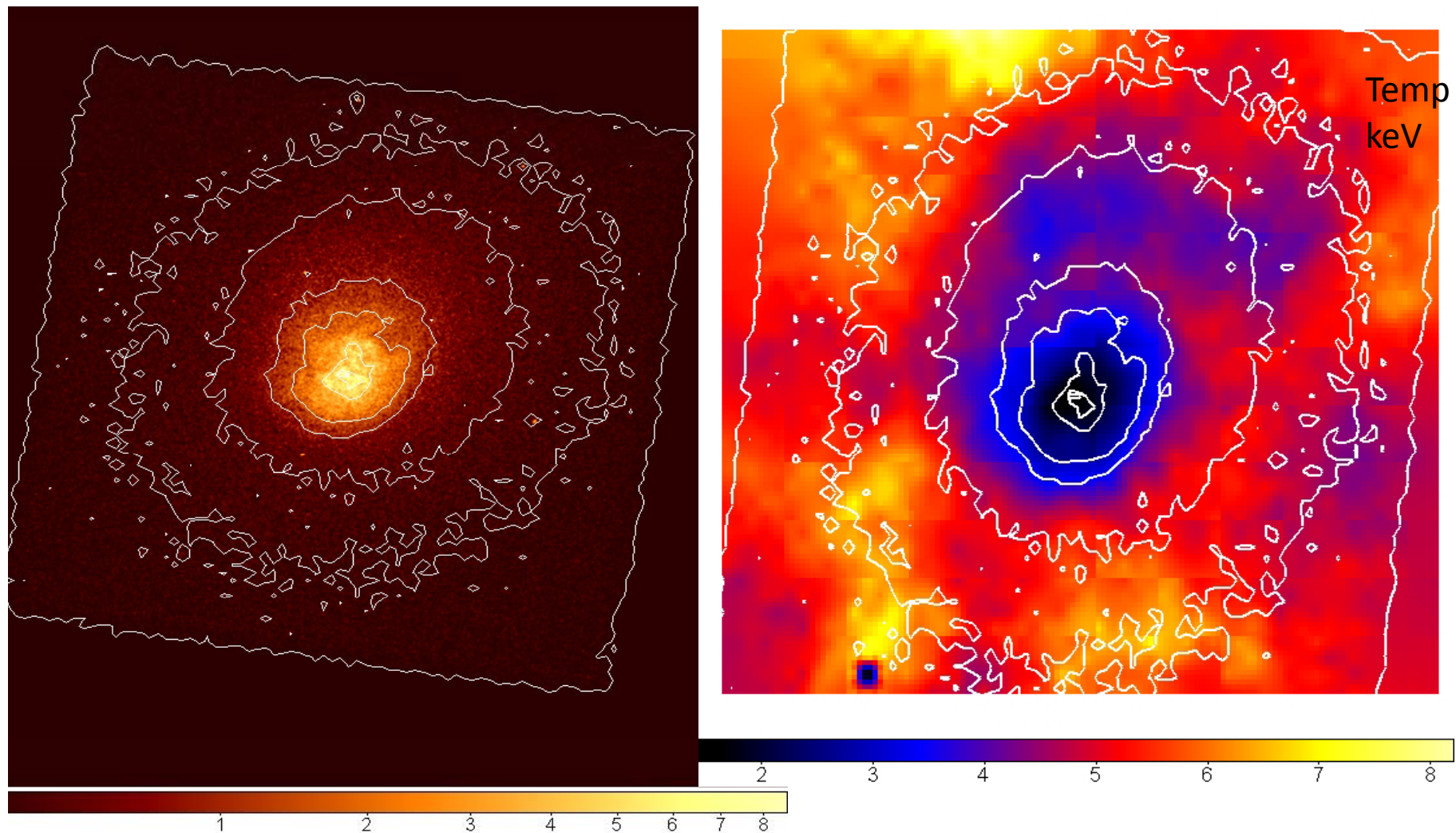
Centaurus

X-ray Raw images

40% of the clusters
in the archive have
cold front like
features

0 20 30 40 50 60

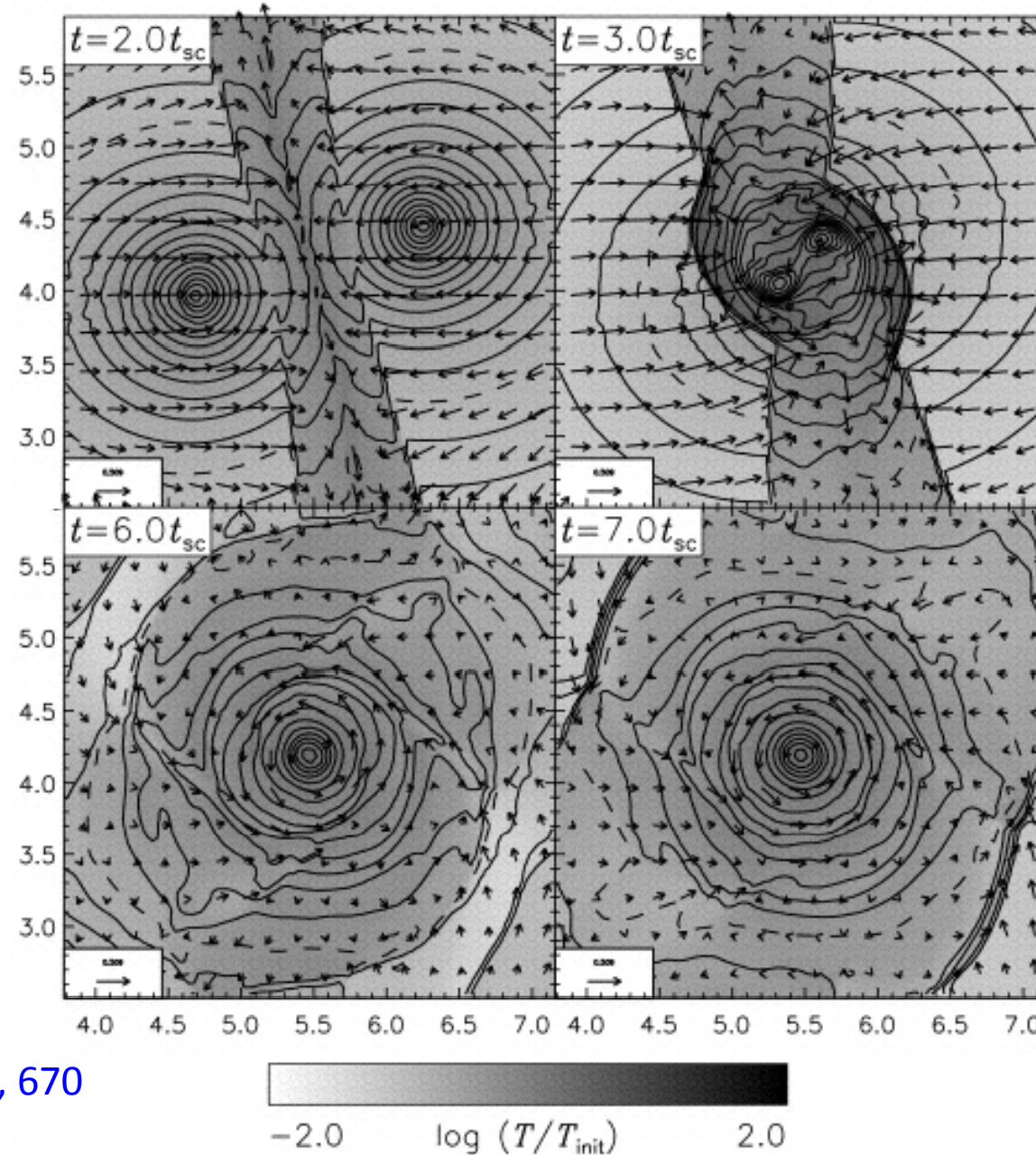
2a0335



Colisões não frontais

$b \sim 10 r_{\text{core}}$

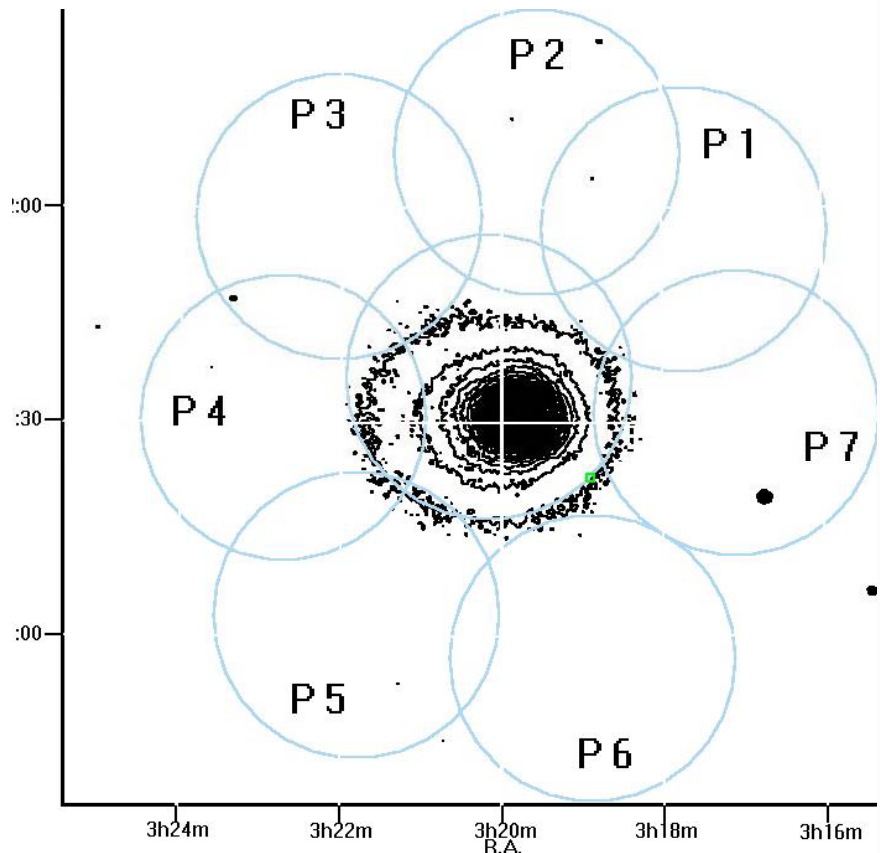
Seta representa
 $v \sim 2000 \text{ km/s}$



Ricker 1998 ApJ, 496, 670

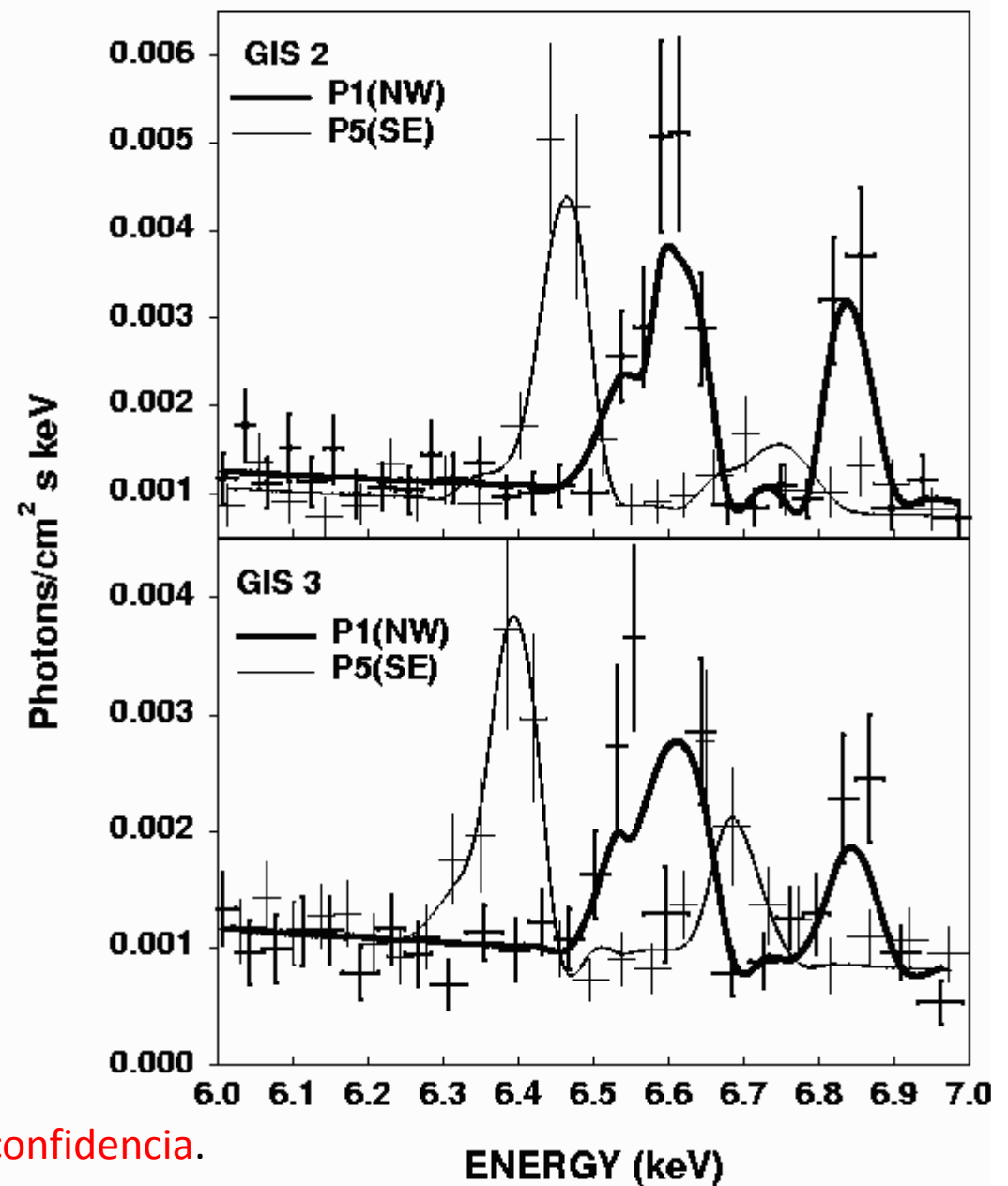
$$\frac{\Delta\lambda}{\lambda} = \frac{V}{c}$$

Doppler Effect



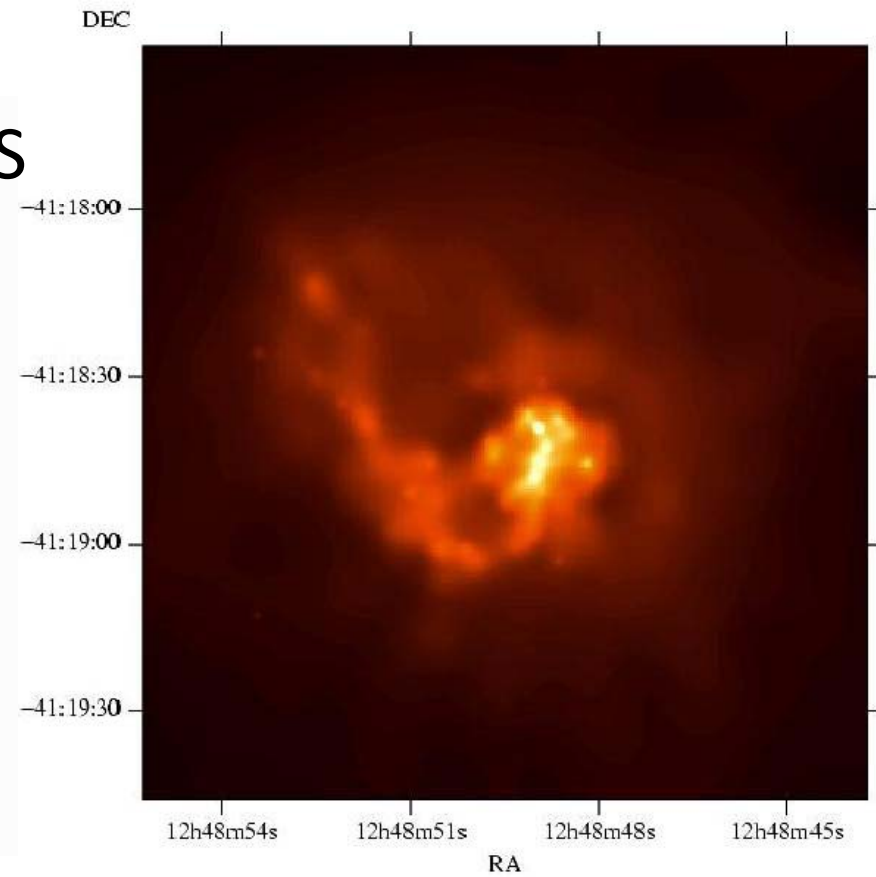
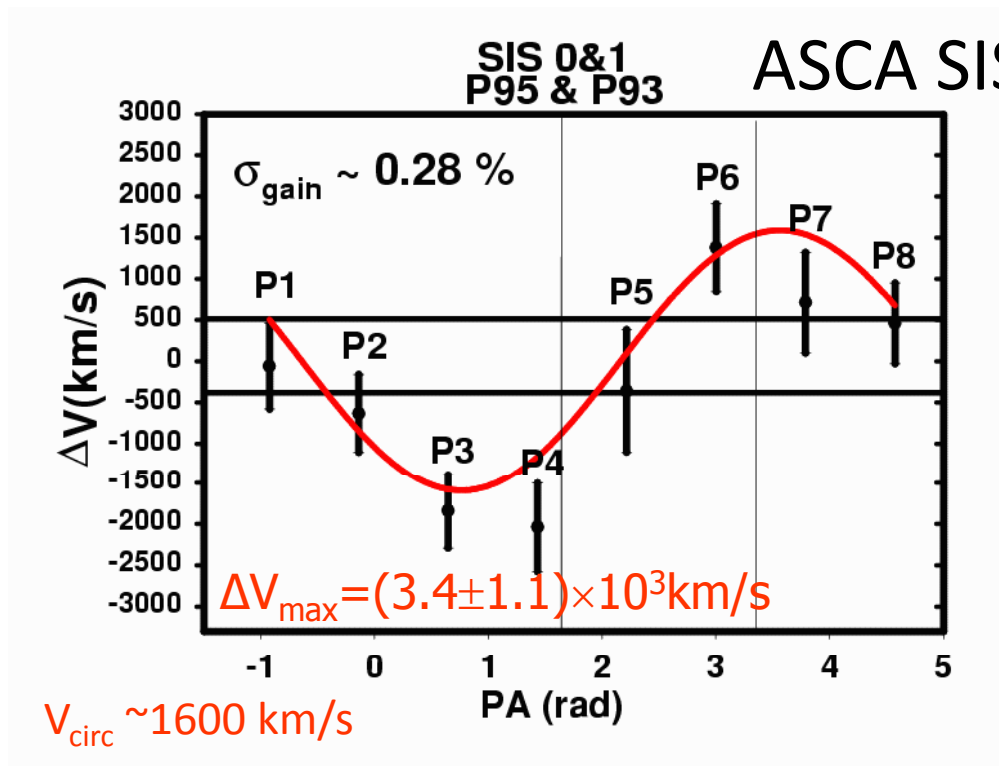
>1500 km/s com 90% confidencia.

Dupke & Bregman 2001, ApJ, 547, 705

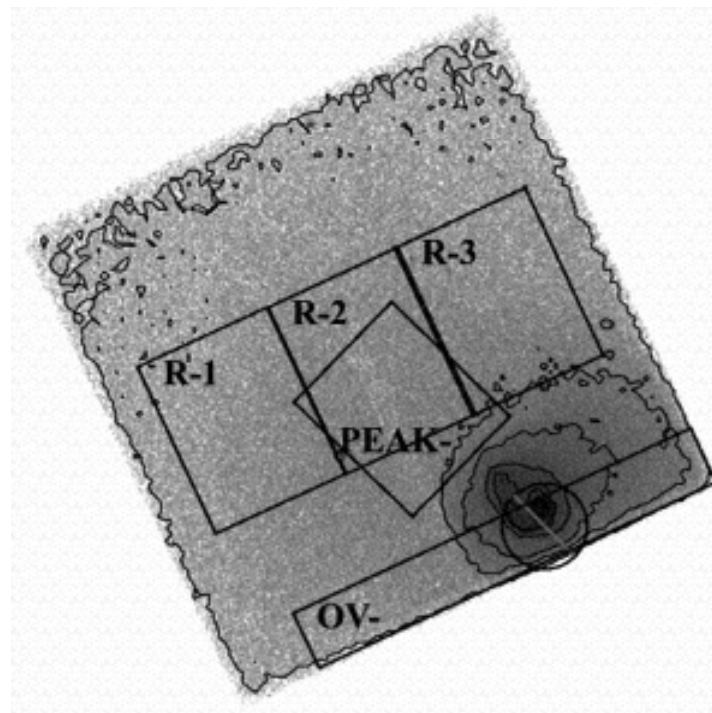


$$\Delta V = \frac{FWHM}{2.35\sqrt{N_{line}}}$$

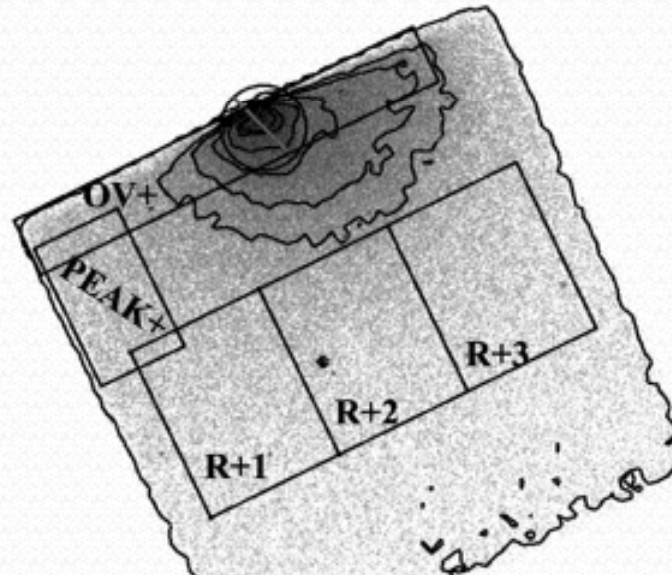
FWHM
 ASCA SIS 2%-4%
 GIS 8%
 To get 500 km/s need ~60 line photons!
 ACIS ~ EPICs ~ XIS ~ SIS



ASCA SIS Systematic search in the archive 10-15% show signs of velocity gradients .
Dupke & Bregman 2005



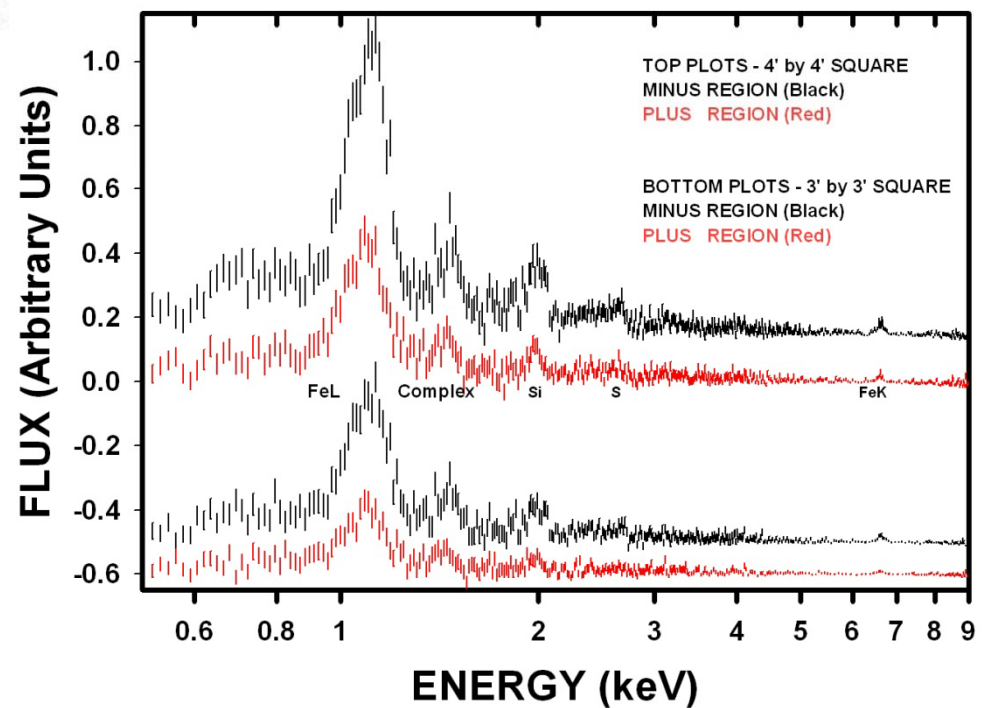
$$V_{\text{circ}} = 1200 \pm 100 (\pm 400) \text{ km/s}$$



Centaurus CCD center

Using multiple Pointings to tailor observations for Velocity Studies.

Best calibrated parts of the CCDs



$$\tau \sim (0.44 h_{50}^{-1})(R/4.5)(V_{\text{circ}}/1.2 \times 10^3 \text{ km s}^{-1})^{-1}$$

$$E_{\text{rot}} \sim (2 \times 10^{61} h_{50}^{-3})(\eta/2.5)(\mu/0.6)(n/10^{-2} \text{ cm}^{-3}) \\ (V_{\text{circ}}/1.2 \times 10^3 \text{ km s}^{-1})^2(R/4.5)^3 \text{ ergs}$$

$$\beta_{\text{gas}} = 2(\eta/2.5)(\mu/0.6)(V_{\text{circ}}/1.2 \times 10^3 \text{ km s}^{-1})^2 \times \\ (kT/3.7 \text{ keV})^{-1} \gtrsim 1$$

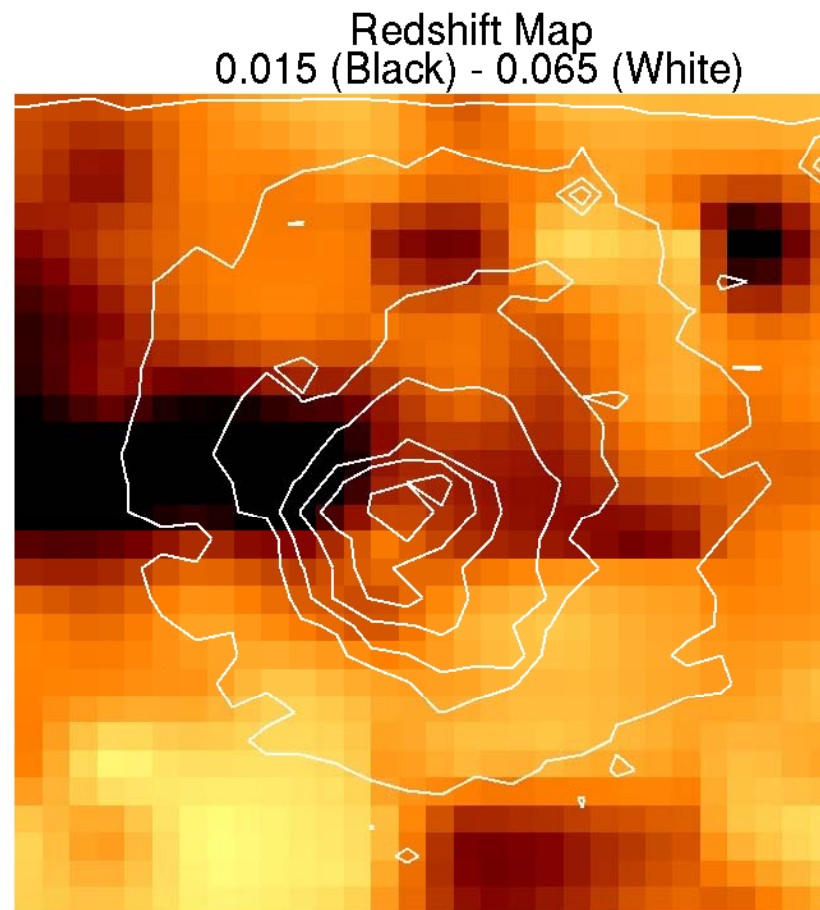
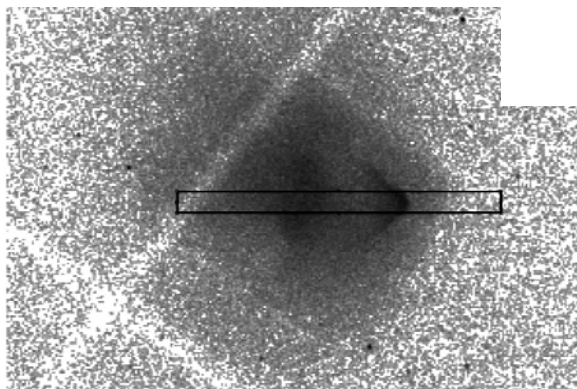
0.1-1% da energia do merger ainda está sob forma rotacional >0.5Gyr depois do evento!

Turbilhões?

First Chandra and XMM results – A576

XMM analysis show a difference of $>3.3 \times 10^3$ km/s at 90% confidence

Dupke, Mirabal &
Bregman 2006

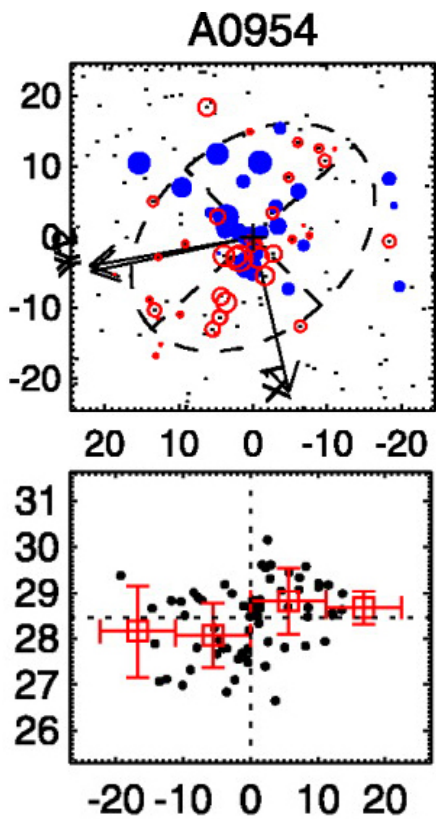


r8 Using two EPIC pointings and an archival Chandra pointings were able to confirm the velocity gradient in A576. It is seen individually in EPIC1 and 2 and ACIS-S3. The resulting velocity gradient is > 3300 km/s! This cluster present several other weird characteristics, Rines found a mass 2.5 times higher than the X-ray derived mass, using the infall velocity caustics. There is a secondary velocity peak seen in the optical 6000-8000 km/s, we also found a significant bimodal Si/Fe ratio distribution right at the center of the cluster. The only hypothesis that explains this is that this is a bullet cluster seen along the merger axis. The high temperature shock front region is overwhelmed by the emission measures of the cold cores and one cannot "see" the merger at all.

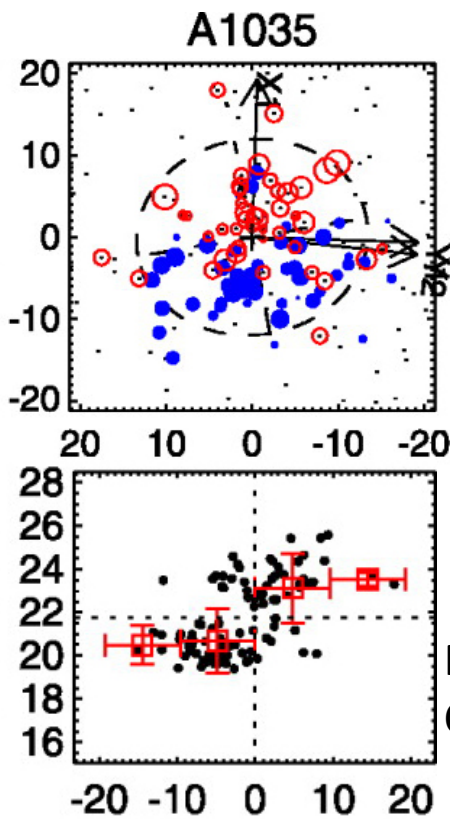
This work I just finished with a posdoc Nestor Mirabal. Here I am showing a velocity map obtained through an adaptive binning code that I have developed, using PERL as a controling language. This code is also used to obtain individual abundance, temperatures, and derived quantities, as I will show in a few minutes.

This opens a new window to explain the discrepancies found in "apparently" nice and relaxed clusters such as A1689 and I am with collaborators at MIT using some GTO to test this scenario in A1689.

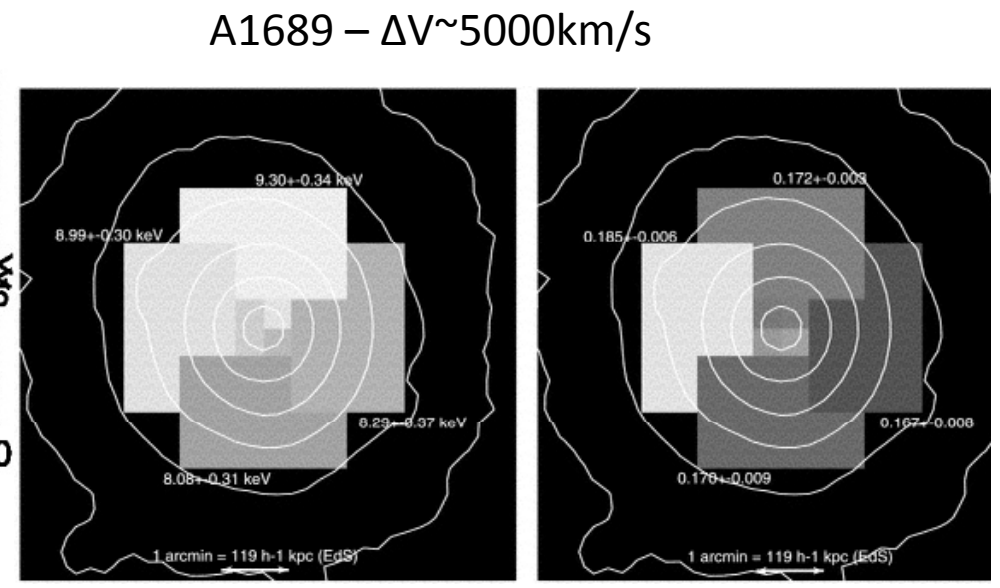
rdupke, 3/28/2006



$V_{\text{rot}} \sim 450 \text{ km/s}$



$V_{\text{rot}} \sim 1400 \text{ km/s}$



From Andersson & Madejski 2004
Confirmed by M. Bautz's group

From Hwang & Lee 2007

Cluster	ΔV	scale	Temp
Perseus	>1000 km/s	~Mpc	7 keV
Centaurus	>1400km/s?	<150 kpc	3-4 keV
Abell 576	>3300 km/s	<100 kpc	3-5 keV
RXJ0419	>1200 km/s	<100 kpc	1.5 keV
Abell 1689	>2400 km/s	<400 kpc	9 keV
1E0657	>4000 km/s	Perpend	>12 keV
Abell 520	>2500km/s	Perpend	>9 keV
Abell 3667	>1100km/s	Perpend	8 keV
CL0016+54	~3000km/s	0?	~4.5 keV
Abell 1035	~3400 km/s	<500kpc	~3.5 keV
Abell 954	~900 km/s	<500kpc	4-5 keV

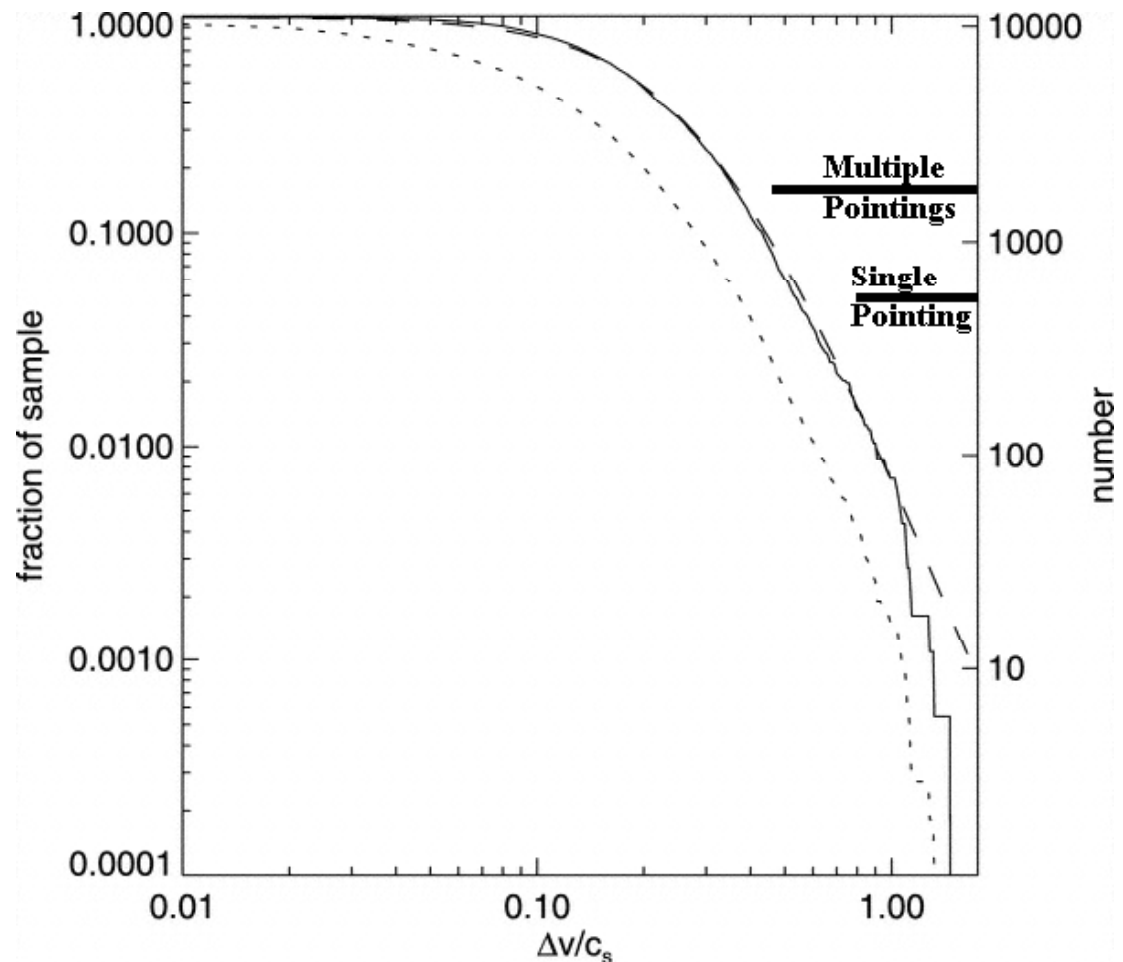
What Does Cosmology Predict?

VCE is a prototype theoretical counterpart to the HEASARC archive for X-ray emitting clusters.

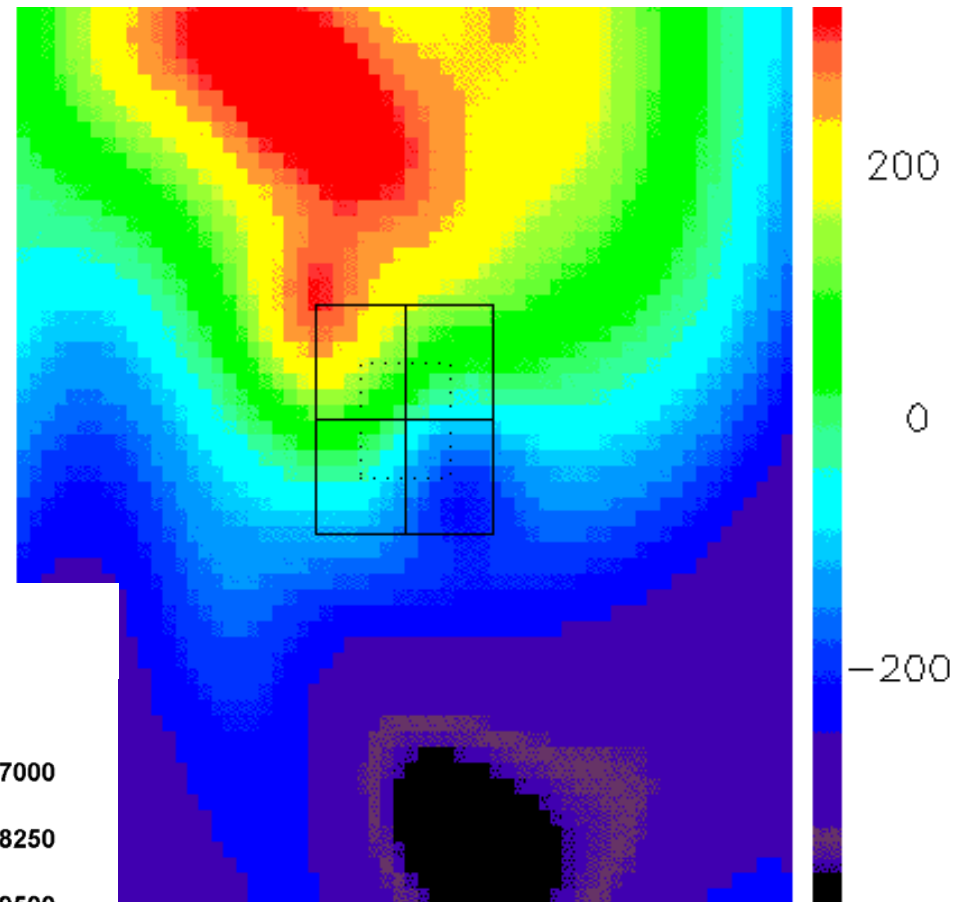
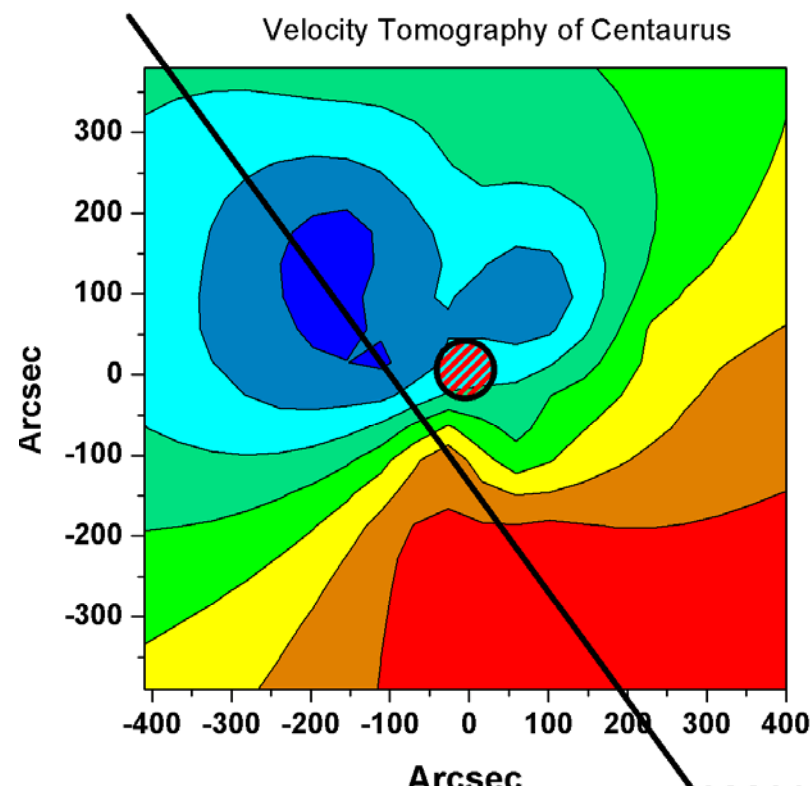
68 preheated simulated clusters.

With 14 outputs per run, this creates a set of 1000 instances of clusters covering $0 < z < 2$

Dashed \rightarrow Max ΔV ,
Dot \rightarrow All pointing pairs recovered from the perfect spectra after passing through Suzaku responses.
 $f(>\Delta V) \propto \Delta V^{-4}$

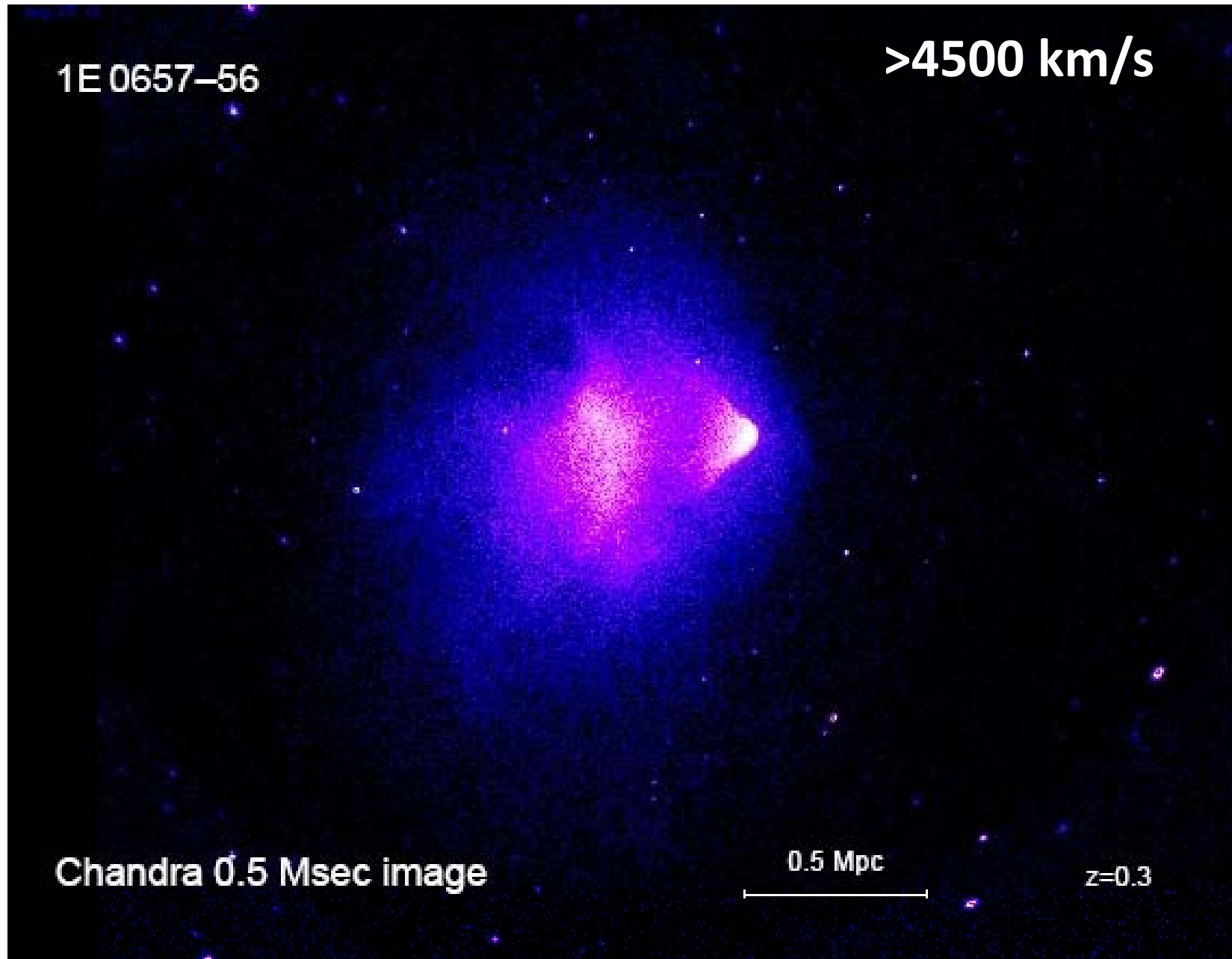


Cluster VCE 64→

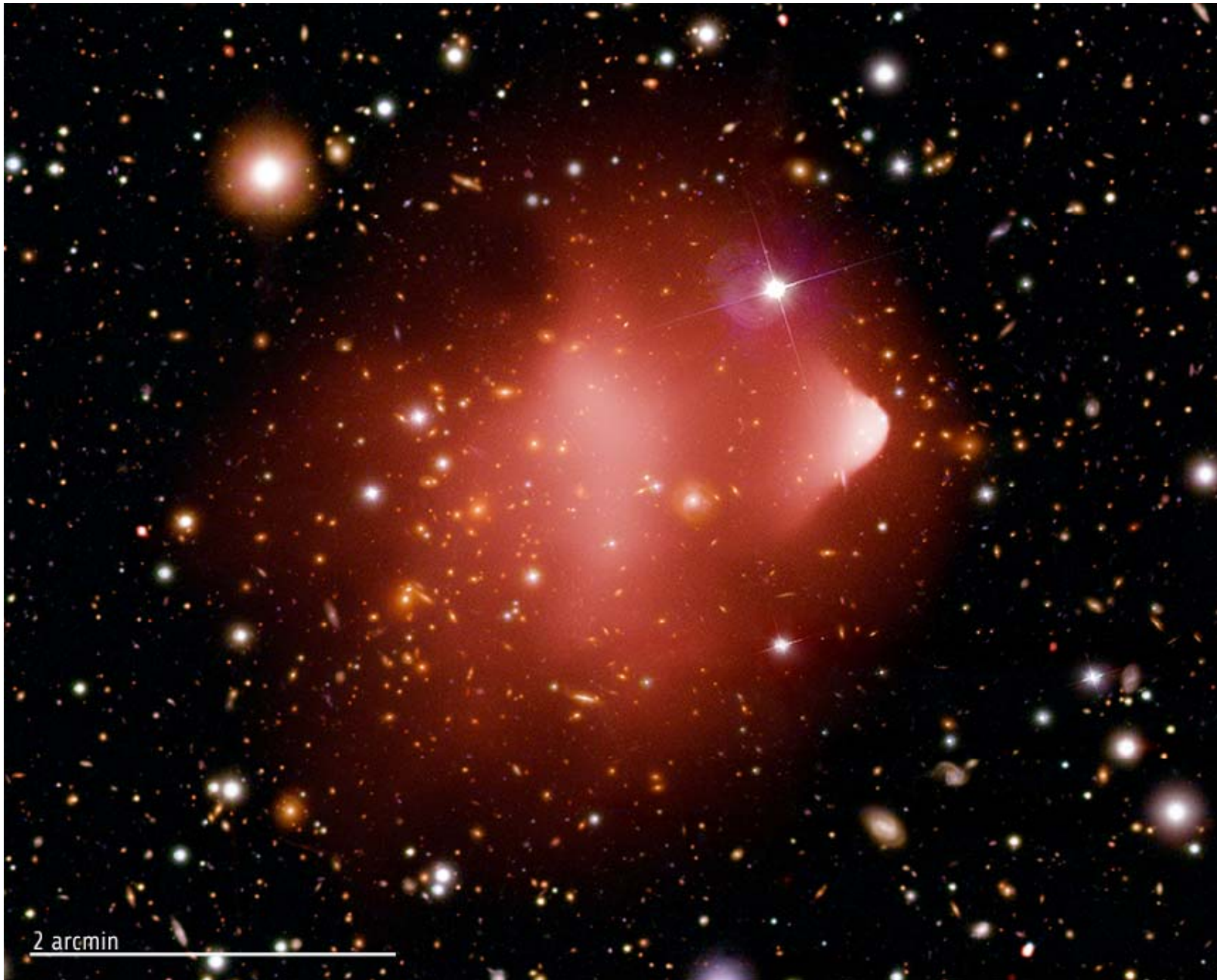


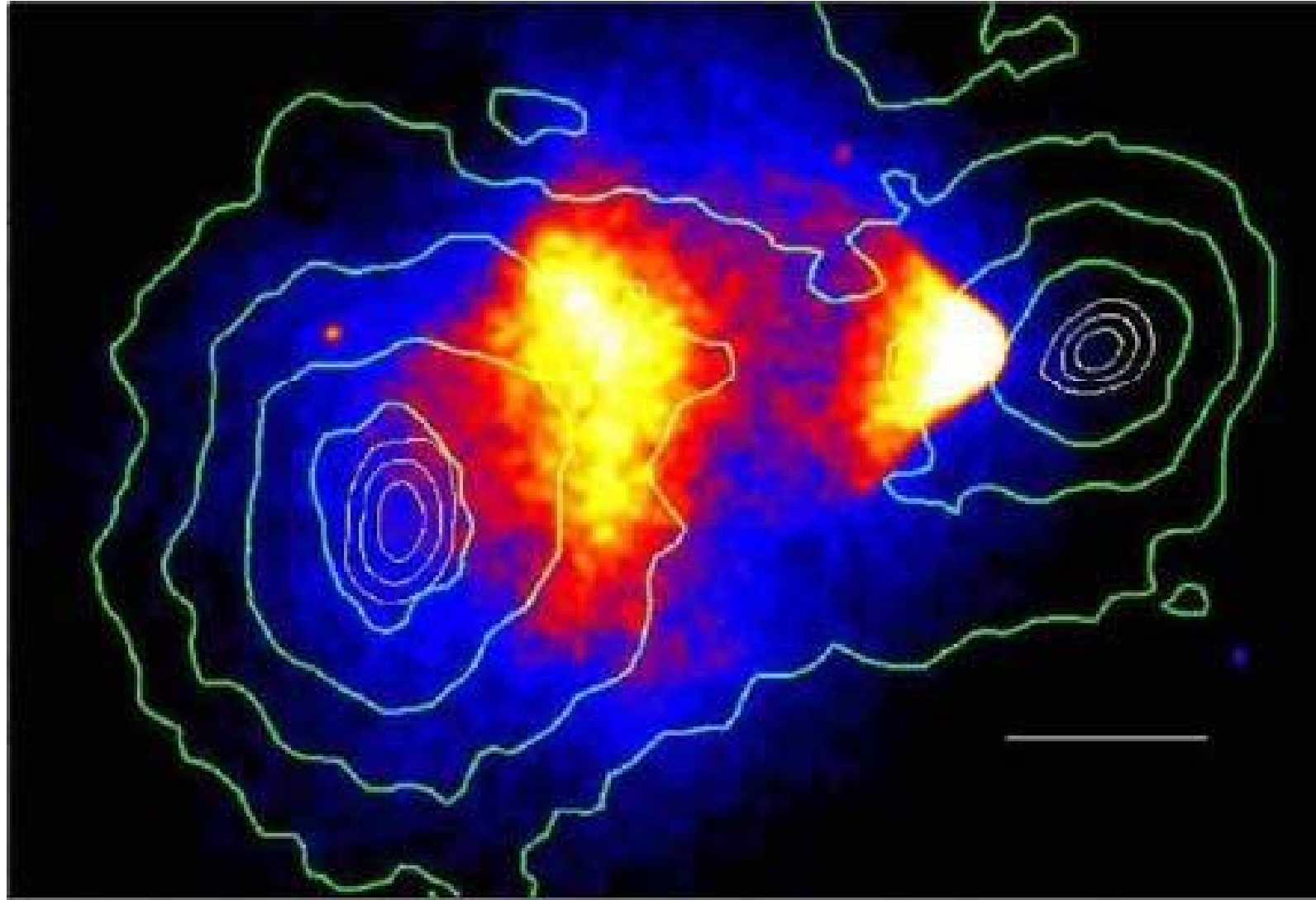
← Both pointings joined sectorial regions centered in the core.

The Bullet Cluster



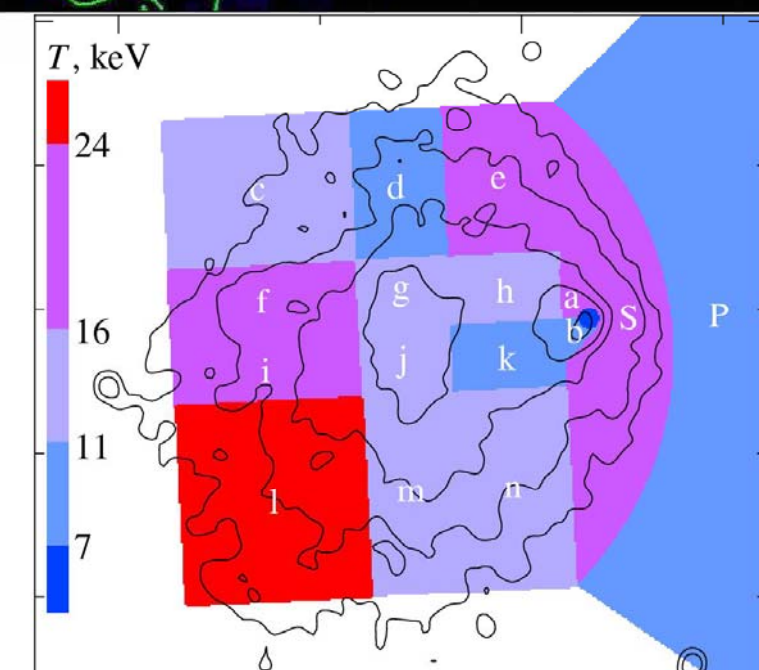
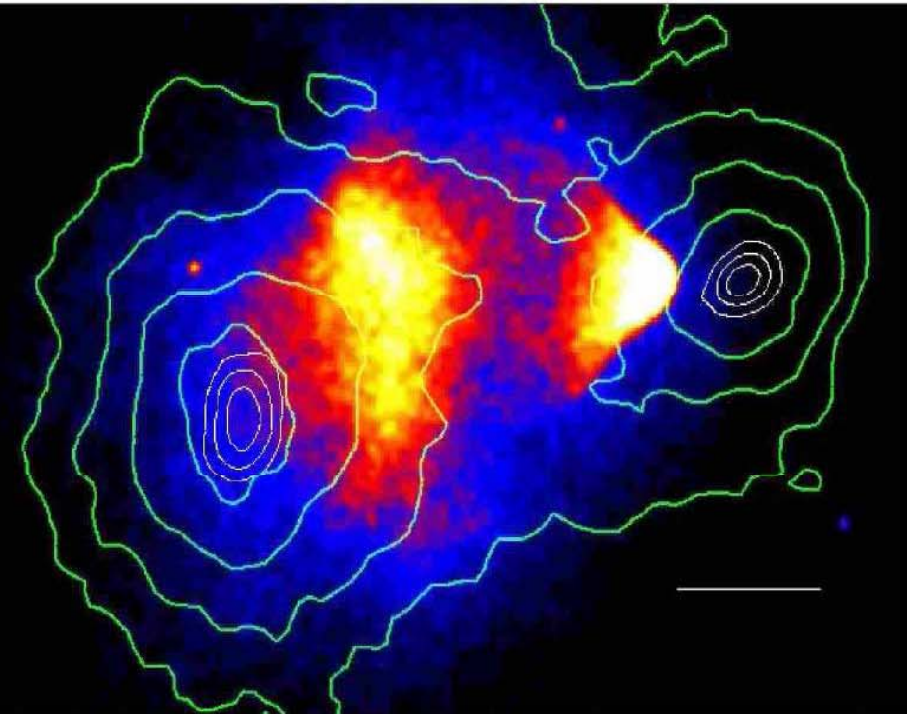
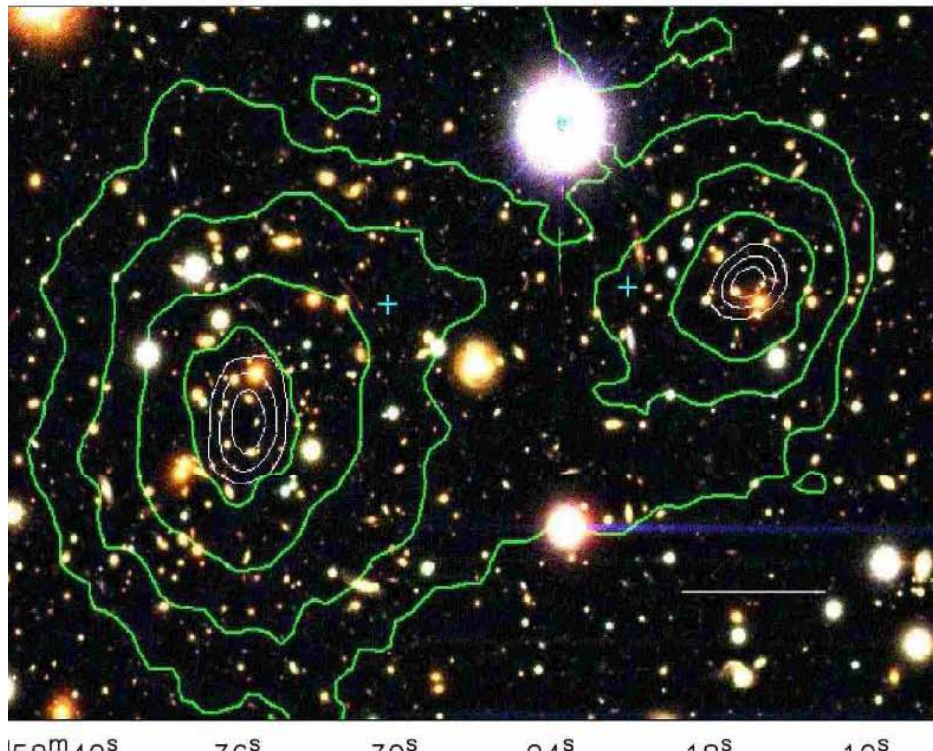
Otico



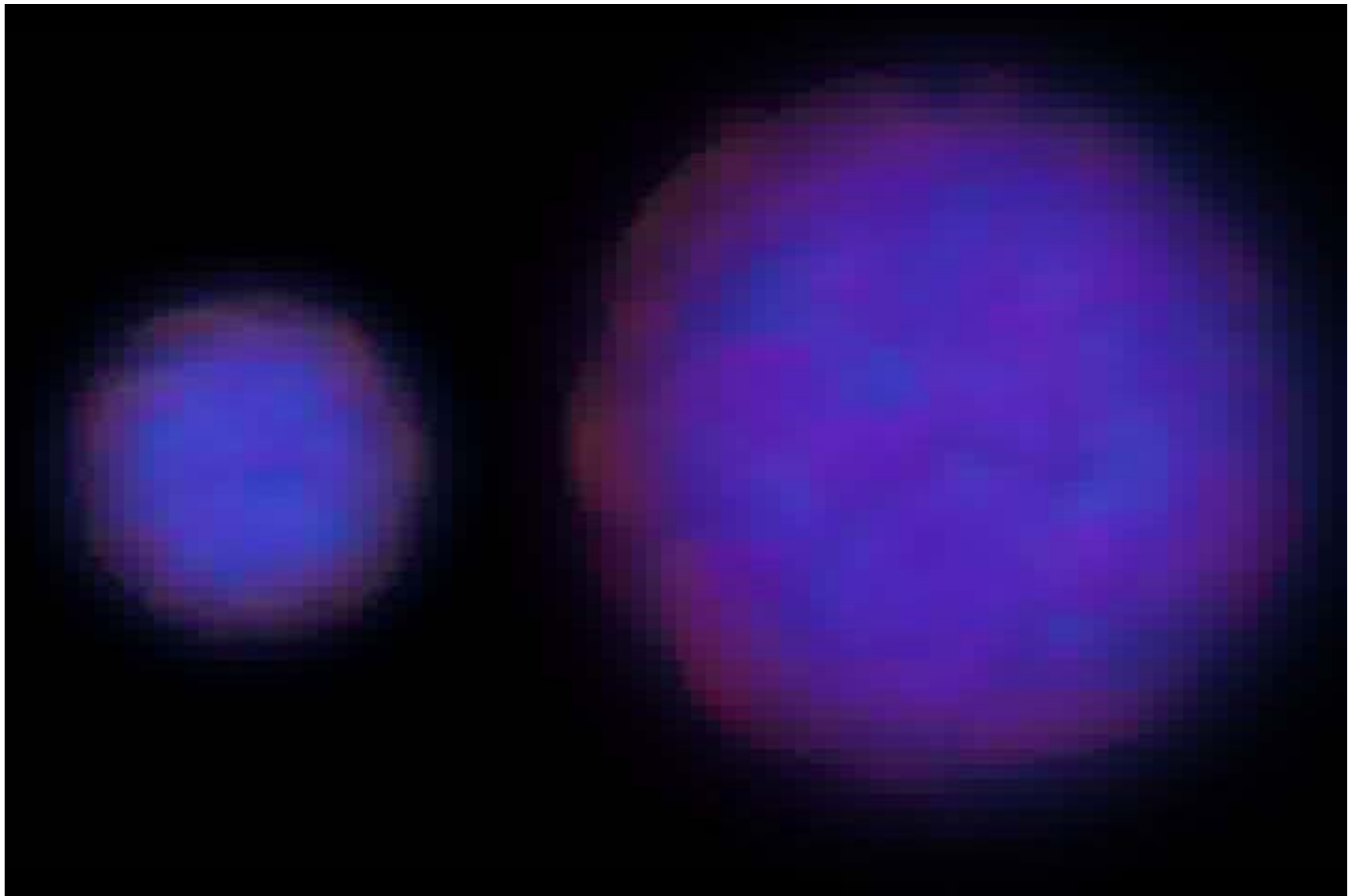


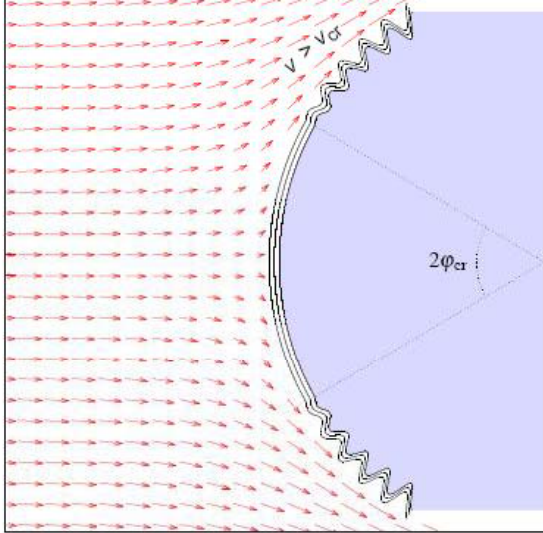
Markevitch et al. 2000, 2001 ,Clowe et al. 2006

Bullet Cluster



Animacao do Bullet cluster





$$\overline{B} > 7-16 \mu G$$

Fig. 29. A schematic illustration of the suppression of Kelvin-Helmholtz instability at the surface of the A3667 cold front. The magnetic layer (shown by parallel curves along the front) can provide surface tension that suppresses the growth of perturbations in the region where the tangential velocity is smaller than some critical value V_{cr} . The velocity field (red arrows) corresponds to the flow of incompressible fluid around a sphere. (Reproduced from Vikhlinin et al. 2001a.)

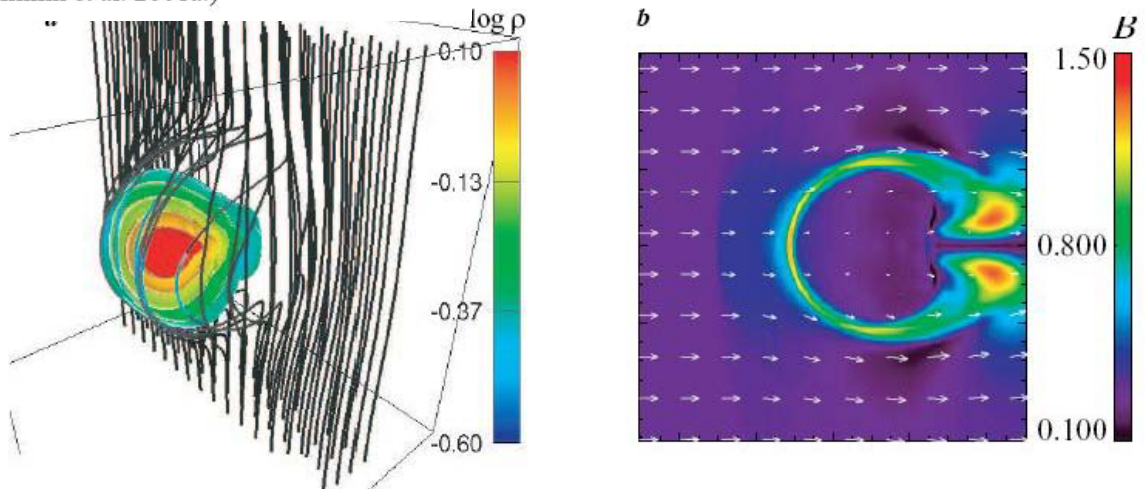


Fig. 30. Simulation of the magnetic field draping around a cold front in the course of a gas cloud's motion through an ICM with a uniform magnetic field. (a) The subcluster gas density (color) and the magnetic field lines. (b) A horizontal cross-section through the subcluster: color shows magnetic field strength, arrows show gas velocities. Compression and shear of the field in the incoming flow creates a narrow layer around the front, in which the magnetic field is strongly amplified. (Reproduced from Asai et al. 2005.)

Groups of Galaxies

Redshift surveys of the nearby universe indicate that most galaxies occur in small groups

Typical group contains only a few luminous galaxies

To first order, groups can be viewed as scaled-down versions of rich clusters.

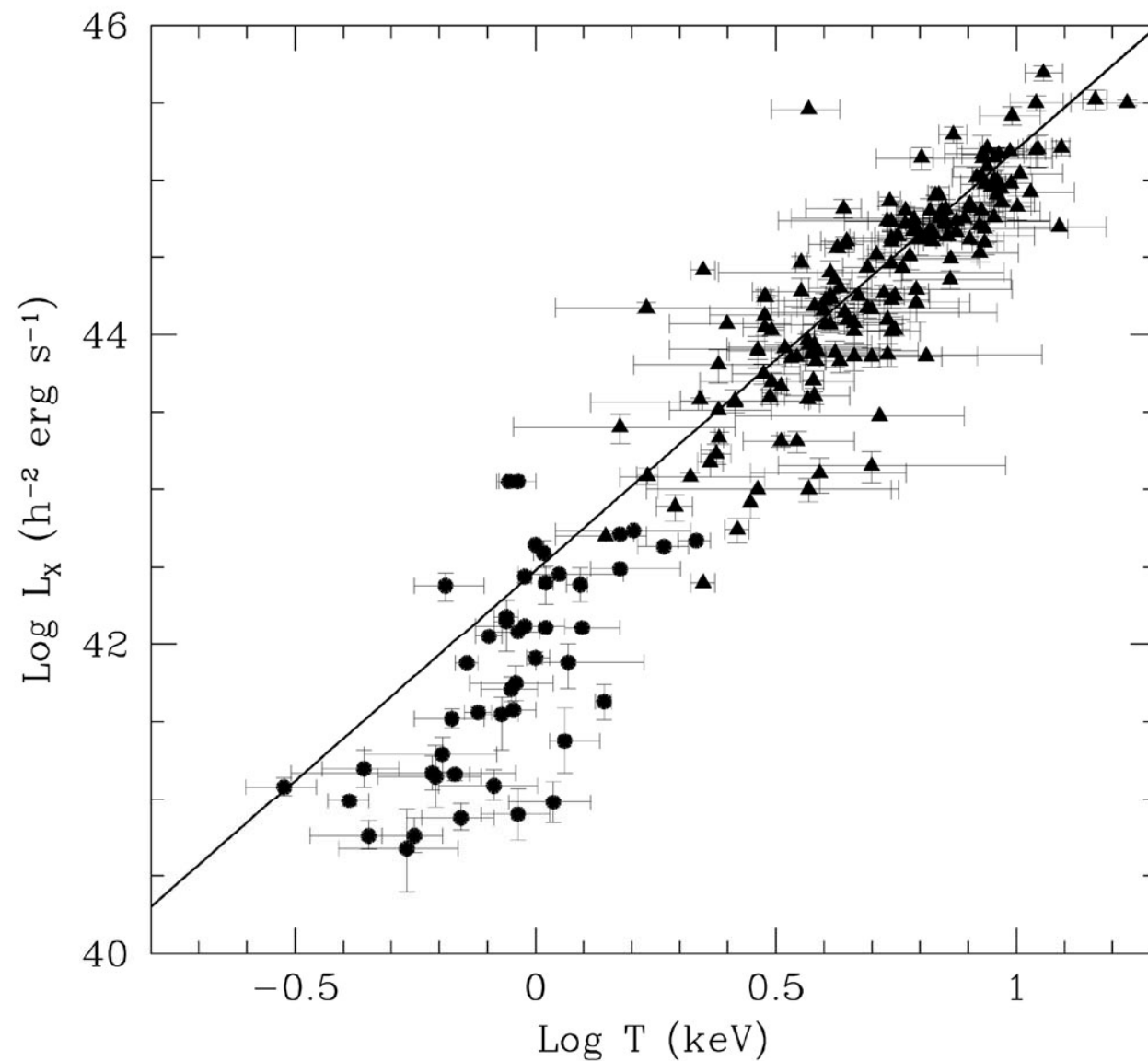
Many of the fundamental properties of groups, such as L_x and T_x , are roughly what one expects for a "cluster" with a velocity dispersion of several hundred km/s.

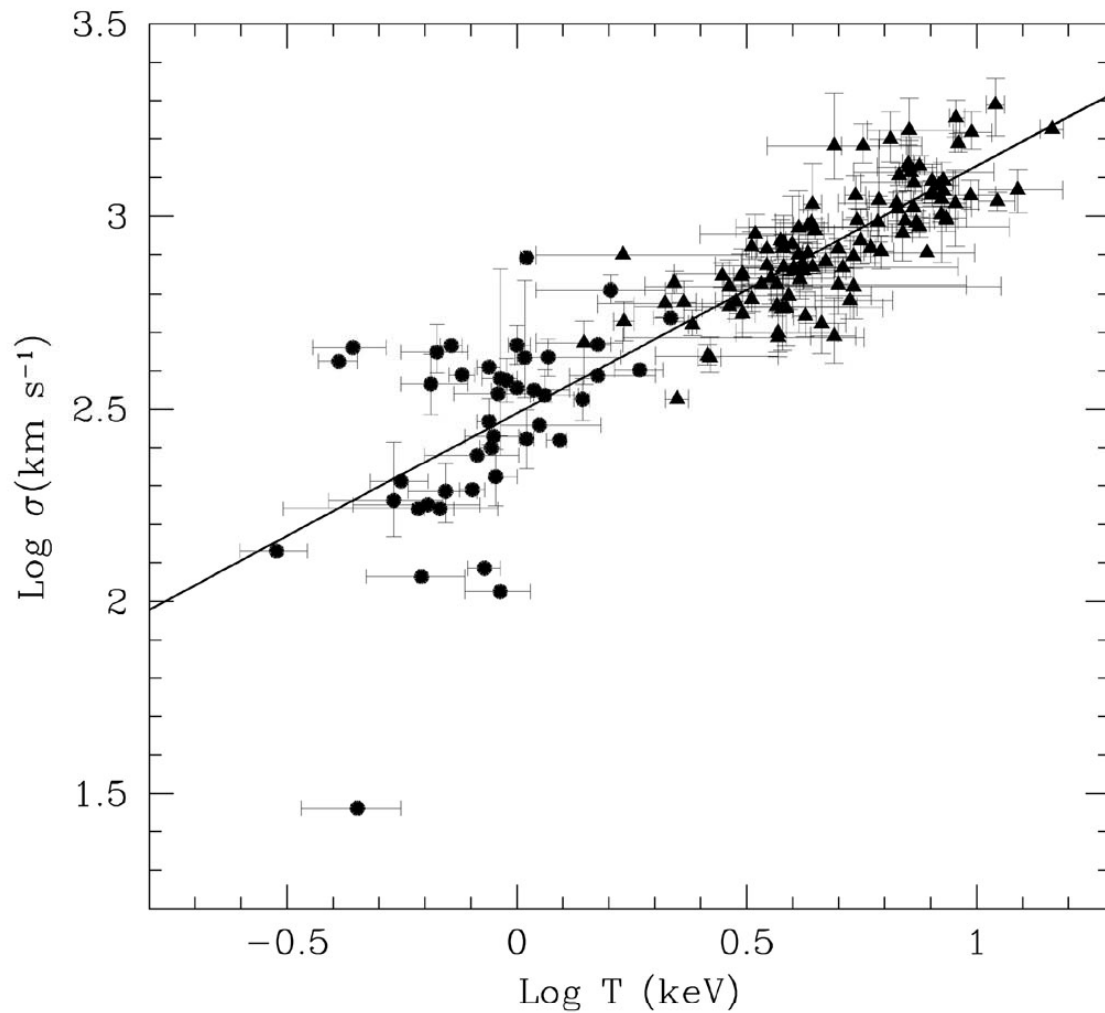
However, some important physical differences exist between groups and clusters. The velocity dispersions of groups are comparable to the velocity dispersions of individual galaxies. Therefore, some processes such as galaxy-galaxy merging are much more prevalent in groups than in clusters.

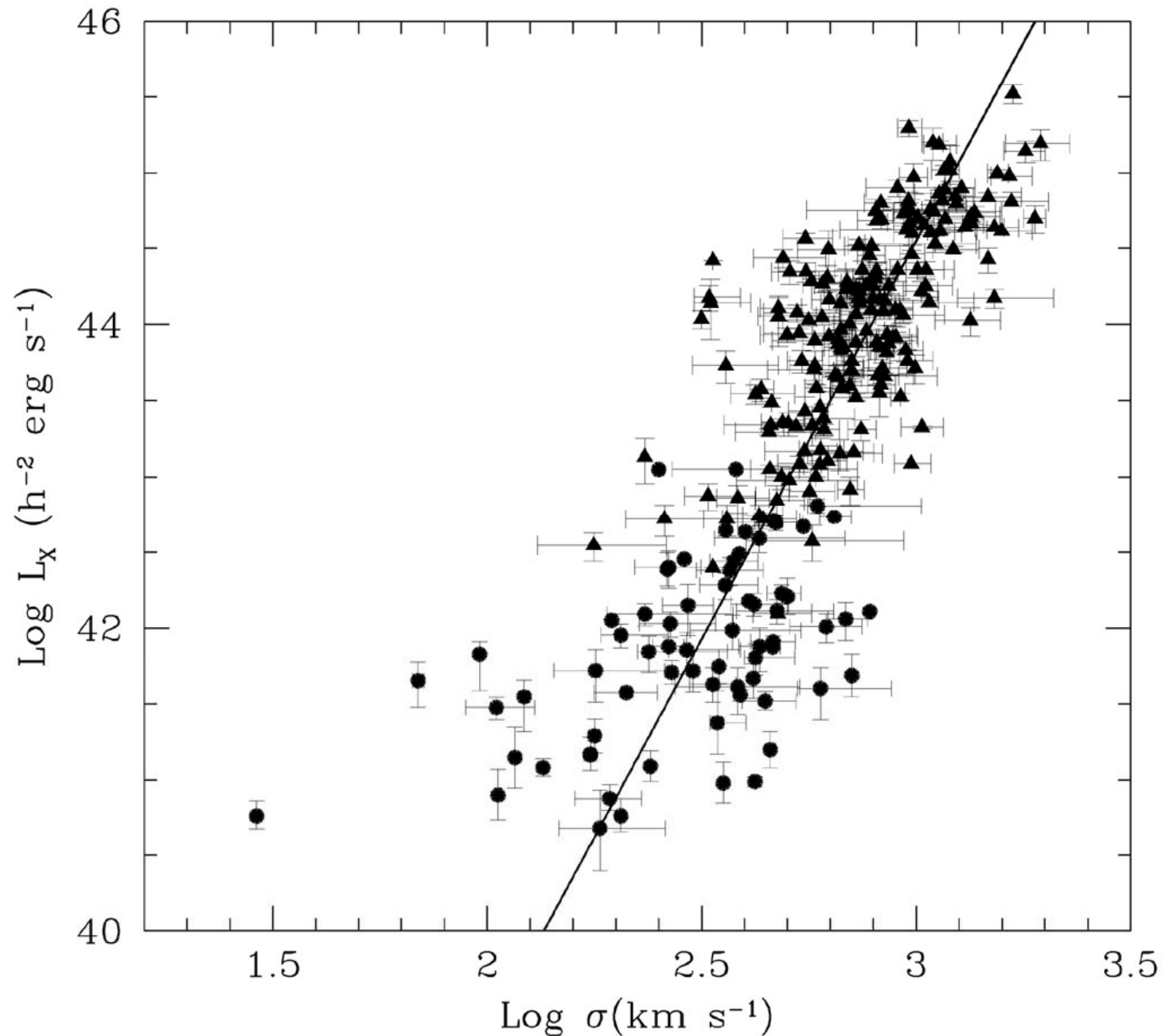
$$L_x \propto T^2$$

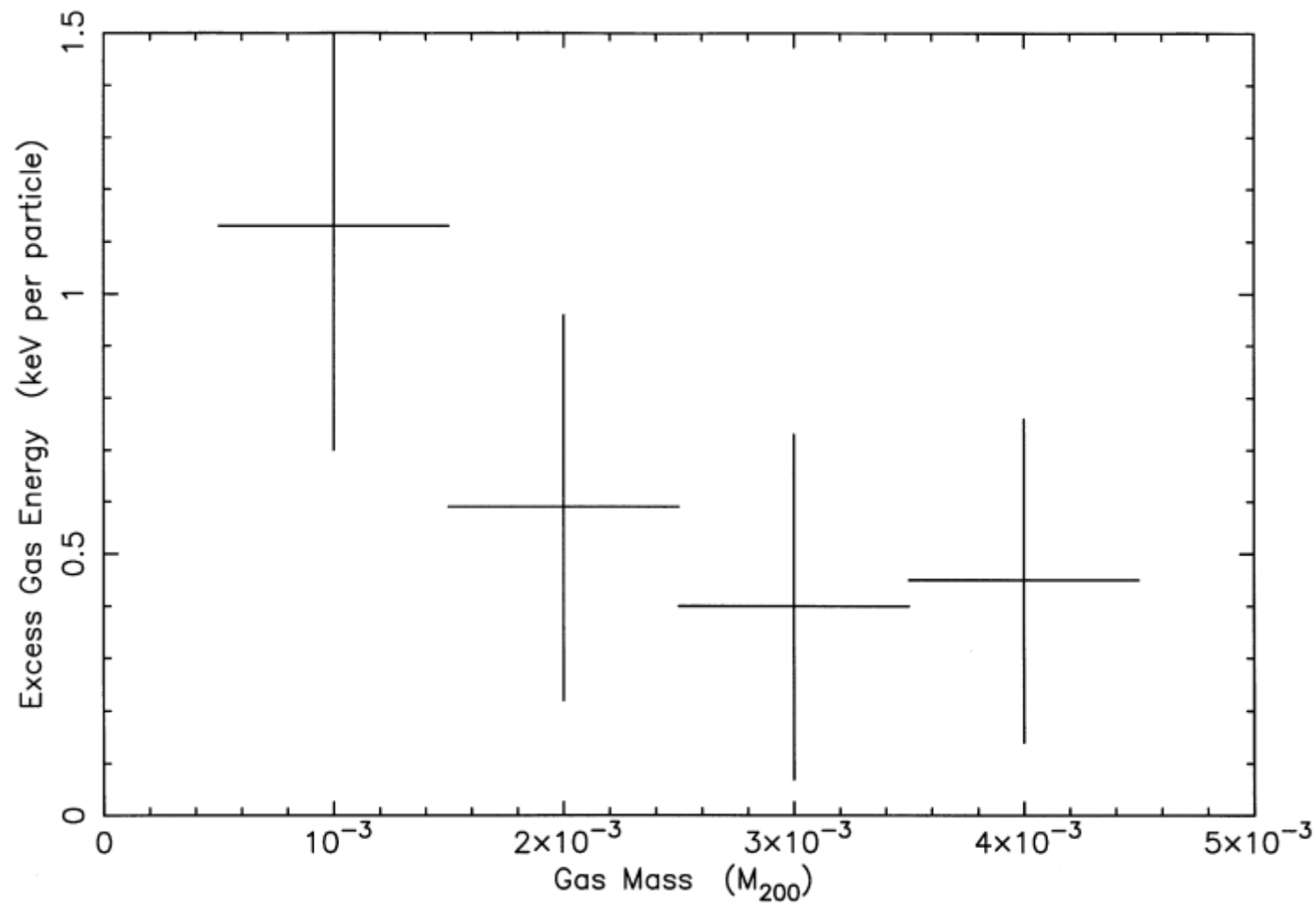
Hierarchical clustering model for the formation of structure in the Universe predicts that dark matter haloes should be scaled versions of each other (Navarro, Frenk & White 1995).

While some energy transfer between dark matter and gas is possible through gravitational interaction and shock heating, simulations suggest that the gas and dark matter haloes will be almost self-similar in the absence of additional heating or cooling processes (Eke, Navarro, Frenk 98)





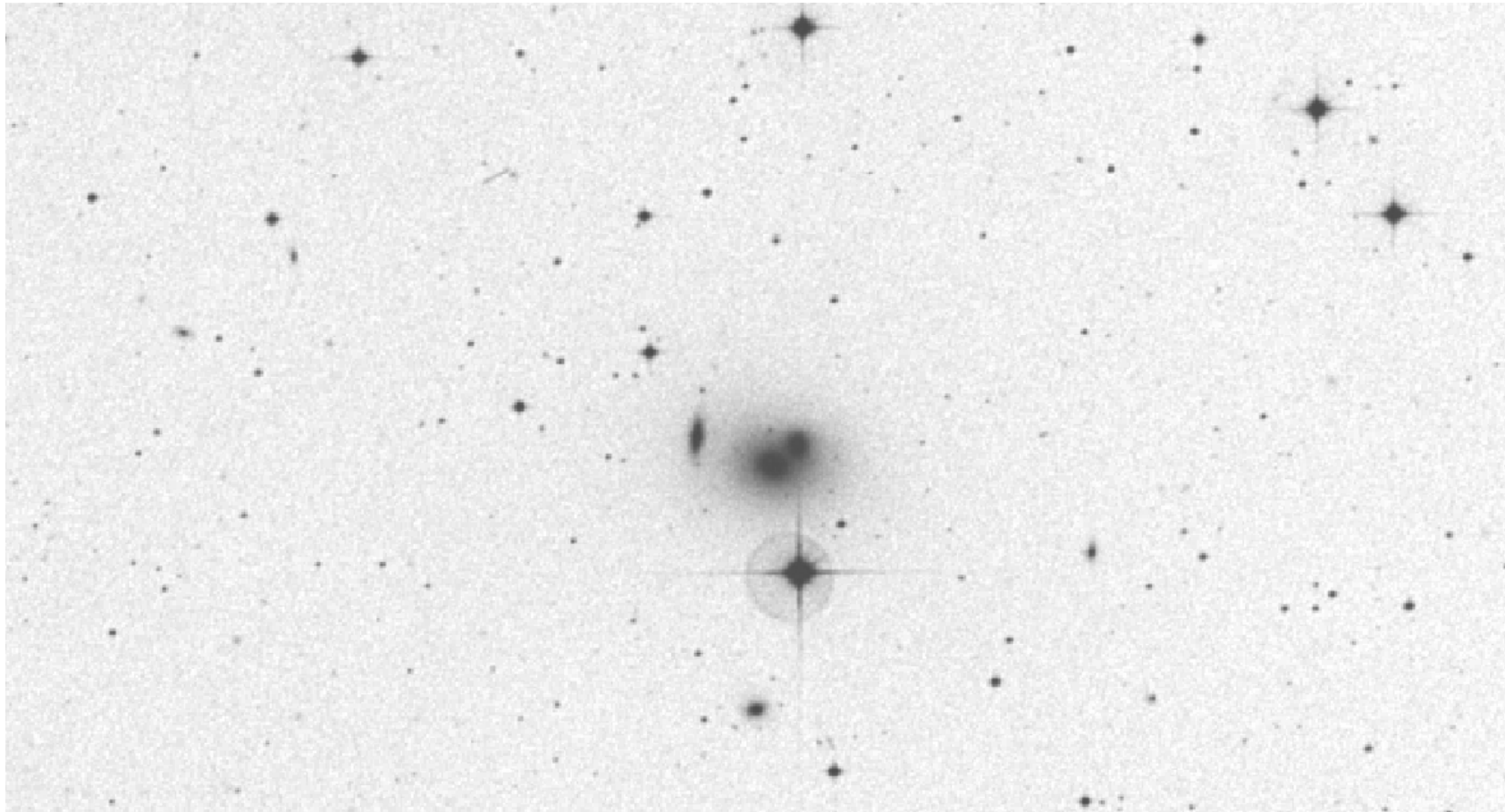


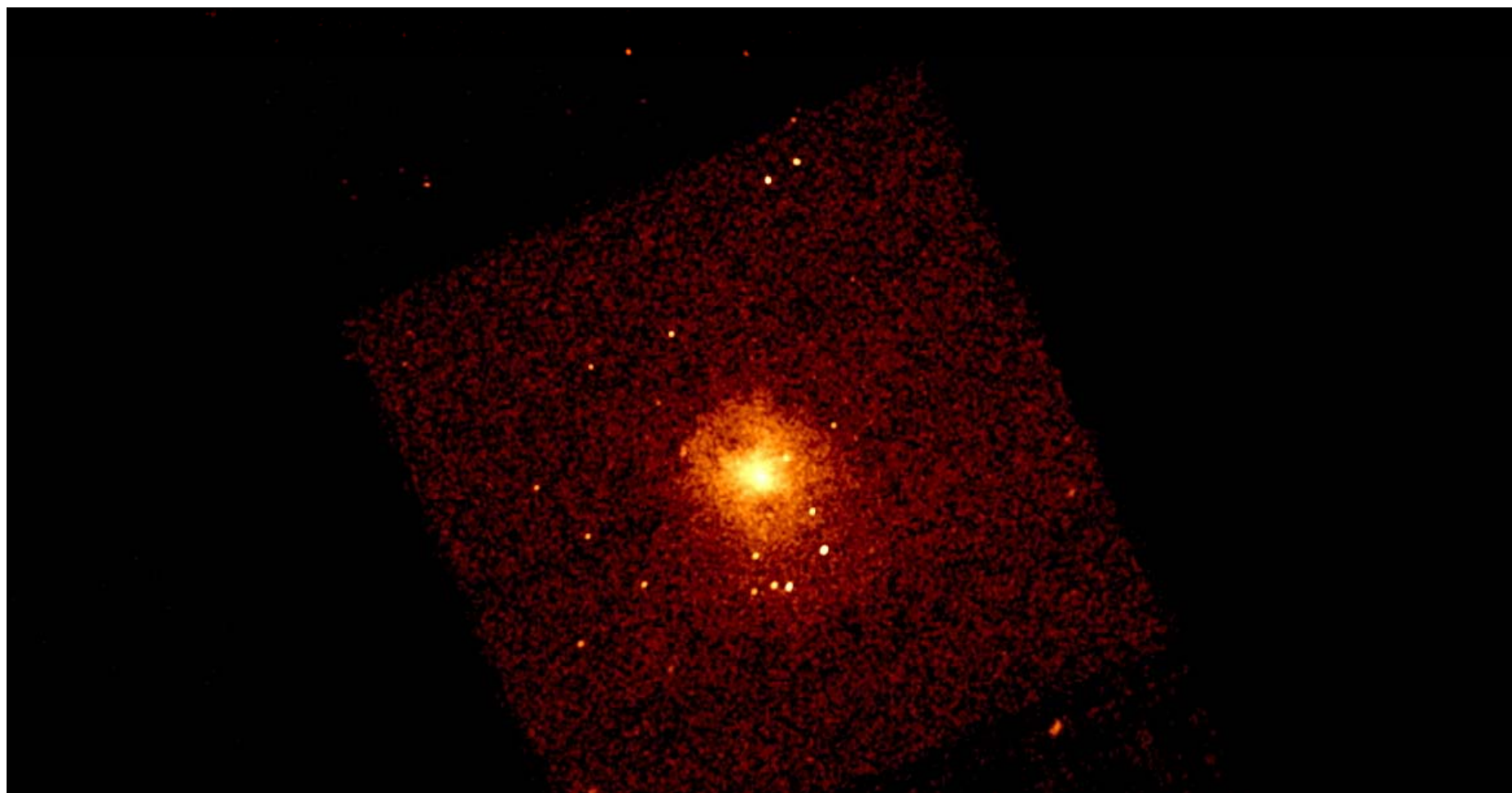


Lloyd-Davies et al. 2000

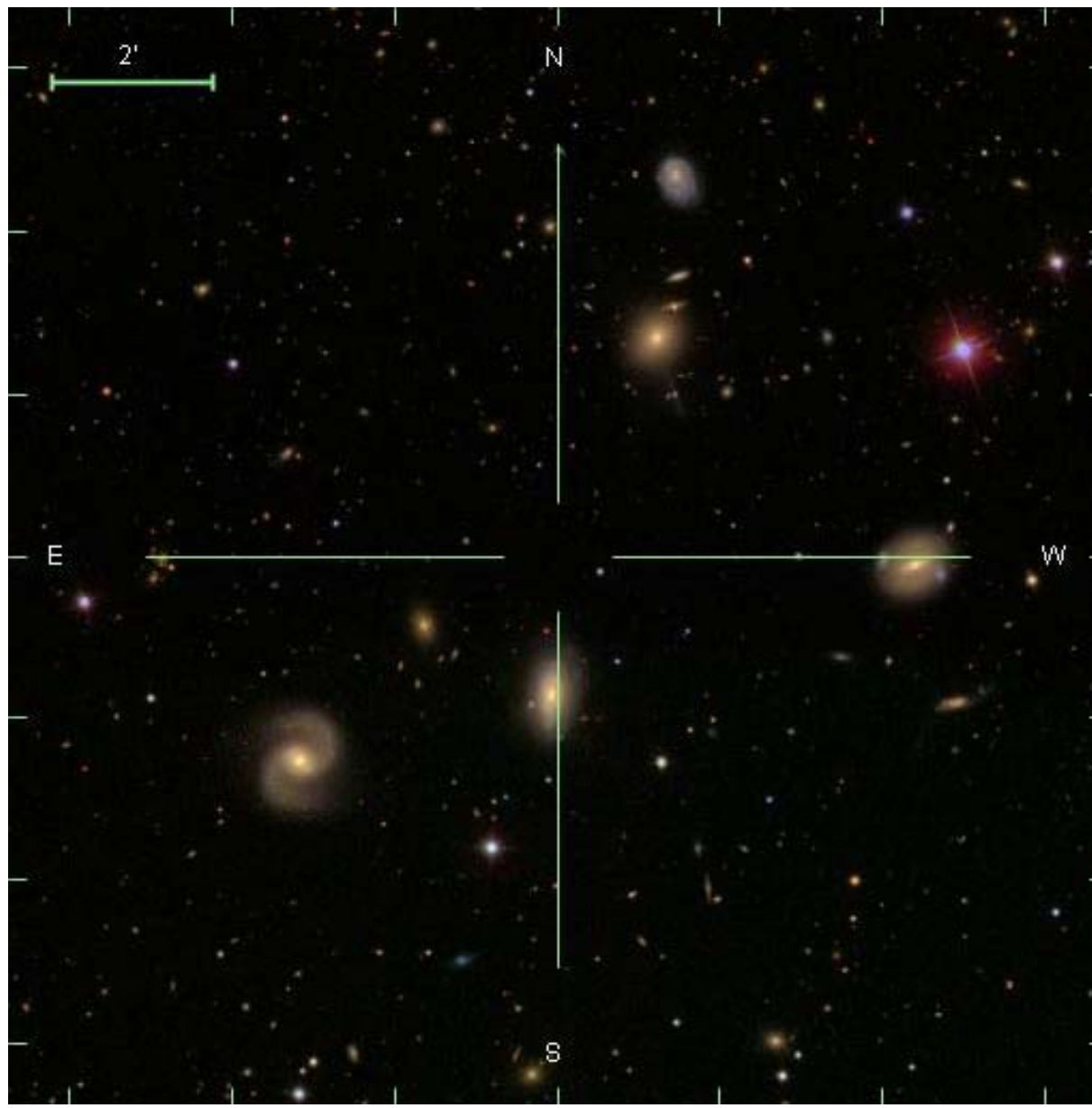
In contrast to hot clusters, galaxy groups are systems where baryon physics (e.g., cooling, galactic winds, and AGN feedback) begins to dominate over gravity. Groups are not just a scaled-down version of massive cluster.

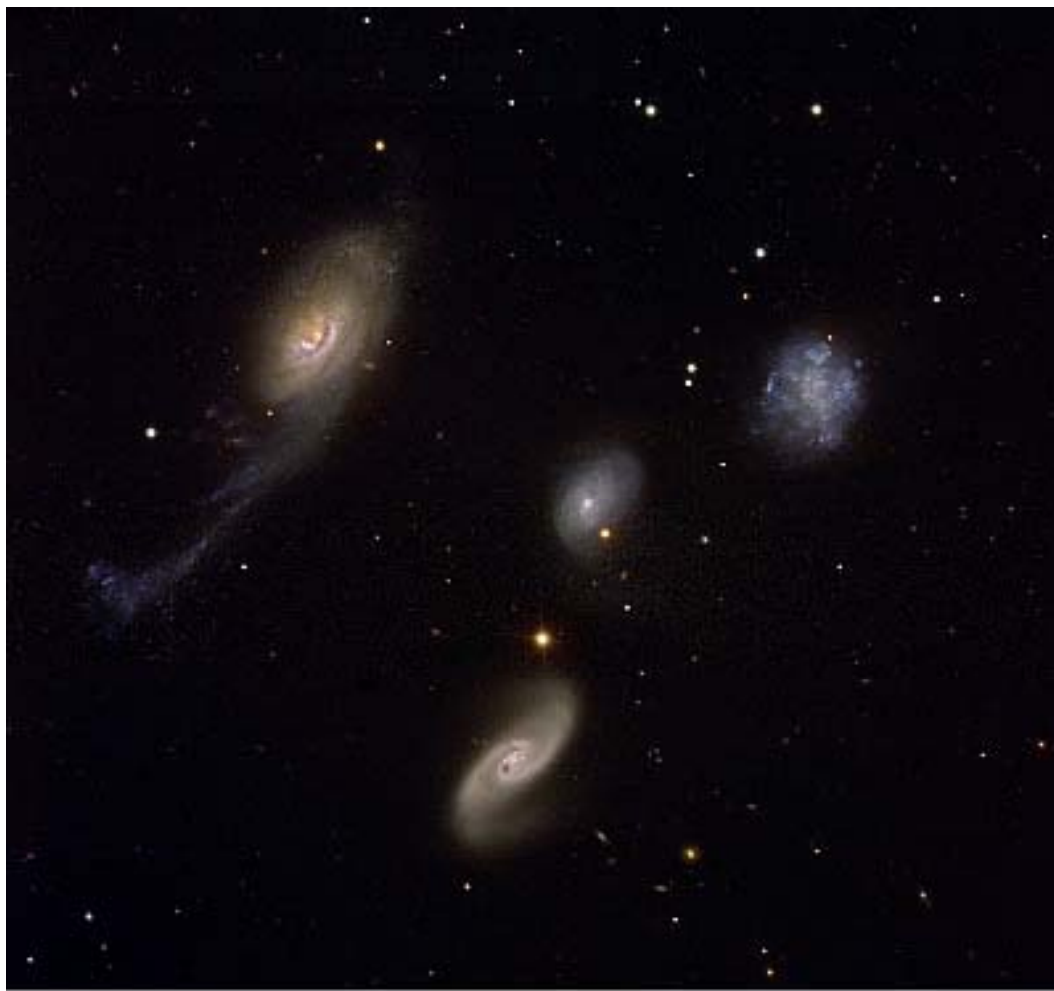
HCG 62 ($z \sim 0.0137$)





MKW10 group



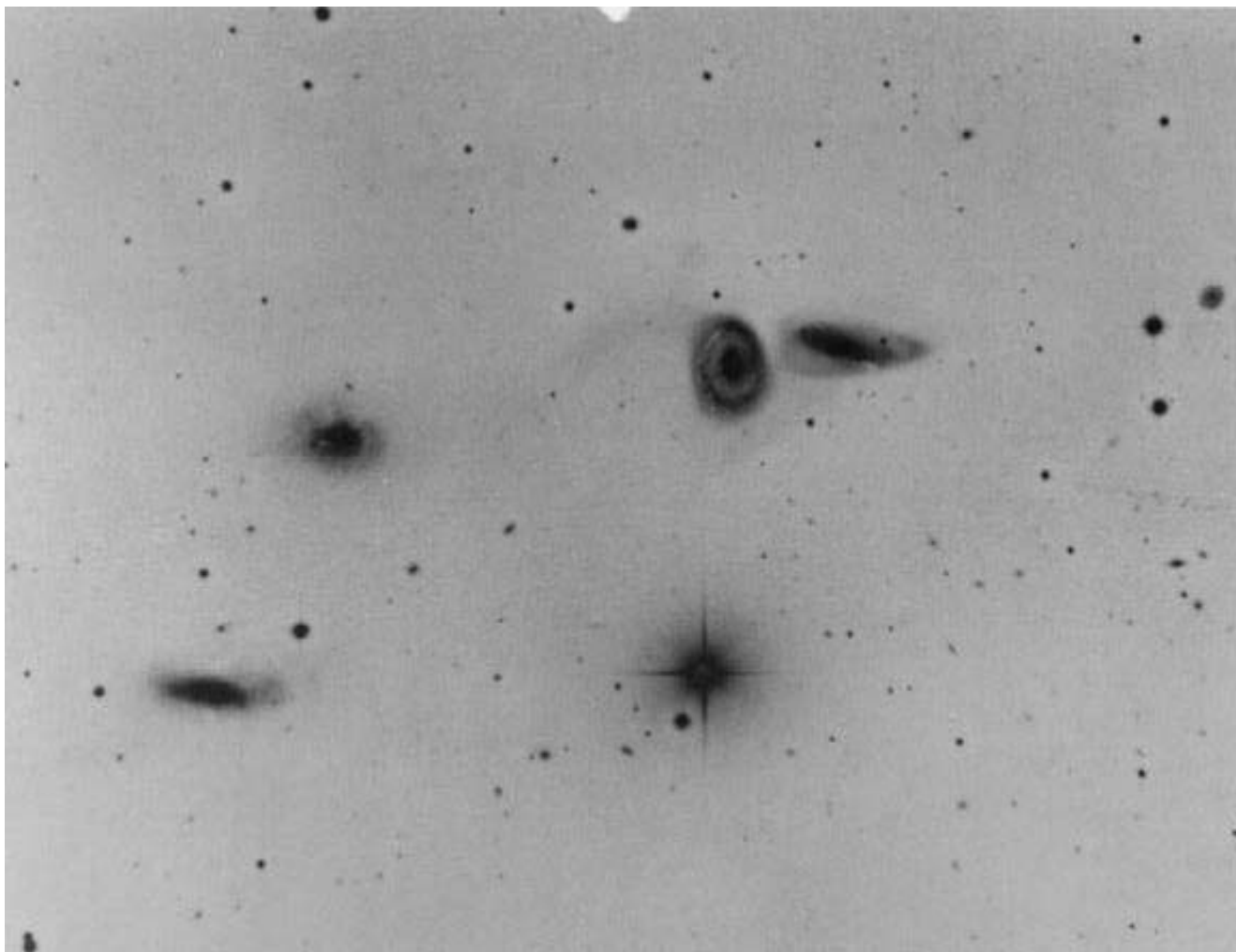


Robert's Quartet
(FORS2/VLT)

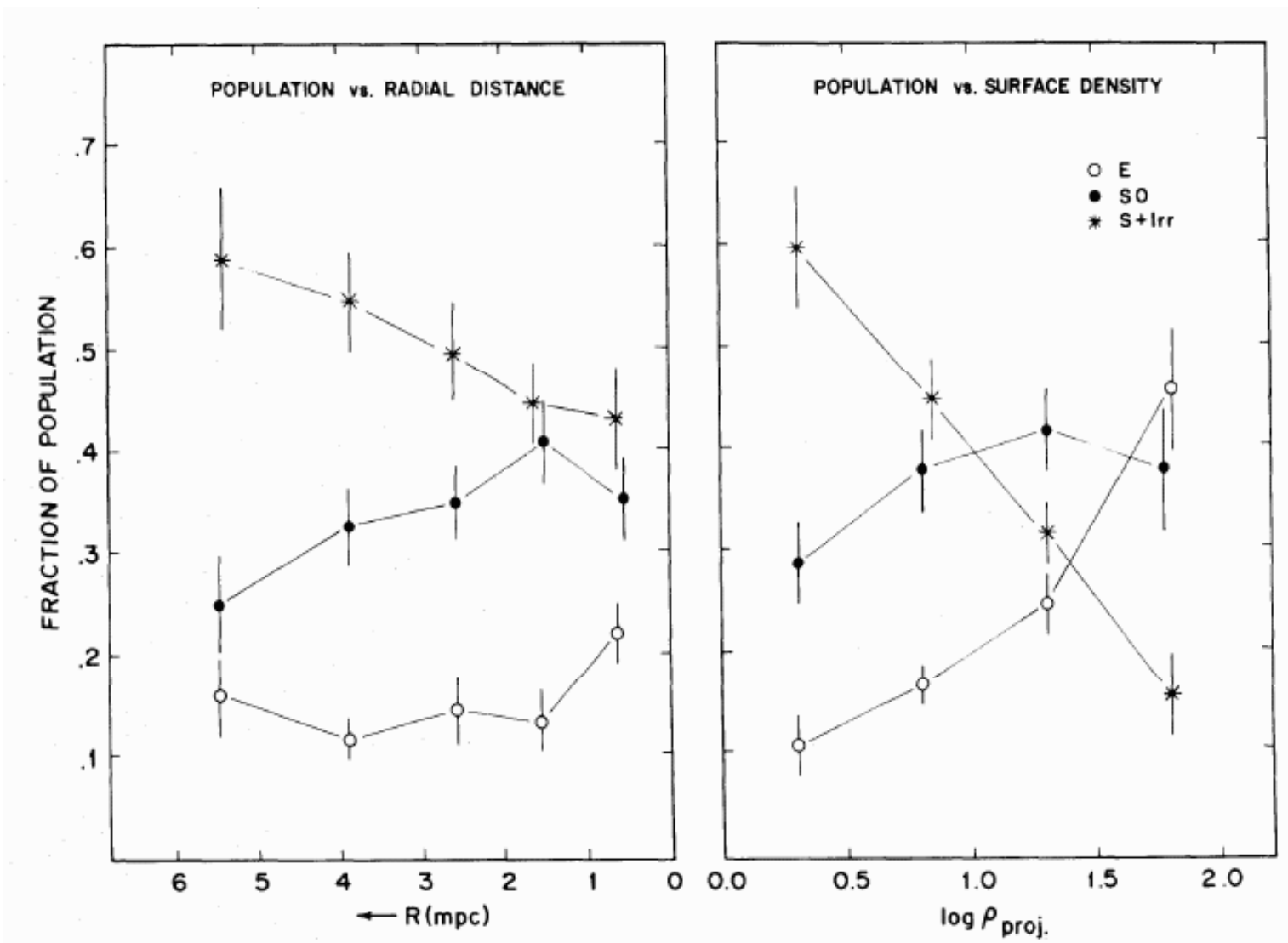
ESO PR Photo 34/05 (November 4, 2005)



HCG 16

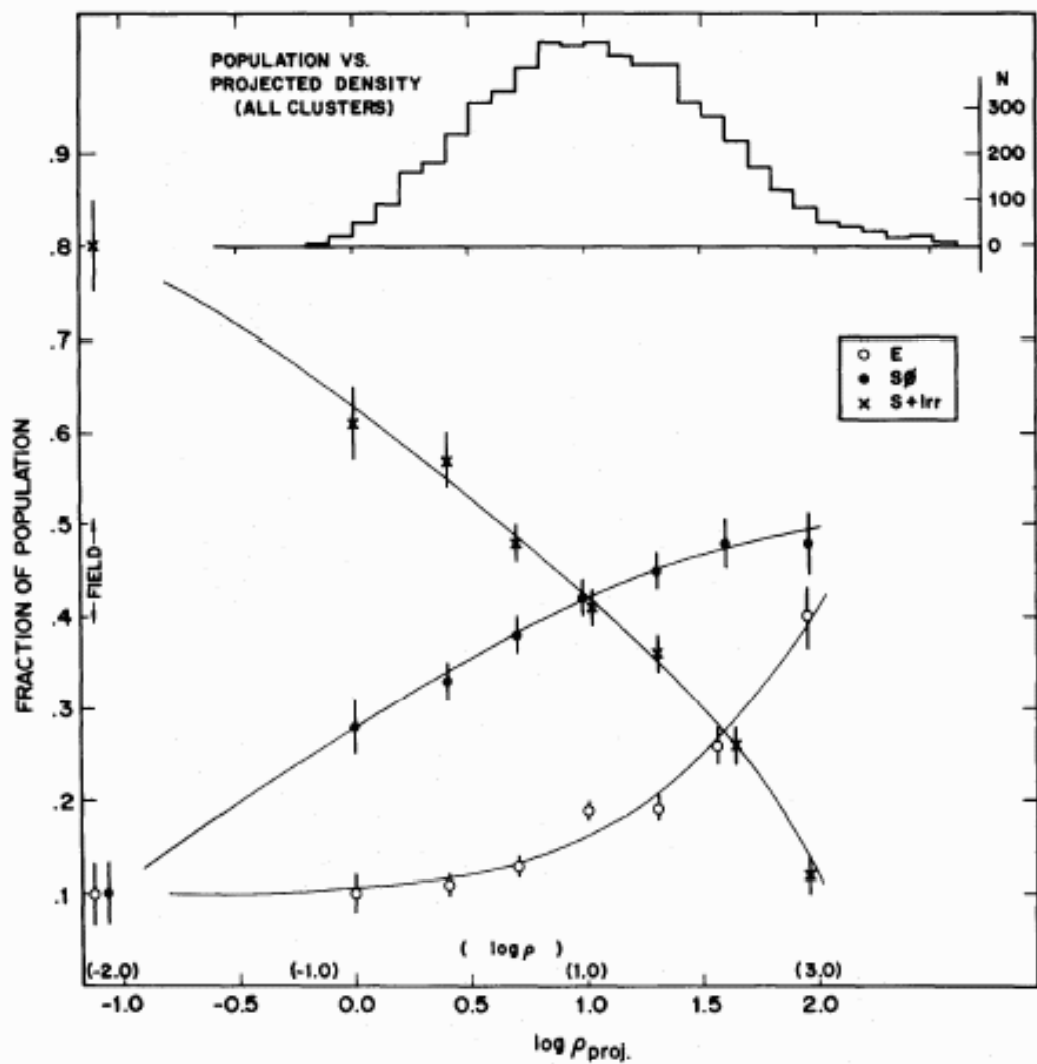


Ok with the density morphology relation



Dressler 1980

For Irregular clusters



Dressler 1980

FIG. 4.—The fraction of E, S0, and S+I galaxies as a function of the log of the projected density, in galaxies Mpc^{-2} . The data shown are for all cluster galaxies in the sample and for the field. Also shown is an estimated scale of true space density in galaxies Mpc^{-3} . The upper histogram shows the number distribution of the galaxies over the bins of projected density.

Compact Groups

Compact groups of galaxies (CG) are usually characterized by a very high projected galaxy density (4 or more galaxies in a typical projected separation of $100h^{-1}\text{kpc}$, low velocity dispersions (on the order of the stellar velocity dispersion within a galaxy).

These characteristics indicate a short collapse time for the system. If the galaxies in a compact group are gravitationally bound they should represent a transient phase between loose associations and giant elliptical galaxies, which would appear as consequence of galaxy merging

a) Selection Criteria

A compact group is defined here by the following criteria:

$$N \geq 4 \quad (\text{population}), \quad (1)$$

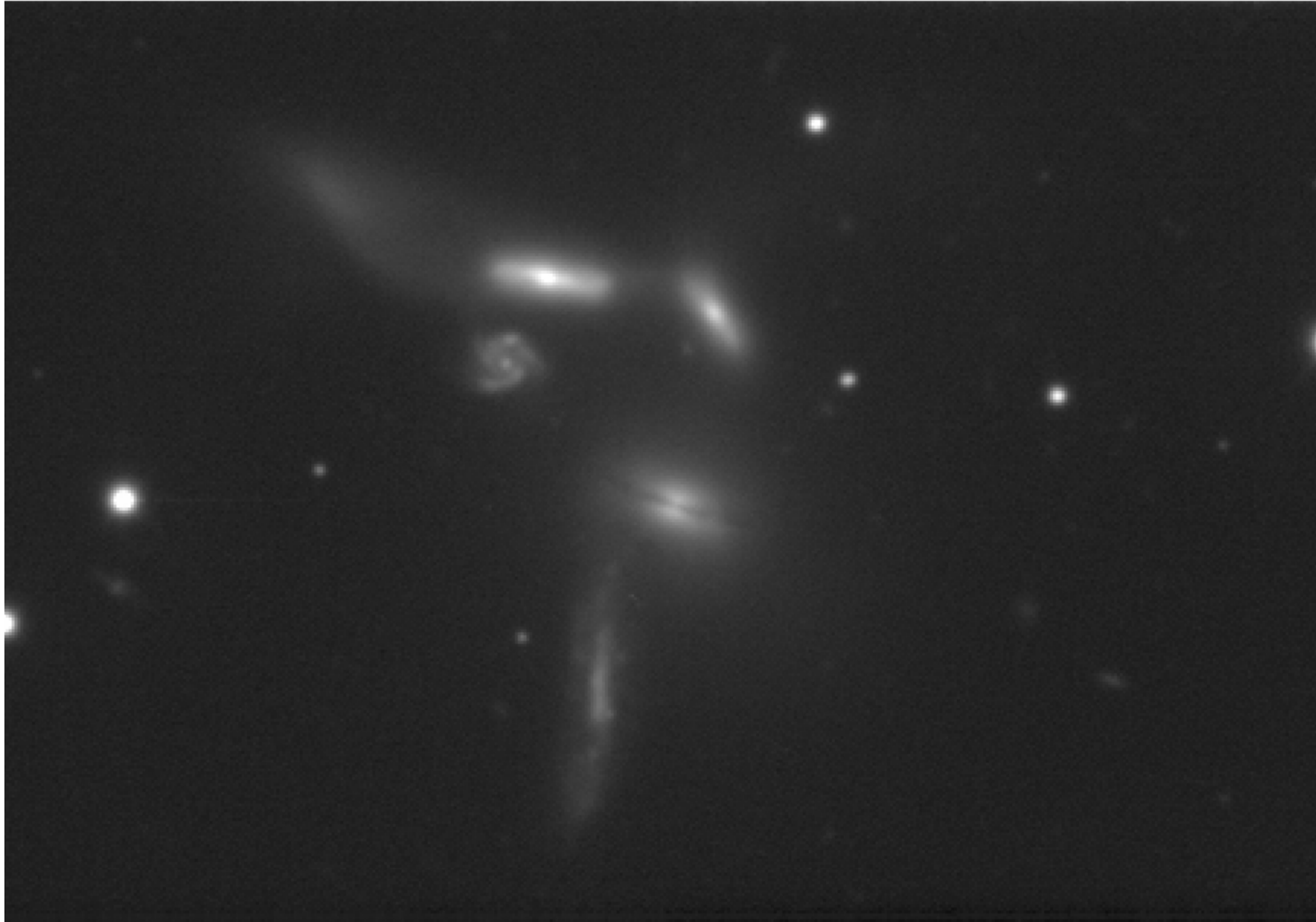
Hickson 1982

$$\theta_N \geq 3\theta_G \quad (\text{isolation}), \quad (2)$$

$$\bar{\mu}_G < 26.0 \quad (\text{compactness}), \quad (3)$$

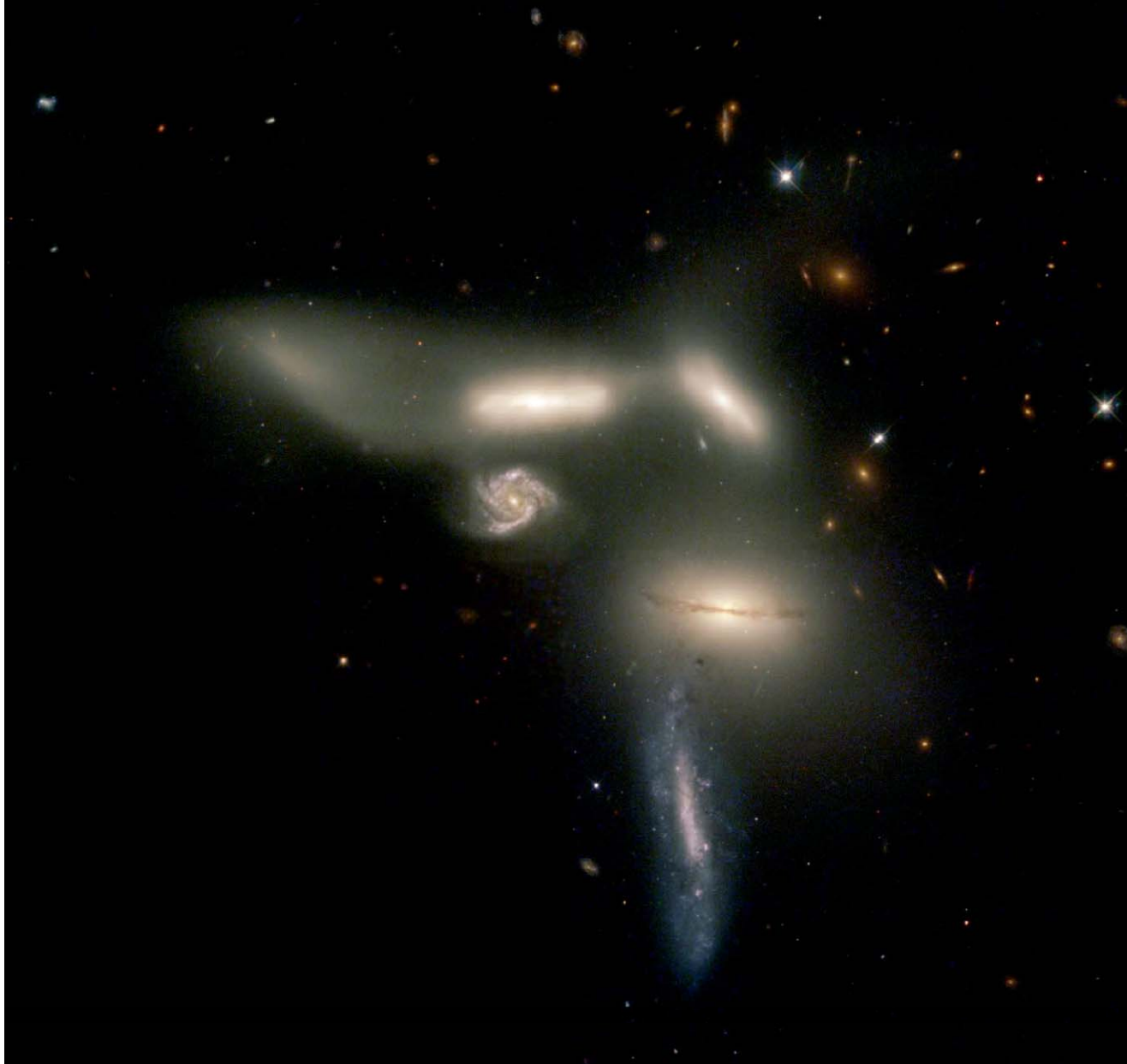
where N is the total number of galaxies within 3 mag of the brightest, $\bar{\mu}_G$ is the total magnitude of these galaxies per arcsec^2 averaged over the smallest circle (angular diameter θ_G) that contains their geometric centers, and θ_N is the angular diameter of the largest concentric circle that contains no other (external) galaxies within this magnitude range or brighter.

Seyfert Sextet



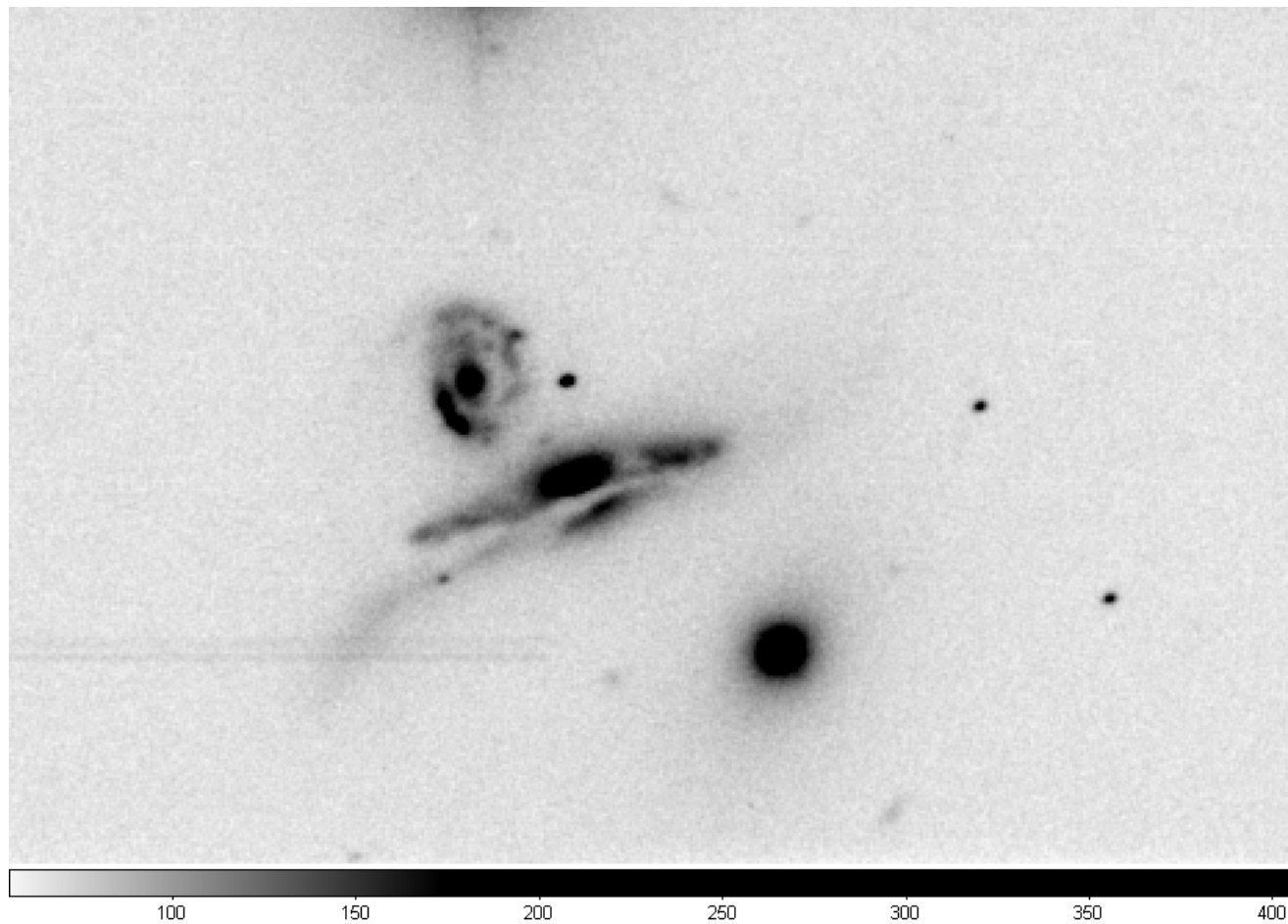
Five of the members show very similar redshifts, from 4000 to 4500 km/s, while the fifth is measured at nearly 20000 km/s

Seyfert Sextet



Five of the members show very similar redshifts, from 4000 to 4500 km/s, while the fifth is measured at nearly 20000 km/s

HCG 44



Fossil Groups

- Dominated by a cD
- **2 mag** difference between the 1st & 2nd rank galaxies (in R-band) within 0.5 r_{200} .
- **Extended X-ray** emission ($L_{X,\text{bol}} > 10^{42} h_{50}^{-2}$ erg/s).
- Discovered more than a decade ago (Ponman et al. 1994)

Fossil Groups



- Originally thought to be the **cannibalistic remains** of galaxy groups that lost energy through dynamical friction (e.g. Mulchaey & Zabludoff 1999).
- Expected large times involved in dynamical friction and the observed lack of X-ray substructures imply that FGs formed early and were undisturbed for a very long time (Ponman et al. 1994; Jones et al. 2000; Vikhlinin et al. 1999).

Fossil Groups – Are they groups? Are they fossil?

Khosroshahi
et al. 2007

Group Name	N_{spec}	σ km s $^{-1}$	$< T >$ keV	L_X^a $10^{42} ergs/s$	M_{vir}^{dyn} $10^{12} M_\odot$	
Khosroshahi et al. 2007	RX J1256.0+2556	8	773 ± 214	2.63 ± 1.13	50	710
	RX J1331.5+1108	6	236 ± 79	0.81 ± 0.04	2.1	24
	RX J1340.5+4017	4	419 ± 187	1.16 ± 0.08	5.2	130
	RX J1416.4+2315	18	694 ± 120	4.0 ± 0.62	170	656
	RX J1552.2+2013	13	721 ± 150	2.85 ± 0.9	60	640
	NGC 6482	5	115 ± 38	0.66 ± 0.11	1.1	6
	ESO 3060170	15	648 ± 160	2.6 ± 0.3	66	469

Mendes de Oliveira et al. 2006-2009 confirm high σ_s with many more galaxies

RXJ 1416 25 gals 584km/s if group included >800km/s (Cypriano et al. 2006)

RXJ 1552 36 gals 623km/s if Elgal included ~800km/s (Mendes de Oliveira et al. 2006)

RXJ 1340 22 gals 565km/s if Elgal included ~800km/s (et al. 2009)

- T_X of the FG's IGM is more **similar to** that of **clusters**, sometimes in excess of 4 keV (e.g. RX J1416.4+2315; Khosroshahi et al. 2006).
- σ in FGs **consistent with** T_X measured, at least for the few FGs with relatively good X-ray data (Mendes de Oliveira 2006; Cypriano et al. 2006; Mendes de Oliveira et al. 2006, 2009).
- **Not atypical** location in the L_X-T_X relation (e.g. Khosroshahi et al. 2007 – Fig1).
→deeper gravitational potential wells,
more typical of poor clusters.

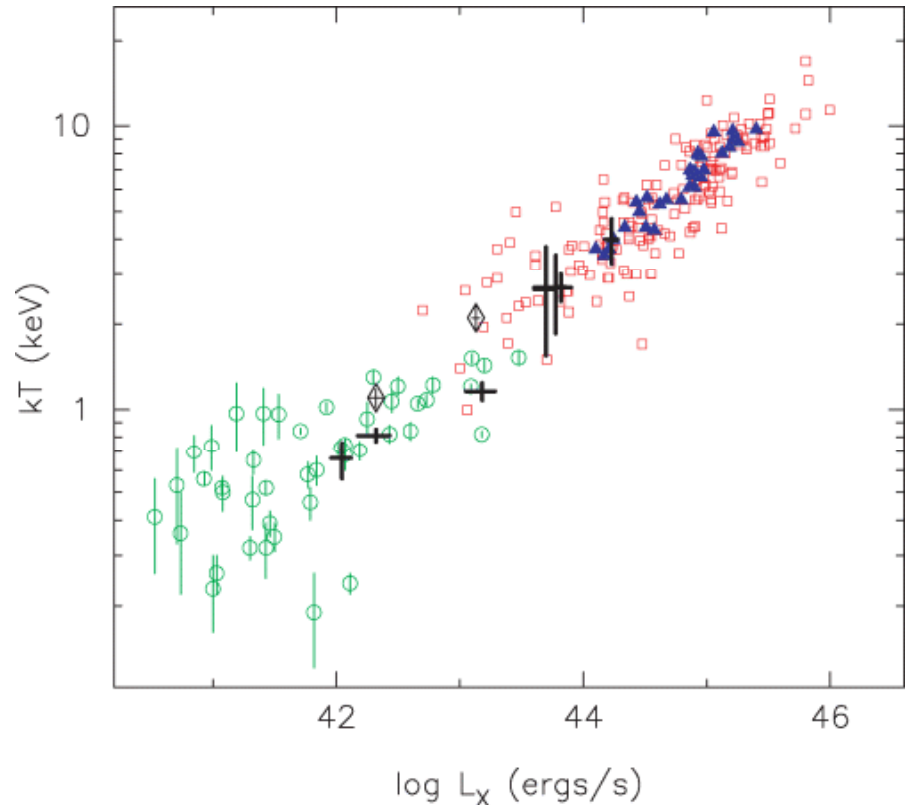
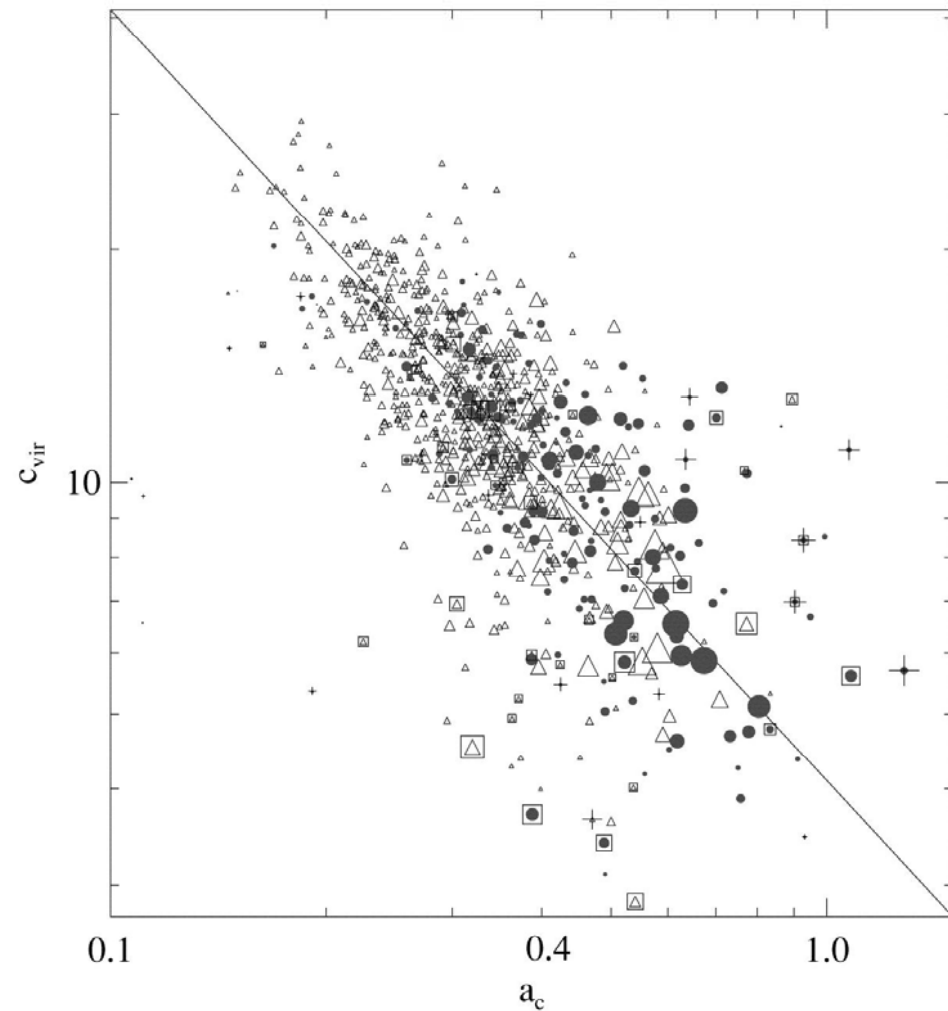


Fig.1 - L_X-T_X relation for FGs, from Khosroshahi et al. 2007 – Clusters are red+blue, groups are green and FGs are the data points.

N-body simulations of Λ CDM cosmologies

($z_{\text{formation}} > 1.5$).

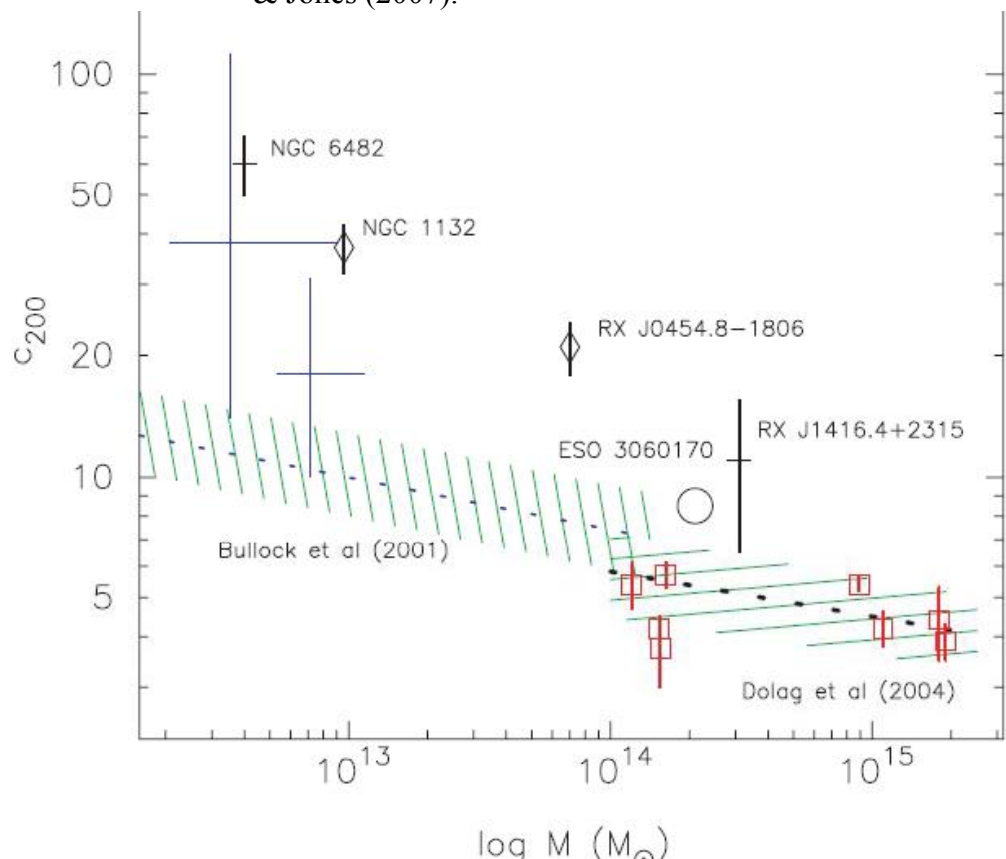
Wechsler et al. 2002



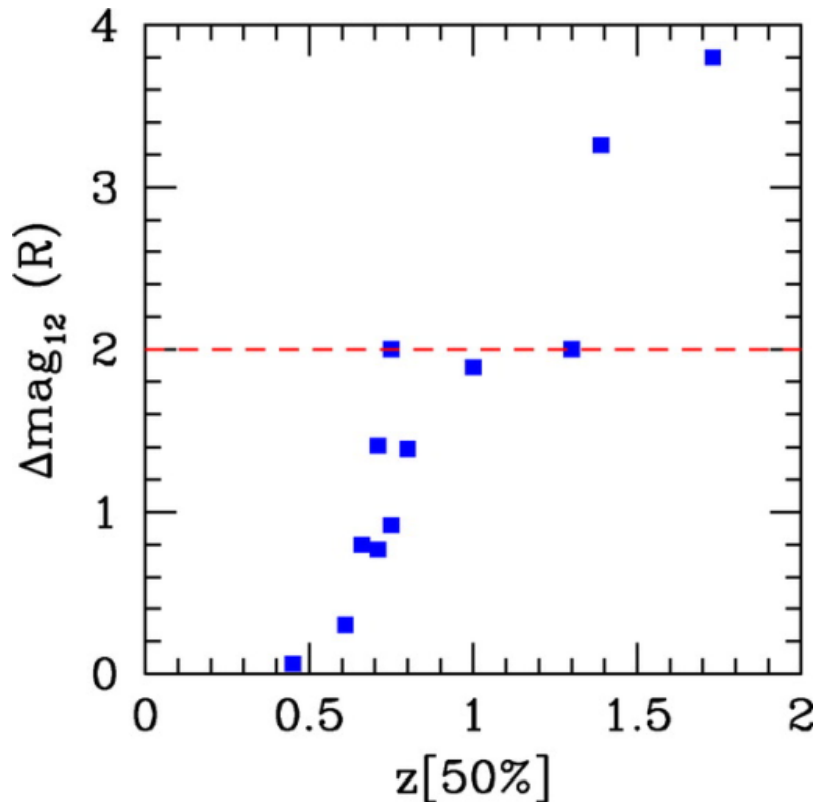
Are They Old?

- X-ray derived mass profiles → **high values of the concentration parameter** c_{200} . Given the correlation found between c_{200} and formation epoch in N-body simulations of Λ CDM cosmologies (Wechsler et al. 2002), FGs should be very old ($z_{\text{formation}} > 1.5$).

3 FG with resolved $T(r)$ & 2 OLEGs (diamonds) are compared with non-FGs clusters (open squares). From Khosroshahi, Ponman & Jones (2007).



Are They Old?



$\Delta m_{12,R}$ of each simulated FG as a function of formation time defined as the epoch in which the group assembled 50% of the system's final mass

Recent numerical+hydro simulations → correlation between **formation epoch and Δmag** , the older groups having higher magnitude differences (e.g. D'onghia et al. 2005). The latter suggest a typical FG formation age of 4.7-6.5 Gyr ($0.75 < z < 1.3$) as opposed to regular groups ($\sim 6.5 - 8.5$ Gyr).

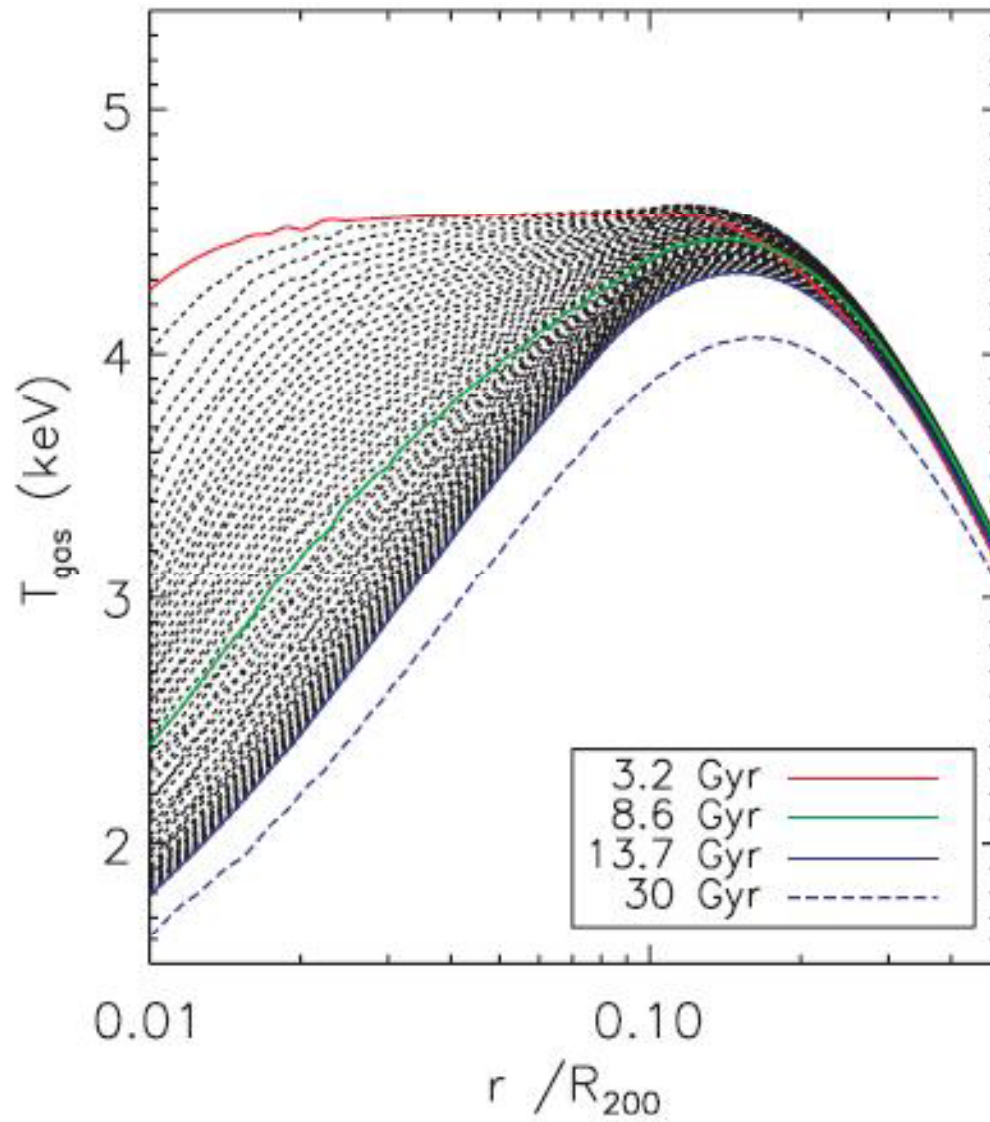
Current State

- The most popular mechanism proposed to “wipe out” the big galaxies surrounding the central dominant galaxy is still considered to be **cannibalism** through dynamical friction.
- **This process per se does not impose strong constraints to the age of FGs.** The characteristic accretion time is directly proportional to the impact parameter r_0 of the satellite galaxies (D’Onghia et al. 2005), which may have a wide range of variation (10-100 kpc corresponding to 1.2-12 Gyr), according cosmological simulations.

$$t_{\text{inf}} = r_0 / (dr/dt) = 12.4 \frac{r_0}{100 \text{ kpc}} \left(\frac{V_h}{700 \text{ km s}^{-1}} \right)^2 \times \left(\frac{V_s}{250 \text{ km s}^{-1}} \right)^{-3} \text{ Gyr}$$

h_{halo}^{ALO} v_{EL} *s_{satellite}^T v_{EL}*

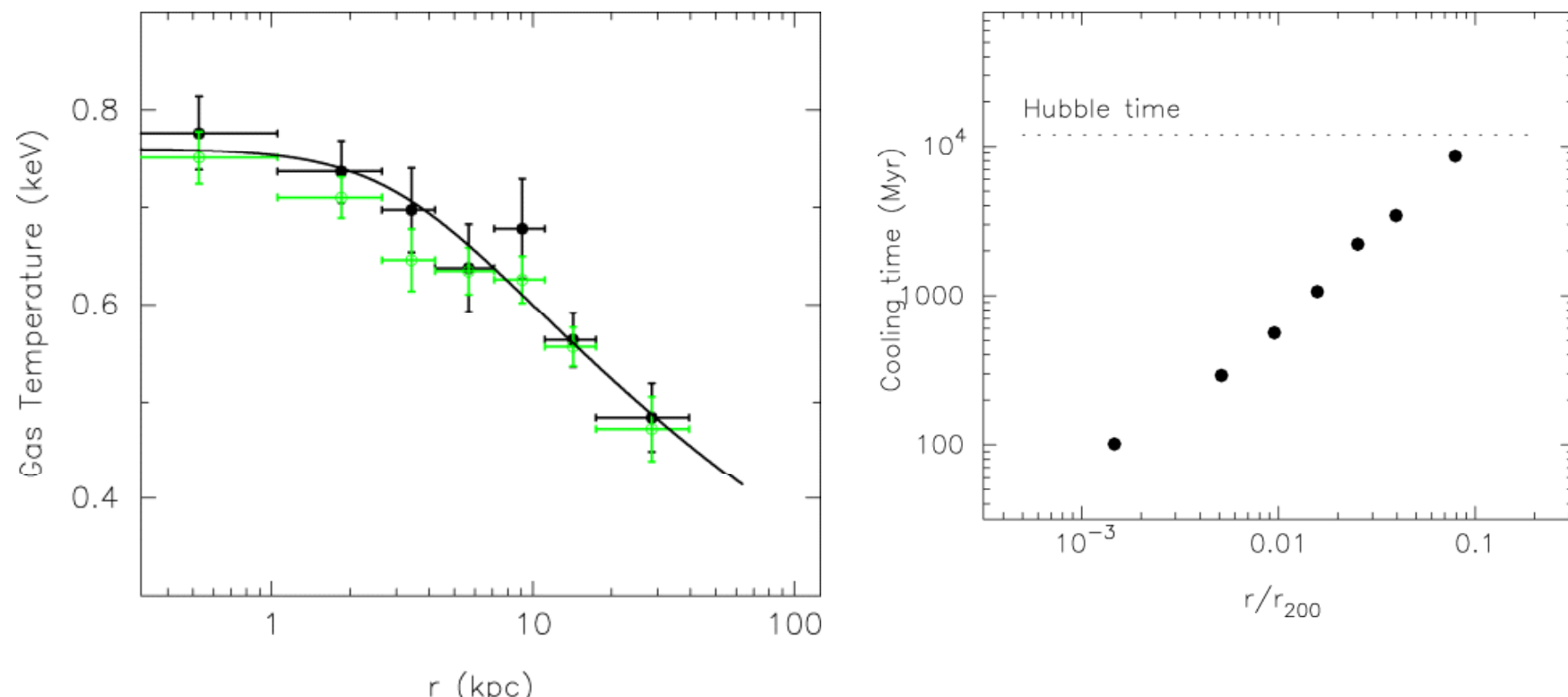
Inconsistencies: Are They Old?



Ettori & Brighenti 2008

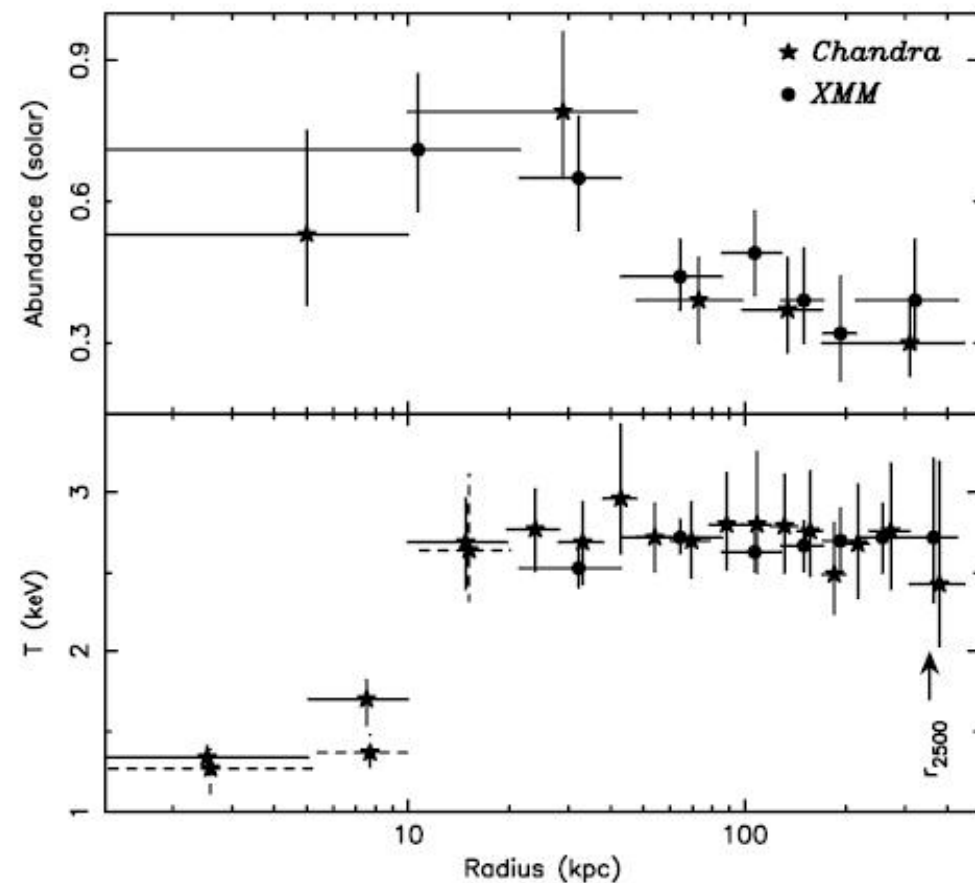
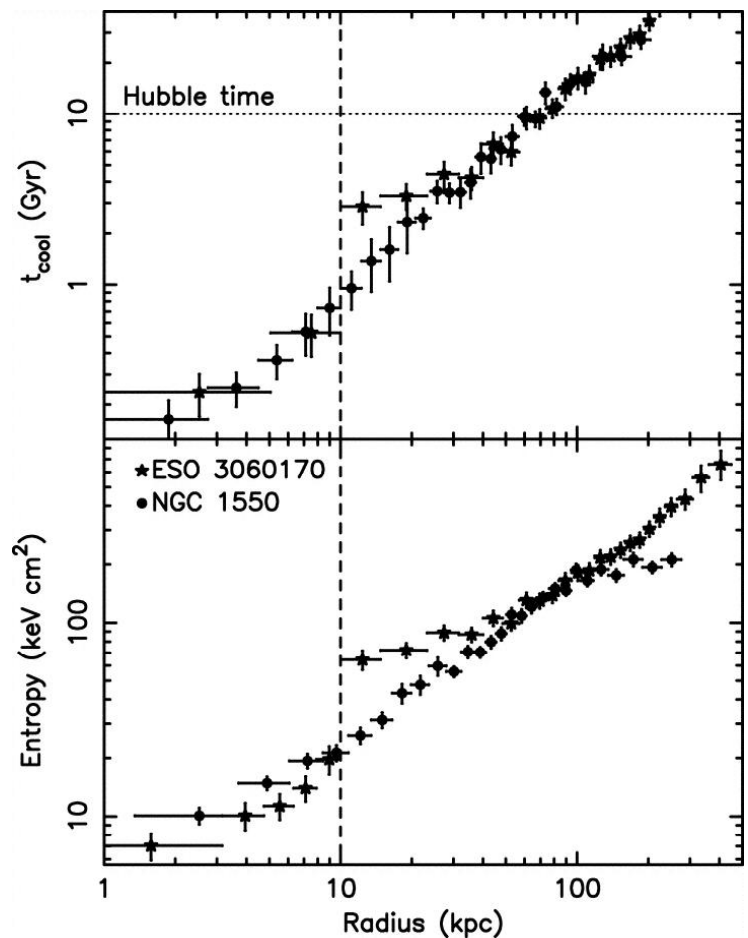
Inconsistencies: Are They Old?

On the other hand, the cooling time of FGs is observed to be significantly below the Hubble time (e.g., RX J1416.4+2315, ESO 3060170, Sun et al. (2004); NGC 6482, Khosroshahi et al. (2004, 2006), ***but they typically lack the expected steep –profile cooling cores***, indicating a more recent formation time.

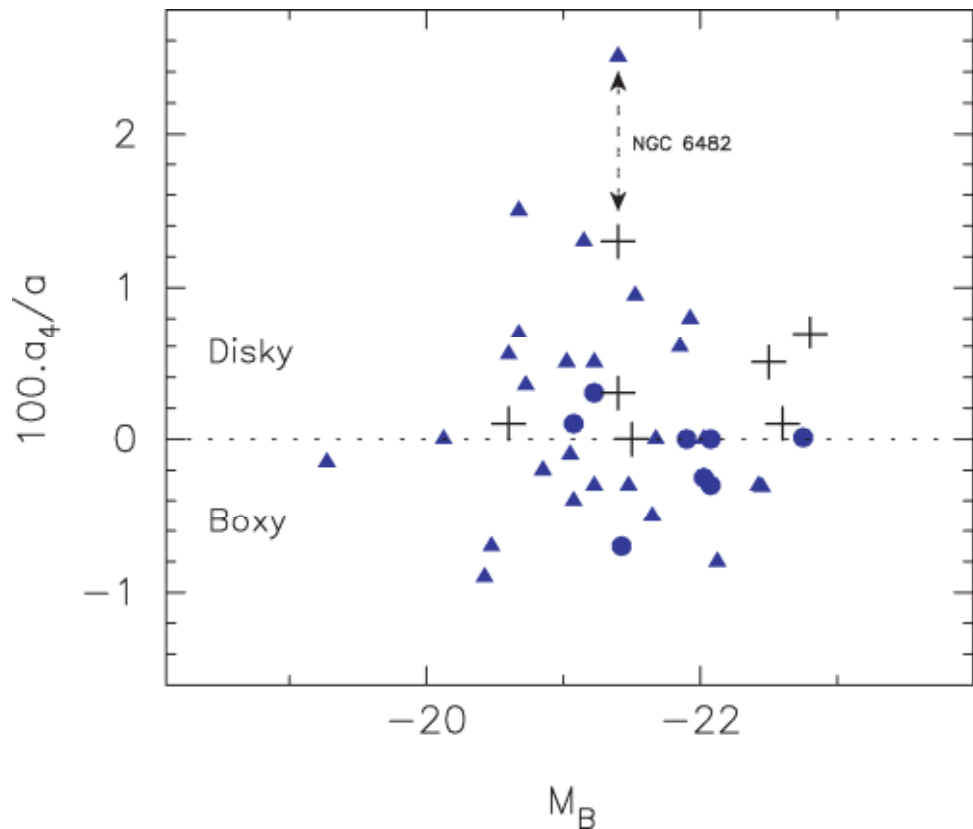


NGC 6482, Khosroshahi et al. (2004)

ESO3060170



Sun et al. (2004)



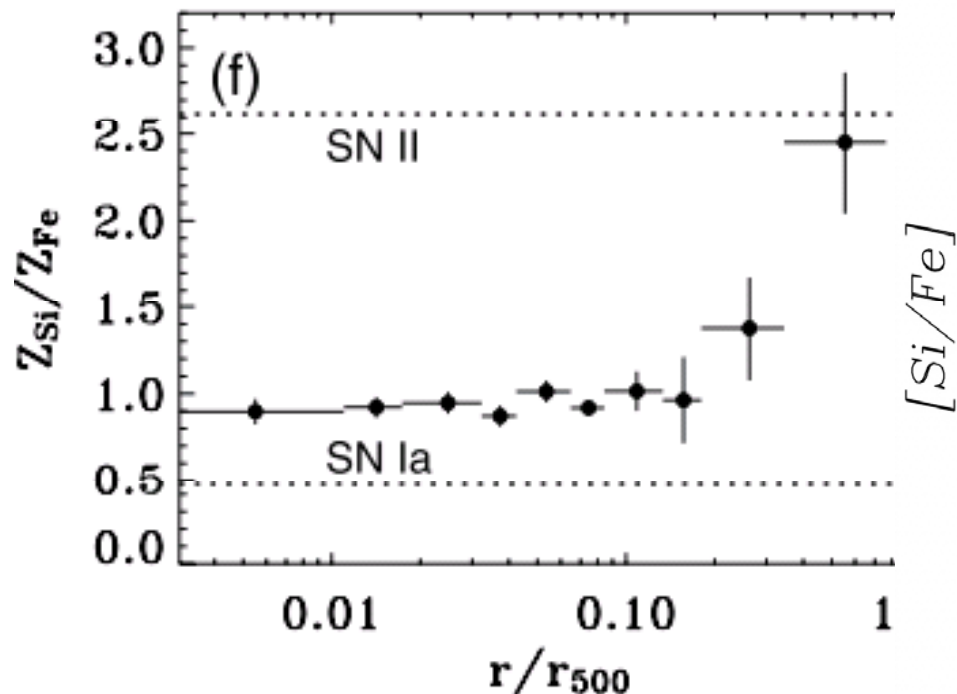
Isophotal shapes of early-type brightest group or cluster galaxies,

Fossil groups (crosses), early-type BGGs (triangles) and BCGs (circles).

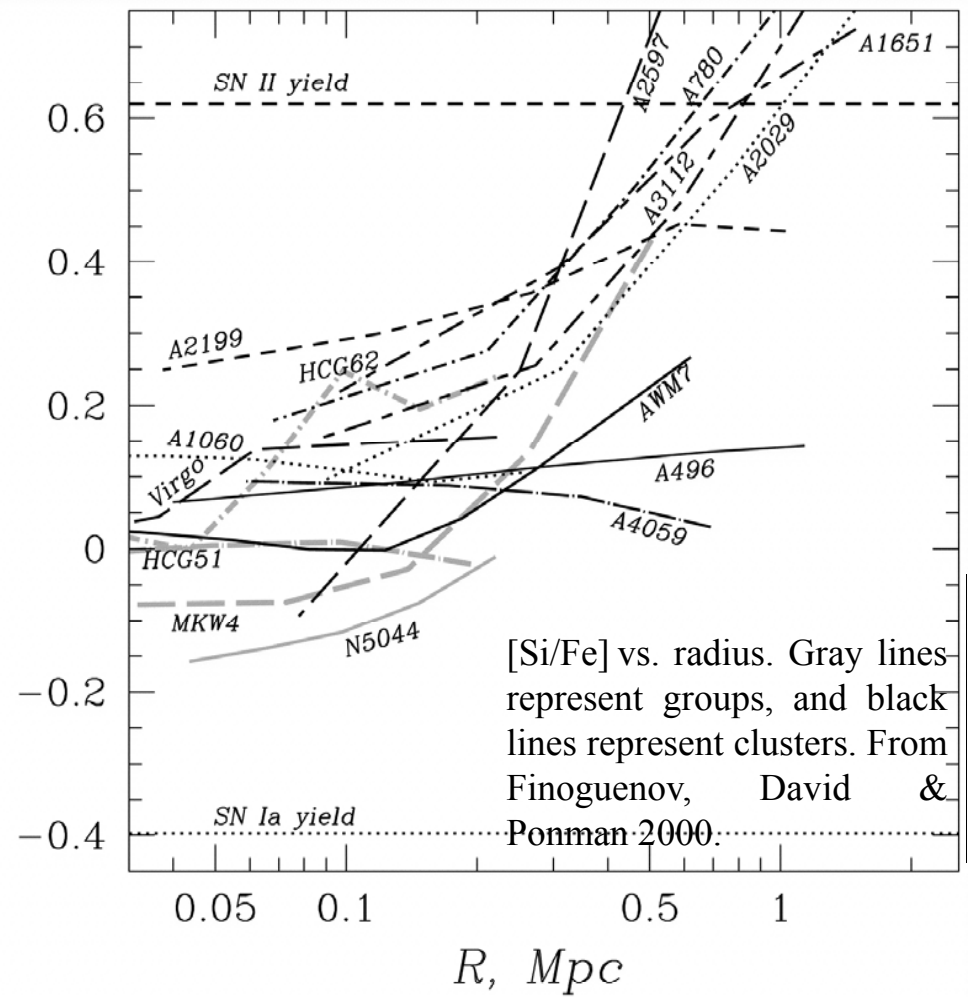
From Khosroshahi, Ponman & Jones (2006).

disky isophotes → secondary gas infall (Khochfar & Burkert 2005), → Spirals took part in the merging. → star formation **bursts** (e.g. van Dokkum et al. 1999), → metal rich SNII-driven galactic winds or **superwinds** (e.g. Strickland et al. 2004, Heckman et al. 1990). → **deposit metals and energy** into the central gas. → **change the chemistry** of the IGM

SN Ia/SN II pollution in the ICM shows often radial gradients, SN Ia/SN II ratio is higher in the central region



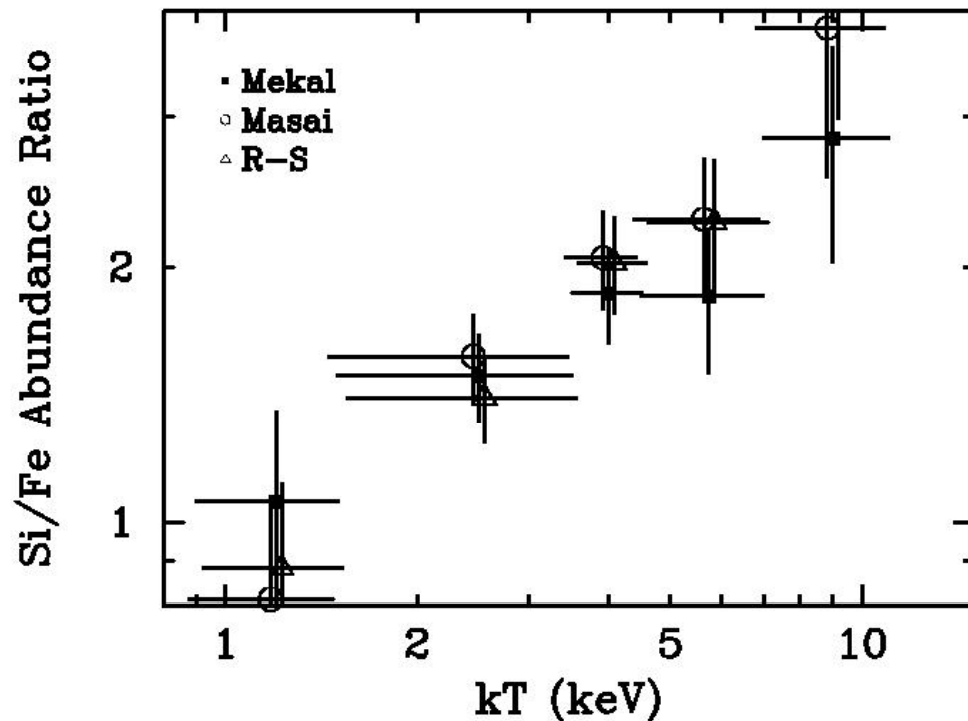
Rasmussen & Ponman 2007



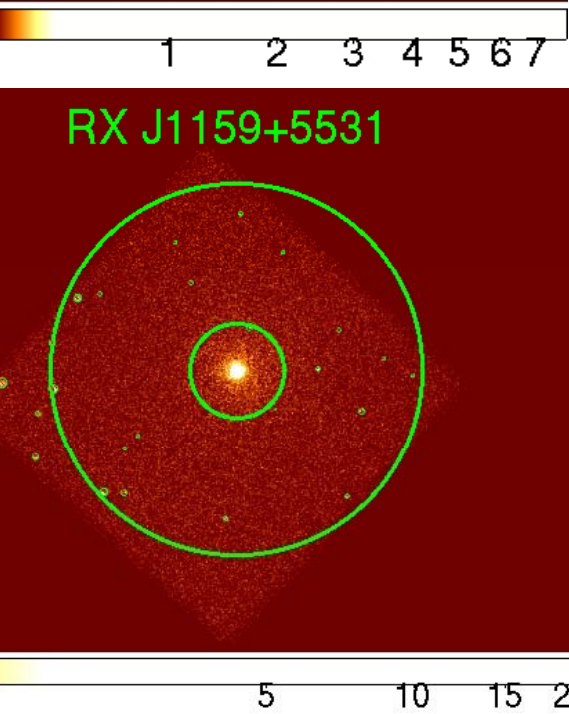
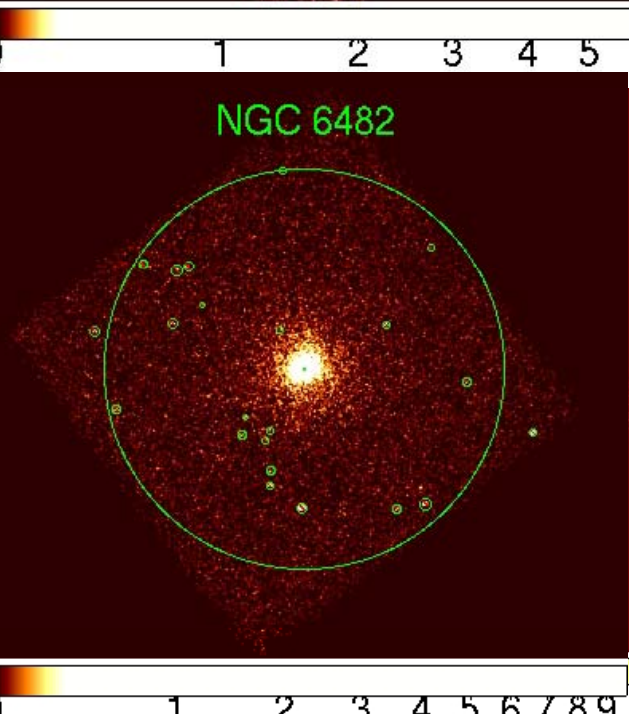
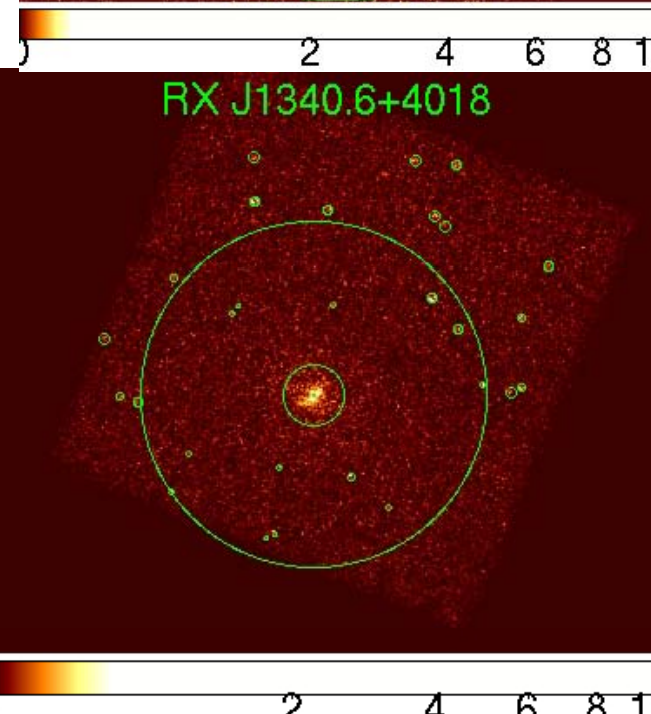
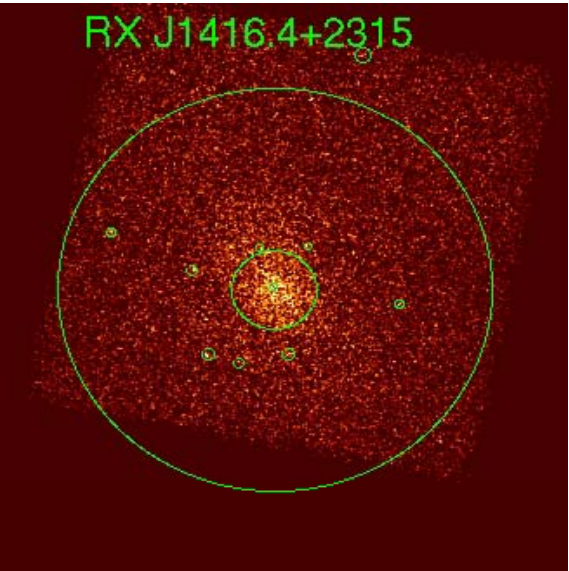
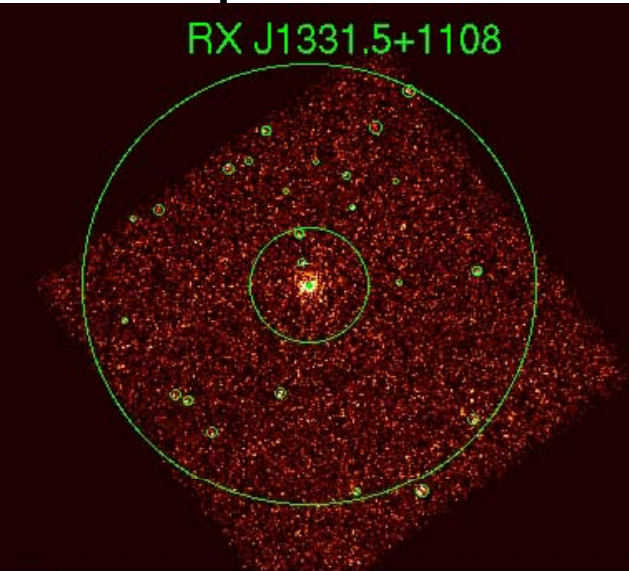
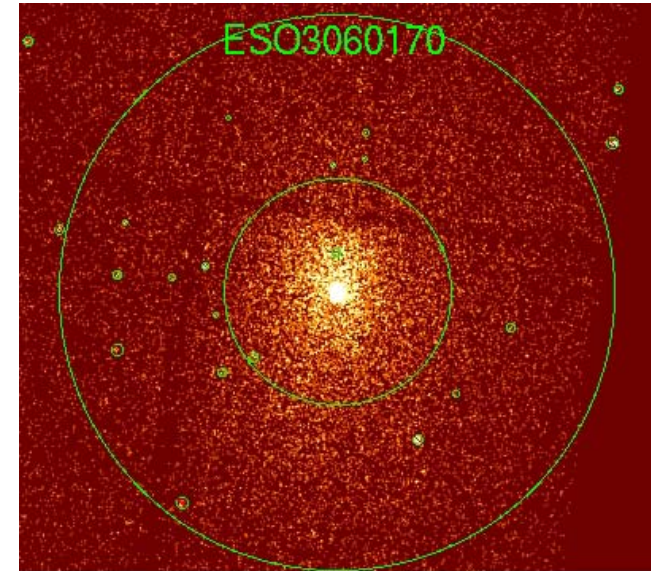
- SN II-powered protogalactic winds will tend to disperse metals into the ICM
- **Ram-pressure stripping** will distribute the SN Ia polluted ejecta in a more centralized way and **is a slower and continuous process** that should the central SN Ia Fe mass fraction with time.

- Induced Secular SN II powered winds (e.g. van Dokkum et al. 1999, Strickland et al. 2004, Heckman et al. 1990).
- Change (Energy and) the Chemical Enrichment Type of the ICM
- Can be seen through elemental abundance ratios
- Evidence for secular SF in cD (in addition to any cooling flow deposition)

Fukazawa et al. 1998



The Sample



2 4 6 8 10

1 2 3 4 5

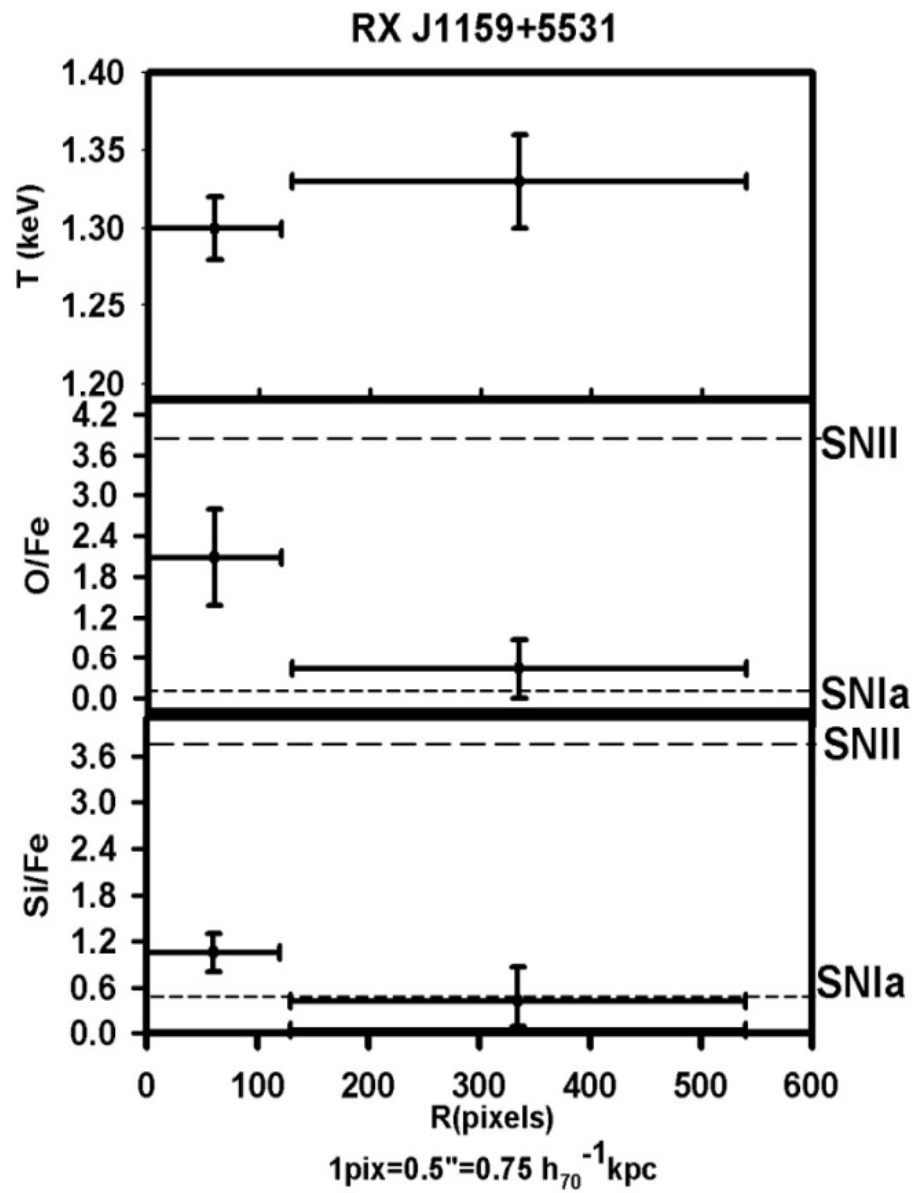
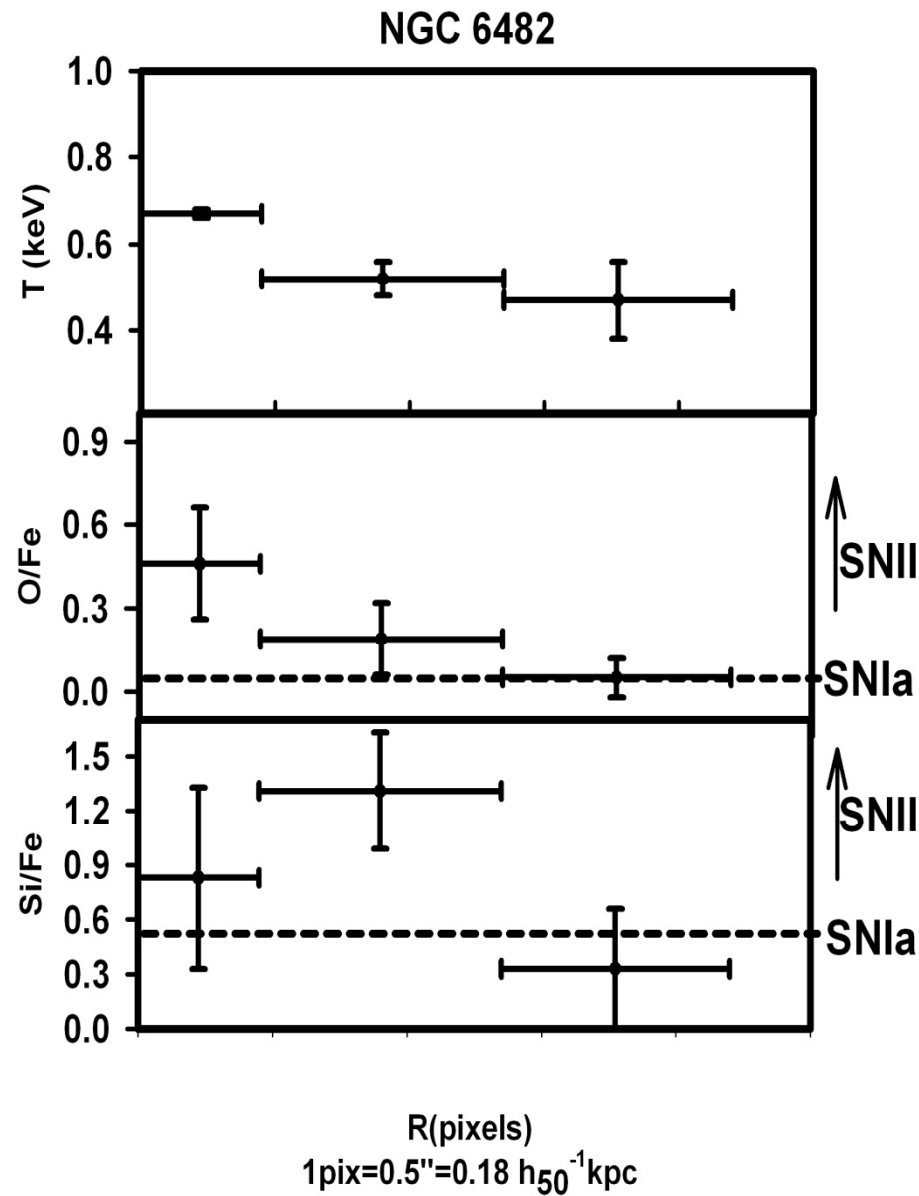
1 2 3 4 5 6 7

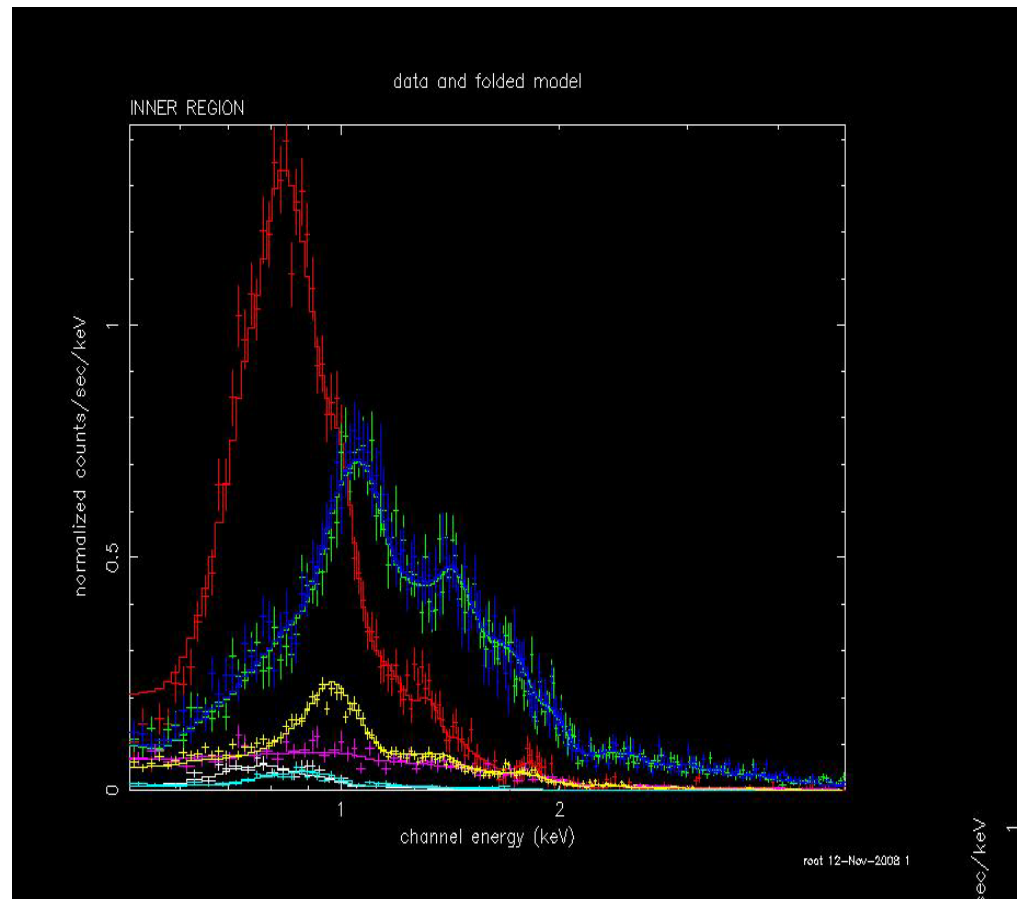
2 4 6 8 10

1 2 3 4 5 6 7 8 9

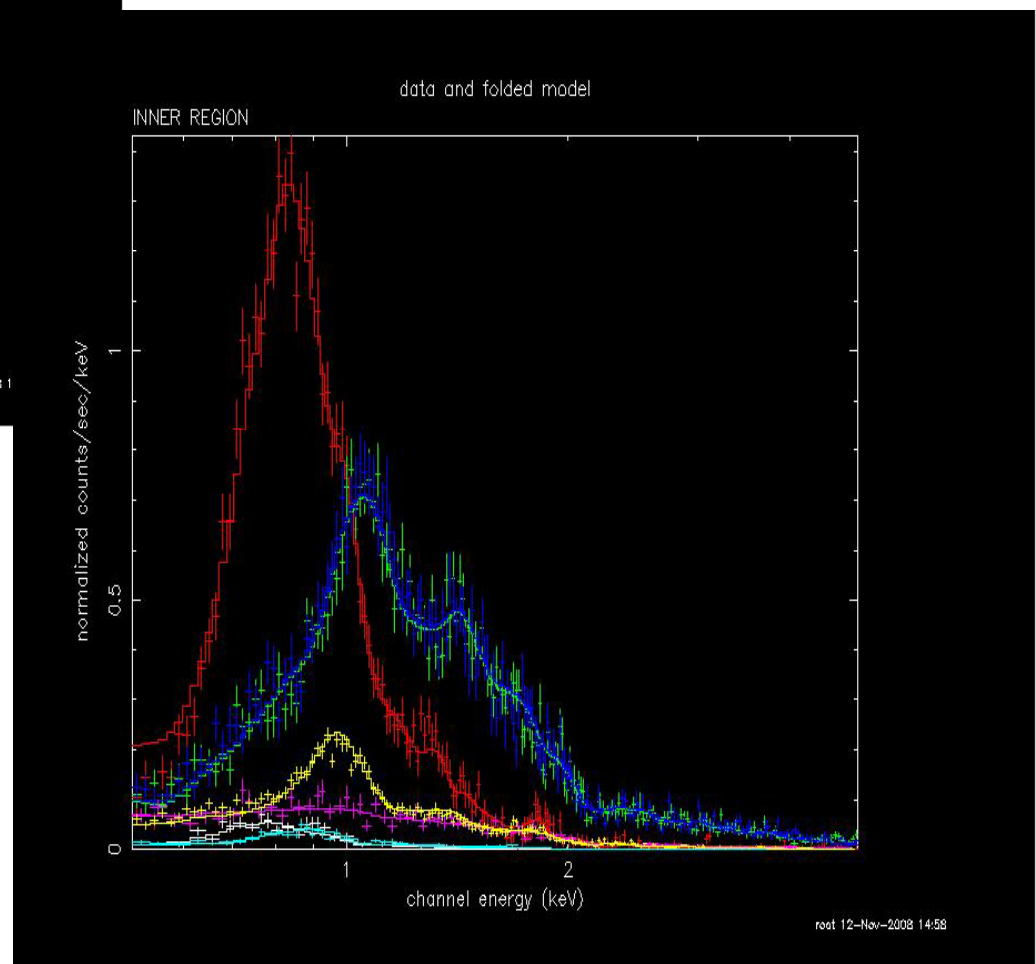
5 10 15 20

Individual Profiles





Inner region
All FGs

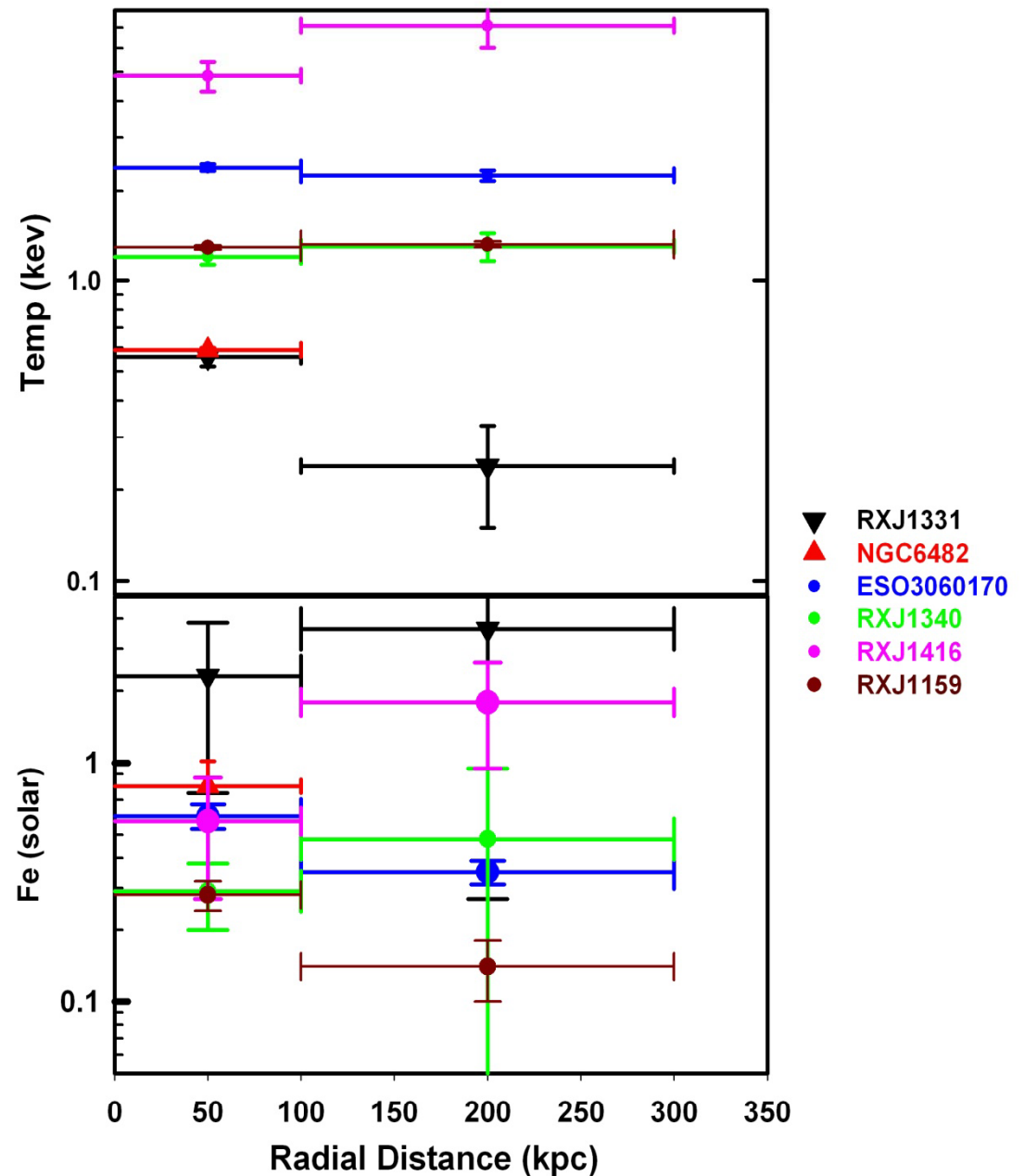


Outer region
All FGs

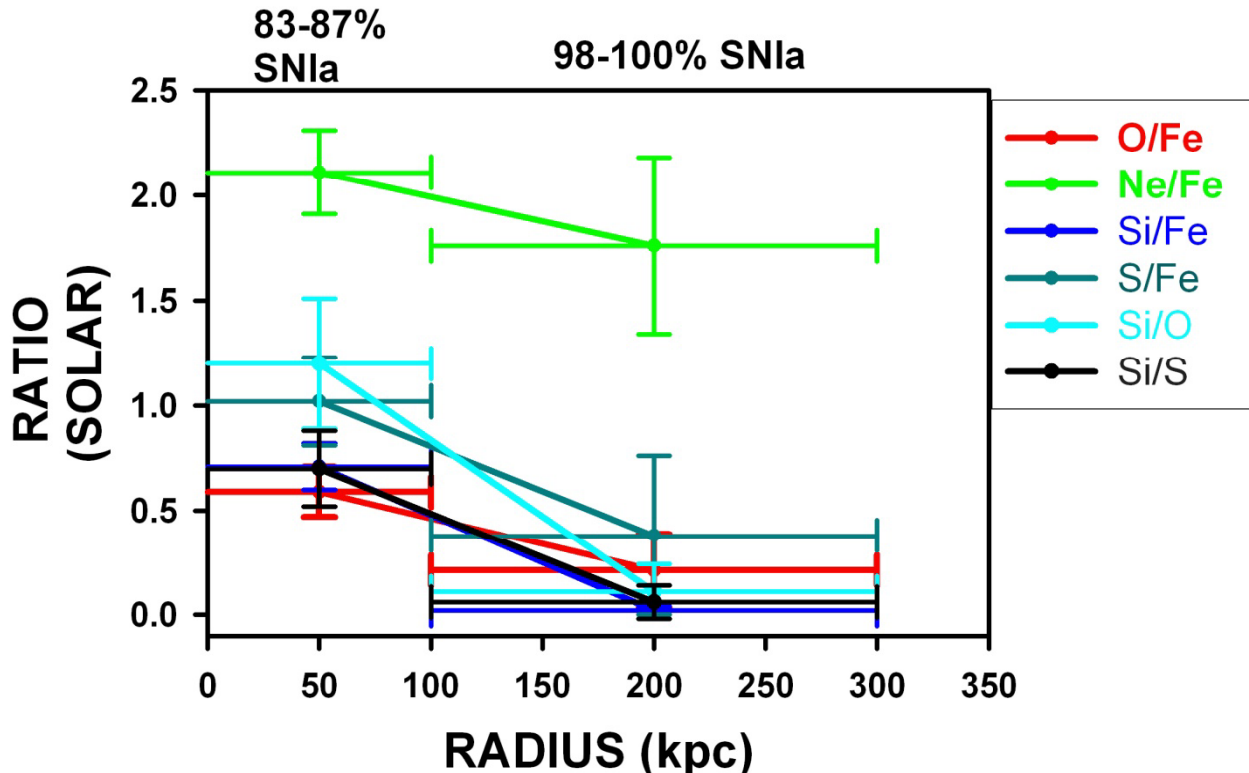
Most FGs show a lack of cooling cores and some even show central temperature enhancements.

The marginally significant central decline in temperature in RX J1416 may be due to anisotropies at ~ 200 kpc, since the temperature profile beyond that radius is consistent with the central values (Khosroshahi et al. 2006).

The Fe abundance profile is well constrained individually only for 2 FGs. No obvious global gradients correlations are found.



RESULTS



The analysis with improved statistics gained by joining all FGs shows a general central enhancement of α -elements and Fe (Top figure), suggesting an central decline of SN Ia dominance. This can be seen more specifically in the abundance ratio profiles.

Using an error-weighted average over all the ratios shown, we find that, despite the overall dominance by SN Ia of $\sim 99\%$ characteristic of the central regions of groups and poor clusters of galaxies, **there is an unusual significant decline of the SN Ia Fe mass fraction towards the center of FGs (85%)**.

Discussion

$$MFe_{SNII} = 1.16 \times 10^7 (f_{0.2}) (M_{gas_{11}}) (Z_{0.2}) (ZFe_{\odot}) M_{\odot}$$

$f_{0.2}$ is the Fe mass fraction injected by SNe II normalized by 0.2

$$E_{inj} = \frac{MFe_{SNII}}{M_{Fe1SNII}} < E_{SNII} >$$

energy needed to keep the IGM from cooling ΔE

$$\frac{E_{inj}}{\Delta E} \sim 1.3 \times 10^{11} \frac{(E_{SNII, S1})(f_{0.2})(M_{gas_{11}})(Z_{0.3})(ZFe_{\odot})}{(4t_g)(L_{42}) \left(\frac{M_{Fe1SNII}}{0.09 M_{\odot}} \right)}$$

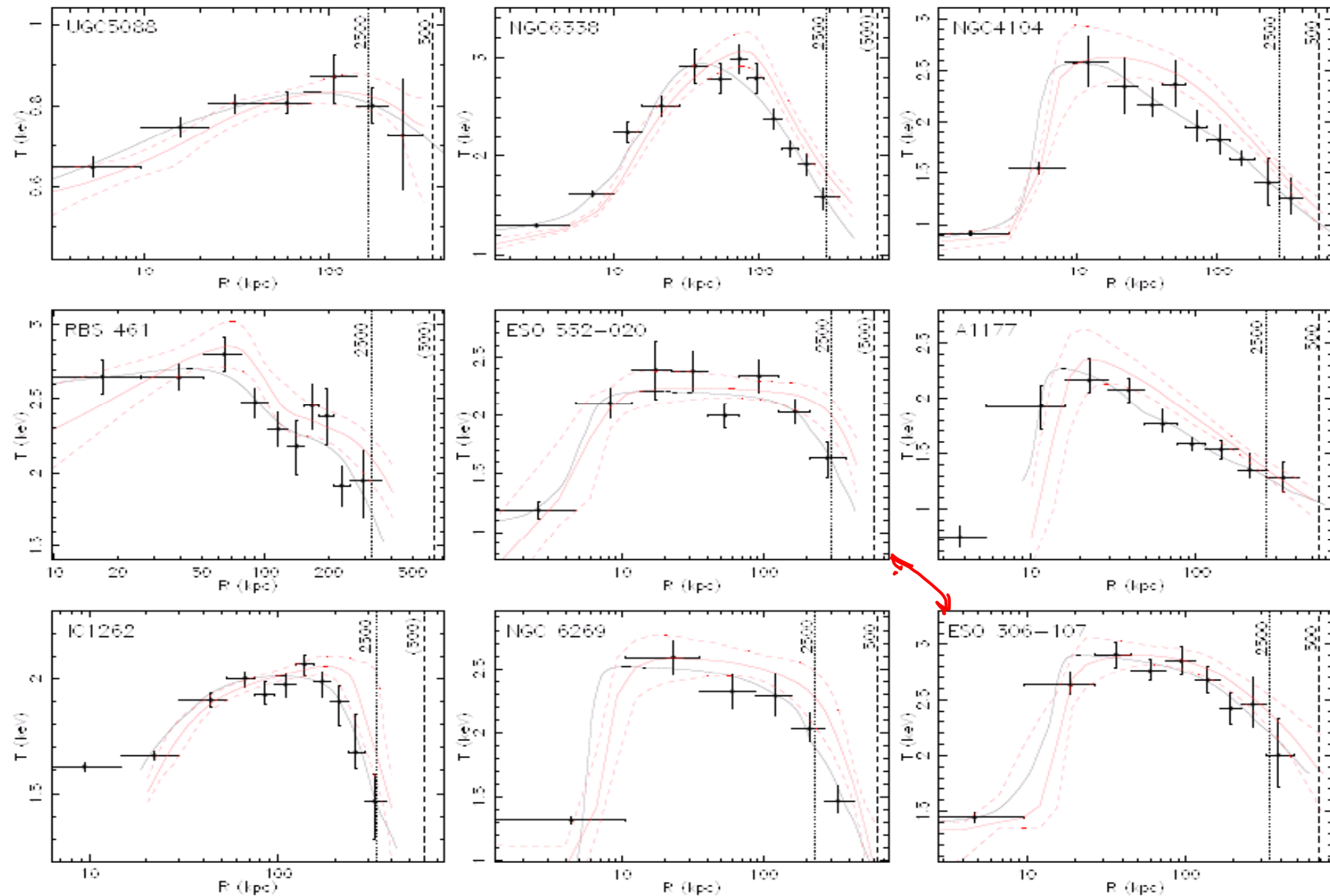
- From the observed decline of the SN Ia Fe mass fraction in the central regions of FGs, it can be shown that the injected energy E_{inj} , is more than twice larger than the energy required to stop gas cooling. The average supernovae rate for this secondary wind would be large (near **10 SNu**), larger, but on the same order as that of M82.

The large velocity dispersion of FGs suggests that these systems have deep gravitational potential typical of poor clusters in agreement with the relatively high X-ray temperatures measured.

Typical lack of cooling cores (or just mini cool cores) and reduction of the SN Ia Fe mass fraction is consistent with a scenario where SN II powered winds resulting from merging late type galaxies erase the original central SN Ia Fe mass fraction dominance. This is also consistent with the recently found disky isophotes of the central dominant galaxies in FGs by Khosroshahi, Ponman & Jones (2006).

Reconciliation with the theoretical models is possible if the “halo” that will eventually become a fossil group is formed earlier than those that will become galaxy groups and clusters, but the BGG of fossil groups are formed later than the central galaxies of groups and cDs. A similar scenario has been put forward recently (Diaz-Gimenez, Muriel and Mendes de Oliveira 2008,) in a study of the properties and merging history of the bright galaxies in simulated fossil groups extracted from the Millenium Simulation Galaxy Catalogue (see also and also La barbera et al 2009 & talk in this conference). T

The small number of FGs observed have short exposures and this substantially limits the constraints that we can place on competing scenarios for the formation of these systems. A larger sample of FGs with medium exposures is a fundamental step to zero in on their nature and evolution.

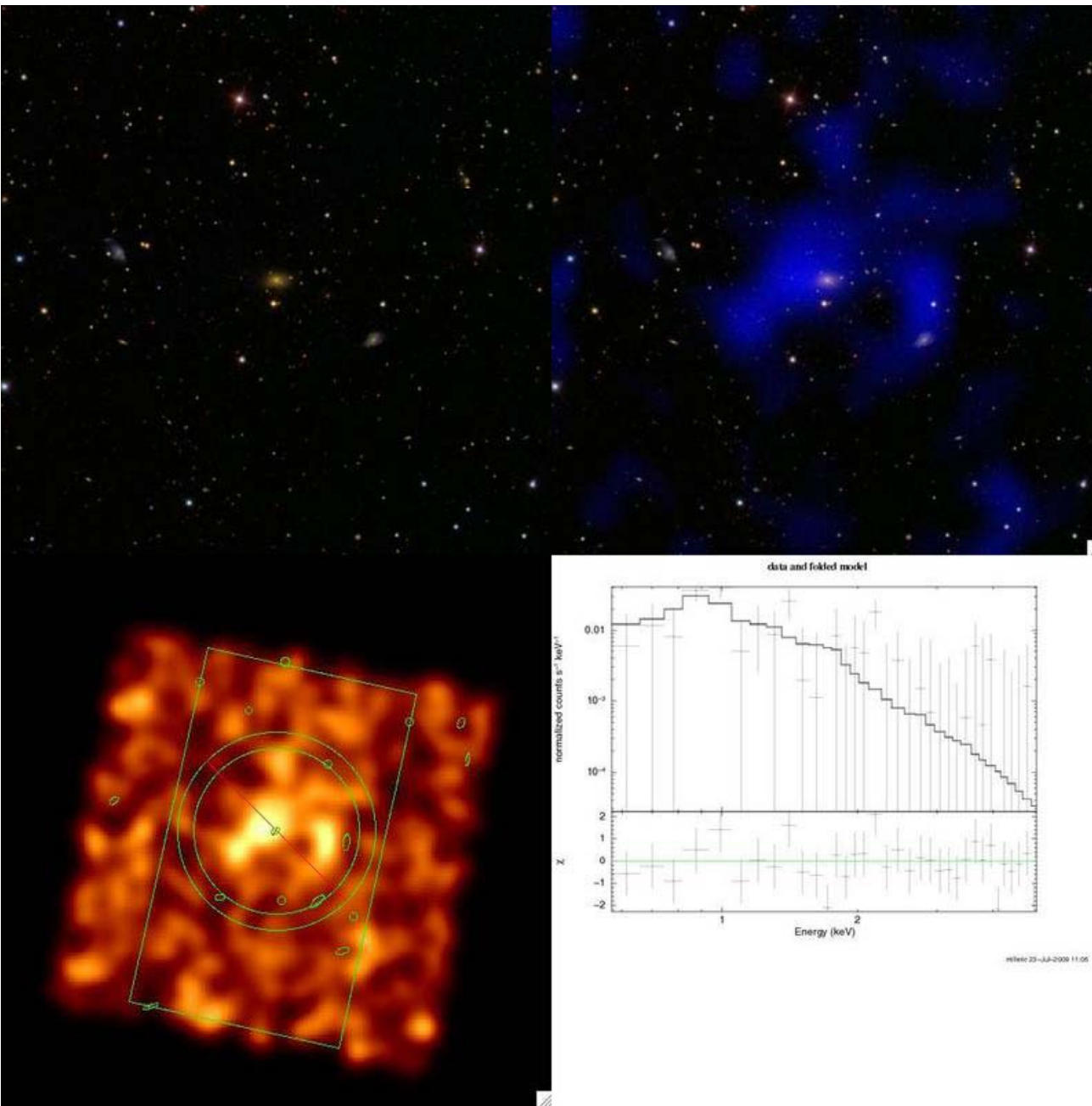


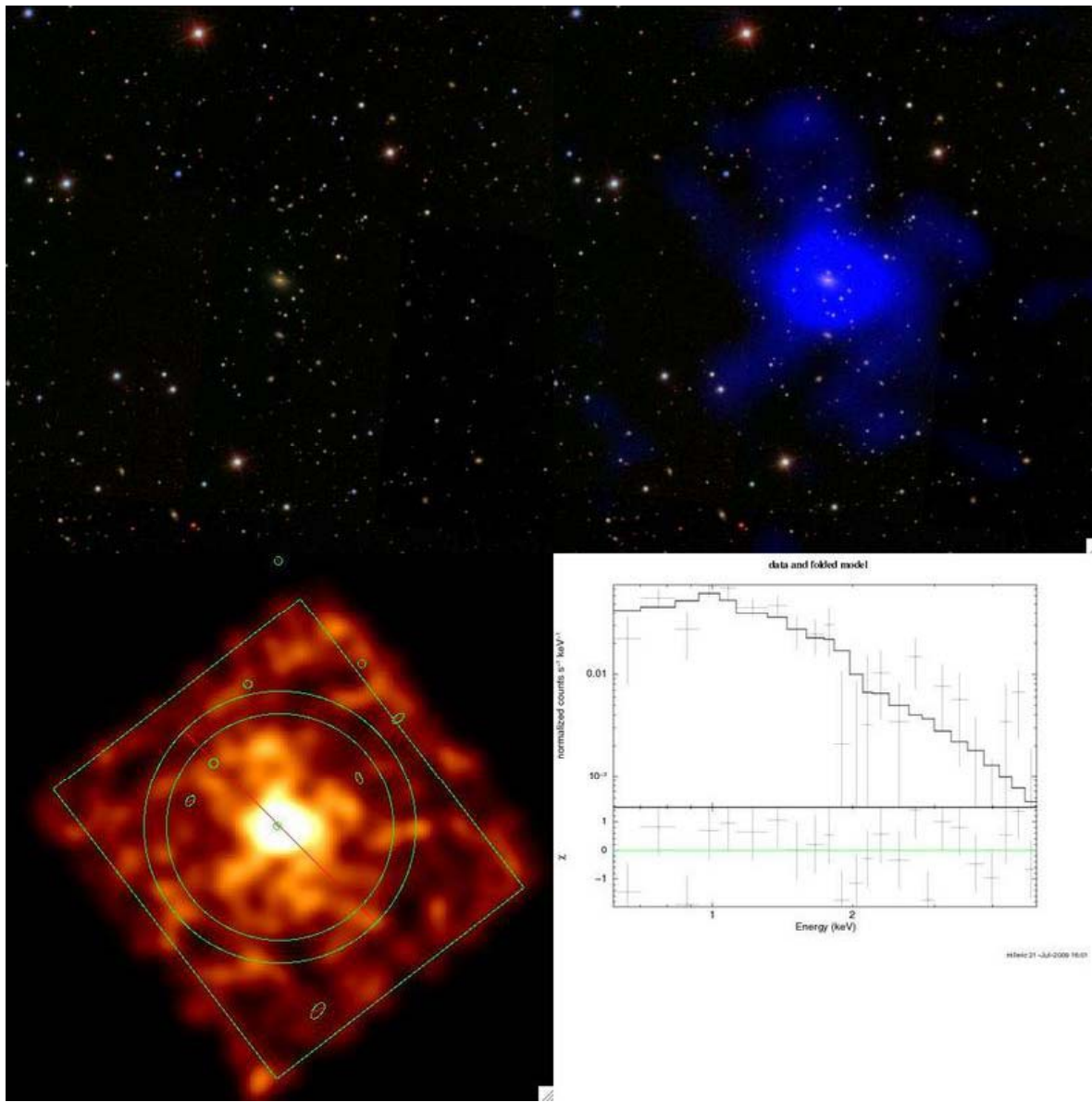
1- Can we join all FGs?.

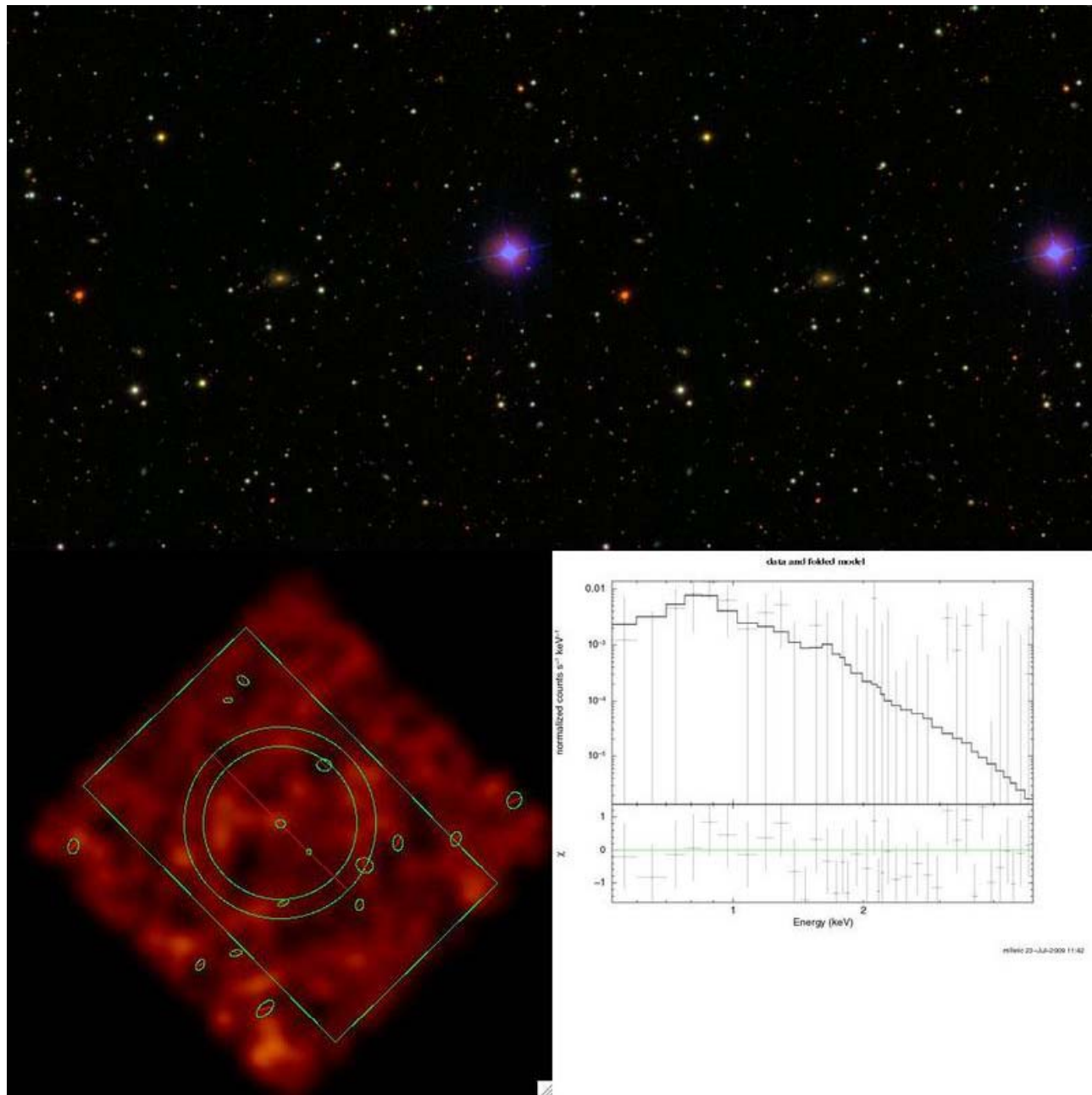
Not clear given the wide variety of group properties

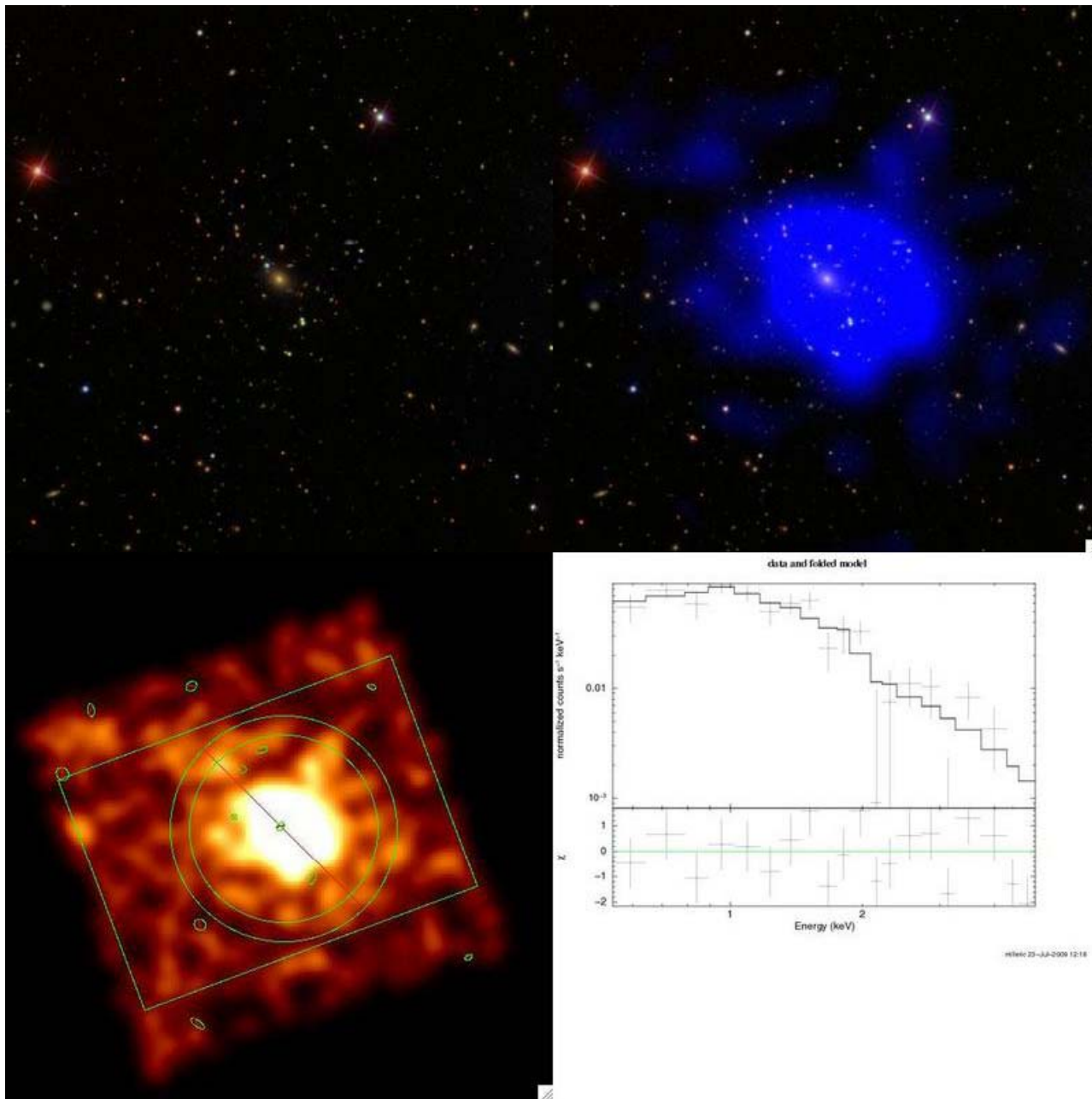
2- Sun's analysis in groups. There is a variety of cold cores in groups. Does it invalidate our assumptions and/or logic?

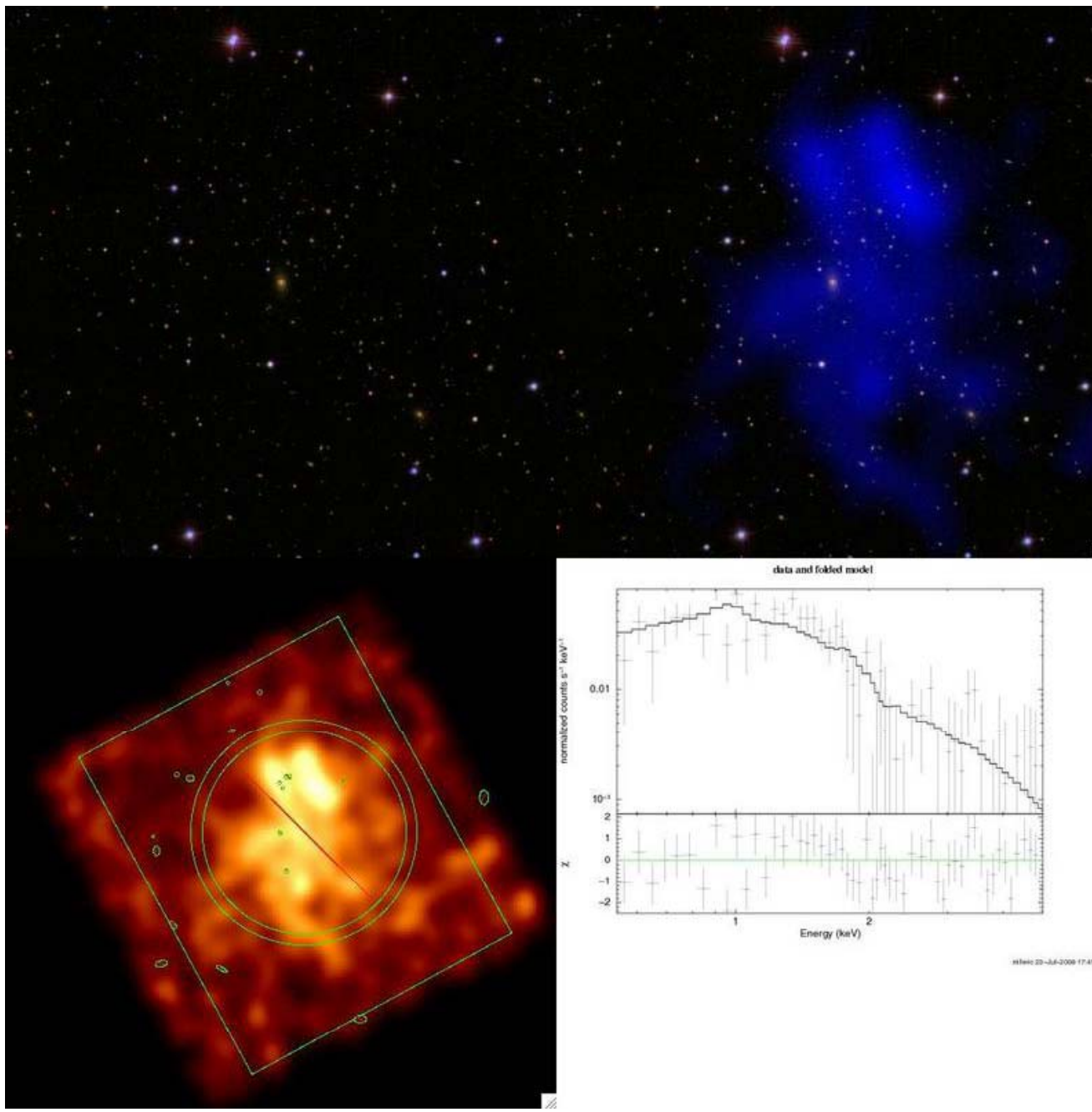
Precautions

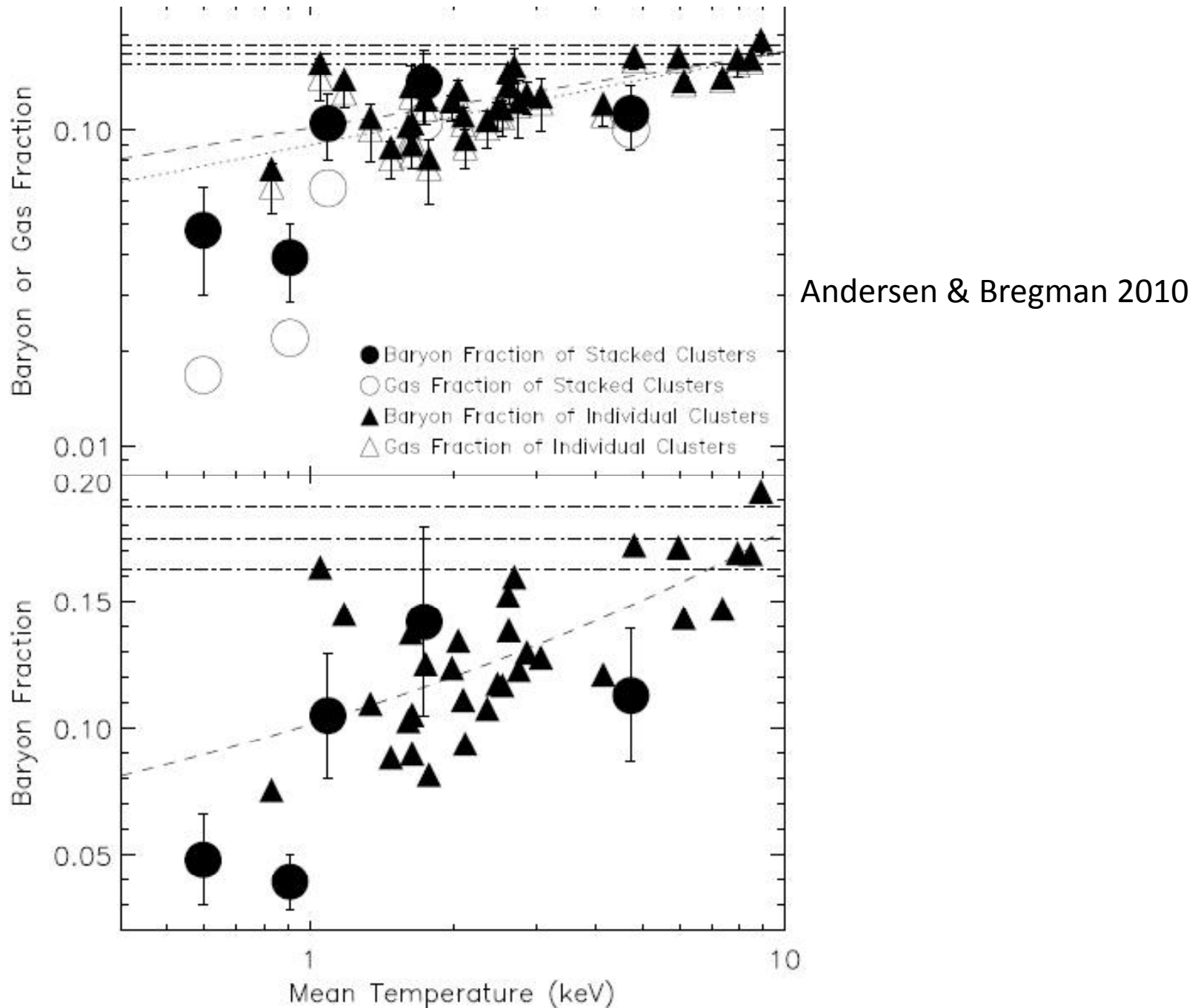












parameter ranges:

Mi,Mo = 0 - 1, Mi+Mo = 1

agei = 0.1 - 2 Gyr

[Fe/H]o = -2.252 - 0

E(B-V) = 0 - 0.5

ageo = 4 - 10 Gyr

results

Name	m-p-f	E(B-V)	Mo	[Fe/H]o	ageo	Mi	agei
RX J1007+3800	52993-1426-498	0.30	0.99	0.00	9	0.01	1
RX J1410+4145	52823-1347-468	0.01	0.97	0.00	9	0.03	1
RX J0856+0553	52668-1189-028	0.00	0.91	0.00	9	0.09	2
RX J1045+0420	52339-0578-070	0.50	0.99	-0.35	9	0.01	0.5
RX J1136+0713	53084-1619-179	0.00	0.97	0.00	10	0.03	1
J1340.5+4017	53050-1377-307	0.50	0.97	0.00	9	0.03	2
J1153+6753	51955-0492-574	0.40	0.99	0.00	9	0.01	1
RX J1133+5920	52409-0952-160	0.30	0.99	-0.35	9	0.01	1
J1411+5736	52669-1159-597	0.20	0.99	0.00	9	0.01	1

RX J1159+5531	52672-1018-383	0.50	0.99	0.00	9	0.01	1

Ann. Rev. Astron. Astrophys. 1980, 18:537-60
Copyright © 1980 by Annual Reviews Inc. All rights reserved

MICROWAVE BACKGROUND RADIATION AS A PROBE OF THE CONTEMPORARY STRUCTURE AND HISTORY OF THE UNIVERSE

R. A. Sunyaev and Ya. B. Zel'dovich

Space Research Institute, USSR Academy of Sciences, Moscow, USSR

RJ

$$\frac{\Delta I_v}{I_v} \approx \frac{\Delta T}{T_r} \quad \frac{\delta T}{T} = -2 \frac{k\sigma_T}{m_e c^2} \int n_e T_e dl$$

$$0 < \tau_T \ll 1, \quad \tau_T = \int_{-\infty}^{+\infty} \sigma_T N_e(l) dl.$$

Thomson scattering has a cross section

$$\sigma_T = \frac{8\pi}{3} \left(\frac{e^2}{m_e c^2} \right)^2 = 6.65 \cdot 10^{-25} \text{ cm}^2$$

$$\left(\frac{\Delta J_\nu}{J_\nu} \right)_1 = 2 \frac{k T_e}{m_e c^2} \tau \frac{x \exp(x)}{\exp(x) - 1} \left\{ \frac{x}{2 \operatorname{th}(x/2)} - 2 \right\}$$

Wien

or

$$\left(\frac{\Delta T}{T} \right)_1 = \frac{2 k T_e}{m_e c^2} \tau \left\{ \frac{x}{2 \operatorname{th}(x/2)} - 2 \right\}.$$

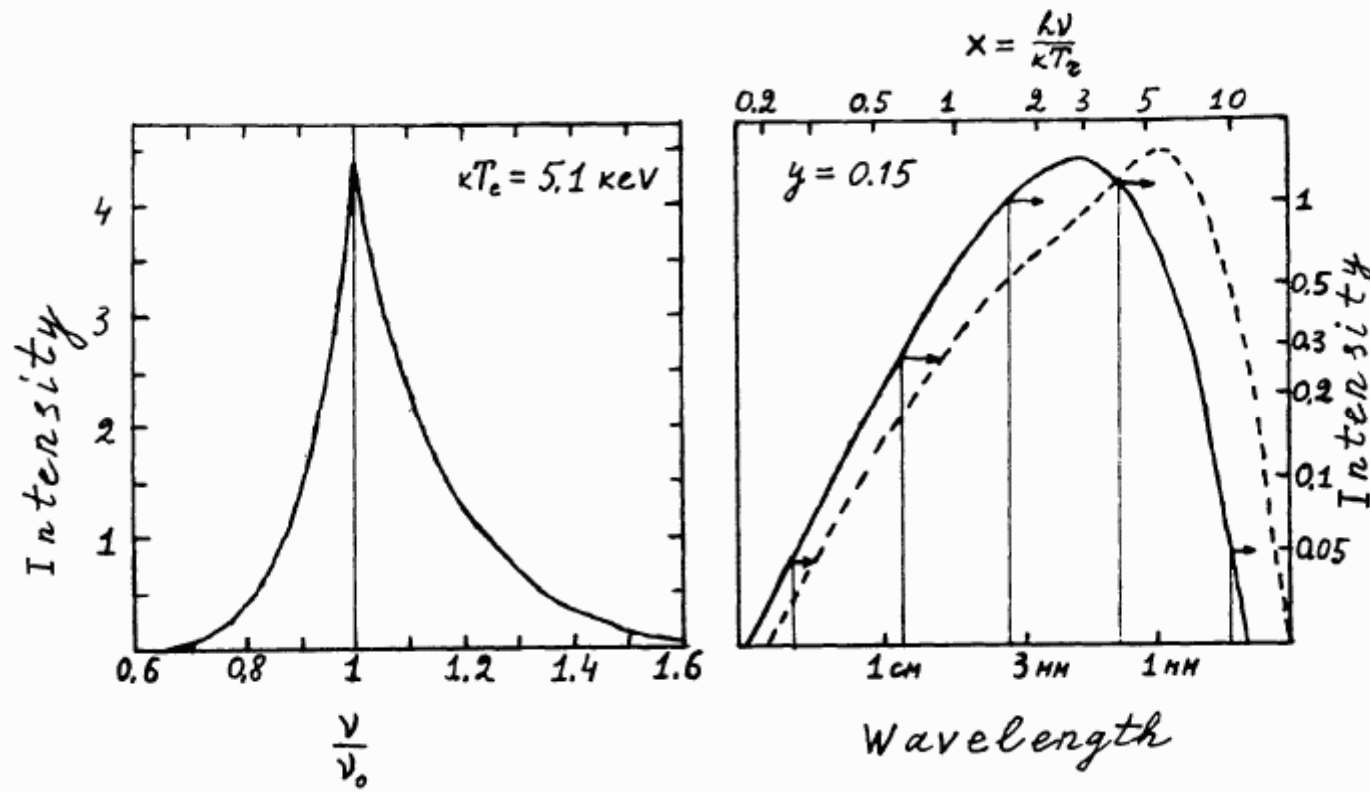


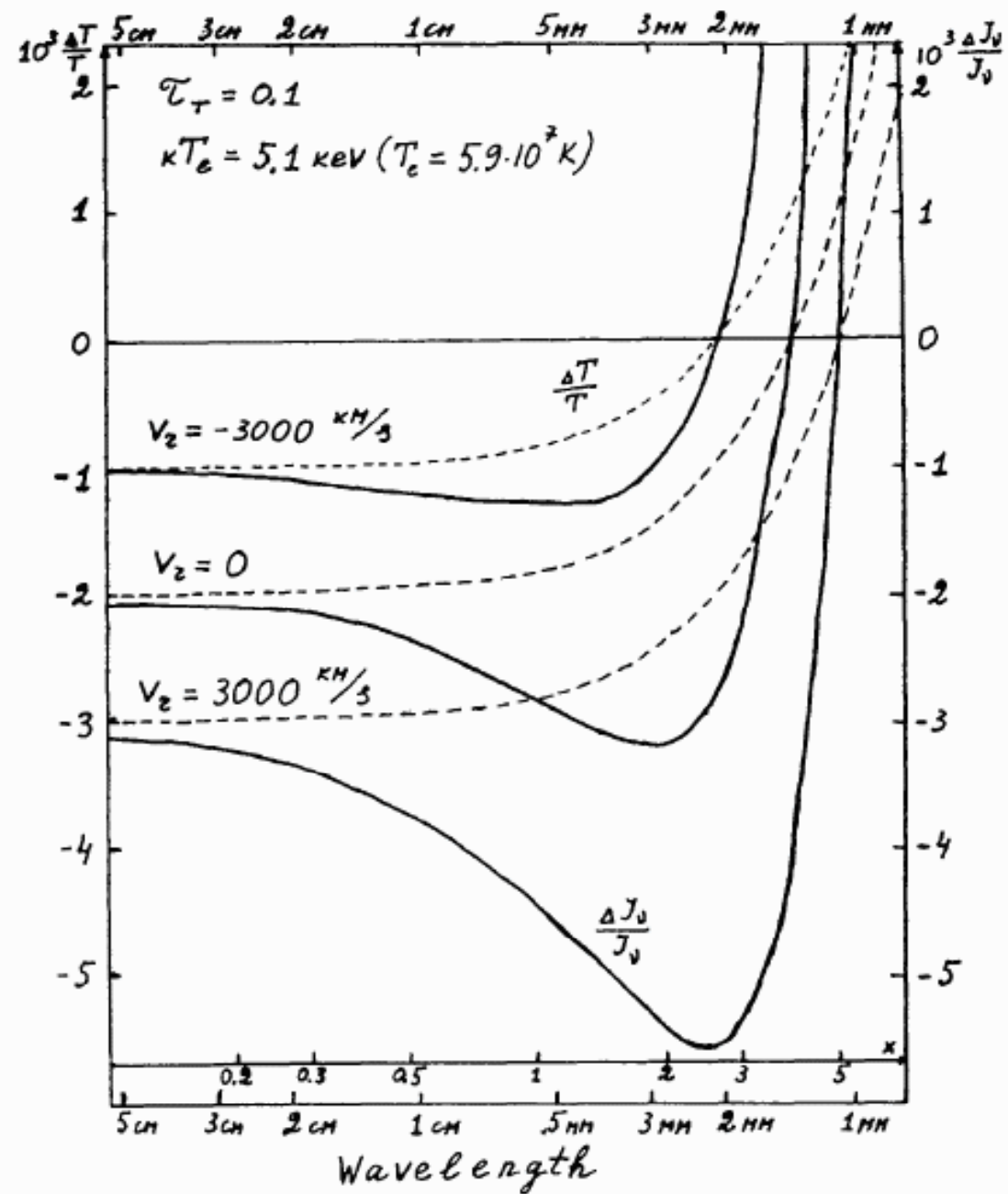
Figure 4 The monochromatic spectral line profile after one scattering by hot Maxwellian electrons (left). The spectrum of blackbody radiation (solid line) after multiple Compton scattering (broken line) is shown on the right.

Kinetic Component too!

$$\left(\frac{\Delta T}{T}\right)_{\text{total}} = \left(\frac{\Delta T}{T}\right)_1 + \left(\frac{\Delta T}{T}\right)_2.$$

If τ is small

$$\left(\frac{\Delta T}{T}\right)_2 = -\frac{v_r \tau}{c}; \quad \left(\frac{\Delta J_\nu}{J_\nu}\right)_2 = -\frac{x \exp(x)}{\exp(x) - 1} \frac{v_r}{c} \tau.$$



$$\frac{\Delta T}{T_r} = -\frac{v_r}{c} \tau_T$$

$$\frac{\Delta T}{T_r} = - \frac{4kT_e}{m_e c^2} \sigma_T N_e R.$$

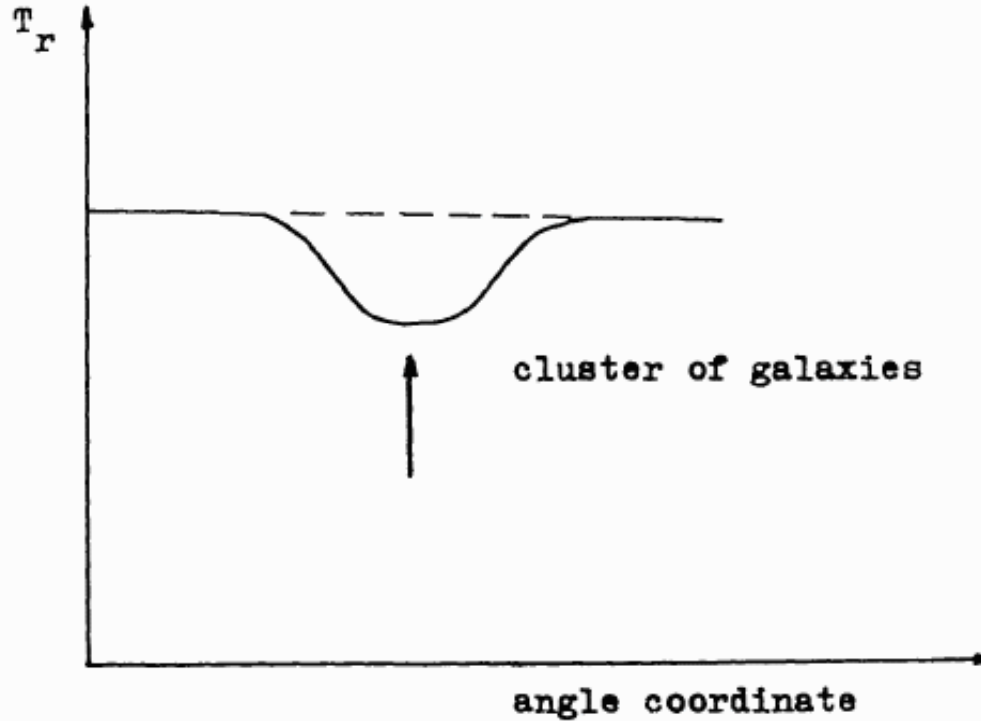


Figure 6 The decrease in the brightness temperature of the microwave background in the direction of a cluster of galaxies. This effect takes place only for $h\nu < 3.83kT_r$.

$$\frac{|\Delta I_\nu^{\text{RJ}}|}{I_\nu^{\text{RJ}}} \propto n_e L T_g ,$$

where L is the extent of the cluster along the line-of-sight. To obtain this relation, we replace the l -integration in (6.45) by a multiplication with L , which yields the correct functional dependence. On the other hand, the surface brightness of the X-ray radiation behaves as

$$I_X \propto L n_e^2 .$$

Combining these two relations, we are now able to eliminate n_e . Since T_g is measurable by means of the X-ray spectrum, the dependence

$$\frac{|\Delta I_\nu^{\text{RJ}}|}{I_\nu^{\text{RJ}}} \propto \sqrt{L I_X}$$

remains. Now assuming that the cluster is spherical, its extent L along the line-of-sight equals its transverse extent $R = \theta D_A$, where θ denotes its angular extent and D_A the angular-diameter distance (4.45) to the cluster. With this assumption, we obtain

$$D_A = \frac{R}{\theta} \sim \frac{L}{\theta} \propto \left(\frac{|\Delta I_\nu^{\text{RJ}}|}{I_\nu^{\text{RJ}}} \right)^2 \frac{1}{I_X} . \quad (6.46)$$

Physics of the SZ Effect

Cosmological Utility

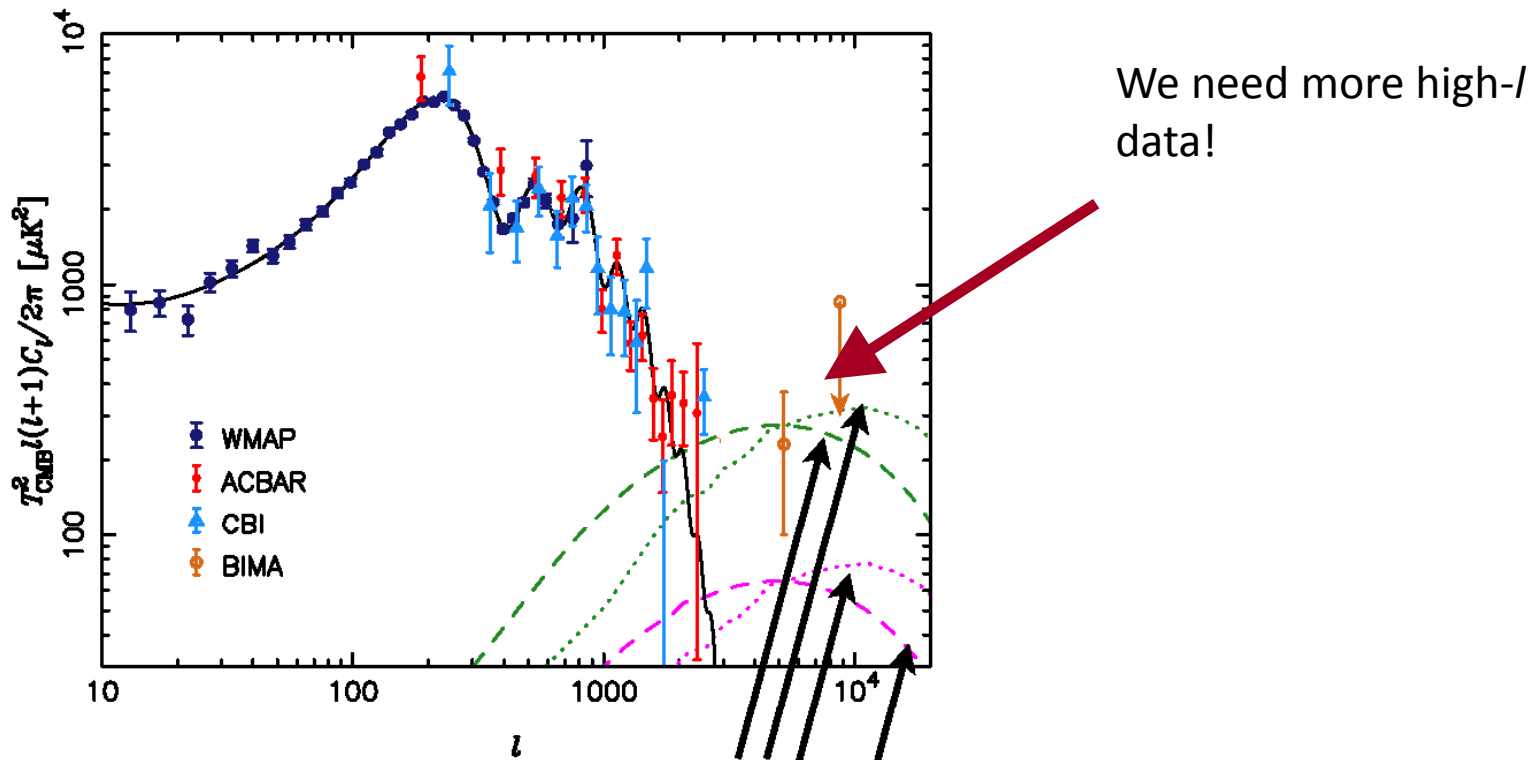
What can be measured when combined with other observations:

- H_0
- Cluster masses
- Cluster abundance as a function of redshift
- Ω , Λ , w
- Spectral index of initial perturbations (non-Gaussianity)
- Cluster evolution

Next, we'll discuss SZ observations and some results

Physics of the SZ Effect

The Angular Power Spectrum

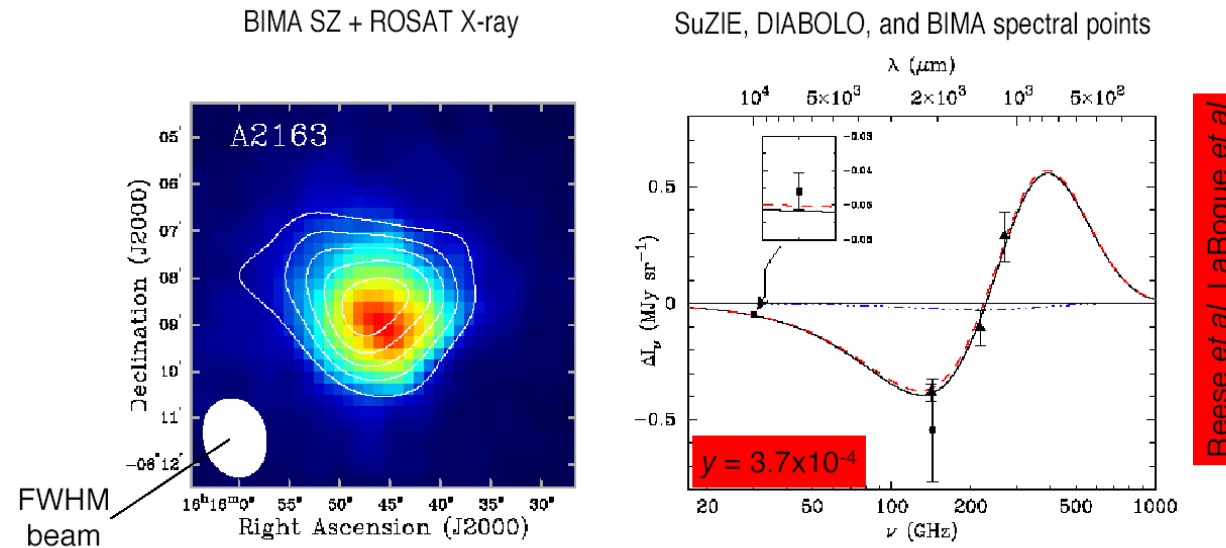


Green is 30 GHz, or 1 cm

Pink is 150 GHz, or 2 mm

Previous Observations

Images from Interferometers



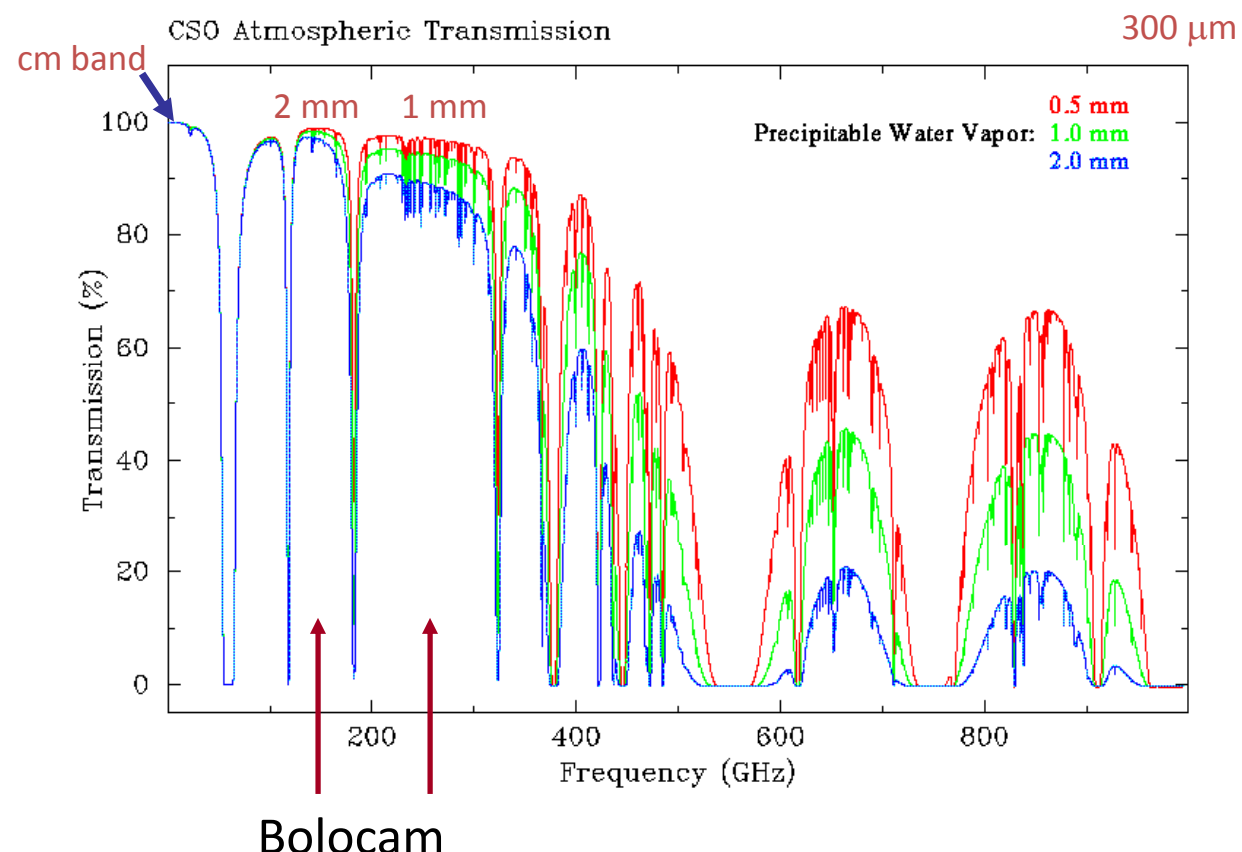
- Image from Carlstrom group using OVRO/BIMA interferometer at 30 GHz
- Spectral measurements a compendium – confirms spectrum through RJ tail
- To date, only pointed observations toward massive clusters
- Measurements of the kinetic effect will be very hard, depending on precision of multiband calibration

Atmospheric Noise

Emission, rather than absorption, is the primary problem: fluctuation in the arrival rate of background photons from water molecules in the sky (and the telescope, the ground, the instrument...)

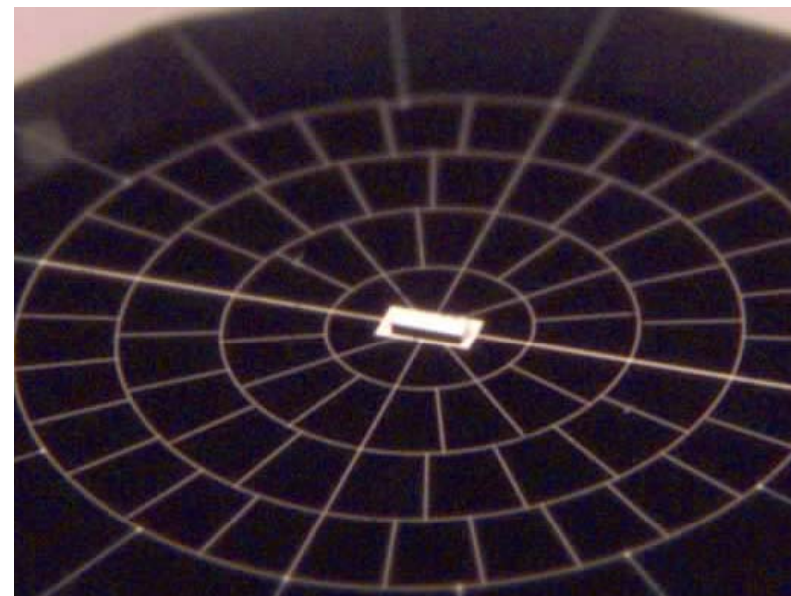
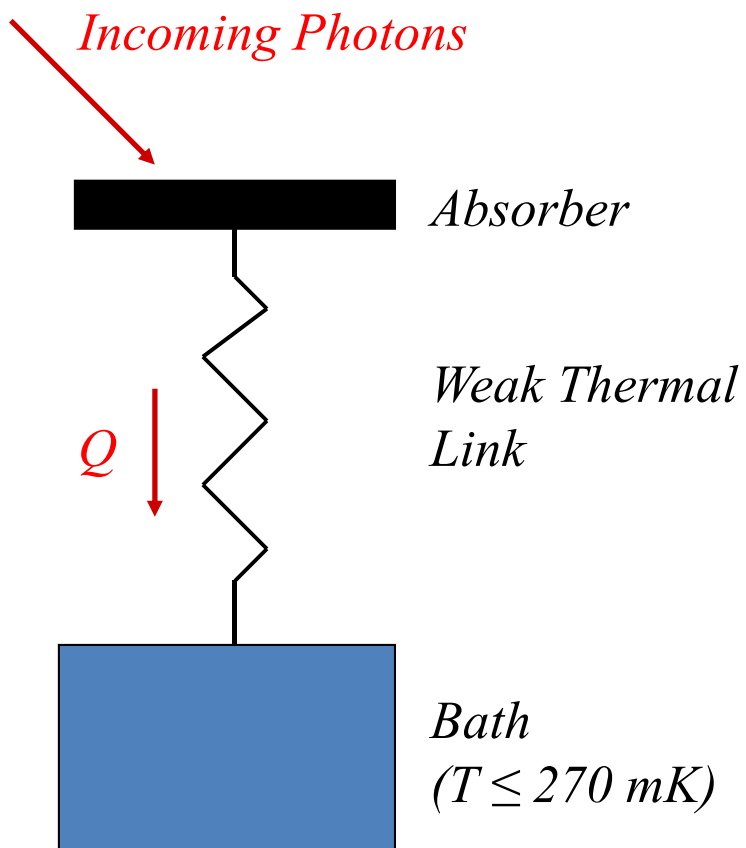
The sky over
Mauna Kea

*Emission = 1 -
Transmission*



Bolocam

Detectors



Si_3N_4 micromesh “spider web” bolometer
JPL Micro Devices Lab

Bolocam

Bolometers

In 1878, Samuel Pierpont Langley invented the bolometer.

Oh, Langley devised a bolometer:
It's really a kind of thermometer
Which measures the heat
From a polar bear's feet
At a distance of half a kilometer¹.

¹Anonymous

Bolocam

Bolometers

In 1878, Samuel Pierpont Langley invented the bolometer.

Oh, Langley devised a bolometer:
It's really a kind of thermometer
Which measures the heat
From a polar bear's feet
At a distance of half a kilometer¹.

¹Anonymous

With Bolocam on the CSO, we can detect a polar bear's foot with a S/N of one at a distance of 3 km in one second of integration time².

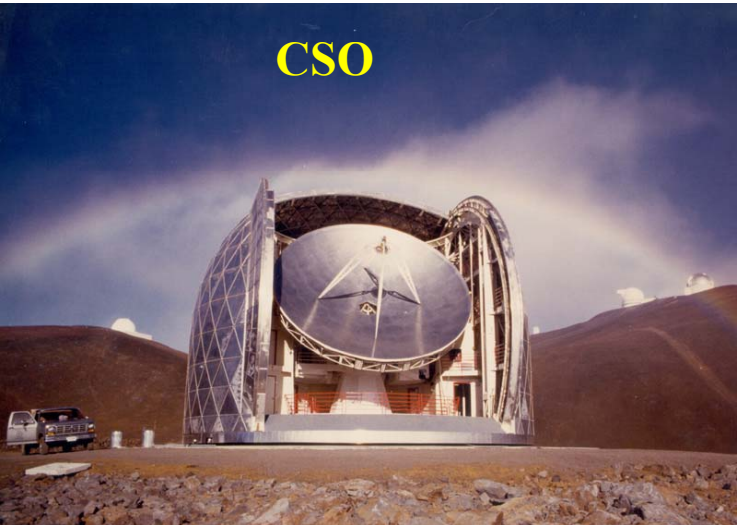
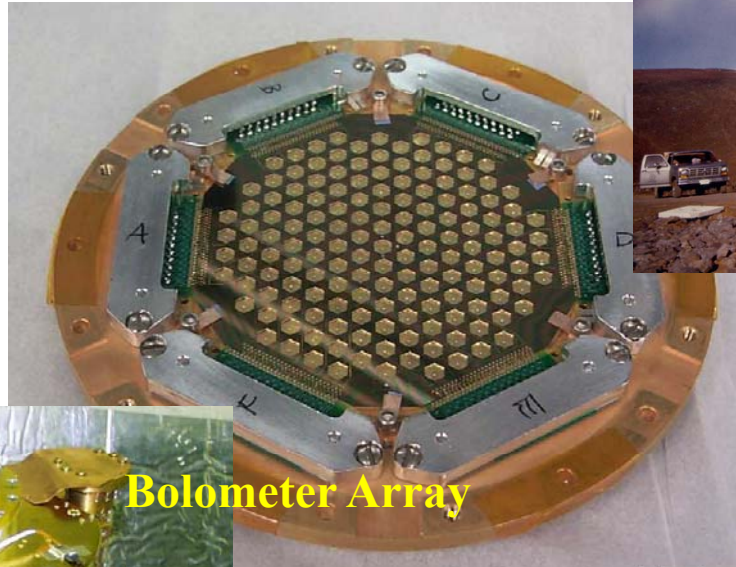
²(In good weather!)

Bolocam

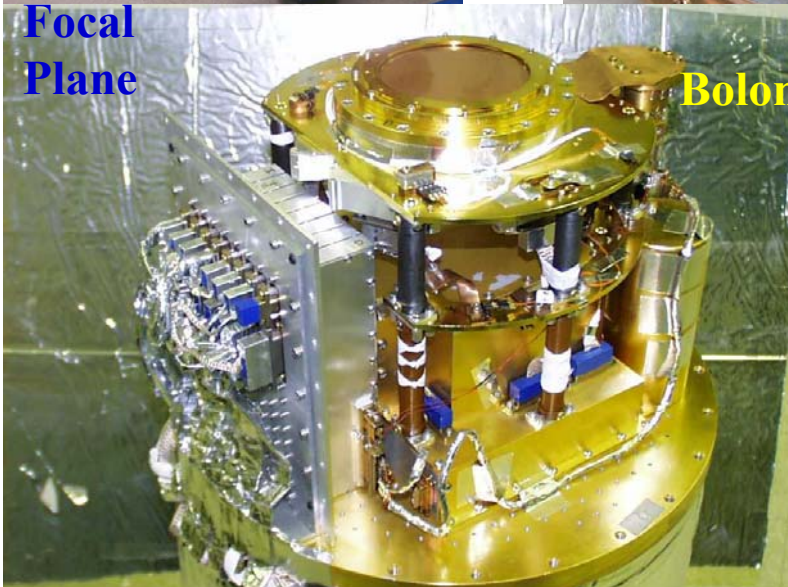


Instrument

← 5 in. →



Focal
Plane



- 144 bolometers
- $\lambda = 1.1, 2.1$ mm
- 300 mK

Imminent MM-Wave Experiments

High-l Anisotropies

- mm-wave experiments (in order of existence and site quality)

- Bolocam: 120 pixels at 150 GHz on 10.4 m CSO, Mauna Kea, data taken, being analyzed

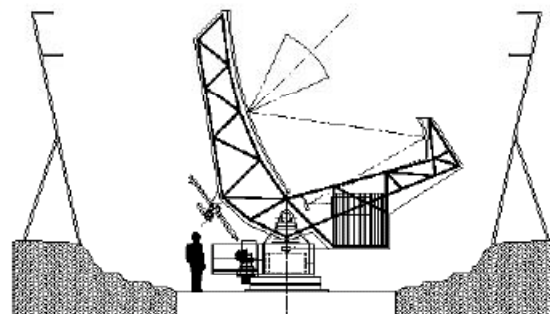
Bolocam/CSO



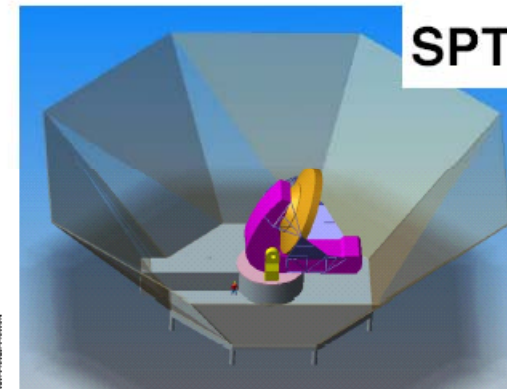
- APEX: 300 pixels at 150 GHz on 12 m ALMA prototype, ALMA site,
- ACT: 1000 pixels each at 150, 220, 275 GHz on 6-m off-axis az-scanning dish, Cerro Toco
- SPT: 1000 pixels distributed across 90, 150, 220, 275, 350 GHz bands on 10-m off-axis dish, South Pole



APEX



ACT



SPT

Nils

References

An excellent review from an observer's perspective and the source of some of the graphics in this lecture: "Cosmology with the Sunyaev-Zel'dovich Effect", Carlstrom, Holder, & Reese, ARAA, 2002, Vol. 40, pp. 643-680

- H0:

project (Reese et al. 2002). A fit to the ensemble of 38 SZE-determined distances yields $H_0 = 60 \pm 3 \text{ km s}^{-1} \text{ Mpc}^{-1}$ for an $\Omega_M = 0.3, \Omega_\Lambda = 0.7$ cosmology, where only the statistical uncertainty is included (at 68% confidence). The systematic uncertainty, discussed below, is of order 30% and clearly dominates.

relations from cluster simulations (Evrard 1997). The resulting mean gas mass fractions are $f_{gh} = 0.081_{-0.011}^{+0.009}$ for $\Omega_M = 0.3, \Omega_\Lambda = 0.7$, $f_{gh} = 0.074_{-0.009}^{+0.008}$ for $\Omega_M = 0.3, \Omega_\Lambda = 0.0$ and $f_{gh} = 0.068_{-0.008}^{+0.009}$ for $\Omega_M = 1.0, \Omega_\Lambda = 0.0$. The uncertainties in the electron temperatures contribute the largest component to the error budget.

the shape parameters (θ_c, β) from X-ray data, they found $v_{pec} = +490_{-880}^{+1370} \text{ km s}^{-1}$ for Abell 2163 and $v_{pec} = +170_{-630}^{+815} \text{ km s}^{-1}$ for Abell 1689, where the uncertainties are at 68% confidence and include both statistical and systematic uncertainties. These results are limited by the sensitivity of the SZE observations, which were limited by differential atmospheric emission. The SuZIE data for Abell 2163 were

Destruam os neurônios que armazenaram essa info depois de entenderem!!!!

Atacama Cosmology Telescope

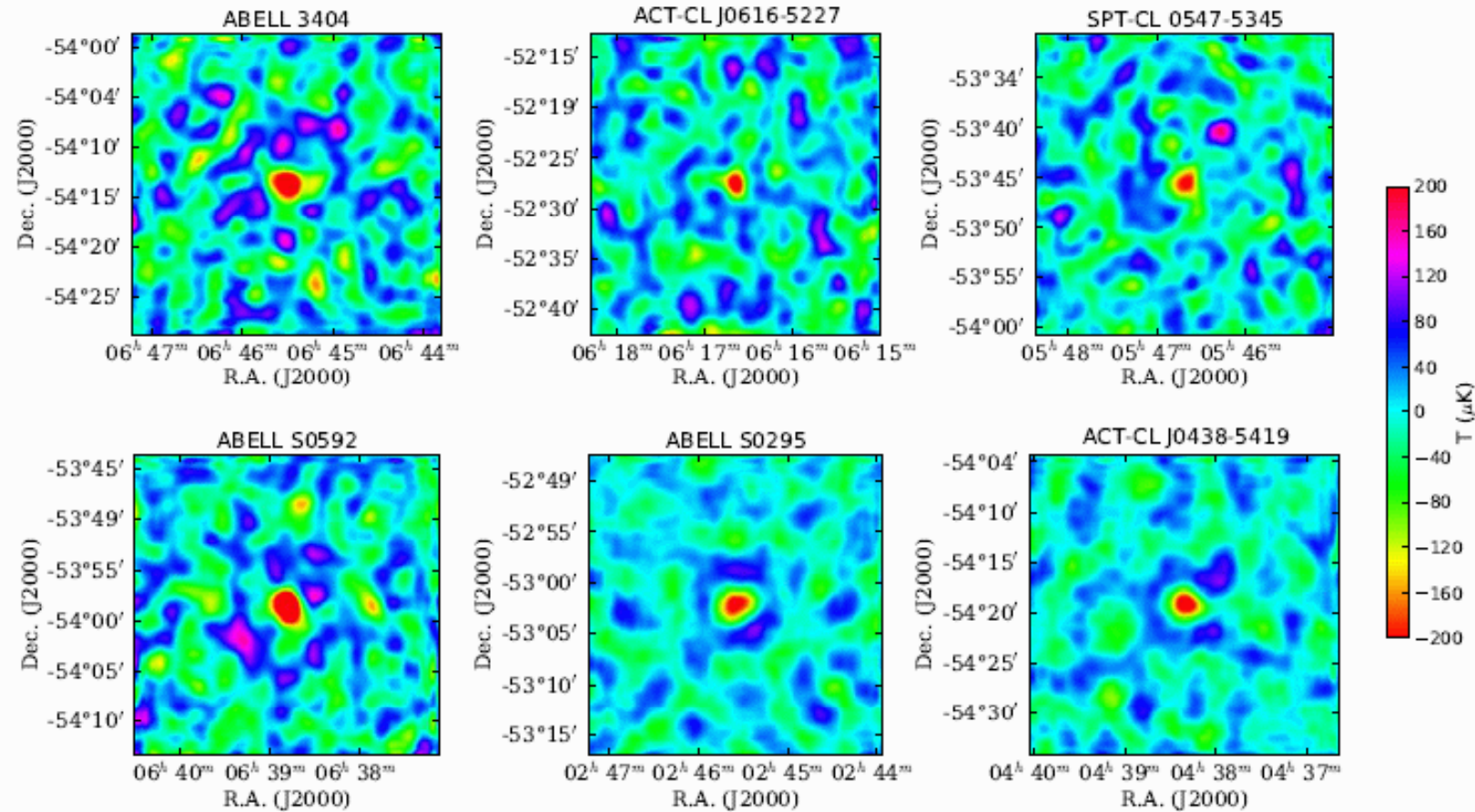


Figure 2: ACT maps of the 148-GHz SZ decrement in the vicinity of several known clusters and cluster candidates. The maps are in units of $\Delta T_{CMB} \mu\text{K}$ with colorbar shown at right. The ringing around (some of) the clusters is an artifact of the filter applied to best estimate the peak decrement.

South Pole Telescope

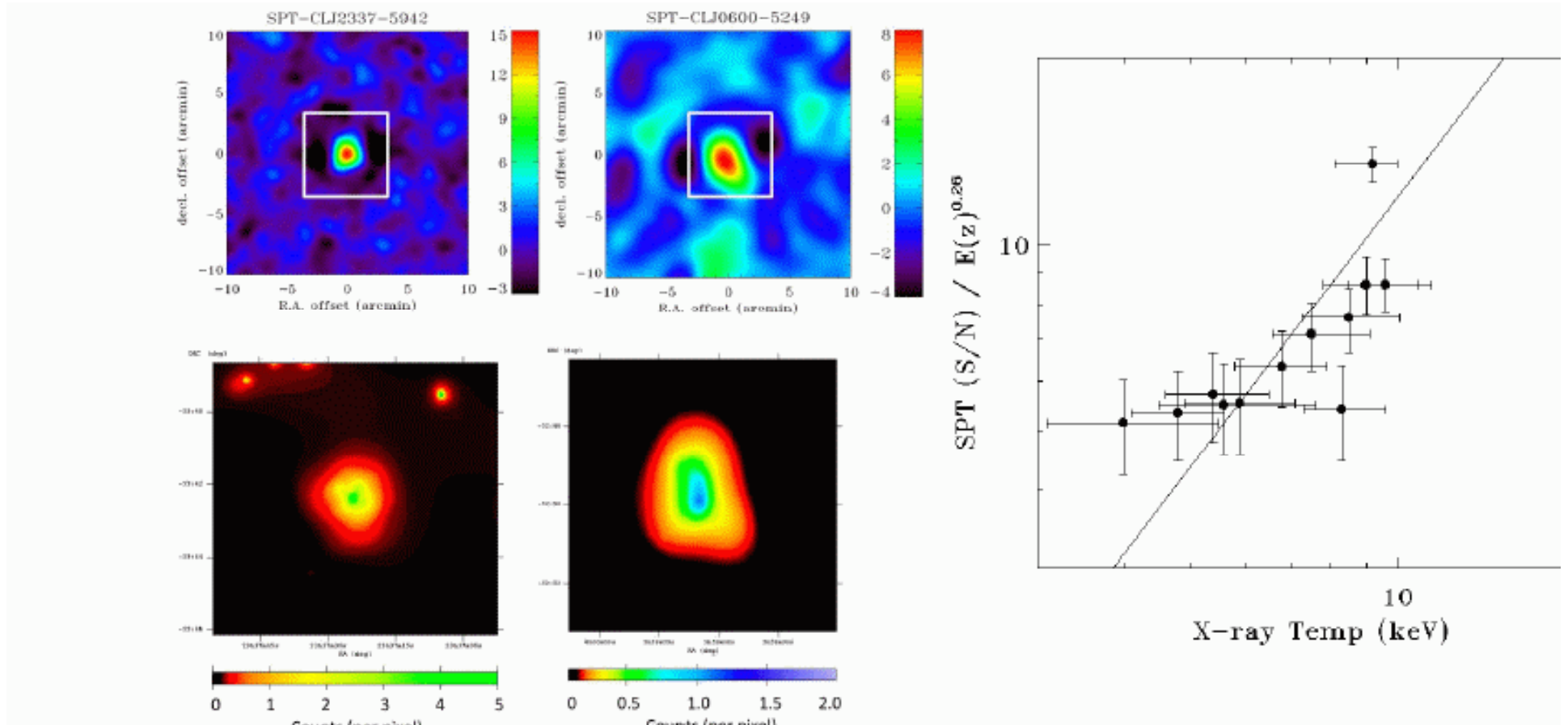


Fig. 1.— *Left panel:* (*Top*) SZ and (*Bottom*) X-ray images of SPT discovered clusters, (*Left*) SPT-CLJ2337-5942 ($z = 0.78$) and (*Right*) SPT-CLJ0600-5249 ($z = 0.60$). The SZ images are SPT optimally filtered 150 in units of S/N. The X-ray images are made from adaptively smoothed MOS images in the 0.35-2.0 keV

bloggerheads.com



$$\Delta I_\nu \approx 2 \frac{(kT)^3}{(hc)^2} \frac{x^4 e^x}{(e^x - 1)^2} [K(T_e, \nu) - \beta_r(b)] \tau(b) ,$$

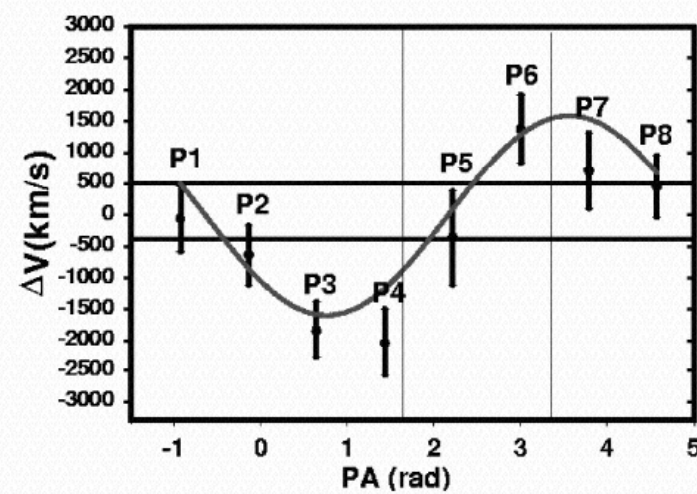
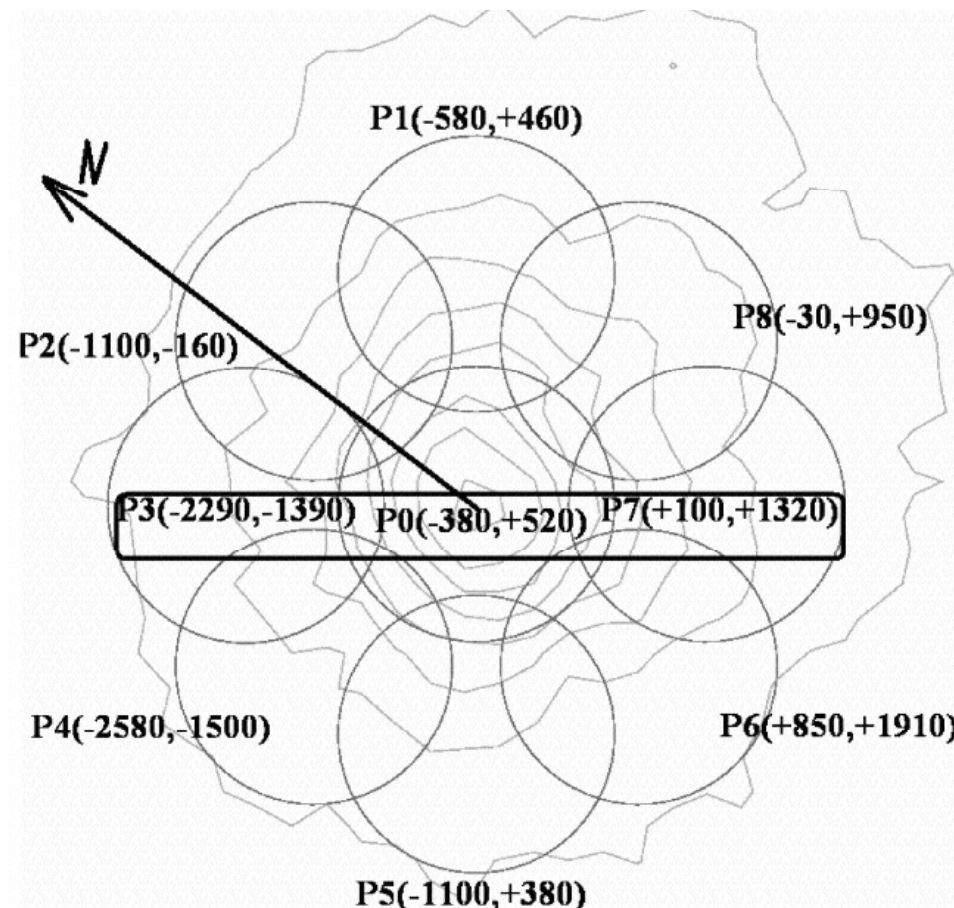
$$\left(\frac{\Delta I}{I}\right)_\nu \approx \frac{x e^x}{e^x - 1} [K(T_e, \nu) - \beta_r(b)] \tau(b) ,$$

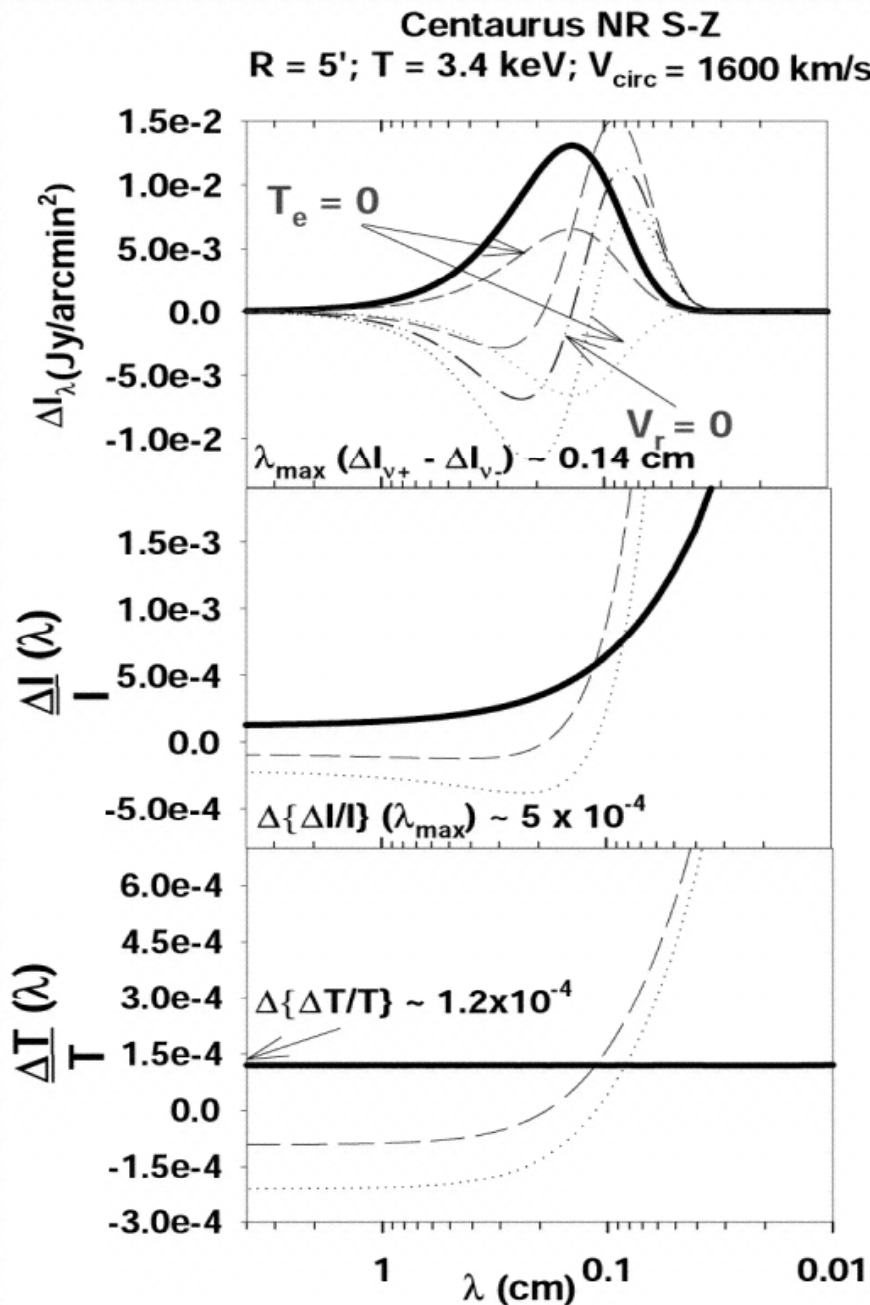
$$\left(\frac{\Delta T}{T}\right)_\nu \approx [K(T_e, \nu) - \beta_r(b)] \tau(b) ,$$

where

$$K(T_e, \nu) = \frac{kT_e}{m_e c^2} \left(x \frac{e^x + 1}{e^x - 1} - 4 \right) ,$$

$$\beta_r(b) = \frac{V_r(b)}{c}, \quad x = \frac{h\nu}{kT} ,$$



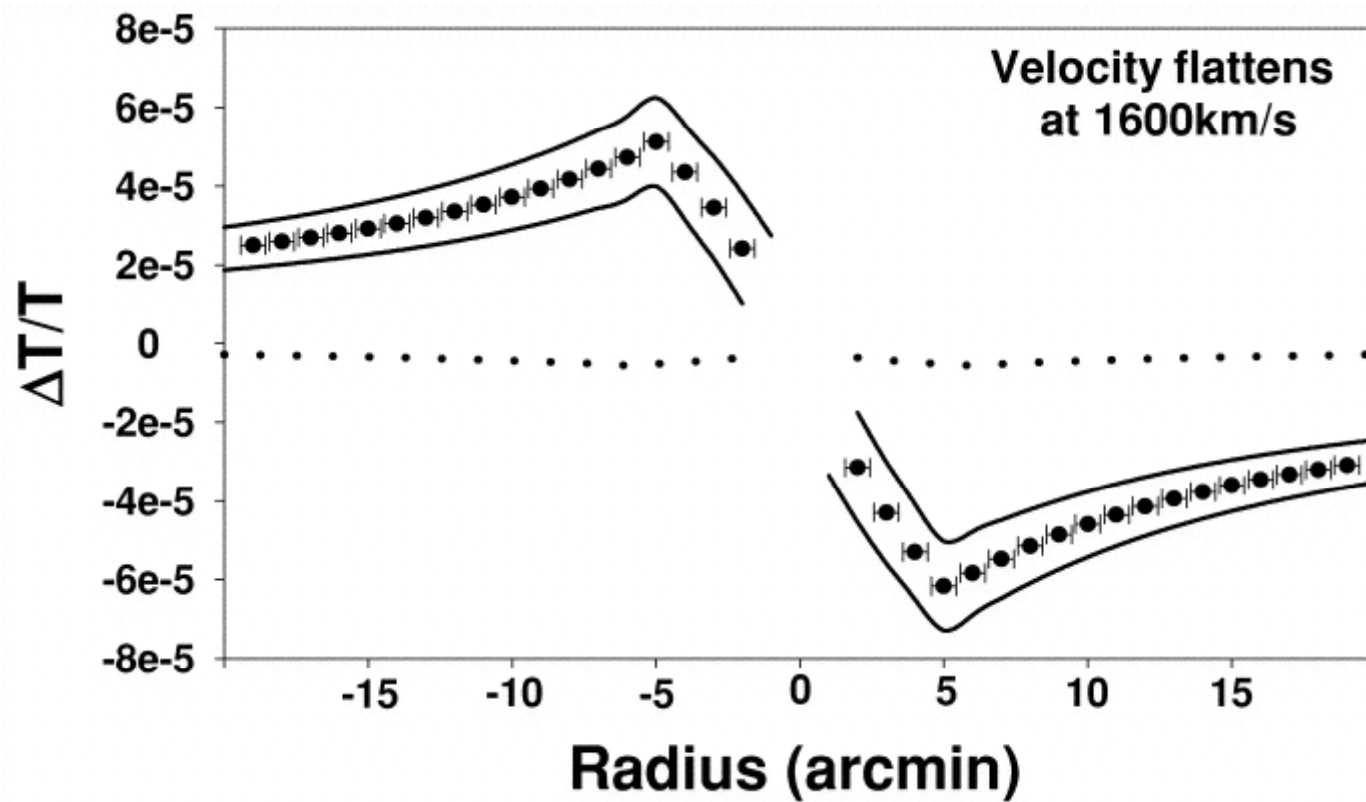


The long-dashed and dotted lines in all plots represent the curves for negative and positive values of radial velocity (V_r), respectively.

The dash-dotted line in the top plot shows the case for the thermal contribution alone ($V_r = 0$).

We also show the intensity variations for the kinetic component alone ($T_e = 0$) in the top plot only, for illustration.

In all plots the solid line shows the magnitude correspondent to the difference between the negative and positive V_r (differential variations). For intensity variations (*top plot*) this difference achieves a maximum at $\lambda = 0.14 \text{ cm}$ ($\nu = 214 \text{ GHz}$)



Missing Baryons

Redshift surveys of the nearby universe indicate that most galaxies occur in small groups

Typical group contains only a few luminous galaxies

$z \sim 0$

- Stars and Remnants in Galaxies
 - M/L ratio (corrected by morphology)
- Atomic and Molecular gas
 - HI surveys
 - H₂/HI ratios
- Baryons in clusters

$$n_{\text{cl}}(>M) = 4 \times 10^{-5} h^3 \left(\frac{M}{M^*} \right)^{-1} \exp \left(-\frac{M}{M^*} \right) \text{Mpc}^{-3}, \quad (15)$$

where $M^* = (1.8 \pm 0.3) \times 10^{14} h^{-1} M_\odot$, and M is the total gravitational mass within a sphere of radius $1.5 h^{-1} \text{Mpc}$

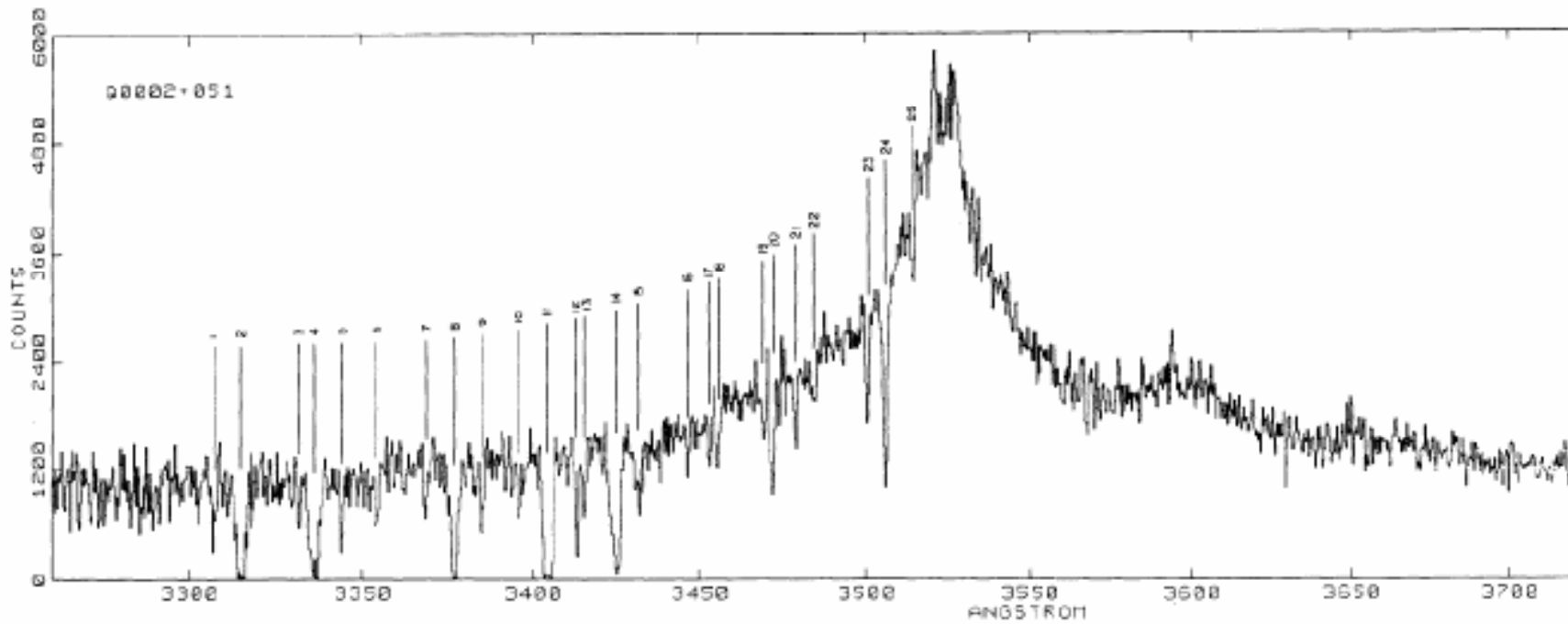
$z \sim 0$

- Similar for Groups
 - IGM
 - Field galaxies
 - Missed gas in groups
- Low surface density clouds (Ly α clouds)

- Voids
- MACHOS
- Dwarfs, LSBG

• $z \sim 3$

- LA systems



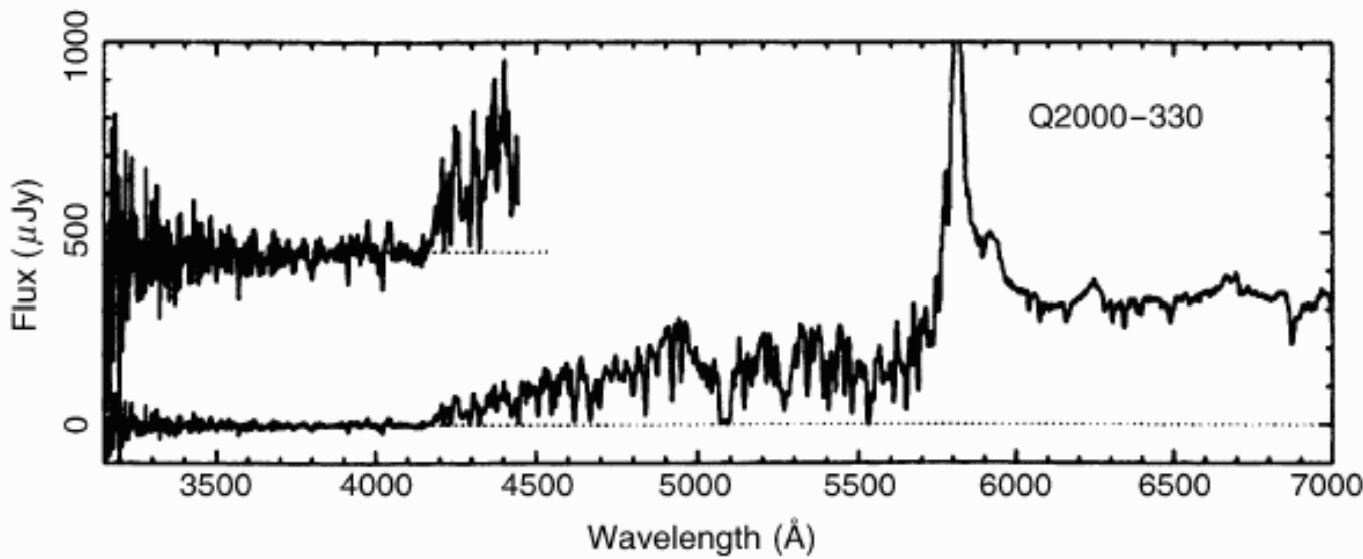


Fig. 5.41. A Lyman-limit system along the line-of-sight towards the QSO 2000–330 is absorbing virtually all radiation at wavelengths $\lambda \leq 912 \text{ \AA}$ in the rest-frame of the absorber, here redshifted to about 4150 \AA

Fukugita et al. 1998

THE BARYON BUDGET

Component	Central	Maximum	Minimum	Grade ^a
Observed at $z \approx 0$				
1. Stars in spheroids	$0.0026 h_{70}^{-1}$	$0.0043 h_{70}^{-1}$	$0.0014 h_{70}^{-1}$	A
2. Stars in disks	$0.00086 h_{70}^{-1}$	$0.00129 h_{70}^{-1}$	$0.00051 h_{70}^{-1}$	A-
3. Stars in irregulars	$0.000069 h_{70}^{-1}$	$0.000116 h_{70}^{-1}$	$0.000033 h_{70}^{-1}$	B
4. Neutral atomic gas	$0.00033 h_{70}^{-1}$	$0.00041 h_{70}^{-1}$	$0.00025 h_{70}^{-1}$	A
5. Molecular gas	$0.00030 h_{70}^{-1}$	$0.00037 h_{70}^{-1}$	$0.00023 h_{70}^{-1}$	A-
6. Plasma in clusters	$0.0026 h_{70}^{-1.5}$	$0.0044 h_{70}^{-1.5}$	$0.0014 h_{70}^{-1.5}$	A
7a. Warm plasma in groups	$0.0056 h_{70}^{-1.5}$	$0.0115 h_{70}^{-1.5}$	$0.0029 h_{70}^{-1.5}$	B
7b. Cool plasma	$0.002 h_{70}^{-1}$	$0.003 h_{70}^{-1}$	$0.0007 h_{70}^{-1}$	C
7'. Plasma in groups	$0.014 h_{70}^{-1}$	$0.030 h_{70}^{-1}$	$0.0072 h_{70}^{-1}$	B
8. Sum (at $h = 70$ and $z \approx 0$).....	0.021	0.041	0.007	...
Gas components at $z \approx 3$				
9. Damped absorbers	$0.0015 h_{70}^{-1}$	$0.0027 h_{70}^{-1}$	$0.0007 h_{70}^{-1}$	A-
10. Ly α forest clouds	$0.04 h_{70}^{-1.5}$	$0.05 h_{70}^{-1.5}$	$0.01 h_{70}^{-1.5}$	B
11. Intercloud gas (He II)	$0.01 h_{70}^{-1.5}$	$0.0001 h_{70}^{-1}$	B
Abundances of:				
12. Deuterium	$0.04 h_{70}^{-2}$	$0.054 h_{70}^{-2}$	$0.013 h_{70}^{-2}$	A
13. Helium	$0.010 h_{70}^{-2}$	$0.027 h_{70}^{-2}$...	A
14. Nucleosynthesis	$0.020 h_{70}^{-2}$	$0.027 h_{70}^{-2}$	$0.013 h_{70}^{-2}$...

^a Confidence of evaluation, from A (robust) to C (highly uncertain).

able. Recent analyses (Rauch et al. 1998; Weinberg et al. 1997) give

$$\Omega_{\text{baryon}} \geq 0.017 h^{-2} = 0.035 \quad (1)$$

from observations of the Ly α forest at $z = 2$, where Ω_{baryon} is the density in units of the critical density, $h \equiv H/100 \text{ km s}^{-1} \text{ Mpc}^{-1}$, and $h = 0.70$ is adopted for the last term in equation

The observed light-element ratios combined with standard nucleosynthesis allow us to compute the expected baryon density for standard models (Burlas & Tytler 1998) as

$$\Omega_{\text{baryon}} = (0.019 \pm 0.001)h^{-2} = 0.039 \pm 0.002 . \quad (2)$$

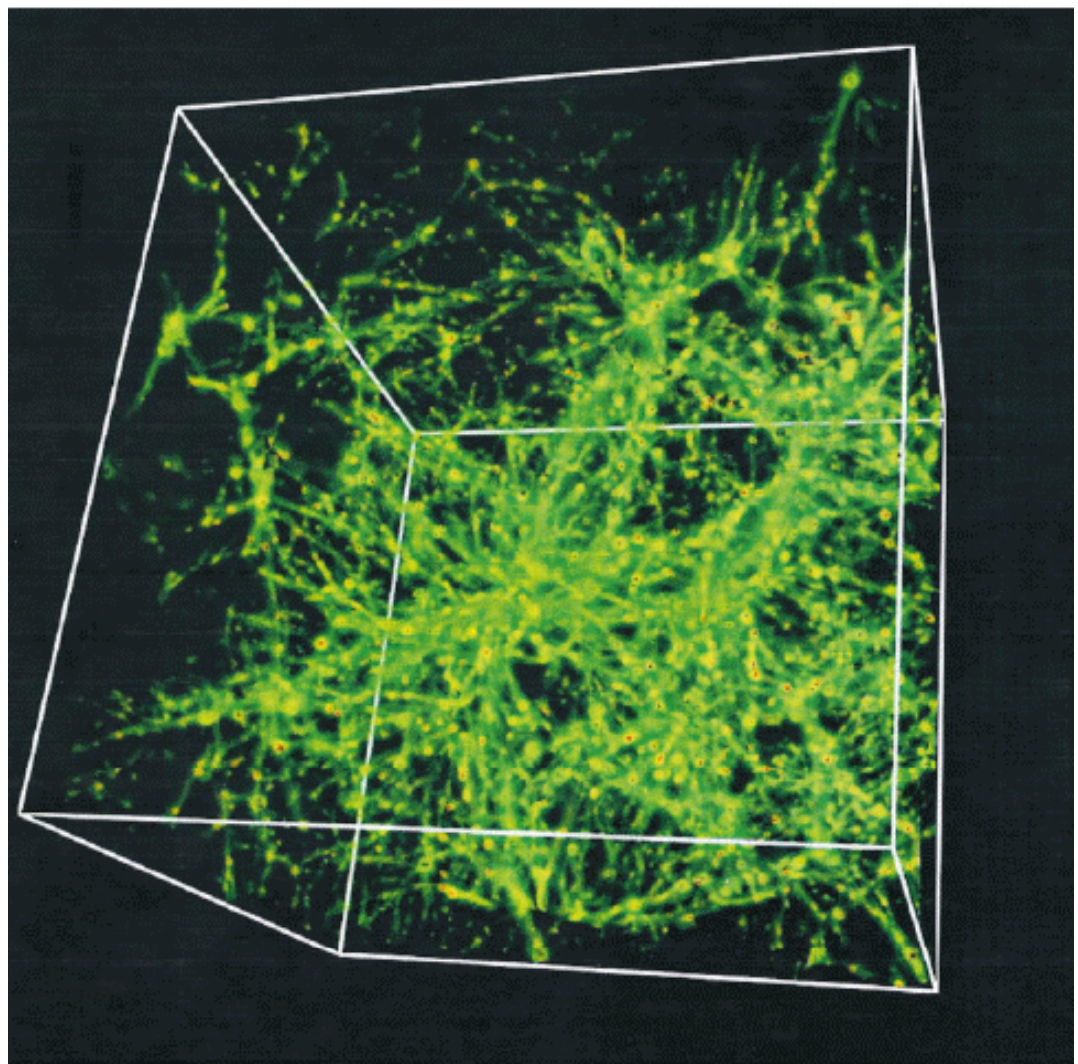
But at $z = 0$ in the present-day universe, every analysis (see, e.g., Fukugita, Hogan, & Peebles 1997) indicates that after summing over all well-observed contributions, the local baryon density appears to be far lower than indicated by equations (1) and (2):

$$\Omega_* + \Omega_{\text{H}_1} + \Omega_{\text{H}_2} + \Omega_{\text{X-ray, cl}} \approx 0.0068 \leq 0.011 \text{ (2 } \sigma \text{ limit)} ; \quad (3)$$

for $h = 0.70$. Thus either most of the baryons in the present day universe are yet to be detected, or a serious error has been made in the arguments that led to equations (1) and

$(\Omega_0, \Omega_b, \Lambda_0, \sigma_8, h)$ 0.37, 0.049, 0.63, 0.8, 0.7

Follow DM, gas, galaxies
Has feedback (SN, wind, UV)



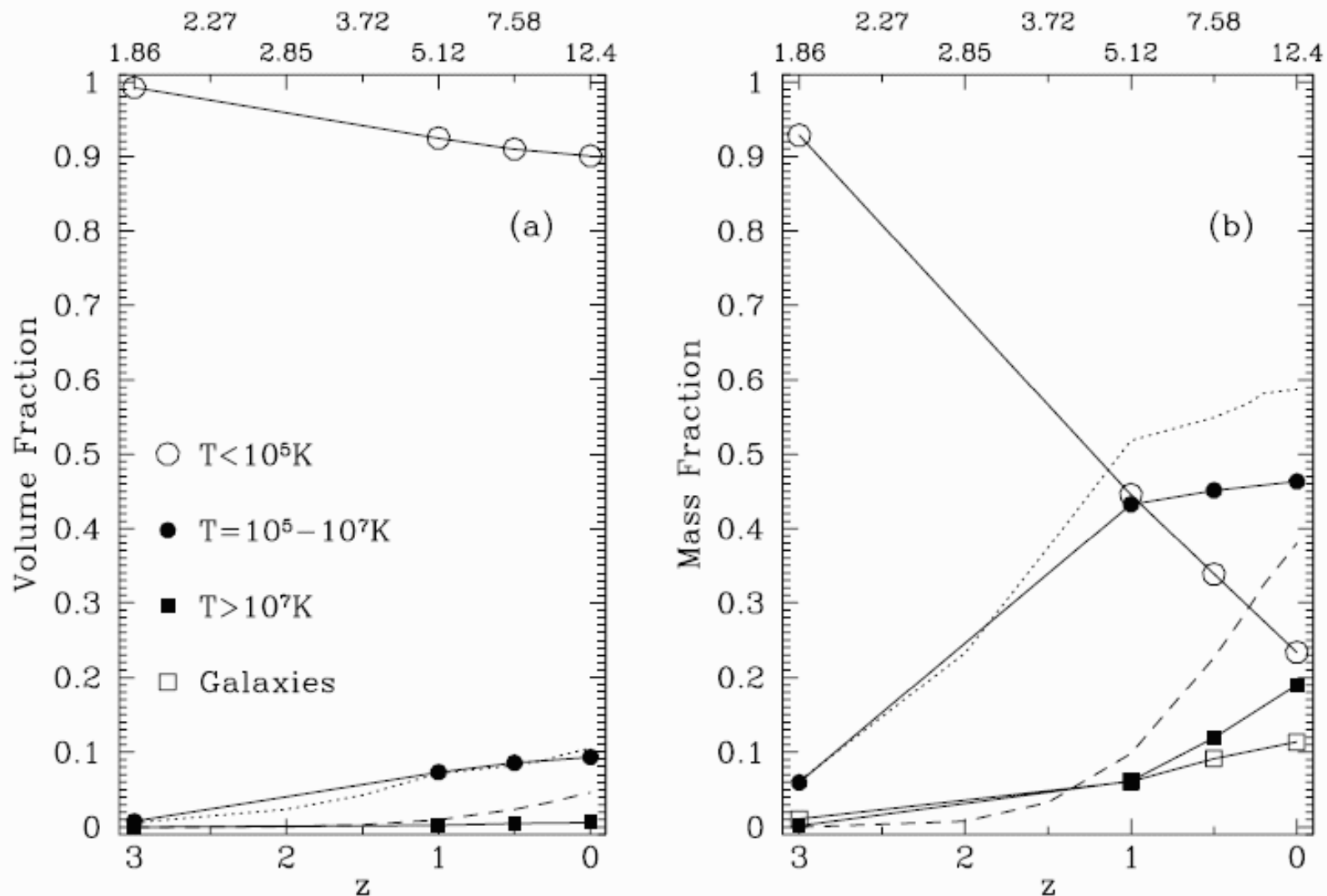
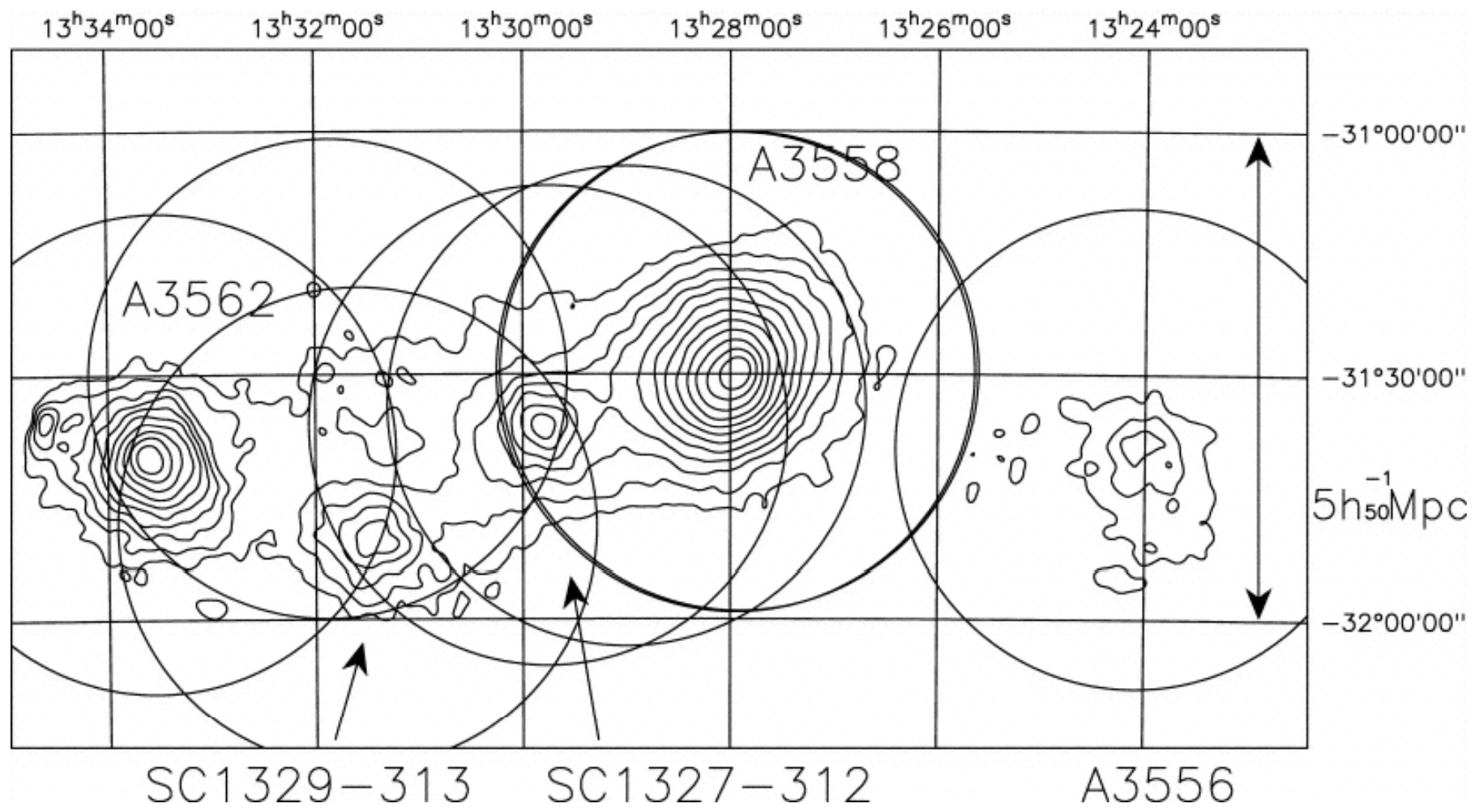


FIG. 2.—Evolution of the four components of cosmic baryons (see text for definitions). (a) Volume fractions of the four components in Gyrs, and (b) mass fractions in Gyrs. Examination of (b) shows that more than half of the baryons at redshift zero are in the temperature range $10^7 \text{ K} > T > 10^5 \text{ K}$. Also shown are the warm/hot components for two other models: an open CDM model with $\Omega_0 = 0.40$ and $\sigma_8 = 0.75$ (dotted lines), and a mixed hot and cold dark matter model with $\Omega_{\text{hot}} = 0.30$ and $\sigma_8 = 0.67$ (dashed lines). These two models were computed completely independently by Bryan & Norman (1998).



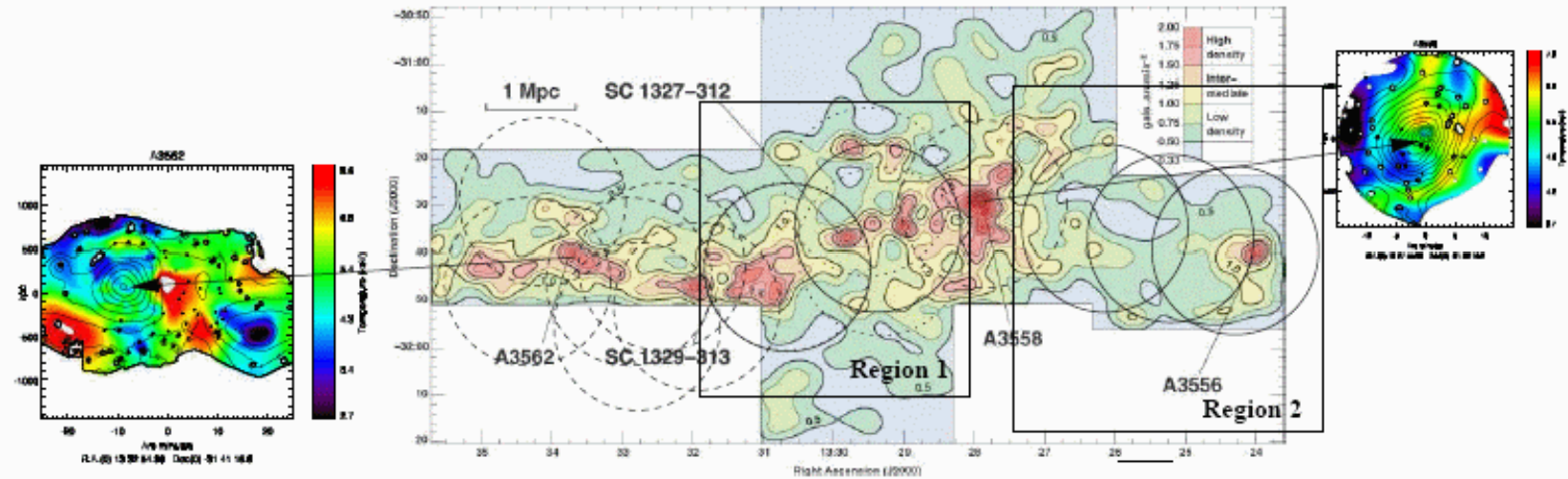


Figure 2: *Middle panel:* Surface density of $R < 21$ galaxies (Mercurio et al. 2006) overlaid to the XMM data set to be obtained including archive, AO8 (dashed and dotted circles) and required pointings (plain circles). *Right and left panels:* Temperature maps in the A3562 and a3558 regions obtained from archive pointings (spectral-imaging algorithm: Bourdin et al, 04).

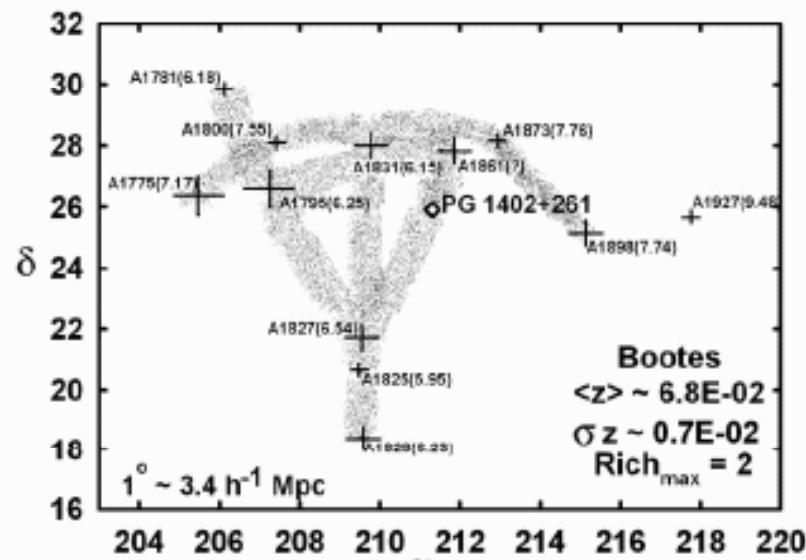


FIG. 1a

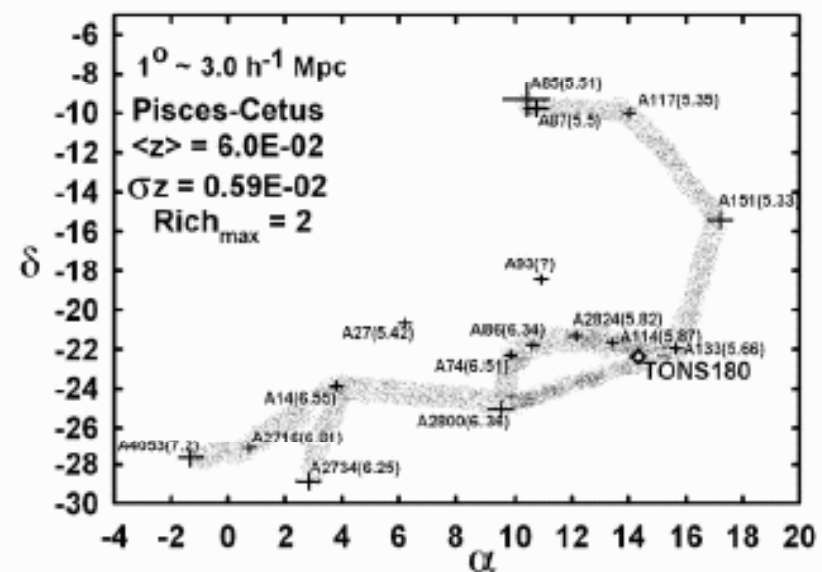


FIG. 1b

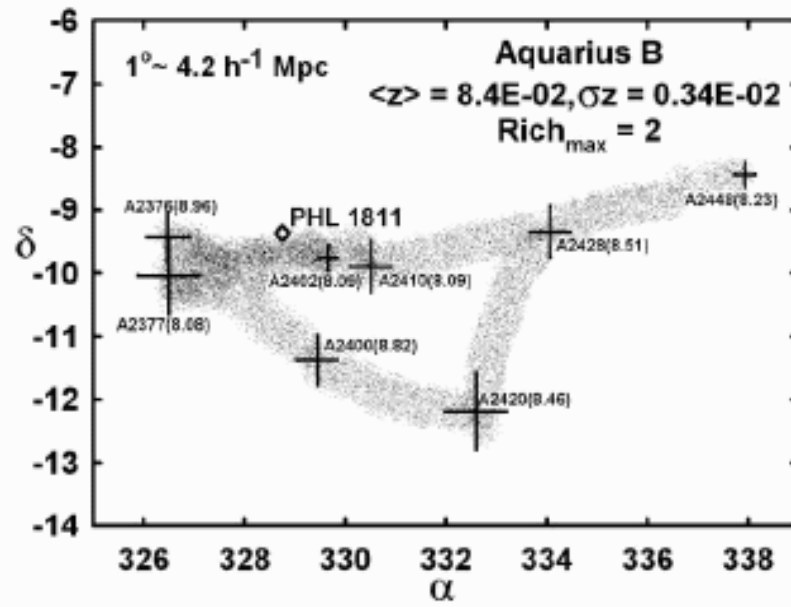


FIG. 1c

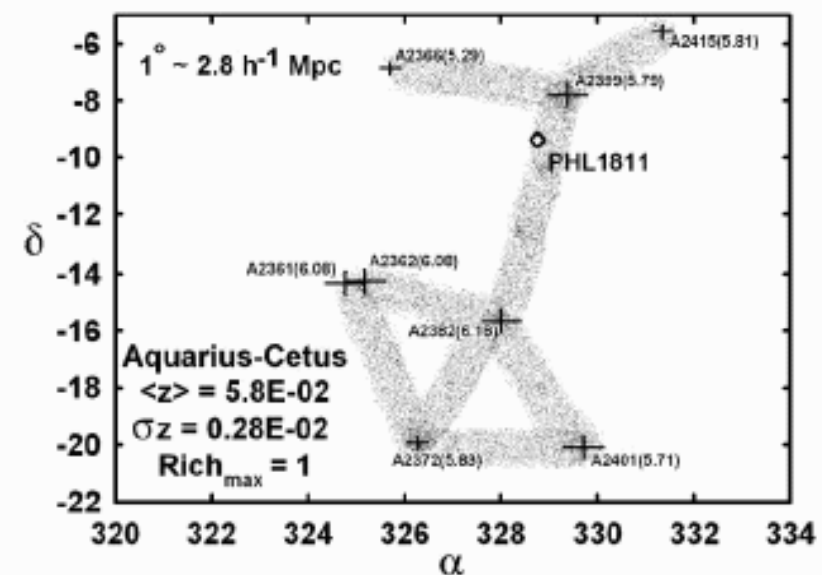


FIG. 1d

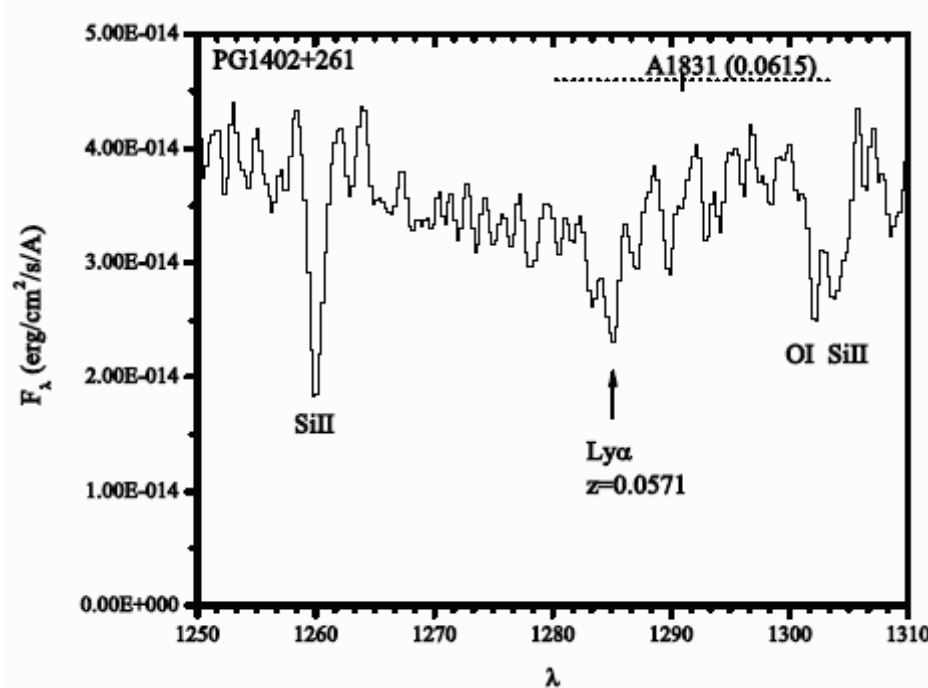


FIG. 2.—*HST* FOS spectrum of PG 1402+261, showing the strong Galactic lines of Si II and O I, as well as an unidentified absorption feature, which is most likely Ly α near the redshift of the Boötes supercluster. The dotted line indicates the region of expected absorption within ± 1300 km s $^{-1}$ of the redshift of the nearest cluster.

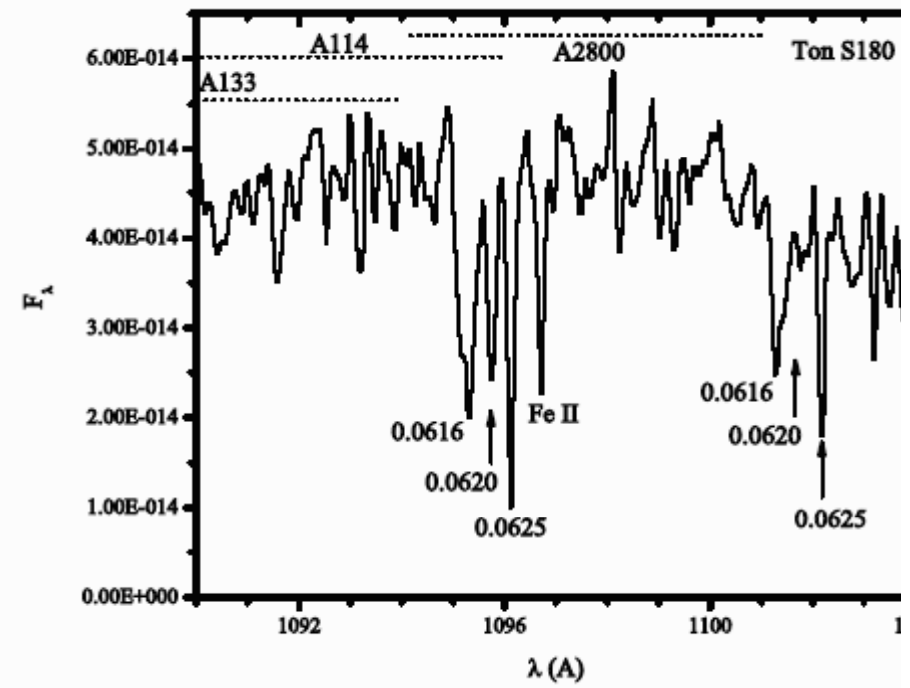


FIG. 3.—*FUSE* spectrum of Ton S180, showing three O VI absorption systems near the redshift of the Pisces-Cetus supercluster, as well as emission-line redshift of Ton S180. The lines have an FWHM of 0.1 which is close to the thermal Doppler width for gas at 3×10^5 K (0.11 Å). dotted line indicates the region of expected absorption within ± 1300 km s $^{-1}$ of the redshift of the nearest cluster.

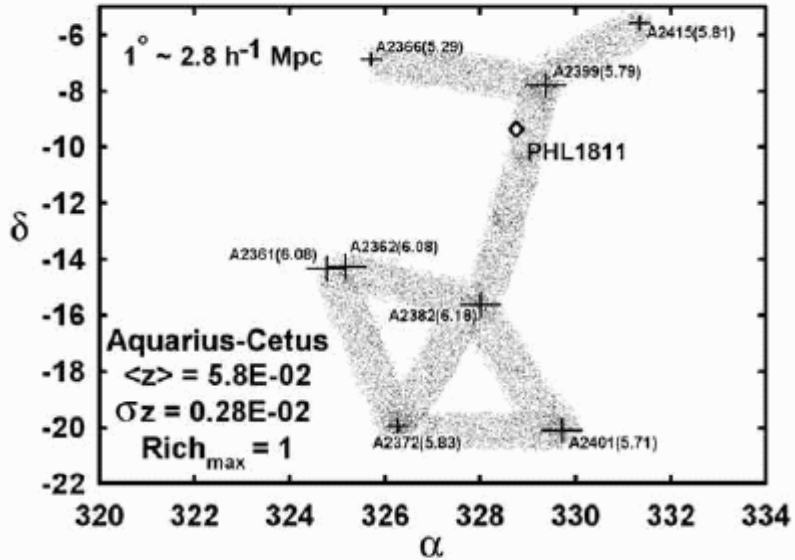
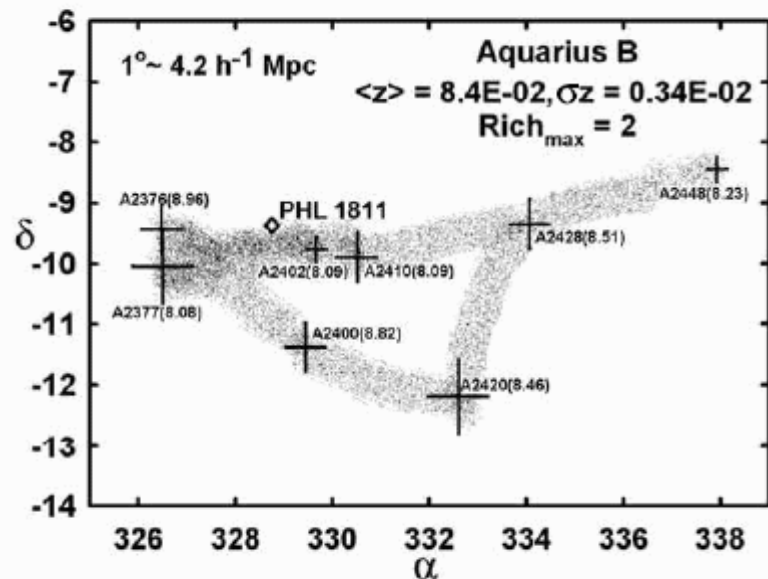
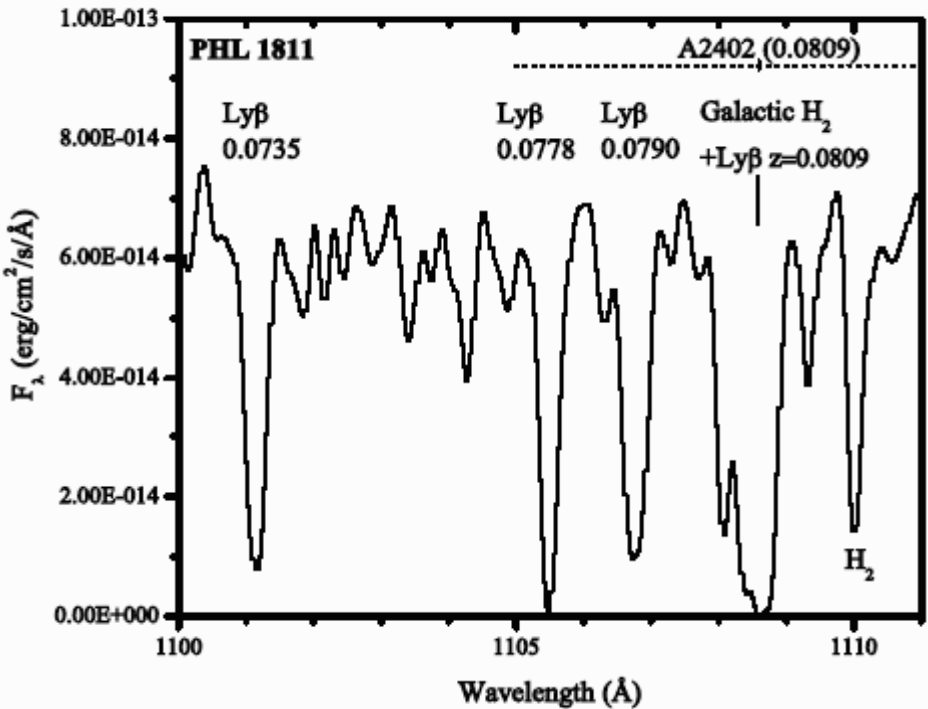


FIGURE 1. Spatial configuration of background A perclusters. The crosses are galaxy clusters (many indicates the relative richness. The linear grey st that are possible filaments projected near the ba proximity and cluster richness; these filaments ar the clusters in parenthesis (in units of 10^{-2}), the standard deviation of cluster redshifts in the sup



AGN	supercluster(s)	z_{AGN}	z_{SC}	HST	FUSE	$W_{\text{Ly}\alpha}$ (mÅ)	W_{OVI} (mÅ)	T_{max} (10^6 K)
PHL1811	Aquarius B	0.192	0.084	•	•	300	50	0.2
	Aquarius-Cetus	0.192	0.056	•	•	600	<250	1.0
PG1402+261	Bootes	0.164	0.068	•	•	300	<100	1.6
Ton S180	Pisces-Cetus	0.062	0.060	•	•	100	150	0.1
KAZ102	North Ecliptic Pole	0.136	0.087	•	...	400	...	6.4
H1821+643	North Ecliptic Pole	0.297	0.087	•	•	50	<150	0.4
WGAJ2153	Aquarius-Cetus	0.078	0.056	•	...	400	...	3.6
RXSJ01004-5113	Phoenix	0.062	0.027	•	...	<150
RXSJ01149-4224	Phoenix	0.124	0.027	○	○
HE0348-5353	Horologium-Reticulum	0.130	0.064	○
TEX1601+160	Hercules	0.109	0.035	○
Ton 730	Bootes	0.087	0.065	○	○

TABLE 1. Summary of AGN sightlines and detected absorption by intervening supercluster filaments. Filled circles indicate that data have been obtained for the given instrument while open circles indicate targets that have been approved. The last column shows the upper limit on the temperature of the absorbing medium, using the width of the narrowest absorption feature as an upper limit to thermal line broadening.

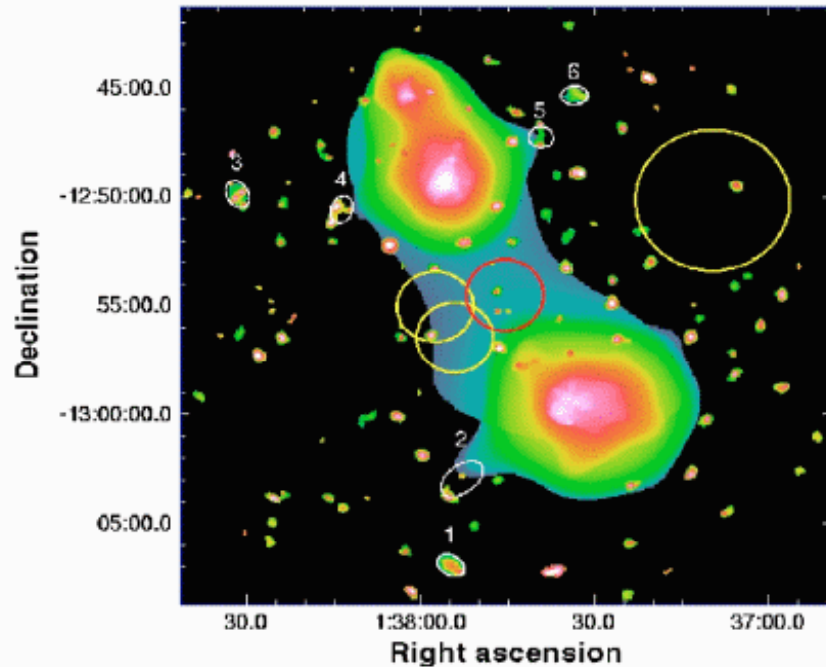


Fig. 1. Wavelet-decomposed 0.5–2.0 keV image of Abell 222 (to the South) and Abell 223 (the two X-ray peaks to the North). We show only sources with $>5\sigma$ detection, but for these sources we follow the emission down to 3σ . The filament connecting the two massive clusters is clearly visible in the image. The regions used to extract the filament spectrum and to determine the background parameters are indicated by red and yellow circles, respectively.

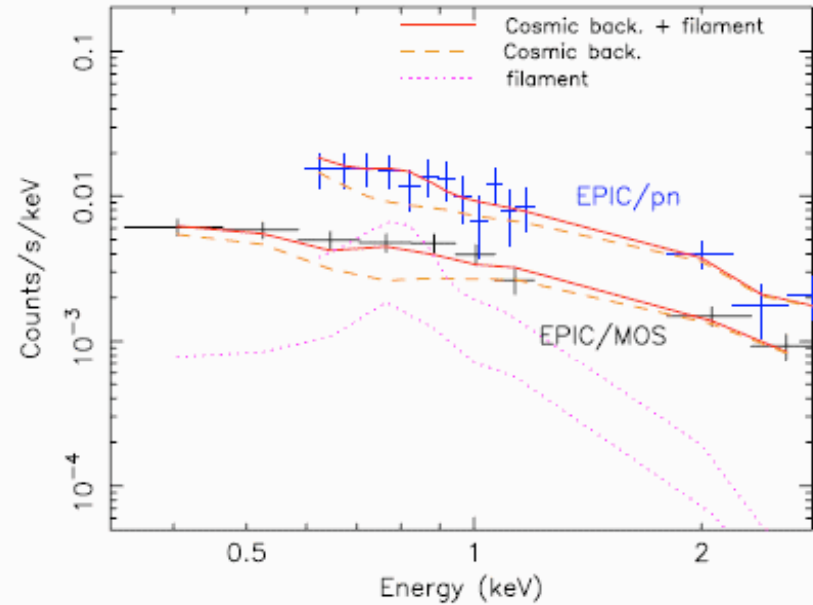


Fig. 2. The spectrum of the filament between the clusters A 222/223 – the data points on the top were obtained by EPIC/pn and below by EPIC/MOS. The contributions from the X-ray background and from the filament to the total model are shown separately.

To verify our result, we created an image modelling the

present observational evidence of X-ray emission from the filament connecting the two clusters. We detect the filament-decomposed soft-band (0.5–2.0 keV) X-ray image with a 5σ significance. Following the emission down to the noise level, the observed filament is ≈ 1.2 Mpc wide. The temperature of the gas associated with the filament, determined from $kT = 0.91 \pm 0.25$ keV, and its emission measure corresponds to a baryon density of $(3.4 \pm 1.3) \times 10^{-5} (l/15 \text{ Mpc})^{-1/2}$, where l is the length of the filament along the line-of-sight. This density corresponds to a baryon over-density of $\rho/\langle\rho_c\rangle \approx$